Petrophysics of Palaeogene sediments

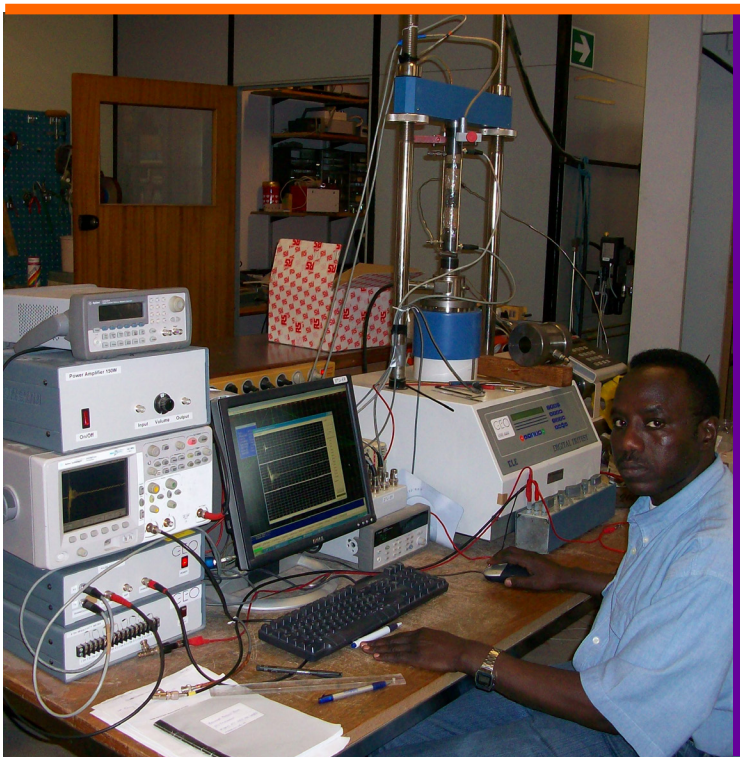

Ahmed Awadalkarim

PhD Thesis

Department of Civil Engineering

2014

DTU Civil Engineering Report R-299 (UK)
2014

DTU Civil Engineering
Department of Civil Engineering

Petrophysics of Palaeogene sediments

Ahmed Awadalkarim

Ph.D. Thesis

Centre for Energy Resources Engineering
Department of Civil Engineering
Technical University of Denmark

March 2014

Supervisor:

Professor Ida Lykke Fabricius, Technical University of Denmark (DTU), Lyngby, Denmark

Assessment Committee (Examiners):

Björn Johannesson, Associate Professor at Technical University of Denmark (DTU), Lyngby, Denmark

Mads Huuse, Professor at Manchester University, Manchester, England, UK

Niels Springer (Ph.D.), Senior Adviser emeritus, at Geological Survey of Denmark and Greenlad (GEUS), Copenhagen, Denmark

Petrophysics of Palaeogene sediments

Ph.D. dissertation

Printed by DTU-Tryk
Department of Civil Engineering
Technical University of Denmark
BYG report no. R-299
ISBN: 9788778773852
ISSN: 1601-2917

Dedication

It is with great pleasure to dedicate this Ph.D. thesis to Asma, Mohamed, Eathar and Emtenan for their patience during my absence from them.

Preface

This dissertation entitled “Petrophysics of Palaeogene sediments” has been prepared and submitted by Ahmed Awadalkarim, as a partial fulfilment of the requirements for the doctor of philosophy (Ph.D.) degree in petroleum engineering (petrophysics). The research presented in this Ph.D. thesis was conducted under the supervision of Professor Ida Lykke Fabricius at the Centre for Energy Resources Engineering (CERE), Department of Civil Engineering (DTU BYG), at the Technical University of Denmark (DTU). Most of the laboratory experiments in this thesis were carried out at DTU. Funding for the Ph.D. programme was provided by DTU for three years. External collaborators were involved in the successful completion of this Ph.D. study by providing samples, information and some data used in this thesis-related research.

The Ph.D. thesis consists of a report (part I), eight papers (part II), and appendixes with additional data, information and detailed XRD analyese methods (part III). The papers listed below comprise three scientific manuscripts submitted to ISI journals and five peer-read extended conference abstracts. The three journal articles represent the main sub-projects of the Ph.D. study that form the basis of the report in part I.

List of the papers:

I. ***Awadalkarim, A***. and Fabricius, I.L. 2013. Porosity and sonic velocity depth trends of Eocene chalk in Atlantic Ocean: influence of effective stress and temperature. Submitted to the Journal of Petroleum Science and Engineering.
II. ***Awadalkarim, A.***, Sørensen M.K. and Fabricius, I.L. 2014. Petrophysical analysis of siliceous ooze sediments, Møre Basin, Norwegian Sea. Petrophysics.
III. ***Awadalkarim, A***., Foged, N.N. and Fabricius, I.L. 2014. Elastic properties of Palaeogene clay from Fehmarn Belt area. Quarterly Journal of Engineering Geology and Hydrogeology.
IV. ***Awadalkarim, A***. and Fabricius, I.L. 2010. Burial diagenesis of Eocene chalk. In: Proceedings of the 72nd EAGE Conference & Exhibition incorporating SPE EUROPE 2010, held in Barcelona, Spain, 14–17 June 2010.
V. ***Awadalkarim, A***. and Fabricius, I.L. 2012. The influence of Biot’s coefficient on the estimation of vertical effective stress on deep-sea sediments. In: Proceedings of the 74th EAGE Conference & Exhibition incorporating SPE EUROPE 2012, held in Copenhagen, Denmark, 4–7 June 2012.
VI. ***Awadalkarim, A***., Altaie, M., Lyonga, A.K., Trads, N. and Fabricius, I.L. 2009. Estimating the effective stress in North Sea ooze In: Proceedings of the Sound of Geology Workshop held in Bergen, Norway, 6–8 May 2009.
VII. ***Awadalkarim, A***. and Fabricius, I.L. 2013. Petrophysical analysis of siliceous ooze sediments, Møre Basin, Norwegian Sea. In the 75th EAGE Conference & Exhibition incorporating SPE EUROPE 2013, London, UK, 10–13 June 2013.
VIII. ***Awadalkarim, A***., Foged, N. and Fabricius, I.L. 2013. Elastic deformation of Palaeogene clay from Fehmarn Belt. 76th EAGE Conference & Exhibition 2014, Amsterdam RAI, The Netherlands, 16-19 June 2014

Ahmed Awadalkarim
Lyngby, Kgs., Denmark
18 January 2014

Summary

Changes of physical properties of sedimentary rocks with increasing burial depth have implications in hydrocarbon explorations. Physical properties of buried sediment are controlled by several factors such as mineralogical composition, depositional texture and burial depth. The main theme for this Ph.D. study is petrophysics of Palaeogene sediments, aiming to gain better knowledge and understanding of the petrophysical characteristics of the studied sediments. To limit the scope, the Ph.D. study focused only on three selected lithologies: 1) the Eocene chalk of the Atlantic Ocean basins, 2) the siliceous ooze sediments from the Norwegian Sea, and 3) the Palaeogene shale from both the Atlantic and the Danish basins. The three geological settings differ in water depths, temperature, effective stress and pressure. If the factors governing physical properties of the studied lithologies are well defined and understood this would benefit various areas in petroleum industry.

The three studied litholgoies are relatively soft and weak sediments, but they are economically important especially in petroleum industry. Drilling through intervals of shale or siliceous ooze sediments could result in severe and very costly borehole instability problems which are closely connected with the "bulk properties" of shale. In practice, the main technological challenge is to keep the borehole sufficiently stable until casing is set. Knowing the real *in-situ* effective stress is crucial to understand and to predict the geomechanical behaviour of shale. Biot's coefficient (β) for elastic deformation is an important parameter involves in the estimation of effective stress. However, engineers usually assume β equal to one when estimating *in-situ* vertical effective stress on buried sediments, but, this assumption is not always right, especially for the deep-sea cemented sediments where the water depth is high, and it may underestimate the real effective stress which may lead to severe engineering consequences such as a petroleum reservoir may suffer compaction or deformations as a result of changing in stress state during drilling operations and hydrocarbon production, or even during massive excavations for building tunnels. If the effective stress exceeds the strength of the rock, failure develops. Thus, estimating a more realistic effective stress allows determining the optimum drilling parameters to reduce problems related to borehole stability. This Ph.D. study stressed on the importance of using correct β value in estimation of vertical effective stress especially on deep-sea sediments. To assess the geomechanical stability and the stiffness of the three studied lithologies, their β was found and used to calculate the *in-situ* vertical effective stress.

The primary objectives of this Ph.D. study were: 1) to investigate and evaluate the influence of mineralogical composition, depositional texture and burial depth on petrophysical properties of Palaeogene sediments and to find out how the physical properties are related; 2) to know the stiffness of the studied lithologies based on their β values; and 3) to link the diagenesis of siliceous ooze with logging interpretation. The secondary goals were: to show how crucial is the use the correct value of β on estimation of vertical effective stress especially on deep-sea sediments; to establish a relationship between static and dynamic modulus of shale which could be used to estimate geotechnical drained elastic modulus from bulk density and sonic velocity.

The influence of burial depth on physical properties of Atlantic Palaeogene shale and Eocene chalk has been studied. Changes in physical properties of the Atlantic Palaeogene shale as a function of burial depth was related to the vertical effective

stress and shale mineralogy. The influence of choice of β value on estimation of effective stress on deep-sea shale was shown. The obtained results could be relevant for drilling, basin analysis, seismic interpretation and hydrocarbon exploration. The diagenesis of Eocene chalk was studied. The changes of porosity and sonic velocity trends of the studied chalk were related to effective stress and time–temperature index (TTI) of thermal maturity of chalk. For each depth, effective stresses as defined by Terzaghi and by Biot were calculated. It is concluded that the use of the Biot's effective stress concept provides more realistic estimate of vertical effective stress of the studied chalk. Bottom-hole temperature data were used to calculate the TTI as defined by Lopatin. Porosity and compressional wave velocity data were correlated with effective stresses and to TTI. Based on the results, an equation to predict porosity reduction with increasing burial stress in chalk was proposed. The proposed equation is relevant for basin analysis and hydrocarbon exploration to predict porosity if sonic velocity (e.g. seismic velocity) data for subsurface chalk are available.

A possible hydrocarbon prospect of the Møre Basin siliceous ooze in the Norwegian Sea has been proposed, but siliceous ooze is significantly different in texture from most commonly known hydrocarbon reservoirs. This Ph.D. study includes results of petrophysical and the amplitude versus offset (AVO) analyses of siliceous ooze. Based on fundamental relationships, ways of correcting density and neutron porosity logs were proposed. Additionally, the values of β and the AVO signature of water saturated siliceous ooze were obtained. A new approach for deriving reliable and accurate porosity of siliceous ooze is proposed here. The true density porosity was calculated by taking the number of electrons per unit volume into account. The true density porosity is similar to the corrected neutron porosity which indicates that the proposed interpretation is consistent. The proposed approach can be applied elsewhere and could be useful for petrophysicis comunity. The studied siliceous ooze intervals apparently do not contain hydrocarbons.

X-ray diffraction (XRD) analyses and surface area by BET method have been done on 116 sediment samples collected from different geological units in the Fehmarn Belt area which is located between Denmark and Germany. Based on the XRD and BET results, ten preserved whole-core samples of the Palaeogene clay were selected and used in the laboratory testing for studying the elastic deformation properties of the naturally water saturated Palaeogene clay. Hence, this Ph.D. study presents the results of a wide characterization of Palaeogene clay. The main focus was on elastic properties which were examined and analysed in terms of mineralogical, physical and geotechnical properties. Elastic wave velocity is controlled by the elasticity and the density of a material. The deformation properties and the velocity of elastic waves were measured here simultaneously during triaxial testing under drained conditions. Geotechnical and elastic wave velocity data were used to model the elasticity and to relate it to clay mineralogy and BET. The mineralogy, BET, classification parameters, elastic wave velocities and strain caused by mechanical loading on the ten studied clay samples were measured and used together to interpret the geotechnical data and to observe the effect of mineralogy on elastic properties. The aim was to see which physical property is a main controlling factor for the elasticity of the Palaeogene clay and whether the deformation behaviour can be explained from elasticity alone. The obtained results can aid in the estimation of geotechnical drained elastic modulus from bulk density and elastic wave velocity and may have implications in engineering practice, including structural design and slope stability analysis.

Dansk sammendrag

De ændringer i sedimentære bjergarters fysiske egenskaber, der sker med stigende begravelsesdybde, har konsekvenser for kulbrinteefterforskningen. Bjergartens fysiske egenskaber styres af flere faktorer såsom mineralogisk sammensætning, aflejringstekstur og begravelsesdybde. Hovedemnet for denne ph.d.-afhandling er palæogene sedimenters petrofysiske egenskaber. Der fokuseres på tre lithologier: 1) Eocæne pelagiske kalkbjergarter fra Atlanterhavet, 2) kiselrigt slam fra Norskehavet, samt 3) palæogent ler fra Det nordtyske Bassin og Atlanterhavet. Det undersøgte materiale kommer således til samtidig at repræsentere forskellig havdybde, temperatur, effektivt stress og poretryk.

De tre lithologier er forholdsvis bløde sedimenter, men er samtidig økonomisk vigtige, bl.a. for olieindustrien. Boring gennem kiselslam eller ler kan betyde risiko for brøndustabilitet grundet bjergarternes egenskaber. I praksis er det største problem at holde boringen tilstrækkeligt stabil indtil foringsrører er isat. Kendskab til den effektive in situ spænding er afgørende for forståelsen og forudsigelsen af sedimenternes geomekaniske opførsel. Til bestemmelsen af den effektive spænding for elastisk deformation er Biot's koefficient, b, en nøgleparameter. I praksis antages det typisk at b er lig 1, men dette kan føre til fejl i vurderingen af det effektive stress, specielt hvis sedimenterne er cementererede og havdybden er høj. Det kan potentielt have alvorlige tekniske konsekvenser for forudsigelsen af reservoirbjergarters deformation under kulbrinteproduktion eller i forbindelse med store udgravninger ved for eksempel tunnelbyggeri. Hvis den effektive spænding overstiger bjergartens styrke kan der opstå sprækker, det er således relevant at kunne skønne en mere realistisk effektiv spænding. I denne ph.d.-rapport understreges vigtigheden af at bruge den korrekte værdi for b ved bestemmelsen af den effektive lodrette spænding for de tre studerede litologier og områder.

De primære mål for dette ph.d. studiun var 1) at undersøge og evaluere indflydelsen fra mineralogi, tekstur og begravelse på petrofysiske egenskaber og sammenhængen mellem disse egenskaber, 2) at bestemme de undersøgte sedimenters stivhed baseret på b, 3) at sammenkæde kiselsedimenters diagenese med tolkningen af petrofysiske logs. De sekundære mål var: at vise hvor afgørende b er for bestemmelse af den effektive spænding, specielt for dybhavssedimenter; at sammenligne statisk og dynamisk elasticitetsmodul for palæogent ler med henblik på at estimere geoteknisk drænet elasticitet ud fra densitet og hastighed af elastiske bølger.

Sammenhængen mellem begravelsesdybde formuleret som lodret effektiv spænding og fysiske egenskaber blev etableret for Atlanterhavets palæogene lerbjergarter og eocæne kalkbjergarter, og betydning af valget af b demonstreret. De opnåede resultater kan have betydning i forbindelse med boring, for bassinanalyse og ved seismisk tolkning. Betydningen af diagenesen af de eocæne kalkbjergarter blev undersøgt, idet porøsitet og hastighed af elastiske bølger vistes at relatere til effektiv spænding og termisk modenhed (TTI). De effektive spændinger for mekaniske kompaktion i henhold til Terzaghi blev sammenlignet med den effektive spænding for elastisk deformation i henhold til Biot. TTI blev estimeret ud fra bundhulstemperatur og biostratigrafi. Ud fra data blev der etableret en ligning der udtrykker porøsitet som funktion af det effektive stress. Ligningen kan have relevans for bassinanlyse og til forudsigelse af porøsitet ud fra seismiske data.

Det kiselrige slam i Mørebassinet i Norskehavet er et muligt mål for olieefterforskning, men det har væsensforskellig tekstur fra andre kulbrintereservoirbjergarter. Nærværende ph.d.-rapport indeholder petrofysisk tolkning og amplitude versus offset (AVO) analyse af dette kiselrige slam. Baseret på de grundlæggende principper for logrespons blev der udviklet metode til at analysere logs gennem disse lag med henblik på at bestemme porøsitet, b og AVO under vandmættede forhold. Densitetsloggen blev tolket ved at tage udgangspunkt i antallet af elektroner per volumen, og den herved beregnede porøsitet svarer til neutronporøsiteten når denne er korrigeret for mineralernes hydrogenindex. Den foreslåede metode bør også kunne anvendes andre steder. Det undersøgte kiselslam indeholder tilsyneladende ikke kulbrinter.

Der blev udført røntgendiffraktionsanalyse (XRD) og måling af specifik overflade (BET) på 116 prøver fra forskellige geologiske enheder i Femern Bælt. På grundlag af resultaterne blev 10 intakte vandmættede kerneprøver af palæogent ler udtaget til laboratorieanalyse med henblik på at undersøge materialets elasticitet. Under de drænede trykforsøg med enakset deformation blev tøjningen målt samtidig med hastigheden af elastiske bølger, således at den udrænede elasticitet kunne beregnes og relateres til mineralogi, BET og klassificeringsparametre, så at de styrende parametre kunne identificeres. Det blev også sandsynliggjort at deformationen af dette ”plastiske ler” kan beskrives som elastisk deformation af lerets faste ramme som ses at have b lavere end 1. Disse resultater kan betyde at geoteknisk drænet elasticitetesmodul kan vurderes ud fra densitet og hastighed af elastiske bølger, hvilket kan have betydning i ingeniørmæssig praksis.

Acknowledgements

I would foremost like to thank my principal supervisor Professor Ida Lykke Fabricius, from DTU BYG, for her continued advices and valuable guidance during the course of my Ph.D. programme. She has been providing both critical feedback on all of the various research projects and endeavours as well as providing motivational support. I would also like to thank DTU for financial support and for giving me this opportunity to undertake the Ph.D. programme. Furthermore, there are external collaborators such as DONG Energy and Rambøll Denmark A/S whom I would like to acknowledge. They were instrumental in the successful completion of two research projects. The Femern A/S, Danish Geotechnical Institute (GEO) and Rambøll A/S are thanked for supplying Palaeogene clay samples for the study. I am also grateful to Femern A/S for facilitating access to its database of results, of the Fehmarn Belt Fixed Link project, for research purposes.

I am so grateful to my colleague Mohammad Monzurul Alam for offering invaluable assistance in many technical aspects during my Ph.D. study. I thank Sinh Hy Nguyen from DTU Environment and Vita Ruth Larsen from DTU BYG for their technical assistances in the laboratory work on Palaeogene clay. During my Ph.D. study, I have benefited from discussions with many colleagues and friends; I thank all of them, especially Pilar Clemente, Ernest Ncha Mbia and Morten Kanne Sørensen.

Outside of the academic research life, I would also like to especially thank and acknowledge the wonderful support of my dear wife, Asma, and for her patience, consideration, understanding and unconditional support. She has been taking care of our children during my Ph.D. study, and I am eternally grateful for that as well. Dear Asma, without your love, moral support and continuous encouragement, the successful completion of this study would have been impossible. Especial thanks must also go to my dear son Mohamed and my dear daughters Eathar and Emtenan for their patience, respect and cooperation with their mother Asma during my long absences from the family.

Ahmed Awadalkarim
Lyngby, Kgs.
18 January 2014

Contents

Part I: Report

1. Introduction

This section of the report comprises an overview of the more significant points in this Ph.D. research project. It aims to illustrate the key points that have been addressed during this Ph.D. study and why. It explains what the investigated problems are, and why they are important for study. The main objectives and what have been done to achieve them were also stated. Finally, the structure of the report is also explained.

1.1. Statement of the problems and the scope of study

Changes of physical properties of sedimentary rocks with increasing burial depth have implications in hydrocarbon explorations. Physical properties of a buried sedimentary rock are controlled by several factors such as mineralogical composition, depositional texture and burial depth (burial temperature, overburden stress, effective stress, pore-fluid pressure and time) of a rock. The main theme for this Ph.D. study is petrophysics of Palaeogene sediments, aiming to gain better knowledge and understanding of the petrophysical characteristics of the studied sediments. To limit the scope, the Ph.D. study focused only on three lithologies: 1) the Eocene chalk of the Atlantic Ocean basins, 2) the Eocene to Mid Miocene siliceous ooze sediments from the Norwegian Sea, and 3) the Palaeogene shale from both the Atlantic Ocean basins and the Danish basin. The three selected geological settings differ in water depths, temperature, effective stress and pressure. Sediments of the Danish basin have maximally been buried to stress equivalent to about 500 m burial depth or shallower, pressure and temperature conditions are presumably normal. In the Norwegian Sea, there is no evidence for overpressure within the intervals of the studied siliceous ooze sediments, whereas in the Atlantic Ocean temperature is low due to the deep cold ocean water.

The three selected litholgoies are characterised as relatively soft sediments composed of fine to very fine grains and having high porosity and relatively low permeability, yet, they are cemented. All the three studied lithologies are economically important. For example, chalk is a porous rock, it can hold a large volume of fluids; hence, it may form a petroleum reservoir (as in the North Sea) or ground water aquifer (as in Denmark). Chalk can be used also as a raw material for cement industry or as a building material. The rock diatomite is an equivalent example of the siliceous ooze deposits. It is a commercial rock because combinations of its physical and chemical properties make it suitable for many specialized applications, especially for filtration, as an absorbent for industrial spills and in many other industrial purposes (Moyle and Dolley 2003). Some siliceous ooze deposits (e.g. diatomite), such as the Monterey Formation in California, USA, contain significant petroleum sources (Moyle and Dolley 2003). Experience has shown that drilling through intervals of siliceous ooze sediments results in borehole instability problems. Shale is the most common sedimentary rock worldwide and it is very important lithology in petroleum industry. It could be a source rock for hydrocarbons, or a seal (cap rock) that prevents hydrocarbons to migrate beyond the reservoir. Shale could also be a gas reservoir (i.e. shale gas). In petroleum industry, shale makes up more than 75% of drilled formations and causes more than 90% of borehole instability problems (Mody and Hale 1993). Drilling through shale layers could result in severe and very costly borehole instability problems as in some North Sea fields. Borehole instability problems are closely connected with the "bulk properties" of the shale, such as stiffness (rigidity/hardness) and strength as a function of depositional environment, porosity, water content, clay

content, minerals composition, and compaction rates. Other factors such as *in-situ* stresses, pore pressure, temperature, time in and length of open-hole interval, depth, and surrounding geological environment are also important. These variables are interconnected and influence the overall behaviour of shale during drilling and directly affect borehole stability. In practice, the main technological challenge is to keep the borehole sufficiently stable until casing is set. Knowing the real *in-situ* effective stress is crucial to understand and to predict the geomechanical behaviour of shale. Biot's effective stress coefficient (β), which is also known as Biot's coefficient for elastic deformation, is an important parameter involves in estimation of effective stress. β is an indicator for sediment elastic stiffness. It is an indicator of how well grains of a sediment are in contact to each other. If β equal to 1, the grains are not in contact (in suspension) and thus the sediment follows the normal compaction trend according to Terzaghi (1923). If β is less than 1, this indicates that the particles are in contact to each other and hence they compact at lower rate than the normal compaction rate of sediment because more overburden stress is supported by the rock frame and therefore the compaction is less. However, engineers usually assume that β is equal to one when estimating *in-situ* vertical effective stress on buried sediments. But, this assumption is not always true, especially for cemented sediments, and it underestimates the real vertical effective stress which in return may cause severe engineering consequences such as a reservoir rock may suffer compaction or deformation as a result of changing in stress state during drilling operations or during production of hydrocarbons. If the effective stress exceeds the strength of the rock, borehole breakouts develop. Thus, estimating a more realistic vertical effective stress allows determining the optimum drilling parameters to reduce problems related to borehole stability. The key message here is to stress on the importance of using the correct value of β when estimating the vertical effective stress especially on deep-sea cemented sediments where β has large influence on estimation of the vertical effective stress. To assess the geomechanical stability and the stiffness of the three studied sediments, the correct value of β for each lithology must be found and used to calculate more realistic *in-situ* vertical effective stress.

Siliceous ooze sediments and shale are usually regarded as non-hydrocarbon reservoir rocks. However, in the last few years this view has been challenged and development of natural gas from unconventional sources such as shale and siliceous ooze is internationally becoming a focus point for research and field tests. Shale and siliceous ooze form thick layers in the Danish Basin and they are expected to be gas-bearing (unconventional gas prospects). If gas can be developed from them, this is not only an addition to the Danish energy reserves, but also it may secure future gas supply.

If the factors governing physical properties of the three studied lithologies are well defined and understood this would benefit various areas such as:
1) Prediction of chalk porosity from elastic wave velocity (i.e. seismic velocity data);
2) Evaluation of hydrocarbon reservoir potential of siliceous ooze;
3) Rock physics interpretation of geotechnical (geomechanical) data of shale.

1.2. The objectives

The primary objectives of this Ph.D. study were: 1) to investigate and evaluate the influence of mineralogical composition, depositional texture and burial depth on petrophysical properties of Palaeogene sediments and to find out how the physical properties are related; 2) to know the stiffness of the three studied lithologies based on

their β values which are relevant for assessing geomechanical stability and compaction (deformation) studies, as well as in estimating the vertical effective stress; and 3) to link the diagenesis of the sediments with logging interpretation. This is not straight forward especially for shale and siliceous ooze because of the complicated nature of their mineralogical composition and texture.

The secondary goals were to show how the choice of β value influences the estimation of vertical effective stress especially on deep-sea sediments. Another important aspect of this Ph.D. study was to investigate the relationship between static (obtained from the rock mechanical loading test or consolidation test) and dynamic (obtained from the elastic wave velocity) uniaxial compressional modulus of shale (Palaeogene clay).

1.3. Study approach

This work is primarily a laboratory and database study. The main factors controlling the physical properties of the studied three lithologies have been addressed here. Velocity of elastic waves is the primary data available for obtaining information about characteristics of subsurface lithologies. Thus, elastic wave velocity is used here as a central tool to study changes in petrophysical and rock mechanical properties of the studied sediments, especially in the study on composition and physical properties of Eocene chalk and Palaeogene shale that was based on the Ocean Drilling Program (ODP) data from Atlantic Ocean drill sites. Terzaghi (1923), Biot (1941) effective stress and Gassmann (1951) fluid substitution methods were applied in this study.

The mineralogical composition of the sediments was determined by X-ray diffraction (XRD) analysis and it is used here as a main tool to identify the effect of sediment diagenesis. Surface area of the grains of the Palaeogene clay (shale) was measured by nitrogen adsorption, BET method (Brunauer et al. 1938). BET surface area data were used here as a tool to interpret the geotechnical data of Palaeogene clays. Shale elasticity is also related to BET surface area and mineralogy of shale.

To assess hydrocarbon potential of the studied siliceous ooze sediments, petrophysical methods were used here. To evaluate reservoir properties from petrophysical logs, siliceous ooze core material should be characterized with respect to properties such as natural radioactivity; carbonate content (CC), surface area of the grains (BET) and cation exchange capacity (CEC). Similarly, to develop rock physics interpretation of geotechnical (geomechanical) data, information about total porosity, bulk density, elastic wave velocities are required. To assess the geomechanical stability of these sediments we need to incorporate geotechnical data and to find the correct value of β which must be used in estimation of *in-situ* vertical effective stress.

1.4. Structure of the report

An overview of the entire thesis structure has already explained in the preface. What is stated here (below) is only about the structure of this report (part I). The Ph.D. research project was divided into three main subprojects (topics). Hence, this report is prepared accordingly as well. The first topic (section 2) focused on the composition and physical properties of Eocene chalk and Palaeogene shale based on the ODP data collected from Atlantic Ocean drill sites. Here, changes in porosity and sonic velocity data of Eocene chalk were related to the vertical effective stress and thermal maturity of chalk. A predictive equation for porosity reduction with burial stress was proposed.

The predictive equation is relevant for basin analysis and hydrocarbon exploration to predict porosity if sonic velocity (i.e. seismic velocity) data for subsurface chalk are available. A manuscript (Paper I: under review) was prepared, and two conference abstracts (Paper IV and V) were published.

The second topic (section 3) was mainly about the characterization, evaluation and interpretation of petrophysical logs of siliceous ooze sediments. Here, petrophysical logs and conventional core analysis data were integrated with XRD analysis and other mineralogical data of the siliceous ooze. The available geological and petrographical data of siliceous ooze provided important information to understand the pore structure, and the grain size and shape of siliceous ooze sediment and how it changes with burial diagenesis. This helped in making reasonable and consistent interpretation by linking diagenesis of siliceous ooze with logging interpretation. A new approach that could be used to correct bulk density and neutron porosity logs to find the true porosity of siliceous ooze is presented here. The effective stress of siliceous ooze was also estimated. A manuscript (Paper II: submitted) and two conference abstracts (Paper VI and VI1) were published.

The third topic (section 4) was about the elasticity of the Palaeogene clay (shale) of the Fehmarn Belt area. The activities in this part of the Ph.D. research generally focused on laboratory experiments such as XRD analysis, measuring surface area by BET method, velocity of elastic wave and electrical resistivity of the Palaeogene clay. The obtained results were evaluated and integrated with the available geotechnical data (obtained from rock mechanical compaction tests that were done during elastic wave velocity measurements as well as those data obtained from the Fehmarn Belt database) to model elasticity of Palaeogene clay by relating its elastic properties to BET surface area and mineralogy of Palaeogene clay (e.g. smectite content). Both petrophysical and rock-mechanics effect of Palaeogene clay were addressed here. However, experimental work only related to petrophysical properties were done under this project. For rock-mechanics properties (pore collapse, shear failure and static elastic moduli) experimental data from Fehmarn Belt database were used. A manuscript (Paper III: submitted) about elastic properties of Palaeogene clay from Fehmarn Belt was prepared.

The fifth section contains the conclusions of the three topics stated above in section 2, 3 and 4. Abstracts of the three SIS journal papers are presented in section 6. The report is ended by a list of references in section 7.

2. Influence of burial depth on physical properties of Atlantic pelagic sediments

2.1. Introduction

Pelagic deposits such as siliceous ooze, siliciclastic, shale and chalk of Palaeogene age (Palaeocene to Eocene) occur in the Atlantic Ocean basins. The Palaeogene siliceous ooze and siliciclastic sediments form relatively thin layers and have very limited geographical distribution in the Atlantic basins, and thus, they were excluded from this study. Palaeogene shale and Eocene chalk form relatively thick layers (about 15–300 m) and have wide geographical distribution within the Atlantic basins. Changes in physical properties of Palaeogene shale as a function of burial depth has been addressed by Awadalkarim and Fabricius (2012) and these will not be repeated here. The primary objective of that study was to show the influence of choice of Biot's coefficient (β) value on the estimation of vertical effective stress on the deep-sea shale. The secondary object was to relate changes in physical properties of shale to the vertical effective stress which may provide a basis to understand how physical properties vary with effective stress and shale mineralogy. In order to limit the scope, this section of the report is solely based on the study of the physical properties of Eocene chalk from the Atlantic Ocean basins (Figure 2.1). The main objective was to relate changes in porosity and sonic velocity with burial depth to the vertical effective stress and thermal maturity of Eocene chalk.

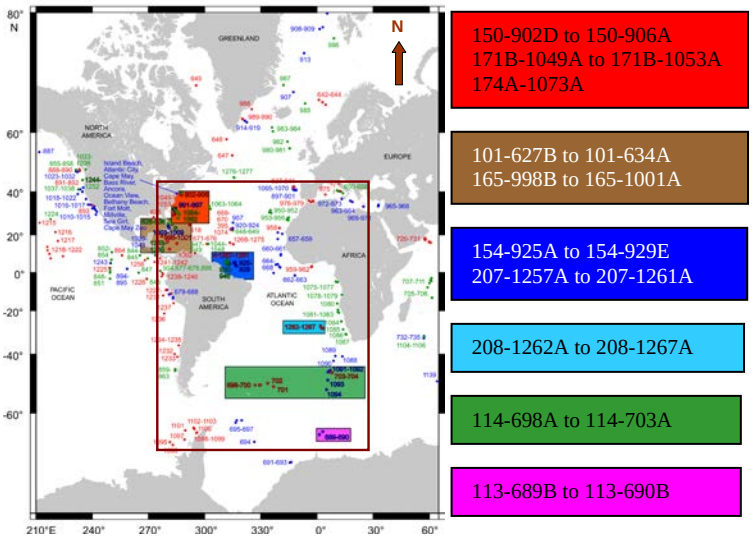

Figure 2.1: *Map showing the locations of Ocean Drilling Program (ODP) sites (modified after http://iodp.tamu.edu/scienceops/maps/odpmap.pdf). The study area is enclosed by a rectangle and highlighted by colouring. The purpose of highlighting the studied sites, by the coloured rectangles, is to help the reader to get an idea about the geographical distributions of the studied ODP sites. The red, brown, dark blue, light blue, dark green and magenta colours used here have nothing to do with the colours used for sample legends in the other figures in this study. Each ODP site in the map comprises only 3 to 4 digits as a site name which may have 2 to 5 drilled boreholes with the names A, B, C, D and E. The following example explains how the name for each site (in this study) is structured; e.g. 154-929E means ODP Leg 154, Site 929,*

Hole E. The ODP sites included within each coloured rectangle in the map are shown in the legend to right of the map.

It is known that both the *in-situ* stresses and thermal maturity (i.e. temperature) acting on subsurface sediments generally increase with increasing burial depth (Fabricius et al. 2008; Wetzel 1989). This causes changes in physical and mechanical properties of sediments such as porosity, sonic velocity, bulk density, permeability, and sediment strength. Therefore, as burial depth increases, a link between vertical effective stress and physical properties such as porosity and sonic velocity of chalk could be established. Moreover, an indirect temperature control on cementation in deep-sea chalk is advocated (Fabricius et al. 2008), and thus it may be possible to establish a relationship between thermal maturity and porosity of deep-sea chalk. This study firstly aimed to compare the present deep-sea Eocene chalk porosity data from the Atlantic Ocean with those of Fabricius et al. (2008) from the Pacific Ocean. Then it focused on establishing porosity and compressional wave (P-wave) velocity depth trends for the Atlantic Ocean Eocene chalks, which is then related to vertical effective stress and thermal maturity (Fabricius et al. 2008). In hydrocarbon exploration, seismic velocity data can be used to obtain Biot's vertical effective stress. Therefore, the present relationship of P-wave velocity to vertical effective stress, taking into account the influence of cementation (Biot 1941), can be used to estimate Biot's effective stress if seismic velocity data are available. The predicted Biot's effective stress could then be used to find its corresponding porosity for any given depth. Hence, a meaningful prediction of porosity of inaccessible subsurface layers of chalk could be made if the vertical effective stress and thermal maturity of chalk is known. This study is relevant for basin analysis modelling and hydrocarbon exploration in chalk sediments especially in deepwater basins where drilling is expensive.

During the Eocene, pelagic carbonate oozes were deposited in the Atlantic Ocean basins. As a result of diagenesis, pelagic carbonate oozes transformed to chalk or even further to limestone. In carbonate sedimentology, limestone is a general term that refers to any carbonate sediment in which the carbonate content is higher than the non-carbonate constituents (Pettijohn 1975). According to the ODP classification scheme of deep-sea sediments, ooze is defined as soft (unconsolidated) calcareous and/or siliceous pelagic sediments whereas chalk and limestone are defined as firm (consolidated) and hard (indurated) pelagic sediments composed predominantly of calcareous pelagic grains, respectively (Mazzullo et al. 1988). However, in sedimentology, the term chalk may refer to any pelagic or hemi-pelagic carbonate sediment regardless of induration of the sediment (Pettijohn 1975). Here, we used the term chalk to refer to all three types of calcareous pelagic sediments: unconsolidated, consolidated, and indurated. Pelagic sedimentation is probably the main process of sedimentation for the studied Eocene chalk. The studied Eocene chalk is not purely calcitic as indicated by the variations in carbonate content that ranges in average from about 50% to 93%. The clay content may be attributed primarily to aeolian processes. The presence of fine clay content may reduce the calcite-to-calcite grain contacts and occupy some of the pore space in the chalk and thus reduce porosity. This may also make the frame of the chalk weaker. Clay can also form locations for initiation of pressure dissolution (Fabricius and Borre 2007). Apart from burial diagenesis, the primary depositional processes, components of chalk mineralogy, depositional texture and fabric could have influence on the physical properties of chalk.

Porosity of newly deposited carbonate oozes near the seafloor is high, but it decreases with burial depth, whereas sonic velocity and bulk density increases (e.g. Hamilton 1980; Japsen 1993). Porosity reduction with burial depth is due to mechanisms such as mechanical compaction and thermo-chemical cementation of sediments (Giles et al. 1998). The porosity reduction with burial depth has been described by several authors not least because of its implications in hydrocarbon exploration (e.g. Schlanger and Douglas 1974; Matter et al. 1975; Hamilton et al. 1976; Scholle 1977; Wetzel 1989; Anselmetti and Eberli 1993; Bassinot et al. 1993; Brasher and Vagle 1996; Borre and Fabricius 1998; Grützner and Mienert 1999; Mallon and Swarbrick 2002; Fabricius et al. 2008; Alam et al. 2010).

Grützner and Mienert (1999), Mallon and Swarbrick (2002), and Fabricius et al. (2008) included data of pelagic carbonate sediments from different geological ages in their studies. However, the present study focused only on the Eocene chalk to avoid possible influence of sediment age in chalk diagenesis. Hence, the present dataset is restricted to chalk samples of the same age that represent only an Eocene time interval. In this way, time since the deposition of the studied Eocene chalks is nearly constant, so they should be compared because they only differ with respect to stress, pressure, temperature, and texture. Here, porosity and comperssional-wave (P-wave) velocity data measured on water-saturated Eocene chalk from the Atlantic Ocean were used to address depth trends for porosity and P-wave velocity. To establish depth trends, the present porosity and P-wave velocity data were correlated with the vertical effective stresses as defined by Terzaghi (1923) and by Biot (1941). The same data were also correlated with the time–temperature index of thermal maturity (TTI) as defined by Lopatin (Waples 1980). Finally, the present results were compared with those obtained by Grützner and Mienert (1999) on the Atlantic carbonate sediments, by Mallon and Swarbrick (2002) on non-reservoir North Sea Chalk, and by Fabricius et al. (2008) on deep-sea chalk from the Ontong Java Plateau of the western Pacific Ocean.

2.2. Previous pertinent studies

There are many studies dealing with the physical properties depth trends on chalk. Hamilton (1974) and several later authors have addressed mechanical compaction of carbonate ooze sediments. Mechanical compaction begins immediately after the deposition of the calcareous ooze. During mechanical compaction of calcareous ooze, porosity decreases primarily through a more efficient packing of particles, but fossils and grain sizes of other particles may remain constant (e.g. Lind 1993; Grützner and Mienert 1999). In response to increasing compression due to overburden load on indurated chalk, particles may break down, grain size reduced, and contact cement may break. For the mud-supported chalk, the presence of very fine matrix (mud) around the calcite particles may act as stress absorber and thus protects the surrounded larger calcite particles from breaking down (Lind 1993). However, textural information of the studied chalk is not available, and thus the same texture as in that deep-sea chalk studied by Lind (1993) is assumed here.

Mallon and Swarbrick (2002) described two linear trends for porosity loss with burial depth for non-reservoir chalk of the Central North Sea. Based on laboratory work on chalk from the North Sea, Alam et al. (2012) studied the effect of pore-fluid pressure in terms of effective stress according to the definition of Biot (1941). They found that

there is no significant difference between static and dynamic β values and both of them are less than one. In this study, the laboratory measured sonic velocity and bulk density data of the studied chalk were used to estimate dynamic β (Alam et al. 2012).

The mechanical compaction, pore-stiffening contact cementation and pore-filling cementation are three different diagenetic processes in chalk as defined by Fabricius et al. (2008). Mechanical compaction rearranges the particles closer to each other and only causes a moderate increase in sonic velocity but a significant decrease in porosity. Mechanical compaction may proceed by breaking contact cement in the chalk if the cement is already formed. When the contact cement is broken, the sediment will have new open frame, thus it may behave as if it is uncemented sediment, and in this respect, Terzaghi's (1923) concept is probably appropriate method for calculating the vertical effective stress. But, when the contact cement makes the rock frame strong enough to hold the overburden load, the mechanical compaction halts, and porosity is preserved. For mechanical compaction to proceed, the vertical effective stress must overcome the strength of the contact cement, either by deeper burial or by depletion of pore-fluid pressure (Fabricius 2003). The second diagenetic process is pore-stiffening contact cementation which fuses grains without porosity reduction, but sonic velocity increases because of the improved grains contact. Where compaction is not active for some time, pore-stiffening contact cement may form in chalk due to recrystallization but this process does not necessarily reduce porosity as it is not associated with pore volume change. The sources of the calcite cement can be calcite dissolved at stylolite surfaces or from outside the system (Delaney 1991). However, in the current deep-sea chalk, cement from external sources is not expected to be involved in the contact cementation process. In this respect, cement is internally derived by dissolution, of calcite particles, and then re-precipitated on other particles within the system. Thus the shapes of the pores may change but the net porosity in the chalk does not change. This diagenetic process prevents porosity loss by mechanical compaction. The third diagenetic process is pore-filling calcite cementation. Due to this process, porosity decreases rapidly whereas sonic velocity increases rapidly. Fabricius et al. (2008) defined mechanical compaction, pore-stiffening contact cementation and pore-filling cementation processes to occur in the ranges of 0–5, 5–7 and 7–10 MPa Terzaghi's effective stress, respectively. Pore-filling cementation apparently requires a threshold TTI possibly reflecting the transformation of opal-CT to quartz and a threshold stress for the onset of pressure dissolution (Fabricius et al. 2008).

Alam et al. (2010) studied the natural porosity reduction mechanisms of deep-sea pelagic carbonates from Kerguelen Plateau in the Indian Ocean. Their study suggested that porosity reduction due to compaction and creep takes place via the matrix porosity reduction, whereas the large (intra-particle) porosity does not change much.

The source of pore-filling cementation of the present studied Eocene chalk is unknown, however, it could be assumed as a result of pressure dissolution at the clay–calcite interface in a stylolite (Maliva and Dickson 1992; Fabricius and Borre 2007) rather than at calcite–calcite interfaces as postulated by Scholle (1977). Thus, a possible local closed-system source of cement (i.e. calcite dissolved at stylolites) could be assumed. The dissolved calcite at the clay–calcite interface re-precipitates in the pore space as overgrowth (i.e. pore-filling cementation) and causes porosity reduction. Fabricius and Borre (2007) argued that an effective stress of about 6 MPa

controls stylolite formation. Based on the above arguments, we assumed that the requirements for stylolite formation are met in the present studied Eocene chalk and thus, stylolites would be expected to develop in the deeply buried Eocene chalk in the Atlantic Ocean basins. Consequently, stylolites could be a possible source for precipitation of calcite cement in the studied Eocene chalk. However, in addition to the burial stress on chalk, the onset of calcite cement precipitation is also governed by other factors such as temperature and the chemical composition of the pore-water (Øxnevad and Meshri 1997). For instance, Fabricius et al. (2008) suggested that the transformation of opal-CT to quartz may be a temperature-dependent controlling chemical process for calcite cement precipitation. This is because when opal-CT is present, a high concentration of silicon (Si) in the pore-water helps calcium (Ca) in dissolution to form complexes. Fabricius et al. (2008) found a threshold TTI value of 0.1 reflecting this process.

Based on the physical property measurements from 81 Deep-Sea Drilling Project and Ocean Drilling Project drill sites in the Atlantic Ocean, Grützner and Mienert (1999) addressed the diagenesis of pelagic carbonate sediments and established an empirical physical model of carbonate diagenesis. Their model is based on averaging done over depth intervals of 40 m for all available discrete sonic velocity, bulk density, and porosity data (measured on water-saturated ooze, chalk, and limestone samples) and related them to depth below seafloor, based on the assumption that diagenesis is mainly controlled by burial depth. In this way, geological age was not taken into account, and also the physical effect of “depth below seafloor” was not addressed.

Bryant and Rack (1990) studied porosity reduction of the siliciclastic, calcareous, and diatomaceous sediments of the Weddell Sea, Maud Rise, and South Orkney microcontinental margin recovered during ODP Leg 113. Their study revealed that porosity reduction is primarily governed by lithology and by vertical overburden stress. Blum et al. (1996) examined the state of consolidation in silty mud sediments at ODP Leg 150 Sites 902D and 903B to estimate the stress history, evaluate the geotechnical significance of methane in recovered cores, and estimate excess pore-fluid pressures in the formation. The maximum depth they investigated in their study was 130 mbsf that covers only the shallowly buried sediments of Pleistocene rather than the Eocene sediments (1071–1150 mbsf) that were included in the present study. Fabricius (2000) studied burial history of pelagic clayey mixed carbonate sediments from the Caribbean Leg 165 Sites 999 and 1001 based on geotechnical data. Based on one dimensional incremental load consolidation and low-gradient flow pump permeability tests, O’Regan and Moran (2007) determined the stress history, permeability, and compressibility of chalk and black shale recovered during ODP Leg 207 Sites 1257, 1258, 1259, and 1261. Only the Eocene chalk from these ODP sites was included in the present study, whereas they included all chalk and black shale from Neogene to Cretaceous in their study which shows that Neogene and Palaeogene sediments tend to be overconsolidated whereas Cretaceous sediments are normally consolidated (Maastrichtian–Paleocene chalk and clays) to underconsolidated (Cretaceous black shale) indicating the presence of overpressure in Cretaceous sediments that has retarded mechanical compaction. Although the authors did not state anything about the mechanism of the overconsolidation process of Neogene and Palaeogene sediments, their results may be in accordance with Schlanger and Douglas (1974) as they also found that softer pelagic carbonate layers may underlie stiffer layers with the same porosity but with more cement and higher acoustic velocity.

2.3. Source and type of the selected data

The geological information, lithological descriptions and water depth data used here were obtained from the proceedings of the ODP initial reports of the Atlantic sites (Figure 2.1 and Table 1 of Paper I). Shipboard physical properties data, such as water-saturated bulk density, porosity, and P-wave velocity, were obtained from the Janus Web Database at this link: http://iodp.tamu.edu/janusweb/links/links_all.shtml.

Initially, more than 242 ODP drill sites across the Atlantic Ocean were screened for obtaining suitable Eocene chalk data for this research. Shipboard bulk density, grain density, and porosity data from 36 ODP drill sites covering a wide geographical area and water depths were selected and included in this research. Shipboard bulk density, grain density, and porosity were measured by gravimetric methods on discrete samples. Shipboard sonic velocity was measured on water-saturated split core sections or on cut samples with no confining pressure or pore-pressure involvement. Shipboard P-wave velocity measurements were made in the horizontal and vertical directions with respect to the core axis and at ambient temperature and pressure after thermal equilibration. P-wave velocity data are obtained from Hamilton-Frame measurements on split cores within the liner (for soft sediments such as ooze), and on discrete samples without the liner (for indurate or hard sediments). The velocity estimate is based on the travel time between two contact transducers. One transducer is placed on the cut surface of the core and the other is directly beneath, in contact with the core-barrel liner. Sample thickness is usually measured by a vertical offset gauge. Fresh water was used to improve the acoustic contact between the sample and the transducers. Further detailed descriptions of the methods and measurement procedures for these physical properties can be found in the explanatory notes chapters of any of the ODP initial reports of the 36 ODP drill sites included in this study (e.g. Robertson et al. 1998; Ciesielski et al. 1991). The P-wave velocity data measured in the vertical direction of the cores (i.e. along core axis and perpendicular to the bedding plane) were used in this paper. The ODP determined the concentrations of carbonate in sediments in the chemistry laboratory. The ODP reported carbonate data included weight percentages of inorganic carbon, organic carbon, total carbon, calcium carbonate, nitrogen, and sulphur. Although other carbonates may be present, all acid-soluble carbon is calculated as calcium carbonate. In this study, the ODP reported weight percentages of the calcium carbonate content was used as an indicator of the purity of the investigated Eocene chalk. All the data used in this study are not averaged or manipulated by statistical methods.

2.4. Theory and methodology

Compaction of sediment is a result of increasing effective stress (Terzaghi 1923). Effective stress and thermal maturity of chalk increase with increasing burial depth. Here, two main methods are presented, one is a detailed procedure for calculation of effective stress as defined by Terzaghi (1923) and by Biot (1941) and the other is the calculation of Lopatin's time–temperature index of thermal maturity (TTI).

The available stratigraphical information from the 36 ODP drill sites was used to estimate the ages of the pelagic and hemi-pelagic sediments from the Eocene to Holocene/Pleistocene. However, due to the lack of bottom-hole temperature data for 12 of the 36 ODP drill sites, the bottom-hole temperature and the age–depth

information from only 24 ODP drill sites were used in the present study to calculate the Lopatin's TTI values (Table 2.1 and Table 4 of Paper I).

2.4.1. Pore-fluid pressure, overburden and effective stress

In this study, pressure refers to the isotropic pore-fluid pressure whereas stress refers to the anisotropic external load acting on sediments. The load exerted by the column of overlying sediments and the water column causes overburden stress (*in-situ* total vertical stress) on the underlying sediments. Effective stress is the actual deforming stress the sediment undergoes in a subsurface condition. It is defined as the stress that acts on the solid material and passes through particles in the sediment matrix. The vertical effective stress rather than overburden stress controls most of the physical properties such as porosity, permeability, elastic wave velocity, etc., of stressed sediments. Because the studied Eocene chalk comprises both uncemented (i.e. calcareous oozes) and cemented chalk sediments, thus, the vertical effective stress as defined by both Terzaghi (1923) and Biot (1941) were calculate. Terzaghi's concept is suitable for uncemented sediments (i.e. sediments with open framework of particles) and it is based on the assumption that pore-fluid pressure is 100% effective in resisting the deformation (strain) due to total overburden stress (overburden load). However, when the grains of sediment are cemented, it is appropriate to apply Biot's (1941) effective stress concept which is just a difference between the total overburden stress and a fraction of the pore-fluid pressure (P_p) known as Biot's coefficient (β). It is clear that effective stress calculated by the latter concept is higher than that calculated by the former concept. Even for small deviations in β values from one, a significant Biot's effective stress can be obtained. Biot's effective stress is a better predictor of the mechanical behaviour of a rock than Terzaghi's effective stress.

Here, the total overburden stress, σ, was obtained, to a fair approximation as follows:

$$\sigma = g\left(h_w \rho_w + \sum_{i=1}^{i=n} (\rho_i h_i) \right) \qquad \text{Eq. 2.1}$$

where g is the acceleration due to gravity (9.81 m/s^2), h_w is water depth (m) measured from sea level, ρ_w is ocean water density (assumed to be 1.05 g/cm^3 throughout), ρ_i is the water-saturated bulk density of sediment at each data point and h_i is depth interval (m) between measured data points. Here, the shipboard water-saturated bulk density data measured on discrete chalk samples were used.

The pore-fluid pressure, P_p, was calculated under the assumption of a hydrostatic fluid pressure gradient of a column of pore-water extending to the surface, as follows:

$$P_P = gh\rho_w \qquad \text{Eq. 2.2}$$

where h is the measured depth below sea level ($h = h_w + \sum h_i$), and pore-water density is assumed equal to ocean water density, ρ_w.

The effective stress, σ', was first calculated as defined by Terzaghi (1923), as follows:

$$\sigma' = \sigma - P_P \qquad \text{Eq. 2.3}$$

Terzaghi's vertical effective stress concept is appropriate for uncemented sediments where β value is one. But, most chalk sediments are cemented to some extent. Thus, β value becomes less than one and the effect of pore-fluid pressure on resisting overburden stress may be reduced (Biot and Willis 1957). Also, because of the high water depth in the Atlantic Ocean which reaches about 4356 m at Site 154-929E, pore-fluid pressure is high and thus a relatively large influence of β on the estimation of vertical effective stress is expected. Thus, for cemented sediments the *in-situ* vertical effective stress, σ', may be calculated according to Biot (1941), as follows:

$$\sigma' = \sigma - \beta P_P \qquad \text{Eq. 2.4}$$

To use Eq. 2.4, the value of β must be determined. In a linear-elastic isotropic sediment, β may be calculated from sonic velocity and density data (e.g. Biot and Willis 1957; Nur and Byerlee 1971; Mavko et al. 1998). In this study, due to the lack of shear velocity data, β was calculated by using iso-frame modelling (Fabricius et al. 2008). The bulk modulus of dry rock (K_{dry}) was estimated from iso-frame values and porosity data. For this modelling, a critical porosity of 100% and calcite mineralogy were assumed, hence considered a bulk modulus for pure calcite, K_o, equal to 71 GPa (citation in Mavko et al. 1998). Thus, β is expressed according to Biot and Willis (1957) as follows (the obtained results are presented in Figure 2.2):

$$\beta = \left(1 - \frac{K_{dry}}{K_o}\right) \qquad \text{Eq. 2.5}$$

where K_{dry} and K_o are bulk modulus of dry porous rock (modulus of the mineral frame) and bulk modulus of the solid material (mineral grains) that makes up the rock, respectively. According to Fjær et al. (1992), values of β lie in the range of porosity (ϕ) and one, (i.e. β cannot become smaller than porosity, $\phi \le \beta \le 1$).

Using Terzaghi's concept to calculate vertical effective stress on cemented sediments leads to underestimation of the actual vertical effective stress and this may cause severe engineering consequences. So, to obtain more realistic vertical effective stress on cemented sediments, it is more appropriate to use Biot's effective stress concept.

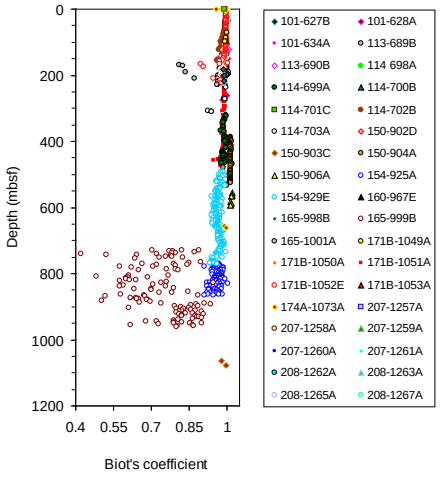

Figure 2.2: *Plot shows the variation in the calculated Biot's coefficient (β) with depth. When the values of β are less than one, this indicates that the effective stress has a greater effect than the pore pressure on the physical properties of that rock.*

2.4.2. The Lopatin's time temperature index (TTI)

Porosity reduction due to pore-filling cementation may also be linked to the thermal maturity of chalk, possibly as a result of increasing burial. Here, thermal maturity of the studied chalk is expressed by the Lopatin's time–temperature index (TTI) (Waples 1980) and also assumed that heating is solely caused by burial as there is no reported evidence of non-burial related thermal processes such as hot fluid flows or proximal igneous activity. The TTI describes the cumulative effect of the time a sedimentary rock experiences in each 10^{o} C temperature interval during burial (Waples 1980).

Lopatin's method was applied by using the bottom-hole temperature data and the stratigraphical information given in the proceedings of the ODP initial reports. The bottom-hole temperature data used here were as reported by the ODP. First, the burial histories for 24 ODP drill sites were reconstructed. This was accomplished according to Waples (1980) by plotting depth of burial versus geological age (Figure 2.3). The ages of the sediments that were included in the reconstruction of the burial histories range from Eocene (37–58 Ma) to Holocene/Pleistocene (0–2 Ma), and thus, represent a broad time interval. However, the TTI was calculated only for the Eocene sediments. A decompaction (i.e. backward) method was also used here to reconstruct the burial histories for the 8 ODP sites (i.e. 150-903C, 150-904A, 150-906A, 154-925A, 154-929E, 165-999B, 171B-1051A and 174A-1073A) with the deepest burial (i.e. 500 mbsf) of the Eocene interval. For each of the 8 deepest ODP sites stated here, a corresponding 'normal' chalk porosity-depth trend for each specific site was used when decompacting the present-day (preserved) thicknesses of the deeper intervals to estimate the past thickness (at deposition). The decompaction was done by using the past thicknesses of the sediments when they were deposited assuming that the amount of solid grain thickness (m) is constant since its deposition. This method was first done by plotting the amount of solid grain thickness (m) versus depth below sea floor (mbsf) from which the past thicknesses of the sediments were obtained (Figure 2.4). The obtained past thicknesses are larger than the present thicknesses because the latter is compacted. The past thicknesses were plotted against the geological ages according to Lopatin's method as introduced by Waples (1980).

Second, the geothermal gradient at each of the 24 ODP sites was assumed to be constant since the Eocene so that the subsurface temperature was specified for every depth. Thus, the temperature grid is defined as a series of equally spaced lines of constant depth. So, 10^{o} C spacing was used to draw temperature grid (Figure 2.3). The regional geothermal gradient in the studied area ranges from 17.1–50^{o} C/km. For Sites 165-999B and 165-1001A, no geothermal data are available; therefore, the minimum (17.1^{o} C/km) and the maximum (50^{o} C/km) geothermal gradients were applied and the results were compared. The Lopatin's TTI was calculated as follows (Waples 1980):

$$\mathrm{TTI} = \sum(\Delta T_n)(r^n) \qquad \text{Eq. 2.6}$$

where n is the appropriate index value for each 10^{o} C temperature interval (n = -1 represents 90–100^{o} C, n = 0 represents 100–110^{o} C and n = 1 represents 110–120^{o} C, etc.), ΔT_n is the time in million years (Ma) the sediments reside in a given temperature interval, and r is a factor which reflects the exponential dependence of maturity on temperature. A constant value of 2 was assumed for r (Waples 1980).

The TTI values obtained by the two approaches were compared in Table 2.1. The decompaction method yields relatively higher TTI values than the compaction method for sediments deeper than 663 mbsf. It gives an average difference in the TTI values of about 6% and 10% at the top and base of Eocene, respectively. However, the two methods give consistent TTI values for the sediments buried at 663 mbsf or shallower.

Table 2.1: Results of the Lopatin's TTI values as obtained by compaction (Method 1) and by decompaction (Method 2) methods.

	Depth	TTI for Base of Eocene			TTI for Top of Eocene		
ODP Site	(mbsf)	Method 1	Method 2	Difference	Method 1	Method 2	Difference
154-925A	777 - 942	0.221	0.292	0.071 (24%)	0.116	0.142	0.026 (18%)
154-929E	494 - 780	0.182	0.232	0.050 (22%)	0.063	0.072	0.009 (13%)
150-906A	547 - 599	0.092	0.092	0 (0%)	0.065	0.064	0.001 (0%)
165-999B	730 - 956	0.229	0.398	0.169 (42%)	0.096	0.13	0.034 (26%)
150-904A	348 - 577	0.089	0.089	0 (0%)	0.038	0.038	0.000 (0%)
150-903C	1070-1150	0.135	0.126	0.009 (7%)	0.086	0.08	0.006 (8%)
171B-1051A	3 - 508	0.057	0.057	0 (0%)	0.002	0.002	0.000 (0%)
174A-1073A	654 - 663	0.058	0.058	0 (0%)	0.038	0.037	0.001 (3%)

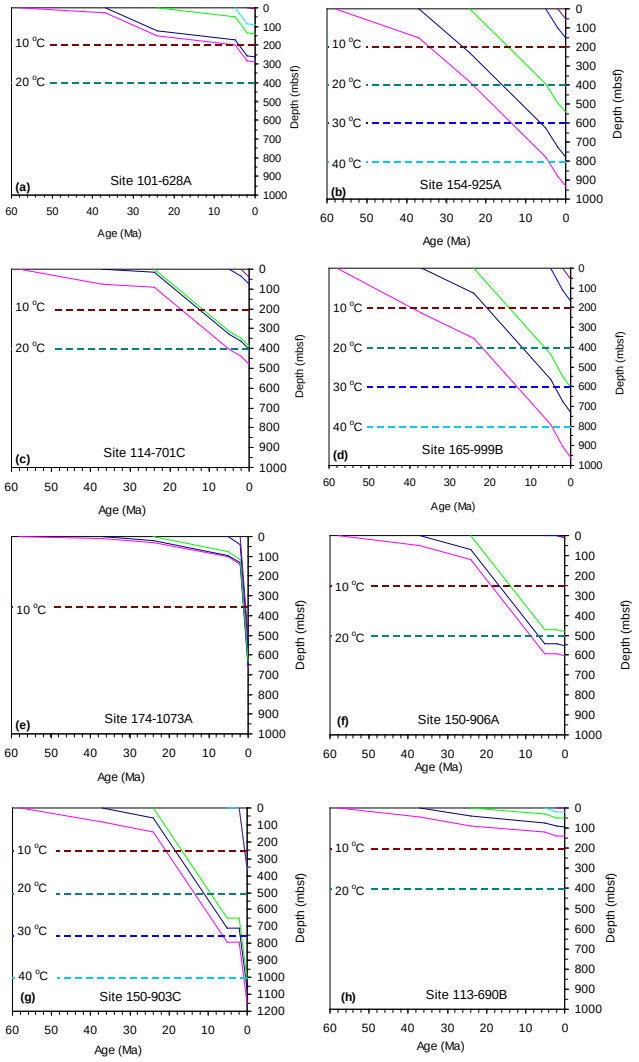

Figure 2.3: *Examples of the reconstructed depositional history for five sedimentary horizons (from Eocene to Pleistocene) for eight ODP sites. Isotherms (dashed horizontal lines) were derived from geothermal gradients that represent the present bottom-hole and seafloor temperatures.*

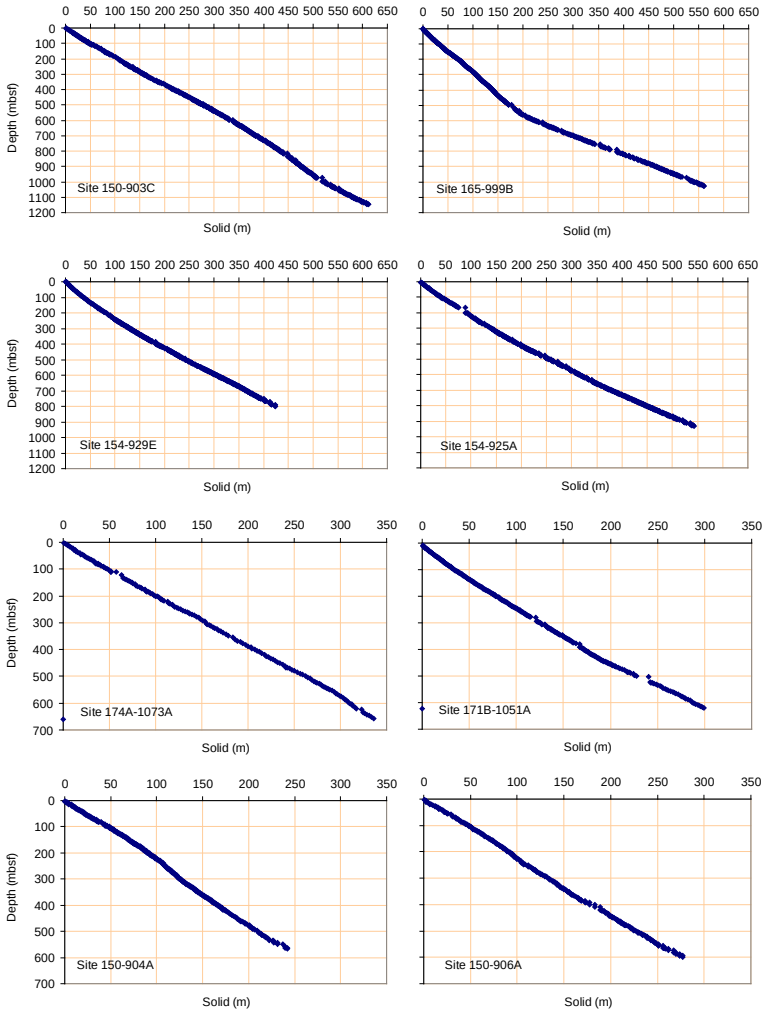

Figure 2.4: *The amount of solid grain thickness (m) versus depth below sea floor (mbsf) for the 8 ODP sites deeper than 500 m.*

2.5. Results and discussion

2.5.1. Physical properties

We assumed that the changes in porosity and P-wave velocity with increasing burial depth are linked to vertical effective stress and it may also be linked, to some extent, to thermal maturity of chalk. Mechanical compaction and chemical dissolution of calcite grains at stylolites are controlled by vertical effective stress (Fabricius et al. 2008). Pore-filling calcite cementation may be related to thermal maturity of chalk. Porosity and P-wave velocity data were used in order to explore how vertical effective stress and thermal maturity influence the porosity and P-wave velocity of chalk with increasing burial depth. Therefore, in this context, the present discussion is based on the correlations of our porosity and P-wave velocity data with the calculated vertical effective stresses and TTI data. The trends of the P-wave velocity and of the porosity were used as function of Biot's effective stress to derive equations that could be used to predict porosity reduction with burial depth. These equations could be relevant for basin analysis and hydrocarbon exploration in chalk. Thus, the present discussion is divided into two parts; the first part focuses on the influence of burial stresses on

physical properties of chalk; and the second part considers the influence of Lopatin's TTI on porosity and P-wave velocity of chalk.

2.5.2. Effect of stress on physical properties of chalk

Figure 2.5 shows the bulk density, P-wave velocity, and porosity plotted versus depth in meters below seafloor (mbsf). The stress–porosity and stress–sonic wave velocity relationships were used to explore how the vertical effective stress obtained by the two different concepts influence the depth trends for porosity and P-wave velocity. When the porosity and P-wave velocity data were plotted versus total overburden stress, σ, rather than depth below seafloor, trends are less easy to define. However, when the same data were correlated with Terzaghi's effective stress; the data cover a wide range for a given effective stress which could be related to the textural variation in chalk and it may also be referred to impurity of chalk (Figure 2.6a). Based on this correlation, it is possible to define more than one trend for porosity decline, and for P-wave velocity increase (Figure 2.6a, d). This implies that porosity reduction trends due to Terzaghi's effective stress may provide information on different mechanisms for porosity reduction with burial depth such as mechanical compaction and pore-filling cementation.

In contrast, when the same porosity and sonic velocity data were correlated with Biot's effective stress, the data show a better correlation (Figure 2.6c, f). The porosity reduction according to Biot's effective stress (Figure 2.6c) does not show similar pattern as that when β is excluded (Figure 2.6a). This implies that porosity and P-wave velocity change as relatively simple functions of Biot's effective stress. This probably suggests that chalk is in elastic equilibrium (Fabricius et al. 2008). The present porosity and P-wave velocity trends in Figure 2.6c, f are adequate to assume that effective stress is most likely the main factor controlling porosity reduction at least at the compaction zone. Therefore, these trends were used here to derive predictive equations for porosity loss with increasing burial depth. An estimation of vertical effective stress is easy to obtain even if drilling information is not available. For instance, if seismic velocity data are available, the Eq. 2.7 could be applied to fairly estimate Biot's vertical effective stress which could be used in Eq. 2.8 to predict a reasonable approximation of porosity value. Eq. 2.7 is derived from the best possible fit of the present P-wave velocity data through what we assumed to be compacted (shallower buried chalk) and pore-filling calcite cementation (deeper buried chalk) intervals (Figure 2.6f). The Eq. 2.8 is derived from the present data trend as shown in Figure 2.6c. The derived equations are presented below:

$$\sigma' = -(11.3 - 0.0076V_p) \qquad \text{Eq. 2.7}$$

where σ' is Biot's vertical effective stress in mega Pascal (MPa).

$$\phi = e^{\left(\frac{65.2-\sigma'}{15.4}\right) MPa} \qquad \text{Eq. 2.8}$$

where ϕ is porosity in percentage (%).

These equations could be relevant for basin analysis and hydrocarbon exploration in chalk, especially in deepwater basins where drilling is expensive. However, a question

may arise, to which extend these equations are reliable. Further investigations were not made to test their reliability, but it is remarkable that the present porosity and sonic velocity data of the Atlantic fall close to the effective stress trend defined in the Pacific Ontong Java Plateau.

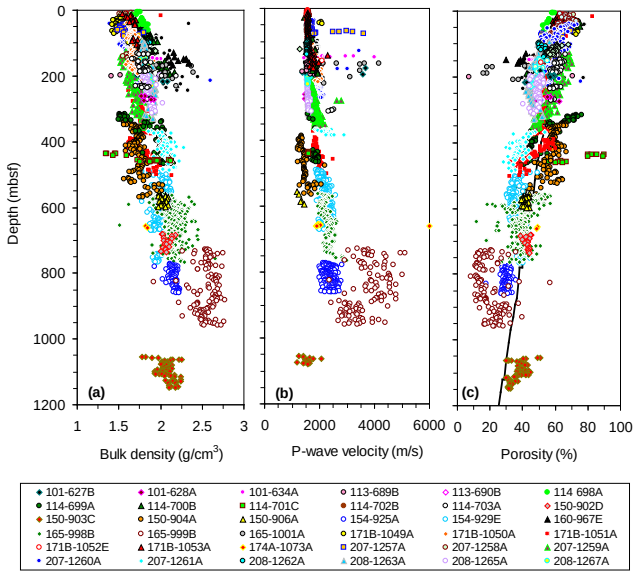

Figure 2.5: *Physical properties for water-saturated Eocene chalk versus depth below seafloor (mbsf). (**a**) Bulk density, (**b**) compressional wave (P-wave) velocity, and (**c**) porosity. Data are from the 36 ODP sites shown in Figure 2.1. The black solid curve in (**c**) represents the shallow porosity depth trend for Mallon and Swarbrick (2002) for data from the North Sea chalk. The bulk density increases with depth due to the compaction and its variations may also reflect the difference in the chalk components.*

Figure 2.6a, c also compare the trends of the current porosity data with those of Fabricius et al. (2008). It is assumed that the average of the lower and upper limits in Figure 2.6c represents the general trend for the present porosity data; it seems to be relatively in agreement with that of Fabricius et al. (2008) for water-saturated chalk samples from the Ontong Java Plateau in the Pacific Ocean. The present porosity data show a broader porosity trend than Fabricius et al. (2008) porosity data. Generally, we conclude that overall agreement is good between the present data and those of Fabricius et al. (2008) especially at deep burial depths. Thus the Eq. 2.8 could be used to predict a reasonable approximation of porosity if the Biot's vertical effective stress is known (e.g. it could be obtained from Eq. 2.7).

Some authors (e.g. Jones et al. 1984; Lind 1993; Fabricius 2003) have documented that mechanical compaction on chalk is the major porosity reduction agent down to porosities of 50% and in some cases even to 40% or lower. Their findings are in agreement with the present porosity results that show porosity change due to mechanical compaction from ~70% to ~35% at about 5 MPa Terzaghi's effective stress (Figure 2.6a). This may be because the studied Eocene chalk contain clay and silt size materials that may enhance mechanical compaction. But, if the mechanical compaction trend is extended through the pore-filling cementation interval (i.e. through the limestone lithology (Figure 2.6b) at greater than 5 MPa Terzaghi's effective stress), it follows the trend of speculative compaction of calcite crystals as in the diagenetic stage five of Grützner and Mienert (1999), or as it is termed as due to

creep on chalk (Alam et al. 2010). The mechanical compaction as defined by Grützner and Mienert (1999) in their diagenetic stage one is only for pelagic carbonate sediments of about 4 Ma old (Pliocene), whereas the present data show mechanical compaction trend for chalk as old as 37–58 Ma (Eocene).

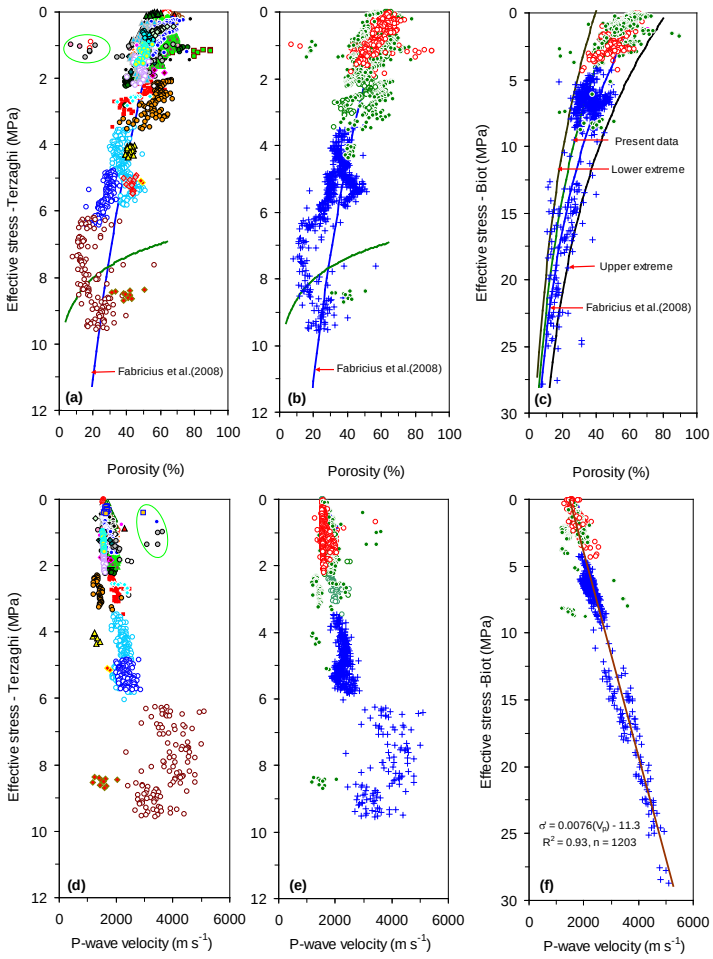

Figure 2.6: *Eocene chalk porosity data versus (**a**, **b**) Terzaghi's effective stress and (**c**) Biot's effective stress of the present data compared with a porosity prediction relations reported by Fabricius et al. (2008). Eocene chalk P-wave velocity data versus (**d, e**) Terzaghi's effective stress and (**f**) Biot's effective stress. In plots (**a**) and (**d**) all data points are annotated according to ODP drill sites. For sample legend, refer to Figure 2.5. In plots (**b, c, e** and **f**), all data points are annotated with respect to lithology (i.e. ooze red open circle, chalk green closed circle and limestone blue cross). The present porosity data are compared with the porosity trend obtained in the Pacific Ontong Java Plateau by Fabricius et al. (2008). The blue and green curves in (**c**) represent the porosity trends for Fabricius et al. (2008) data and the average/best-fit trend of the present porosity data. Some data points are off the trends, they are enclosed by a green oval on plots (**a, d**).*

The present porosity data did not show or at least it is difficult to define a pore-stiffening contact cementation trend as clear as the Ontong Java Plateau chalk (Fabricius et al. 2008). Pore-filling calcite cementation is reflected by increasing TTI values and a gradual decline in porosity as shown by Figure 2.6b. It causes porosity reduction with nearly constant Terzaghi's effective stress (Figure 2.6a, b). It may be

equivalent to the diagenetic stage three of Grützner and Mienert (1999). It may also arise due to calcite pressure dissolution at stylolites (Fabricius et al. 2008) when vertical effective stress is greater than 5 MPa (Figure 2.6a, b, d, e). In the Terzaghi's effective stress interval 5–10 MPa (Figure 2.6a, d) porosity declines and P-wave velocity rapidly increases due to pore-filling cementation which mainly stiffens the whole rock and significantly reduces the amount of porosity.

The current porosity data show a different cementation front (Figure 2.6b) from that shown by Fabricius et al. (2008) from the Pacific Ontong Java Plateau chalk (green curve in Figure 2.6a, b). We would suggest explaining this difference as that pore-filling calcite cementation in the studied Eocene chalk probably started earlier (i.e. at shallower depths) than that in the Ontong Java Plateau chalk. The reason why the pore-filling cementation front (the onset of the formation of limestone) of Fabricius et al. (2008) data does not fit the present data could be due to the different in the deep-sea western Pacific in comparison to the Atlantic Ocean. This interpretation could be supported by the evidence obtained via Lopatin's TTI results that showed the temperature gradient of some of the studied ODP sites is about 50^{o} C. However, none of the studied Eocene chalk is reached the isotherm 50^{o} C, the maximum is about 47^{o} C at the ODP site 154-925A and may be at the ODP site 165-999B as well (Figure 2.3). Moreover, the evidence reported by Moutain et al. (1994) shows that calcite cement is dominant in the Eocene chalk section from 1105 mbsf at Site 150-903C. This supports the above explanation as the present data from ODP Sites 150-903C and 165-999B fall within our pore-filling calcite cementation trend.

2.5.3 Effect of thermal maturity on chalk physical properties

The calculated results of the Lopatin's TTIs are summarized in Table 4 of Paper I. The correlations of our P-wave velocity and porosity data with burial depth as represented by Lopatin's TTI of thermal maturity are illustrated by Figure 2.7. They show non-linear correlations (Figure 2.7). Both P-wave velocity and porosity data show poor correlations at the higher values of TTI (i.e. at high temperature). The present data showed a slow decrease in porosity from around 70% (near the seafloor, log TTI of 0.002) to about 50% (at burial depth corresponding to log TTI of about 0.07) which might correspond to about 5–6 MPa Terzaghi's effective stress (Figure 2.6a). In the same interval, the P-wave velocity slowly increases from around 1500 to about 2000 m/s (Figure 2.7a).

The present porosity–log TTI relationship does not agree with the porosity results of Schmoker (1984) on carbonate sediments where a log-linear relationship between TTI and porosity was obtained. This may be because Schmoker (1984) used data from carbonate sediments of different geological ages. However, we could define compaction and probably pore-filling calcite cementation trends from the present porosity and P-wave velocity data versus log TTI plots in the same way as we did in the previous section as shown in Figure 2.6a.

Due to pore-filling calcite cementation, a gradual increase in P-wave velocity (from around 2000–4250 m/s) and a decrease in porosity (from 50–10%) at the depth interval corresponding to log TTI of about 0.07 and higher (Figure 2.7a, b) were observed. An X-ray diffraction (XRD) analysis on chalk samples from the Sites 165-999B, 165-1001A, 150-904A, and 150-603C shows a change in chalk mineralogy as opal-CT converted into quartz at a depth corresponding to log TTI of about 0.07 (see

Mountain et al. 1994; Sigurdsson et al. 1997). The data from these four sites fall within what we interpreted as a pore-filling calcite cementation trend (between about 5–10 MPa Terzaghi's effective stress, Figure 2.6a, b). The conversion of opal-CT to quartz is in accordance with the observation shown by Figure 12d of Fabricius et al. (2008) at the Pacific Ontong Java Plateau chalk. This agreement is supporting the hypothesis of Fabricius and Borre (2007) which proposed that the activation energy for pore-filling calcite cementation is associated with the transformation of opal-CT to quartz. In this process, calcium (Ca) is released from Ca–silica complexes in pore-water. The conversion of opal-CT to quartz is controlled by temperature, time, and properties of host sediment such as pore-water chemistry (e.g. Kastner 1981; Williams and Crerar 1985). The present conclusions are also in agreement with the results of Wetzel (1989) who observed more calcite cement in chalk at an ODP site where the temperature is high and less cement in chalk at another ODP site where the temperature is low. Thus increasing temperature by progressive burial favours porosity occlusion by pore-filling calcite cementation mechanism. The P-wave velocity and porosity–TTI relationships from this study were not used to derive predictive equations for porosity lost with burial depth, because this link is still controversial.

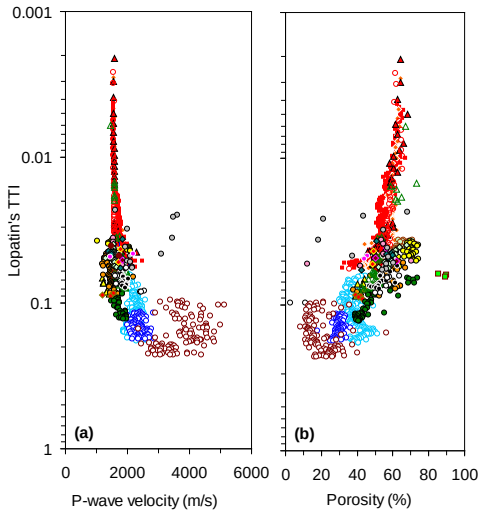

Figure 2.7: *Relationships between Lopatin's time–temperature index of thermal maturity (TTI) and P-wave velocity and porosity. Data from 24 ODP sites were used in this plot. For sample legend, refer to Figure 2.5. In this figure, we look at log TTI as it increases with P-wave velocity (**a**) and porosity (**b**). In this plot, the geothermal gradients at the Sites 165-999B and 165-1001A were assumed to be equal to 50^{o} C/km which is the upper extreme geothermal gradient at the study area.*

The present study has several advantages over other studies in this respect. First, data from many different locations that cover the entire study area which is larger than that in other similar studies were included. Second, only the data that represent chalk sediments of an Eocene age we considered here to avoid any possible influence of sediment age on diagenesis of chalk that may be reflected on physical property depth trends of chalk. The present data were correlated with two main physical property controlling factors such as vertical effective stress and TTI rather than depth. The physical property depth trends for both effective stress and TTI are supporting and confirming each other by telling the same story about the diagenesis of the studied Eocene chalk.

3. Petrophysics of pelagic siliceous ooze

3.1. Introduction

Intervals of pelagic siliceous sediments (composed of diagenetic skeletal remnants of siliceous diatoms frustules, radiolarians and sponge spicules) of Eocene to Mid Miocene occur above the Palaeocene sandstone reservoir of the Ormen Lange Field which is located in the Møre Basin deep-water area (water depth varies from about 800 m to 1100 m) in the southern part of the Norwegian Sea (Figure 3.1). The studied siliceous ooze is not a part of the current gas reservoir of the Ormen Lange Field.

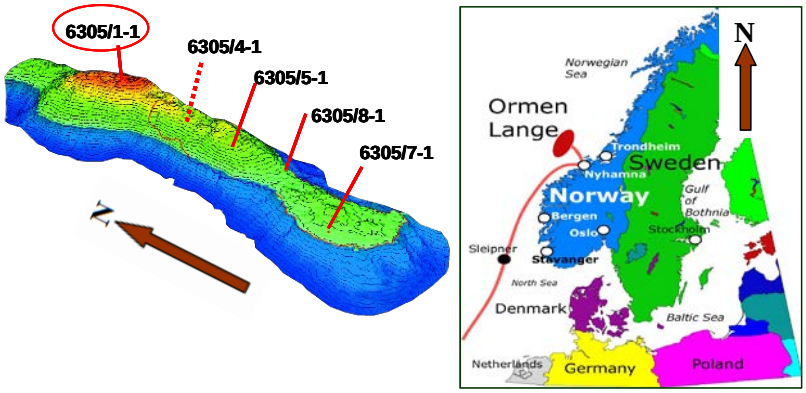

Figure 3.1: Location map of the Ormen Lange gas Field (right), not to the scale (The source of the map is: http://www.rigzone.com/news/image_detail.asp?img_id=317). The five wells included here are shown to the left figure on the North-South trending doubly plunging anticline with two structural highs (The source is the Norwegian Petroleum Directorate, NPD: http://www.npd.no). The well 6305/1-1 was only included on the estimation of vertical effective stress of siliceous ooze in Paper VI.

Biogenic amorphous silica (opal-A) and crystalline silica (opal-CT), clay, microfossils and organic materials are the main components of siliceous ooze sediment. Opal-A undergoes a phase transition into opal-CT where the formation temperature reaches about 43^{o} C (110^{o} F) (Bilodeau 1995; Keller and Isaacs 1985). Because the Eocene siliceous ooze is about 34–56 Ma old and occur at a depth of about 1000 m below the sea floor corresponding to more than 30^{o}C, in sediments of that age, we expect any original opal-A would have converted to opal-CT and perhaps to quartz in a series of dissolution-reprecipitation stages (Figure 3.2). However, for Miocene siliceous ooze of age (5–23 Ma) which occur at shallower burial depth, opal-A could be preserved.

The siliceous ooze at the Ormen Lange area is the target for this study. It is informally divided here into two units: an upper opal-A dominated siliceous ooze interval and a lower opal-CT dominated siliceous ooze interval. The contact between the two units is known as opal-CT contact and it forms a regional seismic reflector with medium amplitude and high continuity, which is believed to represent a diagenetic event of opal-A transformation, at shallow burial depth, into to opal-CT below a critical depth (NPD; Keller and Isaacs 1985). The opal-CT contact is easily identifiable seismic reflector (NPD). This study focused on the opal-A siliceous ooze interval where a core material was extracted (from the well 6305/4-1) and the relevant conventional core analysis data are available to calibrate the present results. Opal-A siliceous ooze

consists mainly of extremely fine-grained diatomaceous ooze with well-preserved opal-A frustules (Figure 3.3).

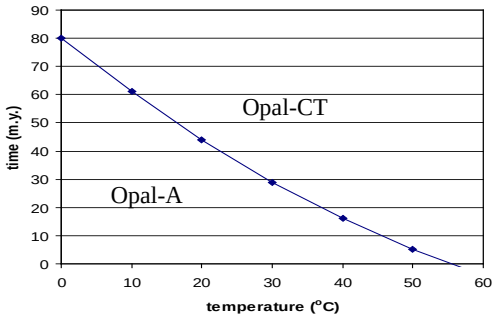

Figure 3.2: *A plot of temperature versus time (in million years) shows opal-A transformation into opal-CT in sediments with low carbonate content (Kastner 1977).*

A possible hydrocarbon prospect of siliceous ooze sediment has been proposed (NPD), but siliceous ooze sediment is significantly different in texture from most commonly known hydrocarbon reservoir rocks, such as sandstone and limestone. For instance, the pore structure of the siliceous ooze is complex and the solids are mechanically fragile and hydrous. So, an electron microscopy is needed to inspect the pore structure of siliceous ooze. Interpretation of petrophysical logs acquired through siliceous ooze intervals is not straight forward. Because siliceous ooze starts as low-density amorphous opal-A ($SiO_2.nH_2O$) which is relatively rich in the water of hydration (nH_2O with n about 0.121) that represents one of the most fundamental attributes of opal-A. During burial diagenesis, opal-A transforms into denser crystalline opal-CT ($SiO_2.nH_2O$, with reduced n) which still contains some water of hydration before further dehydration transforms it into microcrystalline quartz (SiO_2), (Kastner 1977). A further complication is that the opal is often mixed with clay (Pedersen et al. 2004) and possibly organic matter.

Normal petrophysical methods used in formation evaluation might not be suitable for interpreting siliceous ooze. For example, the density and neutron logging tools are calibrated in freshwater saturated pure limestone to give correct porosity readings in a limestone formation, but apparent porosity indications in any other lithology, such as siliceous ooze, should be corrected (Glover 2012). The apparent bulk density and the neutron porosity logging tools are influenced by the hydrogen in opal because they are sensitive to the amount of hydrogen in a formation and less to other elements. Grain density is a main challenge when deriving porosity from a bulk density log acquired through siliceous ooze intervals, because the grain density of siliceous ooze is very low and variable, depending on the amounts of opal content and the hydrated-water content in opal structure, which has an impact on density porosity calculation. If a constant grain density is used to calculate density-derived porosity of siliceous ooze, the obtained porosity is inaccurate. Neutron logging tools measure the hydrogen index (HI) of a formation which is primarily related to fluids in the porosity. The neutron tool obtains the combined signal of the HI of both the solid phase and of the water that occupies the true porosity. In the present work, all the possible contributions to the neutron porosity measurement were considered. Thus, the moderating power (slowing down power) of all minerals that were identified by X-ray diffraction (XRD) analysis on siliceous ooze core material were taken into account.

The primary objective of this study was to develop and use a new approach to accurately characterize and evaluate the studied siliceous ooze sediments to obtain

reliable grain density and true porosity logs. From seismic data, water bearing siliceous ooze can be mistaken for highly porous oil bearing sandstone interval. This may mislead explorationists to drill a dry exploration well. Therefore, the secondary objective was to find and observe the amplitude versus offset (AVO) signature of water saturated siliceous ooze to see if it could be distinguished from oil bearing sandstone, based on geophysical (i.e. seismic) data. Another goal was to estimate the vertical effective stress of the siliceous ooze by taking the Biot's coefficient, β, into account. To achieve these objectives, the conventional core analysis data were used and integrated with borehole logging data from five Ormen Lange wells, and included XRD data. Additionally, total organic content (TOC), carbonate content (CC), backscatter electron micrographs (BSEM), geological and drilling information, and other published data were also used here to make a consistent interpretation. This approach allowed determination of volume fractions of opal and non-opal components which were used with the empirical grain densities for opal and non-opal to calculate the grain density log through the studied intervals. The apparent density porosity was obtained based on the calculated grain density log and the corrected bulk density data. The true porosity was calculated by taking the electrons density into account. The neutron porosity was corrected for the hydrogen index contribution from the solid phase. The obtained present results proved to be reasonably consistent. The studied intervals apparently do not contain hydrocarbons.

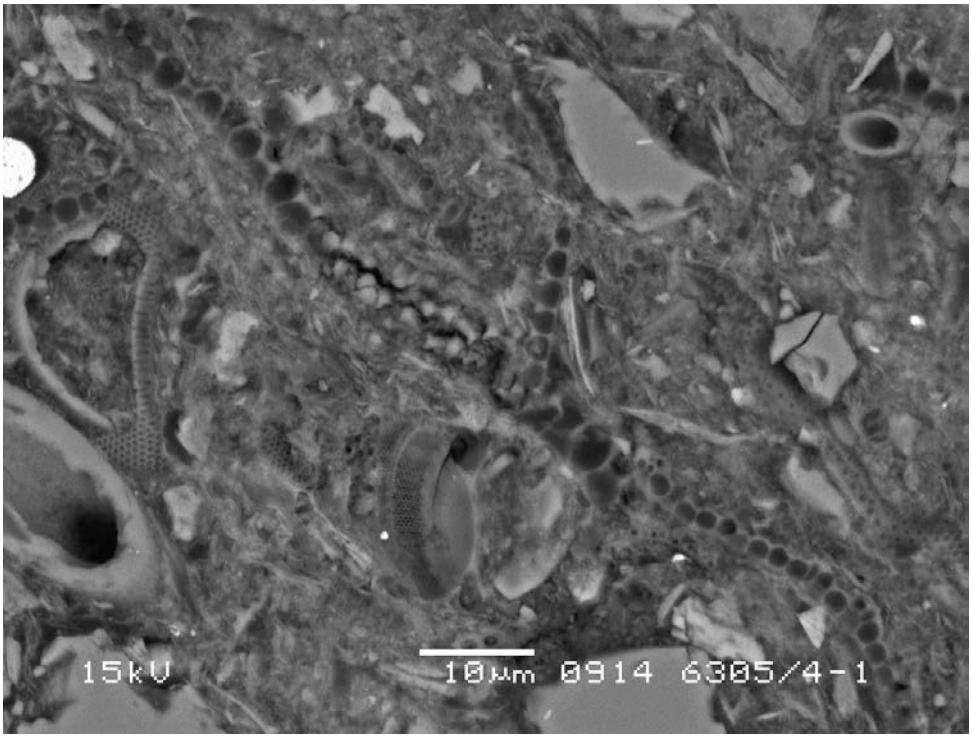

Figure 3.3: *Backscatter electron micrograph (BSEM) image of the siliceous ooze from well 6305/4-1 shows absence of lamination. The diatomaceous ooze contains clay, pyrite and silt. There is a framework of whole diatoms besides fragments and fine diatom dust. The sample has bimodal grain population and very high porosity. There are three kinds of porosity: 1) large-scale intragranular porosity within the uncompacted whole diatoms; 2) small-scale intragranular porosity within individual bits of diatom fragments; and 3) intergranular porosity. The first type is poorly connected porosity and the second one bungs up pore throats.*

3.2. Material and data

Core material of about 18.55 m (from 1761–1779.55 m) was extracted from the opal-A dominated siliceous ooze interval in the Ormen Lange well 6305/4-1. However, neither the extracted core material nor other drilling cuttings are available for the present study. Therefore, this study is based mainly on the available data which include the conventional core analysis, mineralogical and petrographic analyses, and petrophysical logs. The available data are not reported here in detail because they are confidential, except the logging data. The present obtained results include volume fractions of opal and non-opal, grain density log, the amount of hydration water in opal structure, true density porosity and true neutron porosity logs, formation water resistivity, water saturation, permeability, Biot's coefficient for elastic deformation (β), vertical effective stress (from well 6305/1-1) and AVO analysis. The non-opal fraction (componet) of the siliceous ooze has variable mineral composition of different grain densities. Cross plots assisted in finding that illite is a dominating mineral of the non-opal fraction (Awadalkarim et al. 2009). This is confirmed by the XRD analysis that showed illite constitutes about 50% of the total clay minerals in the bulk siliceous ooze material. All the five Ormen Lange wells included in the current research are close to vertical. In this study, where not otherwise stated, all references to depth (in text, tables and figures) are driller's measured depth along borehole, given in metres with reference to rotary Kelly Bushing elevation (m RKB).

3.3. Mineralogical and petrographical analyses

Samples, for mineralogical and petrographical analyses, were selected from the depth interval 1762–1772 m of the opal-A siliceous ooze core material that was extracted from the well 6350/4-1. The grain size distribution analysis on four samples has been conducted by the Norwegian Geotechnical Institute (NGI) using the falling drop, sedimentation, method based upon Stokes Law (Moum 1965). The results showed that the four analysed samples have similar grain size distribution and they mainly consist of silt with fine sand (<0.125 mm) in the larger fraction. The grain density of the four analysed samples ranges from 2.42–2.46 g/cm^3 which is in agreement with the core grain density of the siliceous ooze.

3.3.1. Mineralogical analysis

Data for total organic content (TOC), carbonate content (CC), XRD analyses on four opal-A siliceous ooze samples were available. The CC and the TOC values are low, in the range of 0.15–0.36% and 1.8–2.3%, respectively, with an error of ± 10%. Since the organic content is very small, hence, its influence is neglected. However, high TOC in a formation can cause anomalously high porosity value from standard logging tools (Passy et al. 1990). The XRD results only give the relative contents of the minerals which are possible to quantify from the peaks detected above the background interference and thus excludes opal-A. The results from the bulk sample analysis indicated a high percentage of clay minerals (including mica and glauconite) relative to the total content of minerals. The weighting factor for the clay mineral peak is high, and therefore produces a potentially large error. The peak is not very large and amplifies this effect. However, a content of about 34–48% clay minerals does seem

reasonable. Taking these considerations into account, the four samples analysed by the XRD appeared quite similar.

3.3.2. Petrographic analysis

Results of petrographic analyses by core X-ray computed tomography scans (CT-scans), scanning electron microscope (SEM), and microscopy thin-section analysis are available. The analyses were conducted to determine the core quality, texture and mineralogy of siliceous ooze. CT-scans showed few visible boundaries and little depositional lamination and high bioturbation. Fractures were amongst the most obvious features on the CT-scans, and some fractures appear to be open, indicative of faulting. Textural and morphological observations of the studied siliceous ooze were undertaken with SEM and BSEM images which showed that diatoms are abundant (Figure 3.3), and often associated with pyrite and silts. Fine sands occur, indicative of bottom currents. The 3D view of SEM images (stereo-pair imagery) helped inspecting pore space configuration which shed the light on the high total porosity but low permeability of the studied siliceous ooze. The structure of diatom frustules accounts for the extremely high total porosity.

The results of thin-section analysis, done by optical microscope, were compared with the core porosity and permeability to determine, qualitatively and quantitatively, the mineralogical compositions of siliceous ooze and to classify them. General overview of texture as well as burrows and micro fractures in the siliceous ooze were shown by thin-section analysis. It is also revealed the presence of quartz, feldspar, muscovite, and chlorite. Minor amounts of pyrite, illite, and kaolinite were also present. The analysis also showed that pyritisation of skeletal material occurred to a minor extent (of about 4–5%) throughout the investigated interval partially replaced other siliceous tests. This is in agreement with the XRD results that showed pyrite of about 6%.

3.4. Petrophysical measurements

3.4.1. Conventional core analysis

Ten one-inch core plugs were selected (at approximately every meter) within about 10 m interval from the upper half of the core that was extracted from the wellbore 6305/4-1. Core grain density, helium porosity and nitrogen gas permeability were measured on the ten one-inch core plug samples. The results showed that the grain density is low and variable, depending on the amount of opal and non-opal contents. It varies from 2.38–2.47g/cm^3 (2.43 g/cm^3 in average and 0.03 standard deviation). One important aspect of low and variable grain density is its effect on the calculation of density porosity. The core helium porosity (total porosity) is high and varies from 50–56% (53% in average and 0.02 standard deviation). This is in agreement with the Belridge diatomite porosity (Schwart 1988). As porosity decreases to about 50%, the grain density increases from about 2.38–2.47 g/cm^3. Siliceous ooze samples rich in opal-A have the lowest grain densities (about 2.38 g/cm^3), the highest porosities (about 56%) and the lowest permeability of about 0.210 millidarcies (mD). The core permeability ranges from 0.210–0.412 mD (0.304 mD in average and 0.06 standard deviation). The arithmetic, geometric and harmonic averages of the core permeability values are 0.304, 0.300 and 0.295 mD, respectively, implying that the analyzed siliceous ooze material is homogeneous to some extent (Tib and Donaldson 2004).

At times siliceous ooze sorting is bimodal or even polymodal as evident from BSEM images (Figure 3.3), pore throats can be blocked by a second-stage infiltration of very fine but well-sorted grains. The permeability among the studied siliceous ooze intervals is lower than the permeability of the Lost Hills field diatomite that ranges from 1–10 mD (Stosur and David 1976). Nevertheless, the porosity and permeability of the studied siliceous ooze are higher than most of the Monterey diatomaceous ooze of the Buena Vista Hills field that shows an average permeability of about 0.112 mD.

3.4.2. Characteristics of siliceous ooze petrophysical logs

The 12¼ inch (12.25") borehole sections in the five wells included here were drilled using 1.30 g/cm^3 water-based drilling mud (WBM) system. The logging data from the well (6305/1-1) are used to estimate the vertical effective stress, and excluded from the current logging analysis. Schlumberger's Platform Express (PEX) logging tool string was used in logging the 12.25" borehole sections. For more detailed information about the PEX, please refer to the website of Schlumberger at http://www.slb.com. The suite of well logs used here included calliper, natural gamma ray (GR), bulk density, photoelectric factor, sonic, neutron porosity, and resistivity. Details about the quality of the logging data that were used here are reported in Paper II. They can also be found on the NPD fact pages at www.npd.no.

The results of the petrophysical analysis of the selected siliceous ooze intervals in the four wells are presented in Paper II. Abrupt change in logging values at cycle boundary at the upper part of the opal-A siliceous ooze interval is obvious, especially in the well 6305/4-1 where the core material was extracted. Opal-A dominated siliceous ooze characterized by exceptionally high porosity, extremely low bulk density and low natural GR log readings with respect to the underling opal-CT dominated interval that characterized by a relative increase in bulk density and a decrease in interval transit time (i.e. high velocity) as shown by sonic log. The Opal-CT contact occurs at about 1895 m, 1988 m, 1933 m, 1922 m and 1993 m in the wells 6305/1-1, 6305/4-1, 6305/5-1, 6305/7-1 and 6305/8-1, respectively. Above the opal-CT contact, siliceous ooze is soft to very soft depending on the relative amount of opal-A and shale content. Below it, siliceous ooze is stiff and possibly cherty as well. The notable increase in density and sonic velocity logs at around 1922 m in the well 6305/7-1 corresponds to a diagenetic change from opal-A to opal-CT.

The logging responses of the studied intervals show very low bulk density and GR; and high total neutron porosity and sonic transit-travel time (i.e. very low formation velocity) readings with respect to the same logging responses of the adjacent shale or other lithology intervals. In the siliceous ooze intervals, the neutron porosity log shows quite similar porosity and it is also close to neutron porosity of the shale interval overlies the siliceous ooze in the well 6305/5-1 which is the only well where the logging data of the shale overlies the siliceous ooze are available. The high neutron porosity could be due to matrix effect of siliceous ooze that contains some internal porosity which is detectable by neutron porosity tool and sonic log. The density porosity is therefore lower when corrected for lower grain density. Likewise, the neutron porosity is lower when corrected for HI contribution of the solid.

Sonic log is generally not as good porosity tool as density and neutron logs, especially in unconsolidated formations. It tends to be more qualitative, especially in formations

that contain shale, such as the studied siliceous ooze. Shale affects sonic log very much. An increase in shale content of a formation looks as an increase in porosity to sonic log. Shale effects are the same on all sonic logging tools, since they measure a physical parameter. Shale correction of sonic logs is not accurate, and not as good as shale correction for the density and neutron logs, but it is probably better than nothing. Sonic log can not be considered a reliable gas indicator, either because its zone of investigation can be completely flushed of gas or because the more usual increase of 5-10% in travel time (due to cycle skipping or the tool reading mud travel time) appears as an increase in porosity of similar magnitude. In the present study, the sonic log was disregarded as a porosity tool.

Pyrite over 6% invalidates resistivity measurements due to its conductivity (Palacky 1988; Geonics Ltd. 1980). The average pyrite content (from XRD analysis) of the studied siliceous ooze is about 6% which may be one of the reasons for the low resistivity of the studied siliceous ooze. Therefore, it may be a good idea if one could consider the pyrite effect when interpreting resistivity log response. However, the Pe log does not show any indications or evidence for the pyrite effect on logs. One may need to have cation exchange capacity (CEC) data, to see whether siliceous ooze has matrix conductivity or not. However, CEC data are not available, and even if it is available, CEC will not help with the presence of pyrite. The resistivity logs showed little character and the deep and medium curves approximately read the same values.

3.4.3. Correcting density log to find true density porosity

Here, a new methodology on how to correct the bulk density log and find the true porosity of siliceous ooze is presented. Analysing logging data by integrating geological, core analysis, mineralogical and petrographic data allows determination of more reliable grain density log that can be used in deriving an accurate true porosity.

3.4.3.1. Bulk density log

Density log measures bulk density of a formation (i.e. electron density) which is usually expressed in g/cm^3. Bulk density data usually used to drive density porosity by considering the fluid density and the grain density of the individual solid materials involved. When a density tool is calibrated in freshwater-saturated limestone formation, the apparent bulk density that read by the density tool is related to electron density index (Schlumberger 1989). For water-saturated sandstone and limestone, the density tool reading is practically identical to actual bulk density. However, for other lithologies such as siliceous ooze, the apparent bulk density log should be corrected.

3.4.3.2. Calculation of opal volume fraction and grain density logs

The studied siliceous ooze is a mixture of opal and non-opal minerals (shale) at variable ratios. Here, the studied siliceous ooze is modelled as a mixture of opal, non-opal minerals and water. An assumption that both opal and water are non-radioactive and give no natural GR response is made here, and thus the GR log response of the studied siliceous ooze is due to the contributions from the non-opal minerals only. Based on the available information and on the core analysis data, the grain density log and the exact volume fractions of opal and non-opal of the studied siliceous ooze are unknown, and thus, they must be found.

Since the average core grain density is known, the relative volume fractions of opal and non-opal in the bulk siliceous ooze could be calculated (by assuming opal volume fraction is *x*, and non-opal is *1-x*.) as follows:

$$\rho_{g\_core} = \left(\rho_{g\_opal\,A}\right)\cdot x + \left(\rho_{g\_rest}\right)\cdot(1-x) \qquad \text{Eq. 3.1}$$

The average (arithmetic mean) core grain density ($\rho_{g\text{-}core}$) of the siliceous ooze material is about 2.43 g/cm^3. An average grain density of 2.78 g/cm^3 for non-opal minerals (ρ_{g_rest}) was calculated from the results of XRD analysis of the same core material. Here, the grain density ($\rho_{g\_opal\ A}$) of 2.16 g/cm^3 was used for opal-A (Serra 1984).

By substituting the values of $\rho_{g\text{-}core}$, $\rho_{g\_opal\,A}$, and ρ_{g_rest} g/cm^3 in Eq. 3.1, and solving for *x*, it is found that $x = 0.57$ (i.e. volume of opal is 57% and non-opal is 43%).

The volume fractions obtained by this way depends on the choice of opal grain density which itself varies quite a lot as reported in literature (e.g. Stosur and David 1976). Surely, the opal volume fraction estimated here can be debated, but it is reasonably acceptable for the purpose of this study. Now, since the volume fractions of opal and non-opal and their corresponding empirical grain densities are known, so they could be used here as a first calibration point for calculating a reasonable grain density log as a function of depth, for the entire siliceous ooze interval in each well. Based on the results obtained by Eq. 3.1, we have one fixed data point that can be used for calibration when calculating the volume fraction logs of opal and non-opal through the entire siliceous ooze intervals in the four wells. After applying appropriate environmental corrections, the GR log response is proportional to the weight concentrations of the radioactive material in the formation (Schlumberger 1989). Here, it is already assumed that the GR log response is due to the contributions from the non-opal minerals (shale) only. Thus, the GR log was used to reasonably estimate the volume fraction logs of opal and non-opal as a function of depth. The volume fraction logs were used with the corresponding average grain densities to calculate the grain density log for each siliceous ooze intervals, as follows:

$$\rho_{g\_calcu} = \left(\rho_{g\_opal\ A}\right)\cdot x + \left(\rho_{g\_rest}\right)\cdot(1-x) \qquad \text{Eq. 3.2}$$

where *x* and (1-*x*) are volume fraction logs of opal and non-opal, found from GR log, respectively. The calculated grain density was correlated with the core grain density.

The true density porosity was calculated by taking into account the number of electrons per unit volume (electron density) of the bulk siliceous ooze. To obtain the electron density log of the bulk siliceous ooze, we need to calculate the number of electrons in both fluid that occupies porosity and solid (opal-A and non-opal) phases. Before calculating the number of electrons in opal-A, we tried to establish a reliable relationship between the grain density and the amount of water content in opal structure. If such a relationship could be established, it would help to define and select the correct grain density if the amount of structural-water of opal is known. Several authors have used several different methods to determine water content of opal (e.g. Segnit et al. 1965; Graetsch and Ibel 1997; Herdianita et al. 2000). In Paper II, a detailed literature review about the relationship between structural-water content and

grain density of opal was conducted. However, based on the available published data, it would not possible to establish a significant correlation that could be applied in this study (Figure 3.4).

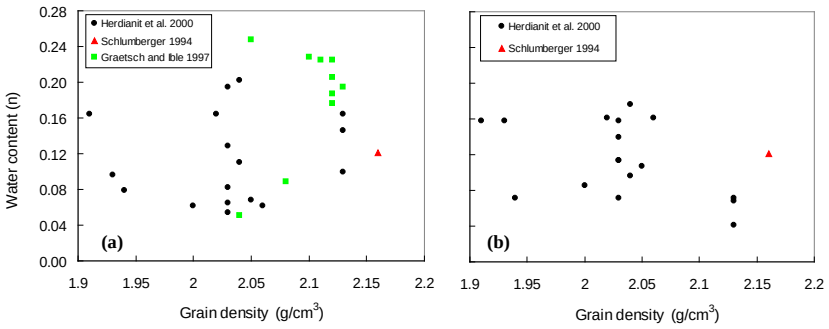

Figure 3.4: *Relationship between water content and grain density of opal. Opal water content is expressed here as a number of water molecules (n) in the structure of opal ($SiO_2.nH_2O$). (**a**) The water content as obtained at temperature less than100^o C; and (**b**) the water content as obtained at temperature greater than 100^o C.*

3.4.3.3. Calculation of opal water content, electron density and porosity

To calculate the number of electrons per unit volume (electron density) of opal-A, the grain density and opal water content of 2.16 g/cm^3 and 3.5 wt. % were assumed, respectively (Serra 1984 and Schlumberger 1994). This value of opal structural-water content is within the range of 1.2–5.8 wt % values that Grange (1937); and Nicholson and Parker (1990) obtained for opal. It is also in agreement with the range of opal water content as reported by Day and Jones (2008). However, some opals elsewhere could have different structural water content and hence different grain density than what has been assumed here. So, in this case, a different result between corrected and apparent bulk density logs is expected. The number of moles of water, *n*, in opal structure ($SiO_2.nH_2O$) was calculated as follows:

$$n = \frac{60.09\, f}{18.02(1-f)} = 0.121 \qquad \text{Eq. 3.3}$$

where *n* is the moles of water (H_2O) in the opal structure, *f* is the opal structural water content, in fraction (i.e. *f* = 0. 035), the 60.09 and 18.02 are the molar mass of silica (SiO_2) and water (H_2O) in g/mol, respectively (Table 3.1).

The number of electrons per cubic centimetre (cm^3) of opal-A was found as follows:

$$\text{Number of electrons per cm}^3 = \frac{\left(\rho_{g\_opal\ A}\right)}{\left(60.09+18.02n\right)} \times \left(30+10n\right) \times N_A \qquad \text{Eq. 3.4}$$

where $\rho_{g\_opal\ A}$ = 2.16 g/cm^3; *n* = 0.121; 30 and 10 are number of electrons per formula unit of silica (SiO_2) and water (H_2O), respectively. N_A is Avogadro's number = 6.022x10^{23} mol^{-1}.

Table 3.1: *Parameters used for calculation of the number of electrons per unit volume of the bulk siliceous ooze sediment. All these components, except calcite, constitute the bulk siliceous ooze.*

Components	Formula	Density (g/cm^3)	Molar mass (g/mol)	Moles/cm^3	Electrons/ formula unit	Electrons per cm^3 of mineral
Water	H_2O	1.00	18.02	0.05551	10	$3.34281x10^{23}$
Calcite	$CaCO_3$	2.71	100.0	0.02710	50	$8.15981x10^{23}$
Opal-A	$SiO_2.nH_2O$	2.16	62.30	0.034688	31.21	$6.51928x10^{23}$
Quartz	SiO_2	2.65	60.09	0.04410	30	$7.94904x10^{23}$
Kaolinite[1)]		2.52	516.70	0.00488	260	$7.67203x10^{23}$
Illite[2)]		2.79	787.90	0.00354	399	$8.40972x10^{23}$
Smectite[3)]		2.79	746.90	0.00374	552	$12.29933x10^{23}$
K-feldspar	$KAlSi_3O_8$	2.52	278.40	0.00905	139	$7.57538x10^{23}$
Plagioclase	$NaAlSi_3O_8$	2.59	262.20	0.00988	131	$7.79415x10^{23}$
Pyrite	FeS_2	4.99	120.00	0.04158	60	$15.02369x10^{23}$

Kaolinite[1)]: $(Al_{3.64},Fe_{0.07})(Si_{4.05},Ti_{0.1})O_{10}(OH)_8$
Illite[2)] 1: $(Ca_{0.02},Na_{0.04},K_{0.86})(Al_{2.75},Fe_{1.18},Mg_{0.08})(Si_{6.98},Ti_{0.13},Al_{0.89})O_{20}(OH)_4(H_2O)_{1,60}$
Illite[2)] 2: $(Ca_{0.1},Na_{0.18},K_{0.92})(Al_{2.94},Fe_{0.64},Mg_{0.38})(Si_{7.00},Ti_{0.08},Al_{0.92})O_{20}(OH)_4(H_2O)_{0.20}$
Smectite[3)]: $Ca_{0.05},Na_{0.23},K_{0.13})(Al_{3.36},Fe_{0.68},Mg_{0.86})(Si_{7.83},Ti_{0.04},Al_{0.13})O_{20}(OH)_4(H_2O)_{16.622}$
Note: the grain densities and chemical structures of kaolonite, illite and smectite used here are based on Table 6.2 of Kurniawan (2005), (after Brindley, 1951). The 2.79 g/cm^3 for illite is the average of the grain densities of illite structure 1 and illite structure 2. The grain density of K-feldspar (orthoclase), plagioclase (albite) and pyrite were obtained from Serra (1984). These grain densities are a bit lower than those reported on Table 6.1 of Hearst et al. (2000). It is assumed here that n = 0.121 in opal-A (Schlumberger 1994 and Serra 1984).

By using the same concept, the number of electrons per cubic centimetre (electron density) of each component (mineral) listed in Table 3.1 is calculated. To calculate the number of electrons per cubic centimetre (cm^3) of non-opal component, the calculated number of electrons per cm^3 of each non-opal mineral was multiplied by its volume fraction in the non-opal component and summed up together. Now the sum of the number of electrons per cm^3 of opal and non-opal components is known, and it represents the electrons density in the solid phase, *c*, that was used in the equation below where the true density porosity was obtained as follows:

$$\phi_{true} = \frac{a-c}{b-c} \qquad \text{Eq. 3.5}$$

where *a* is the bulk electron density log when the density tool is calibrated to calcite matrix (this is because the density logging tool is usually calibrated to freshwater-saturated limestone); *b* is the electrons density log of water occupies the true porosity, and *c* is the electrons density log of the solid phase (opal plus non-opal components).

The calculated true density porosity log correlates well with the overburden corrected core porosity indicative of its reliability. Thus, it is used here with the calculated grain density log and the estimated nominal pore-fluid (brine) density (ρ_f) of 1.025 g/cm^3 to obtain the true bulk density log which was compared with the apparent bulk density log as measured by wireline bulk density tool. The true bulk density log (ρ_{b_corct}) was calculated as follows:

$$\rho_{b\_corct} = \left((1-\phi_{true}) * \rho_{g\_calcu}\right) + \left(\rho_f * \phi_{true}\right) \qquad \text{Eq. 3.6}$$

Apparent porosity is the porosity read by logging tool when the tool is calibrated to a matrix of calcite and pore-space is filled with fresh water. It can be obtained based on the calculated grain density log and the wireline measured bulk density log data. Also a simpler approach is used where the apparent density porosity log ($\phi_{\_Density}$) was obtained by Eq. 3.7 assuming sandstone lithology. This is done based on the quartz grain density and the apparent bulk density log as measured by the density logging tool. The resulting porosity is about 5 to 10 porosity units higher than the true density porosity as calculated by Eq. 3.5. When the calculated grain density log was used instead of the quartz grain density, then the obtained true density porosity (Eq. 3.5) and the apparent density porosity (Eq. 3.7) are similar.

$$\phi_{\_Density} = \frac{\rho_g - \rho_b}{\rho_g - \rho_{fl}} \qquad \text{Eq. 3.7}$$

where $\phi_{\_Density}$ is apparent density porosity; ρ_g is quartz grain density (= 2.65 g/cm^3); ρ_b is apparent bulk density; and ρ_{fl} is the nominal pore-fluid density (= 1.025 g/cm^3).

To derive the most accurate porosity from bulk density log one would have to use the correct grain density. This is because the siliceous ooze grain density varies within the studied intervals depending on the amount of opal and non-opal admixtures. If a constant grain density value is applied, the derived density porosity is inaccurate. When too low grain density is used, the porosity is underestimated by the density log, and the opposite is true when higher grain density is used.

The true porosity (ϕ_{true}) calculated by Eq. 3.5 corresponds well with the overburden corrected core porosity (Figure 3.5e). However, very small variations were observed with some data points, depending on the amount of opal in each sample (Figure 3.5a, d, g). The average ϕ_{true} is around 49%, this is about one porosity unit lower than the average overburden corrected core porosity ($\phi_{\_Core}$) which is around 50%. This is about 2% reduction that represents a reduction in porosity from about 50% to about 49% within the same 10 m depth interval where the core porosity data were measured. The ϕ_{true} represents the total in-situ porosity as obtained from bulk density log. Because of the evident some dead-end pores in some siliceous samples shown by the petrographic analyses, the effective porosity actually may be even lower. In general, the in-situ measured density porosity should be considered much more reliable than the core helium porosity measurements. As helium porosimetry measurements rely upon full penetration of helium molecules into all open pores in the network, honouring proper equilibration time during the measurement is paramount. The derived permeability log agrees reasonably well with the Klinkenberg-corrected gas permeability (Figure 3.5i).

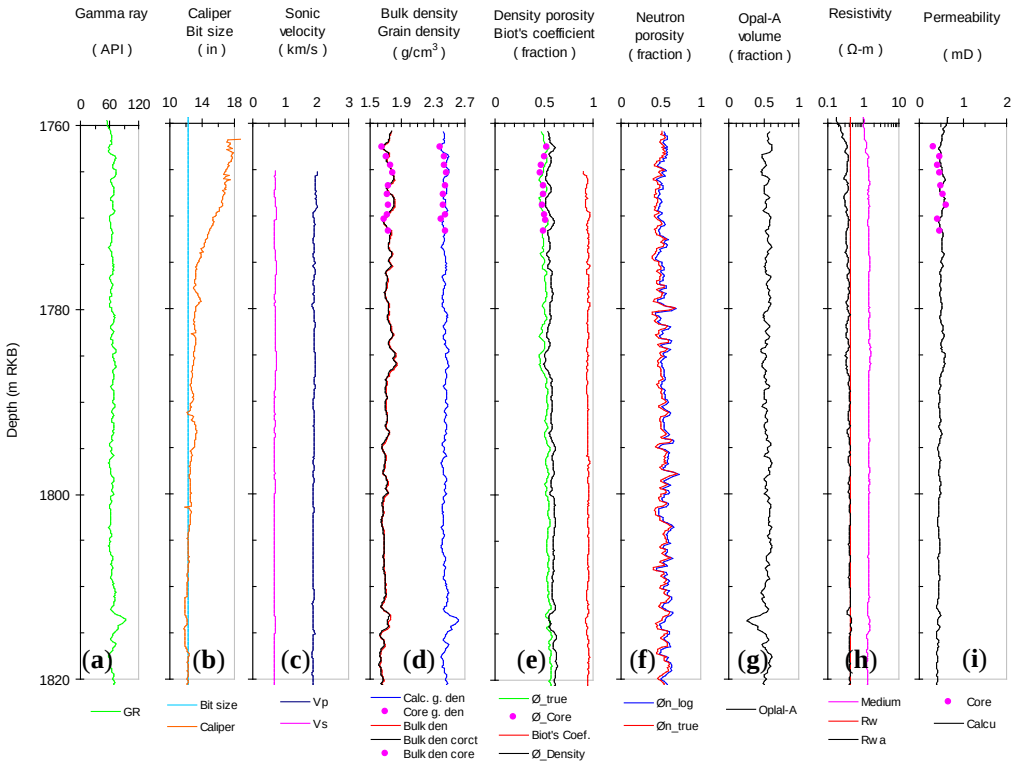

Figure 3.5: *Petrophysics logs of a selected siliceous ooze interval in the wellbore 6305/4-1. This is the only well in which the siliceous ooze interval was cored. Comparison of the wireline bulk density (Bulk den), core bulk density (Bulk den core) and wireline corrected bulk density (Bulk den corct), as well as the comparison of the calculated (Cal. G.den) and core (Core g.den) grain densities are shown in (**d**). The true density porosity (Ø_true), core porosity (Ø_core) and the apparent density porosity when quartz lithology is assumed (Ø_Density) are compared in (**e**). The true neutron porosity (Øn_true) and wireline neutron porosity (Øn_log) are compared in (**f**). The top of the opal-A dominated siliceous ooze is at about 1701 m, but no logging data are available for upper part of this interval, except gamma ray log. The opal-CT contact is at around 1988 m.*

3.4.4. Correcting neutron porosity log for hydrogen index of solid phase

3.4.4.1. Neutron log

Neutron log measures the hydrogen index (HI) of a formation, which is primarily related to fluids in porosity. The HI controls the count rate observed by neutron tool. Hence, it is normally assumed that neutron tool can measure real porosity in water-saturated formations where the matrix minerals contain no hydrogen (Glover 2012). However, neutron tool response is not straightforward as that of sonic and density logging tools. For example, clay minerals reduce porosity of a clean formation and this must be reflected as a reduction in amount of pore water. As a result, the HI of a formation must decrease as well, and hence, neutron porosity must also decrease. However, in reality, the opposite is true. Neutron porosity actually increases when clay minerals are added to a clean formation. This is because clay minerals are hydrated and neutron tool reflects this water of hydration as an increase in porosity even though the structurally bound water is not a part of the pore space of a formation.

Neutron log reads very low porosity when very saline drilling mud is used, because the saline mud attenuates the neutrons; hence they enter the formation with lower energy. In this case, the measured apparent neutron porosity will be lower than the true formation porosity.

It is normally assumed that the contribution to the neutron porosity measurement comes entirely from the hydrogen in fluids fully occupying the pore space, however, elements other than hydrogen that constitute the rock matrix do contribute to the signal; and hydrogen is also present within the water of hydration in the structure of solid phase, and this highly affects the measured HI.

3.4.4.2. Influence of HI of solid phase on neutron log response

A neutron porosity log is equivalent to a HI log as function of depth. Certain minerals, such as opal and clay, contain hydrogen in their crystal lattice. This may be water of crystallisation or structural bound water. Although this hydrogen is not associated with porosity, it is nevertheless countered by neutron tool. Because neutron tool responds to all the hydrogen in a formation, even if some of this hydrogen is not associated with porosity, such as bound water associated with shale and opal. In practice, it is not only hydrogen that affects the passage of neutrons in a formation. Other elements have an effect on slowing down of neutrons in a formation, but their effect is small compared with that of hydrogen (Glover 2012). It is obvious that siliceous ooze has an influence on the measured HI. Thus, the simplistic HI concept no longer describes the situation here adequately. In this study, we considered all the possible contributions to the neutron porosity measurement. Therefore, we estimated the true neutron porosity of siliceous ooze by taking into account the moderating power (the slowing down power which is equivalent to HI) of all minerals that were identified by XRD analysis of siliceous ooze sediment.

The neutron tool reads the combined signal of the HI of the solid phase and of the water (H_2O) that occupies the true porosity. For fully freshwater-saturated pure limestone (assumed 100% calcite), the HI is equivalent to the neutron porosity as measured by the logging tool (Serra1984). This is because Serra (1984) assumes the HI of calcite as equal to zero. In this study, the HI log as function of depth is calculated (by including 0.113 as the calculated HI of calcite) as follows:

$$HI_{Log} = (\phi_n) \times (HI_{water}) + (1-\phi_n) \times (HI_{calcite}) = (\phi_n \times 1) + (1-\phi_n) \times 0.113 \qquad \text{Eq. 3.8}$$

where ϕ_n is the neutron porosity as measured by the wireline neutron logging tool; 1 and 0.113 are the HI for brine (H_2O) and calcite ($CaCO_3$), respectively.

The relative neutron slowing down powers (i.e. HI values) of H, C, O, Si, Cl and Ca elements were obtained from Figure 8-2 of Serra (1984). For the rest of the other elements in Table 3.2, the equation 6.75 of Hearst et al. (2000) was used to calculate the average logarithmic energy decrement, ξ, which is also known as the energy lost per collision, ξ, (Serra 1984). When we compared the calculated ξ of each element with its relative neutron slowing down power (as reported by Serra, 1984) for that element, we found that they are equivalent, (please look at the HI and ξ of the 6 elements mentioned above and reported in the last two right-hand columns of Table

3.2. Therefore, where we do not have the relevant information to calculate the HI of elements such as Ti, K and S, we used the calculated ξ instead of HI.

Table 3.2: *Neutron content and the slowing down power of the principal elements, and the related energy lost per collision (ξ) used in the calculation of the hydrogen index (HI) of the compounds in Table 3.3 (Serra 1984).*

Element	Atomic Number (Z)	Atomic mass (A) (g/mol)	Number of neutrons	Energy[1] (MeV)	Energy lost[2] (%)	Slowing down power[3] (MeV)	HI[4]	ξ
H	1	1.008	0.008	2.23	50	18	1	1
C	6	12.000	6.000	4.95	14	114	0.158	0.158
O	8	16.000	8.000		11	150	0.120	0.120
Si	14	28.090	14.090	6.40	6	257	0.070	0.070
Cl	17	35.000	18.000	7.77	5	329	0.055	0.055
Ca	20	40.070	20.070	6.42	4	368	0.049	0.049
Al	13	26.980	13.980	0.23		290	0.062	0.072
Ti	22	47.870	25.870					0.041
Fe	26	55.850	29.850			539	0.033	0.035
K	19	39.098	20.098					0.050
Mg	12	24.310	12.310	8.16	14	235	0.077	0.081
Na	11	22.990	11.990			190	0.095	0.085
S	16	32.070	16.070	5.43				0.060

[1] Energy of emitted gamma rays
[2] Mean loss of energy by collision
[3] Neutron slowing down power of an element is the number of collisions needed to reduce the energy of a neutron from 2 million electron volts (MeV) to thermal energy of 0.025 electron volts (eV) at 25°C in a medium consisting only of this element, (Serra 1984).
[4] HI here refers to the ratio of slowing down power of hydrogen (H) to that of concerned element (Serra1984). Note that H is about more than six times as effective at slowing down neutrons as carbon (C) and even more than other available elements.

The above calculated HI log (Eq. 3.8) is related to true neutron porosity as follows:

$$HI_{Log} = \left(\phi_{n\_true}\right) \times \left(HI_{water}\right) + \left(1 - \phi_{n\_true}\right) \times \left(HI_{Solid}\right) \qquad \text{Eq. 3.9}$$

The HI of the elements in Table 3.2 was used to calculate the HI of the components in Table 3.3. The HI for the solid (HI_{solid}) and water (HI_{water}) were calculated according to Serra (1984) and Hearst et al. (2000) as explained below.

The HI of each mineral is normalized to the wt % of that mineral (based on XRD analysis results) to find its HI contribution in bulk siliceous ooze. For instance, to obtain the HI of calcite ($CaCO_3$), the weight fraction of Ca, C and O elements in calcite structure are 0.2, 0.2 and 0.6, respectively. Their corresponding slowing down powers (i.e. HI or ξ) are 0.049, 0.158 and 0.120, respectively (Table 3.2). Thus, the HI of calcite was calculated as following: (0.2x0.049) + (0.2x0.158) + (0.6x0.120) = 0.113. The same concept was applied to calculate the HI of each compound listed in the first row in Table 3.3. The calculated HI results of each compound are presented in the second row from the bottom in Table 3.3. To obtain the total HI contribution of all the non-opal minerals, their calculated HI were weighted by their respective

concentrations (in fraction) as reported in the bottom row in Table 3.3. The products were added together. The sum of the HI of all non-opal minerals is about 0.203 which was multiplied by the non-opal volume fraction log as obtained in section 3.4.3.2. The same concept was applied for opal, and its calculated HI is about 0.168, which was multiplied by the opal volume fraction log as obtained in section 3.4.3.2. The HI contributions from opal is combined with that from non-opal components and used in Eq. 3.9 as the HI of solid phase.

Solving Eq. 3.9 for true neutron porosity (ϕ_{n_true}) as follows:

$$\phi_{n\_true} = \frac{d-g}{e-g} \qquad \text{Eq. 3.10}$$

where *d* is the calculated *HI log* that neutron tool reads when is calibrated for limestone; *e* is the *HI* of water occupies the true porosity, and *g* the *HI* of solid phase.

Table 3.3: *The calculated stopping power, ξ, for water, calcite, opal and non-opal components and the parameters used in the calculation of ξ.*

				Non-opal minerals of the bulk siliceous ooze						
Compound	**Water**	**Calcite**	**Opal-A**	**Quartz**	**K-feldspar**	**Plagioclase**	**Pyrite**	**Kaolinite**	**Illie**	**Smectite**
Formula	H_2O	$CaCO_3$	$SiO_2.nH_2O$*	SiO_2	$KAlSi_3O_8$	$NaAlSi_3O_8$	FeS_2	**	**	**
A_H	1		1							
A_i	16	40; 12; 16	28; 16	28; 16	39; 27; 28; 16	23; 27; 28; 16	56; 32			
n_i	1	1; 1; 3	1; 2.121	1; 2	1; 1; 3; 8	1; 1; 3; 8	1; 2			
$\Sigma n_i A_i$	16	100	62	60	278	262	120	509	1204	1037
nH	2	0	0.242	0	0	0	0	8	12	37
Density (g/cm^3)	1	2.71	2.16	2.65	2.62	2.59	4.99	2.52	2.79	2.79
Ca (fraction)		0.200								
S (fraction)							0.667			
O (fraction)	0.333	0.600	0.631	0.667	0.615	0.615				
H (fraction)	0.667		0.072							
C (fraction)		0.200								
Si (fraction)			0.297	0.333	0.231	0.231				
K (fraction)					0.0769					
Al (fraction)					0.077	0.077				
Na (fraction)						0.0769				
Fe (fraction)							0.333			
Calculated ξ	**0.707**	**0.113**	**0.168**	**0.103**	**0.099**	**0.101**	**0.052**	**0.359**	**0.240**	**0.870**
Fractions of non-opal minerals as reported in Table 2				0.362	0.045	0.090	0.073	0.177	0.215	0.038

***** $n = 0.121$

****** For the formulas of kaolinite, illite and smectite, refer to footnotes of Table 3.1

A_H = the atomic mass of hydrogen atoms in the material

A_i = the atomic mass of non-hydrogen element *i*

n_i = the number of non-hydrogen atoms of element *i* in a formula unit of the material

nH = the number of hydrogen atoms in a formula unit of the material

The calculated true neutron porosity obtained by Eq. 3.10 is relatively lower (by about 3 to 4 porosity unit) than the apparent neutron porosity measured by the conventional wireline neutron logging tool. This is because the former is corrected for the HI contribution from the solid phase. Thus it should give low and consistent neutron porosity throughout the studied intervals. The calculated true density porosity (Eq. 3.5) and the corrected true neutron porosity (Eq. 3.10) are very similar which indicates that our interpretation is reasonably consistent.

3.4.5. Formation water resistivity, water saturation and permeability

The formation water resistivity (R_w) was determined from the formation water salinity and temperature data. In the Ormen Lange well 6305/4-1, R_w equal to 0.22 ohm-m at 96.7^o C was reported by the field operator. It seems to be fresh formation water. R_w must be at the temperature of the zone of interest which is the siliceous ooze interval in this study. The temperature profiles were obtained using the temperature gradients which were estimated based on the temperature data measured during the flow period of the two well-tests performed in the wells 6305/4-1 and 6305/7-1. To obtain R_w log as a function of depth for the studied intervals, the R_w reported by the operator was converted to the temperature logs of the studied siliceous ooze intervals. This was done by using the ARPS equation which is a useful method for converting R_w values from one depth to another with different temperature (Schlumberger 1989). Apparent formation water resistivity (R_{wa}) log as a function of depth was obtained as follows:

$$R_{wa} = R_t * \phi_{true}^2 \qquad \text{Eq. 3.11}$$

where R_t is the true formation resistivity from the deep resistivity curve; ϕ_{true} is the true density porosity log as calculated by Eq. 3.5.

The calculated R_w and R_{wa} of the well 6305/4-1 are presented in Figure 3.5h, they are generally the same, because in water zone, the R_w and R_{wa} should be identical. The calculated R_w is not precise because it was obtained based on the temperature logs which themselves are not so accurate. That is why it is not exactly identical to the R_{wa} where it should be. Thus, the estimated R_w needs to be verified carefully.

The water saturation was computed by using Archie's equation. This was based on the calculated R_{wa} log and the calculated true density porosity (ϕ_{true}) log by Eq. 3.5. The Archie's exponents used here were a = 1.30, m = 1.84, and n = 1.95, according to Bilodeau (1995). The saturation results range from 100% to 106%. The structural-water of opal and the structurally bound water in shale and clay particles may account for the calculated water saturation that exceeds 100%. The Archie equation is appropriate in the presence of saline formation water, as most often the case, whereas the formation water of the study area seems to be fresh. The electrical parameters in the Archie's equation were normally determined from special core analysis (SCAL analysis) which is not available for this study. The Archie's cementation and saturation exponents (m and n) are known to take different values for various reservoir rocks, especially for carbonates (Montaron 2009). Determining a suitable average value for m and n to be used in obtaining an accurate water saturation of siliceous ooze is quite a challenge. The four wells included here were drilled with high salinity water based mud, thus the deep laterolog curve should be used for true formation resistivity. The laterolog works better in conductive mud (saline mud). The HALS logging tool was failed in the well 6305/4-1, thus the deep laterolog curve is not available. The shallow laterolog curve was also affected by a problem with bridle. Thus, the medium laterolog curve for this well was used for true formation resistivity.

Lack of permeability measurements from well logs is an undesirable fact of life in well logging industry. The calculated true density porosity log was used here to

estimate permeability log (K_{calcu}) based on the regression from the overburden corrected core porosity and the Klinkenberg-corrected gas permeability cross plot (Figure 3.6), with goodness of fit (R^2) equal to 0.154. This relationship does not show good correlation, and it is expressed as follows:

$$K_{calcu} = (-1.5937*\phi_{true}) + 1.2596 \qquad \text{Eq. 3.12}$$

The derived permeability log (K_{calcu}) agrees reasonably well with the Klinkenberg-corrected gas permeability data (Figure 3.5i).

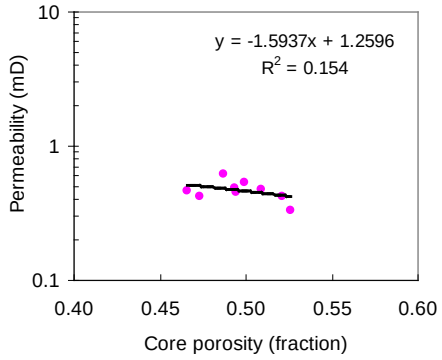

Figure 3.6: *Cross plot showing a linear trend of vertical Klinkenberg corrected gas permeability versus overburden corrected core porosity.*

Despite the high porosity of the studied intervals, the small or the lack of separation between the deep and medium resistivity curves indicates that the permeability is very low. No drilling mud loss was observed during drilling these intervals, which is an indication of low permeability. This is confirmed by the low core permeability. No capillary-pressure data are available, but if it is available, it would be very high and it is expected to reflect this abnormally low permeability due to the very fine grain size and the sub-micro pore category of the siliceous ooze. As shown by SEM and BSEM, the isolated internal micro-porosity would be filled with water and this may explain why the studied intervals have very high porosity and very low permeability values.

3.4.6. Pay zone determination

Pay zones are normally defined as intervals that meet certain cut-offs in porosity, water saturation and shale volume. For a zone to be considered pay, its porosity must be higher, and its water saturation and shale volume must be lower than the cut-offs (the three cut-offs must be satisfied). The studied siliceous ooze could be a potential hydrocarbon reservoir rock if evidences for hydrocarbon shows are observed.

The presence of shale in a formation is an extremely perturbing factor in formation evaluation. The studied siliceous ooze intervals contain significant amount of shale that could affect neutron porosity, bulk density and resistivity logs. The presence of shale may also hide the gas effect if siliceous ooze is a gas bearing. We looked for gas crossover on the calculated true density porosity and the corrected neutron porosity logs as this pair is a powerful combination for detecting gas in a formation. However, it does this in good gas zones, but some gas zones can not be detected. Therefore, if this method detects gas the gas is there. If it does not detect gas, then gas might still be there. Nevertheless, even if we have a neutron-density porosity crossover with mirror imaging, we are not 100% certain of the presence of gas, but it is too realistic

indication for the presence of gas. The resistivity logs were also used here to detect the possibility of pay zones, but, they gave no indication of possible pay zones.

It was expected to observe a clear gas content while drilling the siliceous ooze intervals if they are hydrocarbon bearings. Since no gas shows were detected during drillings, the presence of hydrocarbon is probably unlikely. Evidence of gas shows, within the studied intervals, is neither seen by the neutron log nor by the sonic log. Hydrocarbon shows were not seen in the drilling cuttings (drilling records) and were not reported either in the mud logs. The absence of gas may also be supported by the very high neutron porosity and very low deep resistivity values within the investigated intervals (i.e. they show indications of relatively fresh formation water) compared to the relatively high resistivity readings in the adjacent shale layers, and very high resistivity readings in the Egga Formation which is a gas bearing Palaeocene sandstone reservoir in the Ormen Lange field. If a formation contains hydrocarbons, the resistivity and porosity curves will go in opposite directions. We are aware that shale reduces the amount of separation, but the effect still holds true. It would be very surprising if these siliceous ooze intervals contain producible hydrocarbons. By the above plausible chain of reasoning, a conclusion is made that the studied siliceous ooze intervals apparently do not contain gas or any other hydrocarbon.

3.5. Elastic stiffness and vertical effective stress of siliceous ooze

Diatomite (i.e. siliceous ooze) of the exposed Danish Fur Formation is highly porous (Pedersen and Surlyk, 1983), yet stiff, so it is expected that siliceous ooze when diagenetically transformed might have a relatively low Biot's coefficient for elastic deformation (β), which would be relevant to find for the purpose of pore pressure prediction and hence for estimation of the effective stress.

At the first glance, one could refer the high porosity of siliceous ooze to overpressure or to unusual siliceous ooze stiffness that resists compaction and retains high porosity at relatively high effective stress. Biot's coefficient, β, which is an indicator of how well grains in a rock are in contact to each other (i.e. β is indicator for sediment elastic stiffness), is used here to help us interpret the stiffness of the studied siliceous ooze. The value of β depends on the degree of contact between the particles (grains). The β is estimated here, according to Biot and Willis (1957), (see Eq. 2.5 in section 2). Here, the bulk modulus log of a dry rock frame, K_{dry}, was found by Gassmann's fluid substitution (Gassmann 1951) of the wireline logging data under assumption of 100% water saturation. The mineral modulus of the grains that form the rock, K_o, was considered equal to 5 GPa, based on the results of Awadalkrim et al. (2009).

If β equal to 1, the grains are not in contact and thus the sediment follows the normal compaction trend according to Terzaghi (1923). If β is less than 1, this indicates that the particles are in contact to each other and hence they compact at lower rate than the normal compaction rate of the rock because more overburden stress is supported by the rock frame and therefore the compaction is less. Thus high porosity is maintained (high than it would have been expected without grains contact) because the grains are in contact to each other and not due to overpressure as there is no evidence or sign for overpressure in the studied siliceous ooze intervals (Awadalkrim et al. 2009).

Awadalkarim and Fabricius (2012) addressed the influence of using correct value of β when estimating the vertical effective stress on deep-sea sediments. They notice that even for small deviation in β value from 1, a significant higher vertical effective stress can be obtained. Because the calculated β is less than 1 and the water depth in the Ormen Lange area is very high (from 800–1100 m), thus, β has a relatively large influence on the estimation of effective stress (Awadalkrim et al. 2009). For safety reasons, this is very important to be observed (for pore pressure prediction) especially when drilling in deep-water basins (Awadalkarim and Fabricius 2012).

The calculated β of about 0.90 to 0.97 is less than 1 indicates that the investigated siliceous ooze is relatively stiff (i.e. grains are in contact to each other). Thus, the high porosity of the siliceous ooze can not simply be due to the loosely consolidation. Analogues of unconsolidated sands from Tobermory (W05214/4-01) and Peon (Møre 35/2-1) do not show as high porosity as does the studied siliceous ooze. The high porosity is probably due to the diatomitic intra-fossil porosity of siliceous ooze.

The results of the estimated vertical effective stress of the Møre Basin siliceous ooze are reported in Awadalkarim et al. (2009). It is expected that porosity decreases with increasing overburden stress, especially for those loosely consolidated siliceous ooze sediments. However, the overburden stress has only a moderate effect on the porosity reduction of siliceous ooze (Awadalkarim et al. 2009). The magnitude of porosity reduction, as function of stress, correlates to the degree of purity of siliceous ooze (Stosur and David 1976). This explains why the siliceous ooze porosity decreases very little with depth and why high porosity can be maintained at great depths.

3.6. Amplitude versus offset analysis

Siliceous ooze is characterized by high porosity, very low bulk density and low sonic velocity, and thus low acoustic impedance. Consequently, water bearing siliceous ooze interval can be mistaken (from seismic data) for a highly porous, poorly consolidated oil bearing sandstone and hence constitute a disappointing target for exploration. Knowing the amplitude versus offset (AVO) signature of water saturated siliceous ooze may enable explorationists to distinguish it from sandstone layer and hence avoid drilling dry exploration well in a water-bearing siliceous ooze interval. In this study, the acoustic velocity and bulk density logging data were used to determine the amplitude versus angle of incidence (AVA) response of the studied siliceous ooze sediments. This is done by using Zoeppritz (1919) equations cast in the formulation of Aki and Richards (1980). Here, the AVA of siliceous ooze was compared with a modelled hydrocarbon bearing sandstone interval (layer) having similar reflection strength at normal incidence as that of siliceous ooze. By this comparison we address whether AVO can help to distinguish water saturated siliceous ooze interval from an oil bearing sandstone interval. AVO from logging data is more reliable than that from seismic data, as in the first the lithology can be identified precisely from logs, but in the case of seismic data, the litholgy is unknown and it is inferred based on guess.

Figure 3.7 is a plot of the acoustic impedance (from P-wave (P-impedance) and from S-wave (S-impedance) velocity, and bulk density (ρ_b)) of the different formations encountered in the four Ormen Lange wells included in this study. The opal-A siliceous ooze showed the same P-wave acoustic impedance value of about $3.5x10^{-6}$ Pa.s/min and the same S-wave acoustic impedance value of about $1x10^{-6}$ Pa.s/min for

all the four wells, whereas the opal-CT siliceous ooze showed various acoustic impedance values range from 4 to $4.5x10^{-6}$ Pa.s/m, and from 1.5 to $1.7x10^{-6}$ Pa.s/m for P-wave and S-wave acoustic impedance, respectively.

The plots of the P-wave velocity (Vp), P-wave acoustic impedance (AI), bulk density (ρ_b), porosity, Poisson's ratio, and Vp/Vs ratio versus S-wave velocity (Vs), S-wave acoustic impedance (SI), Vp, Vp, AI and AI, respectively are shown in Figure 3.8.

The P-wave reflection coefficient (R_{pp}) for the interface between the shale (Kai Formation) and the top of the siliceous ooze (opal-A) is illustrated in Figure 3.9. The opal-CT reflector is shown by Figure 3.10, whereas the interface between the base of the opal-CT dominated siliceous ooze and the shale below (Tare Formation) is shown by Figure 3.11. The AVO response of water saturated opal-A dominated siliceous ooze is compared with that of a modelled clean oil-saturated sandstone layer (Figure 3.12. The AI of the sandstone layer is tuned to assure equal reflection strength at normal incidence. The reflection coefficient for the water saturated opal-A dominated siliceous ooze is constant at zero angle of incidence up to around 10^o and then slightly increases with increasing angle of incidence. When the porosity of the hydrocarbon saturated sandstone layer is very high, it is almost impossible to distinguish it from water saturated siliceous ooze especially at low angle of incidence (Figure 3.12). However, at angles of incidence greater than 15^o, oil saturated sandstone layer can be distinguished from water saturated siliceous ooze even though the effect is not great.

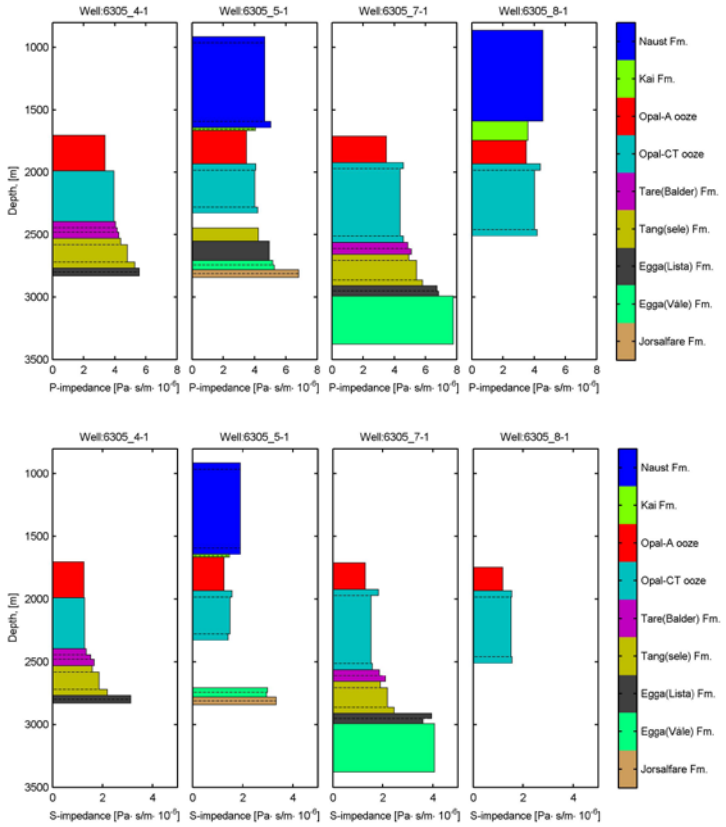

Figure 3.7: *Acoustic impedance (AI), from P-wave velocity and bulk density (top plots), and from S-wave velocity and bulk density (bottom plots), of the different formations encountered in the four wells. No sonic velocity data are available for the Tare Formation in the well 6305/5-1.*

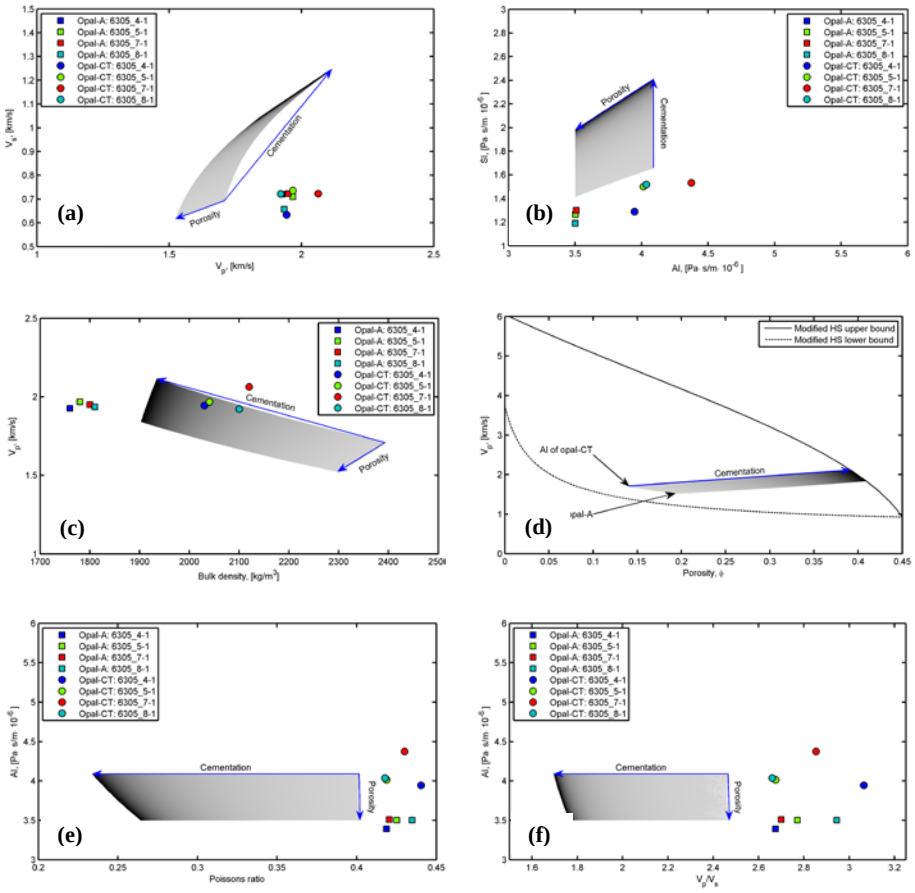

Figure 3.8: *The plots of: (**a**) P-wave velocity (Vp), (**b**) P-wave acoustic impedance (AI), (**c**) bulk density (ρb), (**d**) porosity (ϕ), (**e**) Poisson's ratio and (**f**) Vp/Vs ratio versus S-wave velocity (Vs), S-wave acoustic impedance (SI), Vp, Vp, AI and AI, respectively, compared with the analogous modelled clean oil saturated sandstone.*

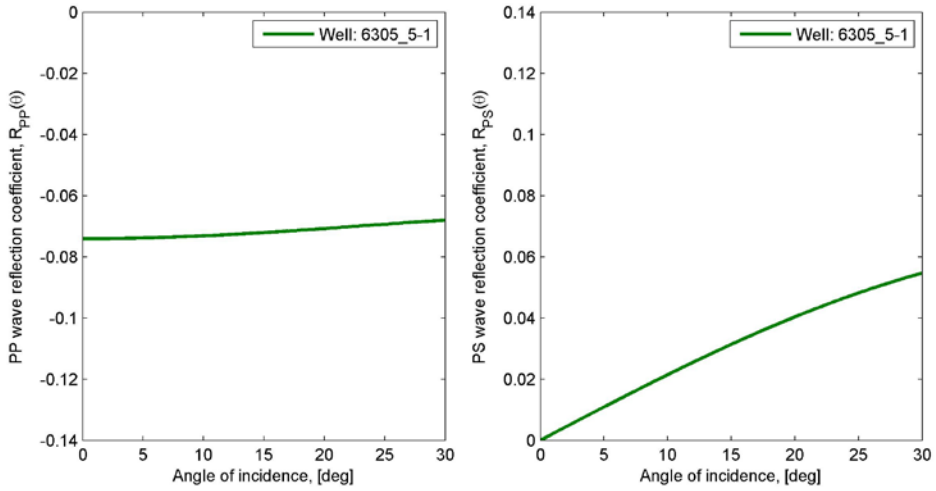

Figure 3.9: *P-wave reflection coefficient, R_{PP} (θ), (left), and S-wave reflection coefficient, R_{PS} (θ), (right), for the interface between the top shale (Kai Formation) and the top of the opal-A (i.e. shale/top siliceous ooze interface). Sonic velocity data for the top shale (Kai Formation) for only the well 6305/5-1 is available. There is only P-wave velocity (no shear velocity) data for the Kai Formation in well 6305/8-1.*

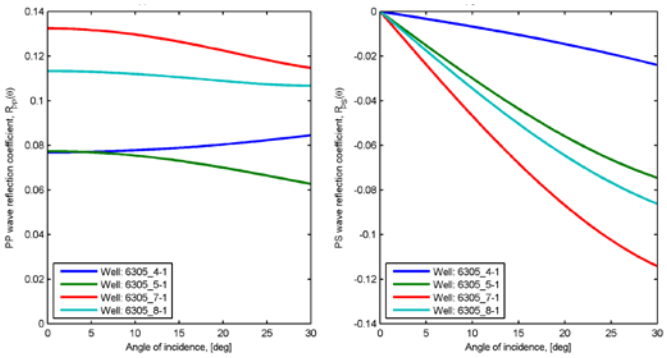

Figure 3.10: *P-wave reflection coefficient, R_{pp} (left) and S-wave reflection coefficient, R_{ps}, (right) of the opal-A/opal-CT interface. Different reflection coefficients values of the four wells may be because opal-CT contact is a diagenetic event through different lithologies.*

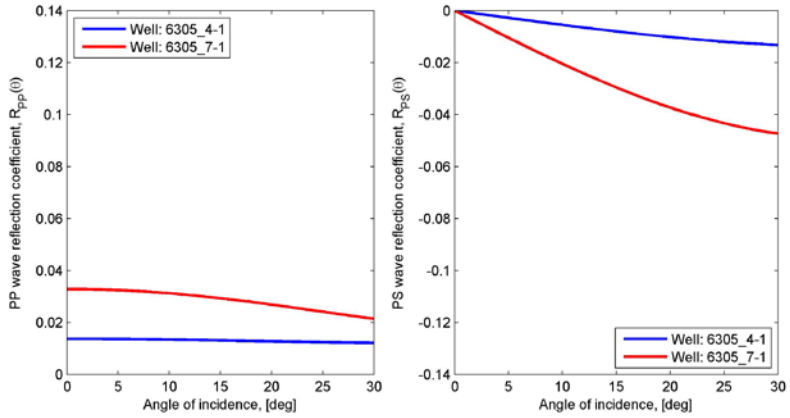

Figure 3.11: *P-wave reflection coefficient, R_{pp} (θ), (left) and S-wave reflection coefficient, R_{PS} (θ), (right) for the bottom of the opal-CT ooze (i.e. opal-CT/shale interface). Sonic velocity data for the Tare (Balder) Formation are available for the wells 6305/4-1 and 6305/7-1 only. No Sonic velocity data are available for the wells 6305/5-1 and 6305/8-1.*

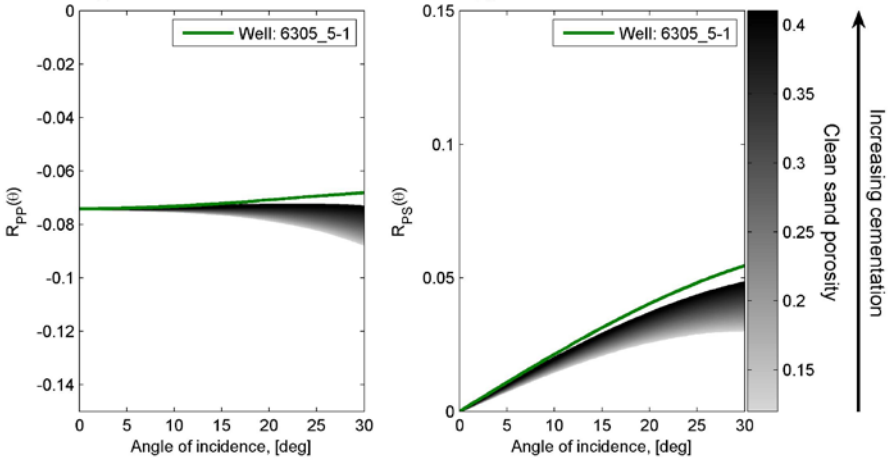

Figure 3.12: *AVO response of water saturated opal-A dominated siliceous ooze and hydrocarbon bearing sandstone (oil saturted sandstone layer). P-wave reflection coefficient, R_{pp} (θ), (left), and S-wave reflection coefficient, R_{ps} (θ), (right), of the top of the water saturated opal-A siliceous ooze compared with that of a modelled clean oil saturated sandstone with irreducible water saturation of 0.1.*

4. Rock physical interpretation of geotechnical data of Palaeogene clay

4.1. Introduction

The sediment samples used in this study are collected from the Fehmarn Belt Fixed Link area that is shown in Figure 4.1. The study area is about 19 km long, and it links Rødbyhavn in Lolland, Denmark, and Puttgarden in Fehmarn, Germany.

Several sediment samples were obtained from different geological units by using visibly undisturbed boring and sampling techniques (Geobore-S system), during the extensive site investigations that have been carried out to help the design and construction of a tunnel (fixed link across the Fehmarn Belt). Comprehensive laboratory tests were done by Fugro-McClelland (in Netherlands) and by Danish Geotechnical Institute, GEO (in Denmark). The major part of the tests has been done on the Palaeogene clay which is the most challenging lithological unit. Some of their laboratory data are included in this study along with the present data.

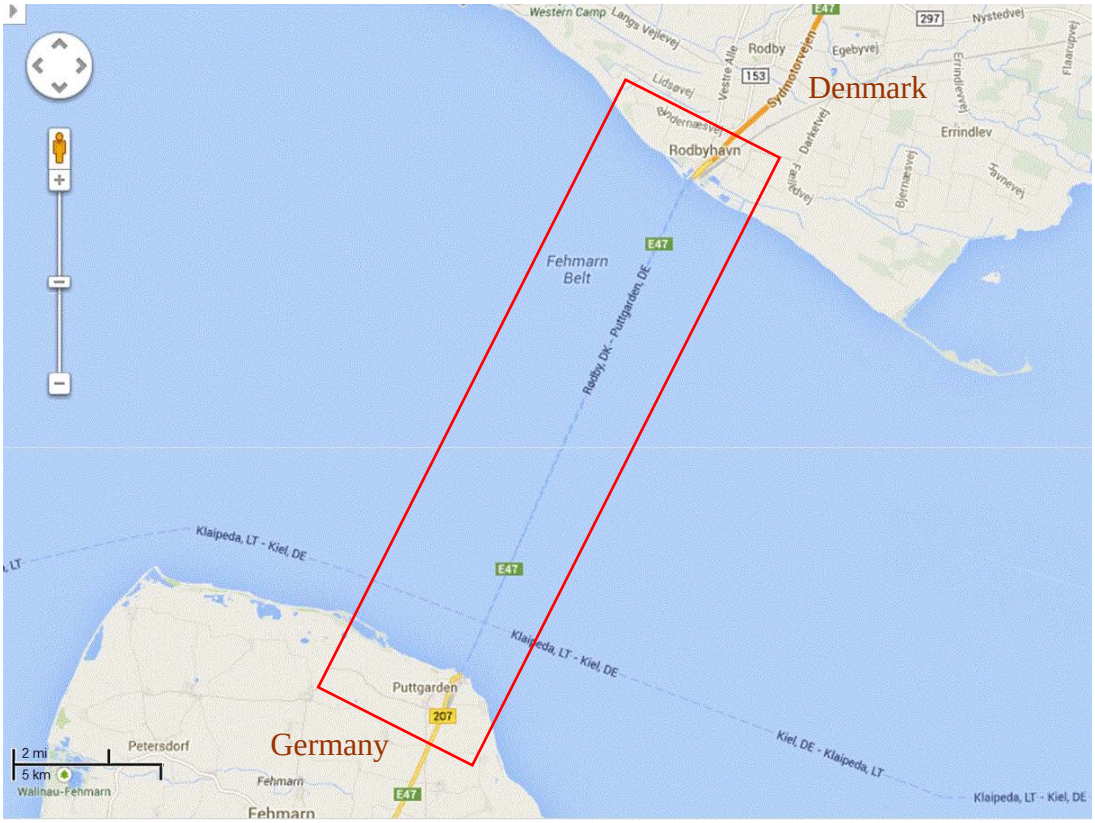

Figure 4.1: *Location map of the study area which is enclosed by a red rectangular which is not drawn to the scale. Modified from: Map data © 2013 GeoBasis-DE/BKG © 2009-Google, at https://maps.google.com/.*

In general, elastic properties of shale (clay) are known to be anisotropic (e.g. Hornby 1998). Kaarsberg (1958) made an in depth study of ultrasonic elastic anisotropy of saturated shale samples coupled with companion X-ray diffraction (XRD) analyses of mineralogical compositions. However, his shale samples were not measured under

stress. To address anisotropic elastic properties of shale, Hornby (1998) used elastic wave velocities of fluid saturated shale samples under drained conditions as a function of confining stress. Results of oedometer tests (swelling and traditional odometer tests) done by Jessen et al. (2011) show that when a Palaeogene clay is mounted in an oedometer cell without access to water and loaded to its *in-situ* vertical effective stress and then saturated with native salt pore water, the clay absorbs water and swells. This behaviour indicates that the Palaeogene clay in nature should expand for its *in-situ* stress. A study by Krogsbøll et al. (2012) on Palaeogene clay from Fehmarn Belt provides clues about the deformation behaviour during unloading and swelling states. In this study, the focus is mainly on the elastic properties of the naturally water saturated Palaeogene clay. Elastic wave velocity is controlled by the elastic stiffness and the density of a material. The geotechnical data and elastic wave velocity data were used to model the elasticity and then to relate it to mineralogy and BET surface area. The mineralogy, BET surface area, bulk density, porosity, water content and saturation, elastic wave velocity, electrical resistivity and strain (deformation) caused by mechanical loading were measured and used together to interpret the geotechnical data. The aim was to see which physical property is a main controliing factor of the elasticity of the Palaeogene clay and whether the deformation behaviour can be explained from elasticity alone.

The obtained results can aid in the estimation of drained elastic parameters from bulk density and elastic wave velocity and may have implications in engineering practice, including structural design and slope stability analysis.

4.2. Geological setting of Fehmarn Belt

The following geological description of the study area is based on Heilmann-Clausen et al. (1985) as well as on the available information in Rambøll/Arup (2011) and on the advanced laboratory testing data. Geological sample description is made in accordance with Femern's Geo Nomenclature and Larsen et al. (1995).

The mapped geological units of the study area are listed here from the youngest first as following: 1) Quaternary deposits; 2) Palaeogene clay and 3) Cretaceous chalk (Figure 4.2a). The water depth at the central part of the study area is grater than 24 m (Figure 4.2b). The Quaternary deposits and Palaeogene clay units consist of several geological formations. Below is a very brief geological description of these two geological units. However, detailed geological information about all the mapped geological units of the study area can be found in Rambøll/Arup (2011).

The Quaternary deposits include postglacial and late glacial marine deposits (peat, gyttja, sand, silt and clay deposits), in addition to the glacial deposits (upper and lower clay tills as well as associated sand and silt deposits). The Quaternary deposits overlay clay of Palaeogene age, described as having high to very high plasticity, which itself overlies the Cretaceous chalk. The Palaeogene clay consists of five formations (Sheldon 2010) which are listed below from the oldest (the one at the base) listed first to the youngest (the one at the top) listed last, with ranges of their estimated thickness given in the brackets: Æbelø (15–60m), Holmehus (3–40m), Ølst (10–15m), Røsnæs (15-28m) and Lillebælt (40–100m) clays. The microfossil analyses of a significant number of Palaeogene clay samples have shown that all the five formations and maybe the younger Søvind marl as well, are present in the borings at the study area

(Sheldon 2010; Rambøll/Arup 2011). The Æbelø, Holmehus and Ølst formations are of Palaeocene age whereas the Røsnæs, Lillebælt and the Søvind marl formations are of Eocene age.

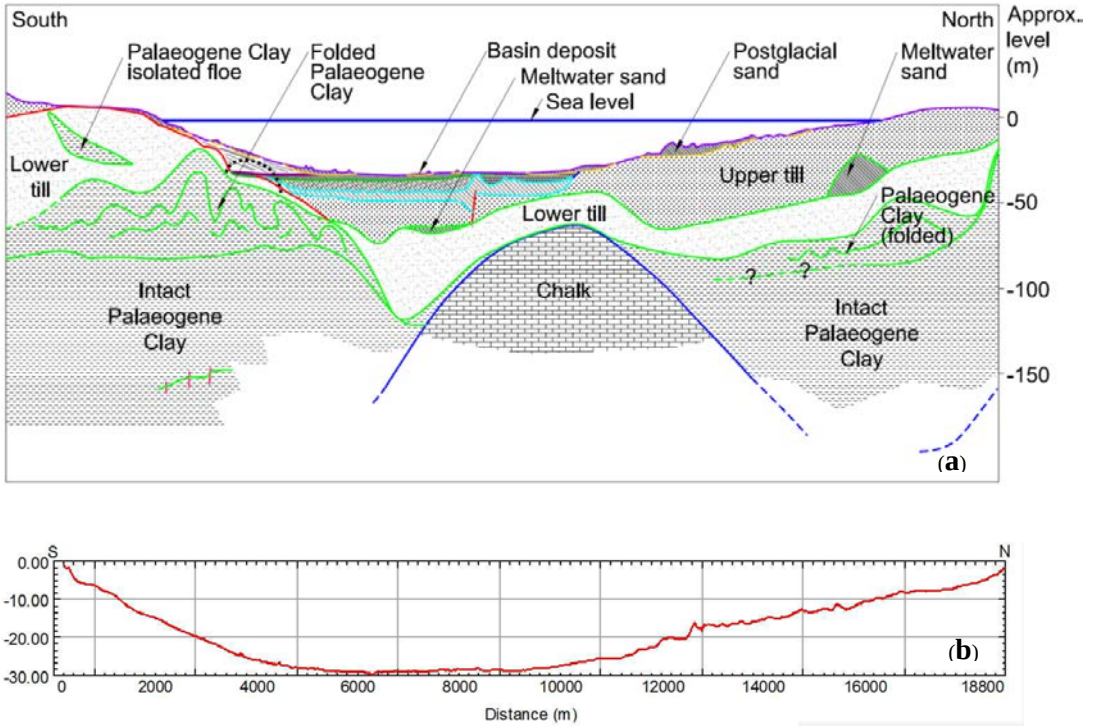

Figure 4.2: ***(a)*** *Simplified geological profile across Fehmarn Belt showing the studied Palaeogene clays. The folds shown in the folded Palaeogene Clay should only be understood as a signature. The real pattern is supposed to be much more intense and complicated.* ***(b)*** *A depth profile to the seafloor across Fehmarn Belt. Both cross-sections are taken from Rambøll/Arup (2011).*

The Æbelø Formation seems to be silty or even very silty, light grey to grey clay. The clays of the other formations are characterised by high to very high plasticity, and have clear, bright colours that vary a lot down through the layers and from one location to another in Denmark (Rambøll/Arup 2011). However, the Lillebælt Clay (which is the youngest Palaeogene clay found in the borings at Fehmarn Belt area) tends to be greenish to dark greyish green, non to slightly calcareous clay with about 70–80% clay content and plasticity index (I_P) of about 50–140%. The Røsnæs Clay is calcareous and silty with some siderite content. Most of it is reddish to brownish. However, for the Røsnæs Clay the colour and the general character of the clay change significantly down through the layer. The Ølst Clay is non-calcareous and often very dark grey to almost black with pyrite concretions. Its clay content is less than 60% and the I_P is about 50–140%. The Holmehus Clay is non-calcareous and bioturbated with about 70–80% clay content and I_P of about 50–140%. Its colour varies between greenish, bluish and reddish. Siderite concretions are present in most of the formations but seem to be most common in the Røsnæs Clay (Rambøll/Arup 2011). A plot of plasticity index (I_P) versus liquid limit (w_L) by Jessen et al. (2011) shows that the Palaeogene clays, except the Æbelø Clay, are very high plasticity, with w_L greater than 80% and all of them arrange above a I_P line represents: $I_P = 0.73(w_L–20)$.

Based on experience from earlier investigations of the Palaeogene Clay in Danish part of the Fehmarn Belt area (Lolland), it was expected that the clays from the different formations would have slightly different geotechnical characters. From other parts of Denmark it is known that the clay mineralogy in the deposits differs from one Palaeogene clay formation to another. Moreover, while the other Palaeogene clay formations are almost always non-calcareous, the Røsnæs Clay is most often slightly calcareous or even calcareous (Rambøll/Arup 2011).

There is rarely a clearly visible layering or lamination in the Palaeogene clay itself, and therefore it can be very difficult during the normal sample description to decide whether a single sample represents intact Palaeogene clay (undisturbed) or folded Palaeogene clay (disturbed) unit. Therefore, it is important that the Ølst Clay but also (in smaller amount) the Røsnæs Clay contains volcanic ash layers which are clearly visible in the samples. In some of the Palaeogene clay samples cross bedding of the coarse ash grains in the bottom of a layer has been observed, indicating that the water depth was shallow at the time of the volcanic ash deposition (Rambøll/Arup 2011).

In most of the Fehmarnbelt area, the Palaeogene clay has been subdivided into an upper and a lower group where the lower group has been interpreted as intact (undisturbed) clay, overlain by the upper folded (disturbed) clay. The interface between the intact and folded clays is identified as a significant, sudden increase with depth of the net cone resistance Rambøll/Arup (2011). On the geological profile in Figure 4.2a, the interface is indicated by a dotted line on the parts of the profile where it has been mapped with insufficient certainty. The folded Palaeogene clay is weakened compared to the intact clay. In this study the folded and the intact clays are considered as one unit even though they possibly have different geotechnical properties. Further detailed information about the areal distribution, post depositional deformations and observations on strength of the Palaeogene clay is given in Jessen et al. (2011) and also in Rambøll/Arup (2011) which can be found at the Fehmern A/S Geo Information System at www.fehmarnlink.com.

4.3. Vertical effective stress and pre-consolidation stress

The *in-situ* vertical effective stress (σ'_{V0}) of the Palaeogene clay is important to know for planning the laboratory tests. The σ'_{V0} has been established by Jessen at al. (2011) using the effective unit weight (the product of bulk density and acceleration of gravity) of the sediment and hydrostatic pore pressure distribution was assumed. The pre-consolidation stress (σ'_{pc}) and the over-consolidation ratio (OCR) are important properties to understand the sediment behaviour and to assess the *in-situ* stress history. Terzaghi et al. (1996) defined the σ'_{pc} as: “The vertical effective stress at which major changes in the natural sediment structure begins to take place.” Jessen at al. (2011) assessed the σ'_{pc} and the OCR of selected Palaeogene clay samples based on the following odometer tests: constant rate of strain (CRS), incremental loading (IL) and incremental loading determination of K_0, (IL K_0), and constant pore pressure ratio (CPR). They have applied the methods of Akai (1960), Becker et al. (1987), Casagrande (1936) and Janbu (1969) for deriving the σ'_{pc}. The method of Janbu (1969) gave more realistic σ'_{pc} results whereas the Casagrande (1936) and the Becker

et al. (1987) methods are sensitive with respect to modelling a straight line with measured data along a curve (Rambøll/Arup 2010a).

Although these stresses corresponds to OCR equal to or above 1, these deposits should generally be anticipated to be normally consolidated corresponding to OCR = 1. The results from the series of the IL, K_0 testes indicate that K_0 approximately equal $0.54OCR^{0.75}$ and $0.54OCR^{0.40}$ as an upper and lower bounds (Jessen at al. 2011).

4.4. Samples and experimental methods

The sediment samples used in this study are obtained from 24 boreholes drilled in 2009 and 2010 in the Fehmarn Belt area and from other 2 boreholes drilled offshore Lillebælt. The boreholes were drilled to a total depth of between 50 to about 100 m (Table 4.1). All boreholes were totally cored in the pre-Quaternary deposits. The use of core material here, rather than ditch cuttings samples, is important as it reduces errors in data caused by false sampling. For locations of the 24 boreholes included here, please refer to Rambøll/Arup (2010b).

XRD analyses and surface area by BET method have been done on 116 sediment samples collected from different geological units in the Fehmarn Belt area. The results are reported in Tables 4.1 and 4.2. Out of the 116 samples, 97 samples are Palaeogene clay from five different formations; and 19 samples are from Quaternary deposits (Table 4.1). Based on the XRD and BET results of the 116 sediment samples, initially, 30 preserved whole-core samples were selected from the Palaeogene clay and the Quaternary deposits for further laboratory geotechnical tests as well as for elastic wave velocity (ultrasonic velocity) and electrical resistivity measurements. However, due to the laboratory time constraint, only ten preserved whole-core samples of the Palaeogene clay were actually used in the laboratory work for studying their elastic deformation properties. Therefore, the discussion here is focused on the elasticity of the Palaeogene clay.

4.4.1. X-ray diffraction analysis

The mineralogical compositions of 116 samples represent different geological units were analysed for the bulk (whole-sample) and for the clay size fraction (<2 μm), using the XRD analysis technique. Sample preparation, analysis and interpretation procedures are modified from Moore and Reynolds (1997). The detailed XRD procedures applied here are presented in the Appendix A-III-1. XRD analyses were done using a Philips 1830 X-ray diffractometer equipped with Ni-filtered Cu K-α radiation generates a wavelength of 1.54051 Å (1 Å, angstrom $=10^{-10}$ m), and an automatic divergent slit. Instrument settings (operating conditions) were 40 kV tube potential and 25 mA tube current. The resulting XRD patterns are plotted as peak intensities versus angle of diffraction (θ). The XRD measurements of the various θ angles were used to calculate lattice distances (d-spacing) by using Bragg's law, and hence minerals were identified.

To determine the bulk mineralogy and the clay minerals of each sample, the XRD analyses were done on randomly oriented powder diffractometer mount of whole sample, and on orientated mount sample of the <2 μm clay fraction, respectively. The randomly oriented sample ensures that the incident X-rays have an equal chance of

diffracting off any given crystal and gives full diffraction pattern for the sample needed for a successful identification of bulk mineralogy. Oriented sample enhances the diffraction peaks caused by interplanar spacing parallel to the flake surface.

For bulk mineralogy, a representative powdered bulk sample was analysed (randomly oriented) from the interval 2°–60° 2θ (2-theta). An additional slow scan at step 0.01^{o} 2θ per 2 seconds was run from the interval 26^{o}–28^{o} 2θ for accurate feldspar determination. Slow scan resolves K-feldspar, plagioclase and quartz peaks needed for semi-quantification. Minerals peak heights were measured, corrected and the bulk mineralogy was semi-quantified. The <2 μm fraction was prepared by centrifuging of sample suspension. For identification and semi-quantification of the clay minerals, XRD analyses were done on the orientated samples of the <2 μm fraction from the interval 2°–35° 2θ with multiple treatments in the following sequences: untreated air-dried, ethylene glycol-solvated at 60^{o} C for 2 days, subsequently oven-heated to 350^{o} C for 2 hours and further heated to 550^{o} C for 2 hours.

Identification of the bulk and clay minerals was made by comparing the resulting XRD diffraction peaks to the standard JCPDS-ICDD diffraction patterns from PDF-2 Sets 1–43 database (Brown 1961). ICDD is the International Centre for Diffraction Data, and PDF-2 is the Powder Diffraction File-2. Based on Poppe et al. (2001), heights and areas of the peaks (as a measure of peaks intensity) of respective mineral phases were measured by an automated procedure developed by the author. Semi-quantification of the minerals is based on calculation of the integrated peak height and peak area measurements on the selected diffraction peaks of respective mineral phases, multiplied by in-house calibrated correction factors developed by Prof. Ole Bjørslev at University of Aarhus. On a bulk sample net peak height, *h*, was measured on the following peaks and multiplied by a correction factor: quartz 0.25*h* (4.25 Å); K-feldspar 0.10*h* (3.25 Å); plagioclase: 0.10*h* (3.18 Å); calcite: 0.076*h* (3.03 Å); dolomite: 0.076*h* (2.88 Å); siderite: 2.79*h* (2.79 Å); and total clay minerals 1.0*h* (4.46 Å, 19.8^{o} 2θ). Then, the bulk minerals were semi-quantified from the corrected peak heights. Clay minerals were semi-quantified from the ethylene glycol treated oriented samples. To estimate the contents of smectite, illite, and combined chlorite and kaolinte, the integrated peak areas at the 17 Å, 10 Å, and 7 Å peaks were measured and multiplied by correction factors 1, 3 and 1.15, respectively. Chlorite and kaolinite were then semi-quantified from the ratio of the height of the 14 Å peak after heating to 550^{o} C to the height of the 7 Å peak (after ethylene glycol treatment) corrected by a factor 1.5. By the above described procedure, the bulk mineralogical composition is assessed semi-quantitatively and the contents of the quartz, calcite, dolomite, feldspar, plagioclase, siderite and clay minerals were determined (Table 4.1). The clay minerals were identified and semi-quantified as main groups: smectite, illite, kaolinite and chlorite. So, all expanding clays were semi-quantified as smectite. Illite here can represent illite, mica, muscovite and glauconite.

The clay minerals were identified according to the following x-ray observations (Bailey et al. 1988): 1) The smectite crystal lattice structure is a stacking sequence of silicate–gibbsite–silicate, and hydrated exchangeable cations occupy the space between lattices. Smectite pattern looks as flowers or wheat bread. It swells when get in touch with water. In air dried, smectite identified by a broad peak at about 15 Å, which expands to about 17 Å upon glycolation, and collapses to 10 Å upon heating to 350^{o} C. 2) The illite crystal lattice structure is similar to that of smectite with silicate

layers sandwiching a gibbsite layer in between. It looks like fine mesh in pattern. It is identified by peaks 10, 5 and 3.34 Å. 3) Generally, the chlorite molecular structure is a stack of silicate–brucite–silicate layers sandwiching a brucite layer in between. Chlorite usually has a broad peak and it is identified by the peaks at 14, 7, 3.5 and 2.82 Å in oriented mount samples, which are stable upon glycolation (e.g. layers do not expand with ethylene-glycol-solvation) and partly replaced by 10 Å upon heating to 550^{o} C. 4) Generally, crystal lattices of kaolinite group compose of silicate sheets bonded to gibbsite layers. The silicate–gibbsite layers are tightly bonded together form a pattern looks as stacking cake sheets. It disperses into formation and flocculates and deflocculates as well. It is usually has a sharp peaks at 7 and 3.5 Å in oriented mount samples. It is stable upon glycolation and heating to 350^{o} C, but it disappears upon heating to 550^{o} C as this temperature decomposes the kaolinite structure (Moore and Reynolds 1997). This heating process distinguishes kaolinite from chlorite. Peaks used to identify kaolinite are located at 7, 3.5 and 2.38 Å.

4.4.2. BET surface area

The internal surface area (i.e. the surface area of the grains in bulk sample per unit weight (m^2/g)) of the 116 sediments bulk samples were done by nitrogen adsorption technique developed by Brunauer et al. (1938) which is known as BET method. A Gemini III 2375 surface area analyzer apparatus (Micrometrics Instruments Corporation) with measuring accuracy of ± 0.5% was used.

The surface area measurement was done on about 2 g of the air-dried then crushed sample. The surface area was determined after each sample was degassed for 4 hours at 70^{o} C on a FlowPrep060 degasser (Micrometrics Instruments Corporation) using nitrogen as a carrier gas. Both multipoint and single point data were recorded. For quality control, the surface area measurement was done in duplicate for each sample and a kaolinite and smectite species were used here as references. By this method, surface area of the grains in meter per unit weight (m^2/g) is estimated. The measured surface areas are presented in Table 4.1 as an average of the duplicate multipoint measurements. In this study, the obtained surface area results are referred to as BET or BET surface area.

4.4.3. Uniaxial strain experiments and elastic wave velocity

Ten preserved whole-core samples (in their natural moisture conditions) of the Palaeogene clay were selected and used for further laboratory experiments. An overview of the ten selected Palaeogene clay samples is given in Table 4.3. From these cores thirty naturally water saturated core plugs of 37.5 mm (1.5 inches) in diameter and nominally 25 mm (1.0 inch) long were prepared and used for measuring elastic wave velocity, electrical resistivity, deformation properties, and classification parameters. The 30 core plugs comprise sets of three core plugs cut in the vertical, horizontal and 45^{o} orientations from each of the ten whole-core samples. The laboratory measurements of uniaxial strain, elastic wave velocity and electrical resistivity were done under drained conditions as a function of uniaxial compressional stress with axial (principal) stress levels increasing from 0.2 to 3 MPa and subsequently unloaded to 0.2 MPa using a triaxial Hoek cell. The ratio of the confining stress (radial stress) to the axial stress is determined based on the values of the coefficient of earth pressure at rest (K_0) reported by Jessen et al. (2011) and by Krogsbøl et al. (2012). The uniaxial stress and the uniaxial strain (uniaxial

deformation) were measured simultaneously during the elastic wave velocity measurements, so the static drained modulus of uniaxial strain (M_{drain}) can be determined from the mechanical loading compaction curve. Here, the term 'drained' refers to a boundary condition in which the change in pore pressure during the experiment is equal to the change in axial stress. Thus, the obtained uniaxial strain from the uniaxial test means no lateral strain is allowed.

The ratio of the confining stress (σ_r) to the axial stress (σ_a) is equal to the over-consolidated K_0, (K_0^{OC}) which is determined here as follows:

$$\frac{\sigma_r}{\sigma_a} = K_0^{OC} = \left(K_0^{NC}\right) \times \left(OCR^{0.55}\right) \qquad \text{Eq. 4.1}$$

where K_0 is the coefficient of earth pressure at rest; K_0^{NC} is the normally consolidated K_0 which is ≈ 0.55 (Jessen et al. 2011); OCR is the over-consolidation ratio which is the ratio between the pre-consolidation stress (σ'_{pc}) and the current *in-situ* vertical effective stress (σ'_{V0}). The σ'_{pc} is the highest stress that a sediment has been subjected to in the past. Based on Jessen et al. (2011) and Krogsbøl et al. (2012), the OCR is assumed here as equal to 1 during the loading (with estimated K_0 = 0.55). See also section 4.3 above.

During geotechnical testing elastic wave velocity (i.e. ultrasonic velocity with a frequency of 200 kHz) was measured for the compressional wave (P-wave, Vp) and shear wave (S-wave, Vs). The general layout of the experimental setup for the elastic wave velocity measurements is shown in Figure 4.3. With this setup the elastic properties of the Palaeogene clay were obtained by means of the pulse transmission technique using an ultrasonic velocity with a frequency of 200 kHz. A triaxial Hoek cell of 37.5 mm in diameter was used for sample loading. Extreme care was taken to avoid, as much as possible, mechanical disturbance during mounting of the core plug specimen into the triaxial Hoek cell, to avoid gaps between the specimen and the triaxial Hoek cell during mounting, and to prevent swelling of the specimen in the early stages of the tests. Initially, about 160 KPa confining pressure and 60 KPa axial stress were used to hold the before starting the test. The sample is allowed to drain via a permeable sleeve (filter stone) placed at the bottom and top of the sample. After each stress level is reached, the sample is allowed to stabilize for about ten minutes before the measurements are taken. So, the velocity and resistivity were measured at reasonably stable conditions. All experiments were done at laboratory temperature of about 22^{o} C. A pair of linear voltage displacement transducer (LVDT) is located between the two transducers on opposite sides of the sample to measure change in sample length (uniaxial strain) during experiments. The measured deformation is used for accurate estimations of elastic wave velocity and electrical resistivity. It was also used to obtain porosity changes during the experiments.

The system delay times were estimated by linear regression of travel time versus distance measured on the three standard steel plugs of different lengths. The system delay times are 3 and 7 μsec for the P-wave and S-wave velocities, respectively.

The elastic wave velocity was estimated based on the measured travel time taken by an ultrasonic pulse to traverse through the tested sample. The determination of the

arrival times of the acoustic elastic waves is taken as the first arrival of the waveform for the P-wave and as the first zero-crossing of the waveform for the S-wave. The P-wave first arrivals are relatively easy to pick, but it was more difficult to determine the exact first zero-crossing for the S-wave. All velocity data are recorded as a function of axial stress.

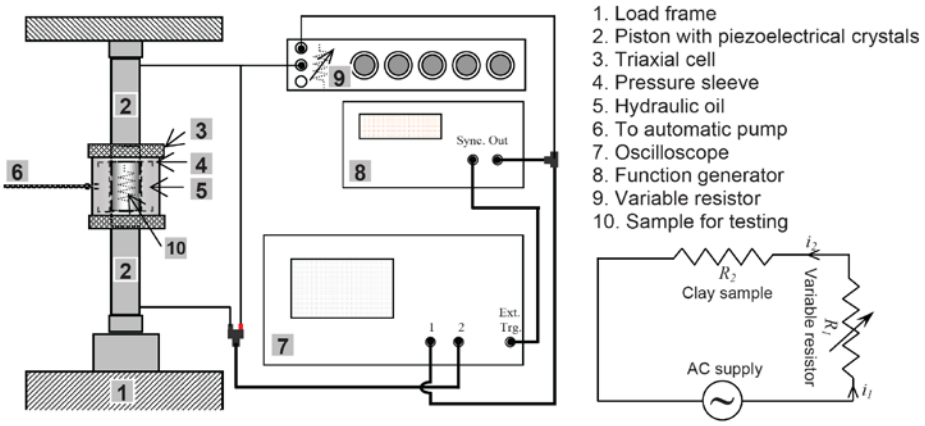

Figure 4.3: *Schematic drawing of the experimental setup used for elastic wave velocity and electrical resistivity measurements (Alam 2011). Not to the scale.*

The initial length of each tested sample is measured by the calliper. Knowing the arrival times ($t_{arrival}$) of transmitted ultrasonic pulses, the sample length (L) and the system delay times (t_{delay}), the elastic wave velocity (V) was computed using the following expression:

$$V = \frac{L}{t_{arrival} - t_{delay}} \qquad \text{Eq. 4.2}$$

where ($t_{arrival} - t_{delay}$) is the interval travel time across the tested sample; L is the actual sample length corrected for uniaxial deformation. The change in sample length with increasing stress is calculated by taking into account the corresponding uniaxial strain (as measured by LVDTs) resulted from sample being deformed. Overall accuracy of the velocity measurements is ±50 m/s for the P-waves and ±100 m/s for the S-waves.

4.4.4. Electrical resistivity measurement

Electrical resistitivy measurements as a function of axial stress are carried out simultaneously with the elastic wave velocity measurements in the same triaxial Hoek cell and at about 22 ^{o}C. The measurements are conducted by using the setup depicted in Figure 4.3, under uniaxial confined stress state of 0.2 to 3 MPa during loading and unloading cycles (drained condition). A low frequency (1 kHz) power supply of 1 volt was used in order to maintain the phase angle shift close to zero. The current flows through the core plug sample is similar to that of the variable resistor (i.e. $i_1 = i_2$). This is done by adjusting the resistance of the variable resistor such that the voltage over the sample equals half the output voltage from the function generator. By this way, the resistance of the variable resistor is equal to the resistance of the sample (Rc). Thus, the sample resistivity (Ro) is determined as follows:

$$R_o = \frac{A}{L} \times R_C \qquad \text{Eq. 4.3}$$

where *Ro* is sample electrical resistivity (ohm-m), *Rc* is sample resistance (ohm), *A* is sample cross sectional area (m^2), and *L* is actual sample length (m) corrected for uniaxial deformation.

4.4.5. Classification parameters and other geotechnical data

The bulk and dry densities, water content (moisture content), void ratio, total porosity, water content if the sample is saturated and the water saturation were collected, in three different orientations, from the same ten Palaeogene clay samples that were used for elastic wave velocity and electrical resistivity measurements. The present classification parameters are obtained based on the measured sample dimensions, volume and weight before and after each test and once again after sample drying at 60^o C in the oven. The standard geotechnical approach is to measure the water content at 105^o C, but it was measured here first at 60^o C to avoid possible change in interlayer water of smectite. For comparisons, the water content is measured once again at 105^o C. This is outside the original work scope but it was a useful exercise in validating the obtained water content. However, for consistency only those classification data that were measured at 60^o C were used here for further calculations and interpretations of the results. For instance, the initial porosity (ϕ_i) was calculated here (by using Eq. 4.7) from the initial void ratio that was obtained at 60^o C. The resulting initial porosity was used in Eq. 4.8 to calculate the change in porosity (ϕ) with stress which will be explained later in the following page.

The initial and the final bulk densities are obtained from the corresponding sample weight and volume before the test starts and at the end of the test (after unloading completed), respectively. The initial and the final dry densities are calculated from the initial and final bulk densities and the initial and final water content (in fraction), respectively. Water content is the ratio between the weight of water and the weight of grains. The initial and the final water contents are obtained before and after the sample is compressed (tested), respectively. It was obtained from the weight loss on sample drying at 60^o C, as follows:

$$\text{water content, w (\%)} = \frac{weight\ of\ water}{dry\ weight\ of\ sample} \times 100 \qquad \text{Eq. 4.4}$$

The dry density (ρ_d) is calculated as follows:

$$\rho_d = \frac{\rho_b}{1+w} \qquad \text{Eq. 4.5}$$

where ρ_b is the bulk density and *w* is the water content in fraction.

Void ratio (*e*) is a ratio between volume of pores and volume of grains. It is obtained here form the dry density (ρ_d) and grain density (ρ_g) of Jessen et al. (2011), as follows:

$$e = \frac{\rho_g}{\rho_d} - 1 \qquad \text{Eq. 4.6}$$

Porosity (ϕ), in fraction, is related to void ratio (e) as follows:

$$\phi = \frac{e}{1+e} \qquad \text{Eq. 4.7}$$

Continuous changes in porosity (ϕ) with stress is calculated using the initial porosity (ϕ_i) and the uniaxial strain (ε_A) as resulted from sample being deformed, as follows:

$$\phi = \frac{\phi_i - \varepsilon_A}{1-\varepsilon_A} \qquad \text{Eq. 4.8}$$

The saturated water content (w_{sat} %) can be obtained from void ratio (e) and grain density (ρ_g) or from porosity and dry density. It was calculated here as follows:

$$w_{sat}\% = \frac{e}{\rho_g} \times 100 \qquad \text{Eq. 4.9}$$

The water saturation (S_w %) was calculated from the initial water content (w) and the saturated water content (w_{sat}), as follows:

$$Sw\% = \frac{w}{w_{sat}} \times 100 \qquad \text{Eq. 4.10}$$

4.4.6. Elastic moduli of Palaeogene clay

The elastic properties of a linear elastic material such as clay may be described by elastic moduli (Fjær et al. 1992; Mavko et al. 1998). The P-wave velocity of water-saturated sediments depends on the relative proportion of water and sediment, the chemical composition of the pore water, and the mineralogical composition of the sediment particles. It also depends on the stiffness of the contacts between the grains of sediment. The P-wave modulus (M_{sat}) and the S-wave modulus (G) describe the propagation of acoustic elastic waves. In this study, the P-wave velocity (Vp), the S-wave velocity (Vs) and the bulk density (ρ_b) of the naturally water saturated Palaeogene clay samples were measured. Thus, the elastic undrained (saturated) uniaxial moduli were calculated as follows:

$$M_{sat} = \rho_b V_p^2 \qquad \text{Eq. 4.11}$$

$$G = \rho_b V_S^2 \qquad \text{Eq. 4.12}$$

The bulk density (ρ_b) of water saturated Palaeogene clay can be obtained as follows:

$$\rho_b = \rho_g(1-\phi) + \phi\rho_{water} \qquad \text{Eq. 4.13}$$

where ρ_g is grain density of clay, ϕ is porosity, and ρ_{water} is the density of pore-water.

When the clay sample is dried out, the density of pore water becomes zero and the bulk density (ρ_b) is termed as dry density (ρ_d). So, the Eq. 4.13 can be rearranged as:

$$\rho_g = \frac{\rho_d}{1-\phi_f} \qquad \text{Eq. 4.14}$$

where ϕ_f is the final porosity after the sample being compressed.

Poisson's ratio (ν) is the ratio between lateral and vertical deformation resulting from a vertical stress. It is estimated here from the P- and S-wave velocities as follows:

$$\nu = \frac{V_P^2 - 2V_S^2}{2(V_P^2 - V_S^2)} \qquad \text{Eq. 4.15}$$

where V_p and V_s are the compressional and the shear wave velocities, respectively.

The static uniaxial compressional drained modulus (M_{drain}) is an elastic property describing the stress increment ($\Delta\sigma$) relative to the strain increment ($\Delta\varepsilon$) under linear elastic uniaxial confined condition. It was obtained here for each sample as follows:

$$M_{drain} = \frac{\Delta\sigma}{\Delta\varepsilon} \qquad \text{Eq. 4.16}$$

The static uniaxial compressional drained modulus (M_{drain}) of each sample was determined on a series of selected slopes on the compaction curve. The M_{drain} was compared with both the undrained, uniaxial compressional modulus (M_{sat}) and the dry uniaxial compressional modulus (M_{dry}). The M_{sat} was estimated by using Eq. 4.11. The M_{dry} was estimated from M_{sat}, porosity (ϕ) and uniaxial mineral modulus (M_{grain}) based on approximated Gassmann's equation (Gassmann 1951, Mavko et al. 1998):

$$M_{dry} = \frac{M_{sat}\left(\phi M_{grain}/M_{fl} + 1 - \phi\right) - M_{grain}}{\phi M_{grain}/M_{fl} + M_{sat}/M_{grain} - 1 - \phi} \qquad \text{Eq. 4.17}$$

where M_{fl} is the P-wave modulus for the pore water which is assumed as 2.4 GPa.

In order to do this, we must establish uniaxial mineral modulus (M_{grain}): we assumed that Young's modulus of grains to represent a lower bound for M_{grain}. Young's modulus of grains (E), in GPa, can be estimated from grain density (ρ_g), in kg/m^3, according to the correlation of Chen & Evans (2006):

$$E = -377 + 0.189\rho_g \qquad \text{Eq. 4.18}$$

Biot's coefficient for elastic deformation (β) can thus be calculated according to Alam et al. (2012):

$$\beta = \left(1 - \frac{M_{dry}}{M_{grain}}\right) \qquad \text{Eq. 4.19}$$

4.5. Results and discussion

4.5.1. XRD analysis

The results of the estimated mineralogy based on XRD analyses of 116 sediment samples are expressed in weight percentages (wt %) and presented in Table 4.1 for bulk sample and in Table 4.2 for the <2 μm clay size fraction. The following constituents were detected in the bulk samples: 1) non-clay minerals (quartz, calcite and feldspar); 2) trace minerals (siderite and dolomite); and 3) clay minerals (smectite, illite, and kaolinite/chlorite). The relative abundances of these minerals are established on the basis of integrated peak intensity.

The XRD analysis of the <2 μm clay size fraction reveals the presence of smectite, illite, kaolinite and chlorite (Table 4.2). Smectite and Illite occur in all samples and form a major part of the clay mineral assemblage. In most samples, smectite content exceeds that of illite. Smectite is the most important constituent of the clay fraction and it often forms more than 50% of the solid of some Palaeogene clay samples. Kaolinite and chlorite form a minor part of the clay mineral fraction of most of the analysed Palaeogene clay samples. However, the amount of chlorite is lesser than that of kaolinite. It was difficult to identify kaolinite in the presence of chlorite by X-ray powder diffraction method, thus heat treatment was used to confirm the clay mineralogy. However, consideration must be given to variations in thermal behaviour of kaolin mineral varieties and chlorite mineral species (Brindley 1961). The smectite content of the Quaternary sediments is lower than 10%, whereas in Palaeogene clays the smectite is often higher than 10% and reaches about 74% in the sample no. 82.

Quartz and feldspar were detected in all the samples (Table 4.1). They are more common in the bulk samples than in the <2-μm clay fractions. In all the analyzed samples, quartz percentage is higher than feldspar, but never reaches 50% of the bulk composition except in seven sand-dominated samples from the Quaternary deposits. The feldspar percentages are never higher than 3% except in few sandy samples of Quaternary deposits. The presence of quartz in the deep Palaeogene clays could indicate the influence of deep sea currents in this area at the depositional time.

Siderite was detected in only seven samples. The sample no. 76 was the only one that contains significant siderite content of about 59%, whereas in the other six samples it ranges from 1% to 9%. Only traces of dolomite are observed (about 1% to 2%), but it forms a very small persistent proportion of most of the analysed sediments throughout the study area, yet it reaches about 6% in two samples only (Table 4.1).

Generally, the clay mineralogy of the studied clay does not show large differences. However, the sample no. 95 contains less smectite and illite but substantially greater amount of calcite (66%) than do the other samples. One possible explanation for this may be the sample portion analysed by the XRD is not fully representative.

Plots of the plasticity index versus smectite content and BET surface area are shown in Figure 4.4a and Figure 4.4b, respectively. Figure 4.4a shows two trends for Røsnæs clay and one trend for the rest of the other Palaeogene clays. This indicates a rather significant variation in smectite content within the five Palaeogene clay formations. The plot of plasticity index versus the BET surface area shows a relatively clear trend

Table 4.1: *XRD analysis and BET results. Semi-quantitative mineralogy (in weight percentage, wt %) based on XRD analysis of bulk sample. Smectite (sm) and illite (Il) are semi-quantified as separate phases although they may occur as inter-layered phases. Kaolinite and chlorite are combined together (Ko/Ch). Feldspars (Fd) included plagioclase.*

Sample		Depth		Geological unit		σ'_{vo}	Non-clay minerals (%)					Clay minerals (%)				BET
no.	Boring	(mbsf)	Core no.	Origin	Environ	kPa	Qz	Ca	Dl	Fd	Sd	Sm	Il	Ko/Ch	Total	(m^2g^{-1})
1	09.A.013	94	09-100196	Æbelø	Intact	1125	26			2		22	48	2	100	61
2	09.A.013	95.55	09-100310	Æbelø	Intact		30			1		38	29	2	100	66
3	09.A.014	74.1	09-100128	Ølst		835	14			6		55	18	7	100	84
4	09.A.014	65.65	09-100099	Røsnæs		780	22			1		50	18	9	100	56
5	09.A.008	7.75	09-100415	Claytill			48	21	1	24		1	3	2	100	7
6	09-A.003	13.8	09-101869	Claytill			58	24	6	2		0.3	6	3	99	14
7	09.A.002	54.6	09-101479	Røsnæs	Folded	490	25	0.4	2	2		12	38	21	100	66
8	09.A.002	85.05	09-101463	Røsnæs	Intact	765	26	1	1	2		12	37	22	101	61
9	09.A.014	33.7	09-100104	Claytill	Lower		32	43	2	17		1	3	2	100	7
10	09.A.002	48.8	09-101478	Røsnæs	Folded	435	24	1	1	3		10	37	24	100	57
11	09.A.001	22.3	09-101215	Røsnæs	Folded	175	28		2	3		29	27	11	100	66
12	09.A.602	49.55	09-101169	Røsnæs		475	15	1	1	1		20	40	22	100	64
13	09.A.002	99.5	09-101456	Røsnæs	Intact	890	17	8	1	2		17	36	19	100	56
14	09.A.014	61.2	09-100111	Claytill			34	32		13		7	10	4	100	14
15	09.A.602	20.1	09-101191	Røsnæs	Floe	185	30			2		30	27	11	100	62
16	09.A.605	15.45	09-101985	Claytill			45	33	3	5		1	8	5	100	15
17	09.A.001	10.15	09-101201	Røsnæs	Folded	75	26	0.4		2		19	33	20	100	64
18	09.A.001	32	09-101205	Røsnæs	Folded	255	29	1	1	2		22	29	16	100	63
19	09.A.001	17.4	09-101214	Røsnæs	Folded	140	28	1	1	2		26	30	13	101	63
20	09.A.001	4.2	09-101240	Røsnæs	Folded	50	26		1	2		22	33	16	100	62
21	09.A.001	32.95	09-101435	Røsnæs	Folded	295	20		1	2		14	24	38	99	64
22	09.A.002	29.55	09-101437	Røsnæs	Folded	265	17			1		31	31	20	100	64
23	09.A.002	11.5	09-101439	Røsnæs	Folded	105	22			1		29	29	19	100	66
24	09.A.002	22.5	09-101477	Røsnæs	Folded	200	20			1		20	39	20	100	67
25	09.A.003	15.65	09-101855	Claytill			79	9	2	4		1	3	2	100	13
26	09.A.003	23.35	09-101856	Røsnæs	Folded	225	32	2	1	2		29	24	10	100	63
27	09.A.003	34.25	09-101858	Røsnæs	Folded	320	29	0.3	1	3		31	25	11	100	62
28	09.A.003	16.5	09-101868	Claytill			47	22	6	13		2	7	3	100	14
29	09.A.010	49.35	09-101082	Røsnæs	Intact	415	26		1	3		15	34	20	99	62
30	09.A.010	39.05	09-101085	Røsnæs?	Folded	325	30	2	1	3		27	26	11	100	66
31	09.A.010	31.25	09-101096	Ølst	Folded	260	22	0.1		3		51	20	4	100	75
32	09.A.010	5.1	09-101102	Clay mrine	P.Glacial		46	26	6	5		2	9	6	100	19
33	09.A.010	10.25	09-101103	Claytill	Lower		42		0.3	2		35	18	2	99	53
34	09.A.010	14.25	09-101105	Ølst	Folded	120	20	0.1		2		53	22	3	100	65
35	09.A.010	19.75	09-101108	Ølst	Folded	165	19	1	0.2	4		46	25	4	99	72
36	09.A.001	25.85	09-101199	Røsnæs	Folded	206	30	3	2	2		29	25	9	100	67
37	09.A.001	45.1	09-101232	Røsnæs	Folded	360	32	0.3	2	2		23	28	13	100	64
38	09.A.002	44.75	09-101472	Røsnæs	Folded	400	26		2	2		26	30	14	100	60
39	09.A.002	56.2	09-101494	Røsnæs	Folded	505	29		2	3		27	27	12	100	64
40	09.A.003	41.8	09-101847	Røsnæs	Folded	385	25	0.1	2	2		14	35	22	100	64
41	09.A.003	45.85	09-101850	Røsnæs	Folded	420	22	0.6	1	0.7		33	30	13	100	65
42	09.A.010	40.05	09-101090	Røsnæs?	Folded	337	21	2	1	1		42	22	11	100	68
43	09.A.010	11.3	09-101104	Ølst	Folded	96	38	0.2		3		41	16	2	100	53
44	09.A.010	17.2	09-101110	Ølst	Folded	144	22	0.5	0.4	3		54	18	2	100	70
45	09.A.002	90.2	09-101462	Røsnæs	Intact	809	28	1	2	2		26	28	13	100	65
46	09.A.002	67.6	09-101493	Røsnæs	Intact	606	33	1	2	2		25	25	12	100	65
47	09.A.002	6	09-101509	Røsnæs?	Fole?	55	19	1	2	1		33	29	14	99	64
48	09.A.001	15.7	09-101195	Røsnæs	Folded	125	33	1	2	2		24	26	12	100	64
49	09.A.001	11.3	09-101211	Røsnæs	Folded	90	22	0.1		2		28	32	16	100	59
50	09.A.002	14.5	09-101431	Røsnæs	Folded	130	24	0.3	1	2		25	31	17	100	60
51	09.A.002	25.25	09-101436	Røsnæs	Folded	225	27	0.1	1	2		33	25	12	100	67
52	09.A.002	15.45	09-101476	Røsnæs	Folded	165	30	0.1	1	1		22	32	14	100	67
53	09.A.003	18.55	09-101873	Røsnæs	Folded	180	30		1	3		31	25	10	100	64
54	09.A.701	29.05	09-102950	Røsnæs	Folded	360	25	1	1	2		18	34	19	100	63
55	09.A.701	37.5	09-102951	Røsnæs	Folded	435	24	1	2	2		19	33	19	100	67
56	09.A.701	30.1	09-102973	Røsnæs	Folded	370	29		2	3		8	35	23	100	66
57	09.A.001	17.4	09-101214	Røsnæs	Folded	140	31			3		29	26	11	100	62
58	09.A.001	45.1	09-101232	Røsnæs	Folded	360	30		2	2		27	27	12	100	64

Environ = environment.
Non-clay minerals are quartz (Qz), calcite (Ca), dolomite (Dl), feldspar (Fd), siderite (Sd). Clay minerals are smectite (Sm), illite (Il), kaolinite and chlorite (Ko/Ch).
BET is the surface area measured by nitrogen adsorption (BET method).

Table 4.1: *continued*

Sample	Boring	Depth		Geological unit		σ'_{vo}	Non-clay minerals (%)					Clay minerals (%)				BET
no.	no.	(mbsf)	Core no.	Origin	Environ	kPa	Qz	Ca	Dl	Fd	Sd	Sm	Il	Ko/Ch	Total	(m^2g^{-1})
59	09.A.001	37.85	09-101235	Røsnæs	Folded	305	32	1		5		27	25	10	100	63
60	09.A.002	14.5	09-101431	Røsnæs	Folded	130	33	0.1	1	2		24	25	14	99	60
61	09.A.002	18.45	09-101476	Røsnæs	Folded	165	27	0.1	1	2		21	29	20	100	66
62	10.A.051	24.85	10-105043	Røsnæs	Folded	215	29		1	3		18	32	17	100	61
63	10.A.051	15.8	10-105072	Røsnæs	Intact	140	21	12		1		13	30	23	100	64
64	10.A.051	36.75	10-105085	Røsnæs	Folded	315	30		1	3		21	29	16	100	68
65	10.A.051	38.9	10-105091	Røsnæs	Folded	340	32	1	1	2		27	24	13	100	61
66	10.A.051	42	10-105116	Røsnæs	Folded	360	28	0.2	1	3		25	27	15	99	64
67	10.A.055	29.55	10-105202	Røsnæs	Folded	270	25		2	3		24	30	16	100	63
68	10.A.055	36	10-105231	Røsnæs	Folded	325	21	0.2	2	2		16	37	22	100	57
69	10.A.055	41.55	10-105248	Røsnæs	Folded	390	28		2	4		24	27	15	100	64
70	10.A.051	8.15	10-105051	Røsnæs	Folded	72	24	3	2	6		12	31	22	100	61
71	10.A.055	46.4	10-105224	Røsnæs	Folded	440	27	1	2	3		27	27	13	100	63
72	10.A.055	35.45	10-105235	Røsnæs	Folded	320	29	0.1	1	4		17	30	19	100	62
73	10.A.055	43	10-105272	Røsnæs	Folded	380	34	2	1	2		29	21	11	100	66
74	10.A.054	40.85	10-105377	Røsnæs	Folded	420	31	1	1	1		29	26	11	100	63
75	10.A.054	37.85	10-105430	Røsnæs	Folded	395	34	0.2	2	2		20	28	14	100	63
76	09.A.001	7.2	09-101240	Røsnæs	Folded	50	9	0.2	0.3	1	59	17	9	4	100	53
77	10.A.803	4.5	10-105027	Lilleblt			13	6	1	1		56	11	12	100	75
78	10.A.055	27.25	10-105204	Røsnæs	Folded	250	26	2	1	2		52	14	3	100	63
79	10.A.055	58.05	10-105236	Røsnæs	Intact	515	28	0.1	2	2		34	23	11	100	61
80	10.A.054	32.95	10-105400	Røsnæs	Folded	350	26	0.3	1	3		43	19	8	100	64
81	10.A.054	50.75	10-105425	Røsnæs	Folded	505	25	0.3	1	4	9	32	19	10	100	61
82	10.A.058	30	10-105784	Holmehus	?	290	19	0.2		1		74	6		100	76
83	10.A.055	72.45	10-105201	Røsnæs	Intact	635	18	9	2	2		19	31	19	100	60
84	09.A.007	20.75	09-100712	Æbelø?	?	270	44	17	0.1	3		23	11	2	100	42
85	09.A.002	80.45	09-101467	Røsnæs	Intact	720	37	0.2	2	3		16	27	15	100	63
86	09.A.002	71.35	09-101495	Røsnæs	Intact	640	33	0.3	2	4		20	27	14	100	62
87	09.A.003	5.25	09-101863	Sand	Marine		28	0.5	1	2		23	31	15	101	6
88	09.A.003	4	09-101877	Gyttja			31	39	1	12		1	11	4	99	6
89	10.A.803	12.5	10-105031	Lilleblt		214	22	2	1	2		28	21	24	100	65
90	10.A.051	55.4	10-105046	Røsnæs	Folded	475	30	0.1	1	2		25	29	13	100	55
91	10.A.054	59.95	10-105442	Røsnæs	Intact	580	26		1	2	5	13	33	20	100	33
92	10.A.057	38.55	10-105988	Røsnæs	Intact	400	28		1	3		12	36	20	100	54
93	10.A.057	58.8	10-106007	Ølst	Intact	575	11	1	0.3	7	4	60	14	3	100	84
94	10.A.056	58.55	10-106067	Røsnæs	Intact	540	24	0.1	1	2		10	39	24	100	59
95	10.A.802	2.4	10-108030	Lilleblt		40	6	66		2		14	5	7	100	45
96	10.A.802	13.8	10-108041				19	5	1	1		35	20	19	100	73
97	09.A.015	3.5	09-101944	Gyttja			57	0.5	0.1	9	7	2	19	6	101	9
98	09.A.015	5.5	09-101945	Clay			35	32	5	4	2	4	13	5	100	22
99	09.A.005	10	09-102707	Lillebelt			54	21	2	7		1	9	6	100	13
100	10.A.055	4	10-105254	Gyttja			69		0.1	5	3	3	14	5	99	11
101	10.A.060	5	10-105725				32	32	3	2	0.4	3	18	10	100	39
102	10.A.057	10.5	10-106038				48	22	8	8		1	8	5	100	12
103	10.A.056	3	10-106150				58	19	3	4		4	8	4	100	16
104	10.A.056	9.8	10-106155				56	11	1	19		5	6	3	101	21
105	09.A.602	32.1	09-101186	Lillebelt		275	27	0.1	1	2		27	28	15	100	64
106	10.A.051	14.15	10-105049	Røsnæs	Folded	125	23	5	2	1		13	31	25	100	66
107	10.A.051	32.25	10-105078	Røsnæs	Folded	277	28	0.4	1	2	0.5	18	33	17	100	63
108	10.A.055	30.15	10-105237	Røsnæs	Folded	274	30	0.4	1	1		19	32	16	99	59
109	10.A.054	40.25	10-105376	Røsnæs	Folded	415	23		1	1	14	14	31	16	100	62
110	10.A.054	30	10-105428	Røsnæs	Folded	325	24	2	1	2		15	35	21	100	63
111	10.A.052	63.55	10-105514	Røsnæs	Intact	515	29	0.1	3	2		13	33	20	100	66
112	10.A.052	19.25	10-105529	Røsnæs	Folded	140	27	0.2	1	2		25	32	13	100	65
113	10.A.052	6.5	10-105537	Røsnæs	Folded	40	28	0.1	1	1		25	30	15	100	61
129	10.A.058	36.55	10-105732	Holmehus	?	340	21	17	0.3	0.3		43	14	5	101	56
130	10.A.058	44.05	10-105733	Holmehus	?	405	29	0.1	0.4	2		43	15	10	100	54
131	10.A.058	56.85	10-105771	Holmehus	?	510	38	0.1		2	2	38	19	1	100	55

Environ = environment.
Non-clay minerals are quartz (Qz), calcite (Ca), dolomite (Dl), feldspar (Fd), siderite (Sd). Clay minerals are smectite (Sm), illite (Il), kaolinite and chlorite (Ko/Ch).
BET is the surface area measured by nitrogen adsorption (BET method).

which indicates that plasticity index may possibly be linked with the BET surface area (Figure 4.4b). There is a very poor correlation between the smectite content and the BET surface area (Figure 4.4c), although the smectite content controls the physical properties of the studied Palaeogene clay.

Table 4.2: *XRD estimated mineralogy results (in weight percentage, wt %) of the <2 μm clay fraction.*

Sample	Boring	Depth		Clay minerals (%)				
no.	no.	(mbsf)	Core no.	Sm	Il	Ko	Ch	Total
1	09.A.013	94	09-100196	30	67	3		100
2	09.A.013	95.55	09-100310	55	43		2	100
3	09.A.014	74.1	09-100128	69	22	5	4	100
4	09.A.014	65.65	09-100099	65	24	10	1	100
5	09.A.008	7.75	09-100415	17	54	20	9	100
6	09-A.003	13.8	09-101869	3	62	30	5	100
7	09.A.002	54.6	09-101479	17	54	23	6	100
8	09.A.002	85.05	09-101463	16	53	27	4	100
9	09.A.014	33.7	09-100104	17	53	24	6	100
10	09.A.002	48.8	09-101478	14	53	28	5	100
11	09.A.001	22.3	09-101215	44	40	13	3	100
12	09.A.602	49.55	09-101169	24	49	21	6	100
13	09.A.002	99.5	09-101456	23	50	23	4	100
14	09.A.014	61.2	09-100111	33	46	16	5	100
15	09.A.602	20.1	09-101191	44	40	14	2	100
16	09.A.605	15.45	09-101985	5	61	14	20	100
17	09.A.001	10.15	09-101201	27	46	26	1	100
18	09.A.001	32	09-101205	33	43	23	1	100
19	09.A.001	17.4	09-101214	38	43	18	1	100
20	09.A.001	4.2	09-101240	31	47	21	1	100
21	09.A.001	32.95	09-101435	18	32	47	3	100
22	09.A.002	29.55	09-101437	37	38	23	2	100
23	09.A.002	11.5	09-101439	37	38	24	1	100
24	09.A.002	22.5	09-101477	25	49	22	4	100
25	09.A.003	15.65	09-101855	12	60	17	11	100
26	09.A.003	23.35	09-101856	46	38	14	2	100
27	09.A.003	34.25	09-101858	46	38	14	2	100
28	09.A.003	16.5	09-101868	18	54	19	9	100
29	09.A.010	49.35	09-101082	22	49	26	3	100
30	09.A.010	39.05	09-101085	42	40	15	3	100
31	09.A.010	31.25	09-101096	68	26	4	2	100
32	09.A.010	5.1	09-101102	11	55	23	11	100
33	09.A.010	10.25	09-101103	64	33	2	2	101
34	09.A.010	14.25	09-101105	68	29	2	1	100
35	09.A.010	19.75	09-101108	61	34	3	2	100
36	09.A.001	25.85	09-101199	45	40	13	2	100
37	09.A.001	45.1	09-101232	37	43	17	3	100
38	09.A.002	44.75	09-101472	37	43	18	2	100
39	09.A.002	56.2	09-101494	41	41	16	2	100
40	09.A.003	41.8	09-101847	19	50	28	3	100
41	09.A.003	45.85	09-101850	43	40	15	2	100
42	09.A.010	40.05	09-101090	56	30	14		100
43	09.A.010	11.3	09-101104	70	27	2	1	100
44	09.A.010	17.2	09-101110	73	25	1	1	100
45	09.A.002	90.2	09-101462	39	42	17	2	100
46	09.A.002	67.6	09-101493	41	40	17	2	100
47	09.A.002	6	09-101509	43	38	17	2	100
48	09.A.001	15.7	09-101195	38	42	18	2	100
49	09.A.001	11.3	09-101211	37	42	18	3	100
50	09.A.002	14.5	09-101431	34	42	21	3	100
51	09.A.002	25.25	09-101436	47	36	15	2	100
52	09.A.002	15.45	09-101476	32	48	17	3	100
53	09.A.003	18.55	09-101873	48	37	13	2	100
54	09.A.701	29.05	09-102950	25	48	24	3	100
55	09.A.701	37.5	09-102951	27	47	24	2	100
56	09.A.701	30.1	09-102973	12	53	31	4	100
57	09.A.001	17.4	09-101214	44	39	15	2	100
58	09.A.001	45.1	09-101232	41	41	17	1	100
59	09.A.001	37.85	09-101235	44	40	14	2	100
60	09.A.002	14.5	09-101431	38	39	20	3	100
61	09.A.002	18.45	09-101476	30	42	26	2	100
62	10.A.051	24.85	10-105043	28	47	22	3	100
63	10.A.051	15.8	10-105072	20	46	32	2	100
64	10.A.051	36.75	10-105085	32	44	21	3	100
65	10.A.051	38.9	10-105091	42	37	18	3	100
66	10.A.051	42	10-105116	36	41	21	2	100
67	10.A.055	29.55	10-105202	35	42	21	2	100
68	10.A.055	36	10-105231	22	49	26	3	100
69	10.A.055	41.55	10-105248	37	40	21	2	100
70	10.A.051	8.15	10-105051	19	47	31	3	100
71	10.A.055	46.4	10-105224	40	40	17	3	100
72	10.A.055	35.45	10-105235	26	46	26	2	100
73	10.A.055	43	10-105272	48	35	15	2	100
74	10.A.054	40.85	10-105377	44	39	15	2	100
75	10.A.054	37.85	10-105430	31	46	21	2	100
76	09.A.001	7.2	09-101240	57	31	11	1	100
77	10.A.803	4.5	10-105027	71	14	13	2	100
78	10.A.055	27.25	10-105204	75	20	3	2	100
79	10.A.055	58.05	10-105236	50	34	15	1	100
80	10.A.054	32.95	10-105400	62	27	10	1	100
81	10.A.054	50.75	10-105425	52	32	15	1	100
82	10.A.058	30	10-105784	93	7			100
83	10.A.055	72.45	10-105201	27	46	25	2	100
84	09.A.007	20.75	09-100712	63	32	3	2	100
85	09.A.002	80.45	09-101467	28	46	23	3	100
86	09.A.002	71.35	09-101495	32	44	22	2	100
87	09.A.003	5.25	09-101863	33	46	17	4	100
88	09.A.003	4	09-101877	8	66	19	7	100
89	10.A.803	12.5	10-105031	38	29	31	2	100
90	10.A.051	55.4	10-105046	37	43	17	3	100
91	10.A.054	59.95	10-105442	19	50	29	2	100
92	10.A.057	38.55	10-105988	17	53	28	2	100
93	10.A.057	58.8	10-106007	78	19		3	100
94	10.A.056	58.55	10-106067	14	54	29	3	100
95	10.A.802	2.4	10-108030	53	21	24	2	100
96	10.A.802	13.8	10-108041	48	27	23	2	100
97	09.A.015	3.5	09-101944	8	71	12	9	100
98	09.A.015	5.5	09-101945	19	57	17	7	100
99	09.A.005	10	09-102707	7	58	23	12	100
100	10.A.055	4	10-105254	15	64	15	6	100
101	10.A.060	5	10-105725	10	58	24	8	100
102	10.A.057	10.5	10-106038	8	59	20	13	100
103	10.A.056	3	10-106150	24	52	16	8	100
104	10.A.056	9.8	10-106155	34	43	20	3	100
105	09.A.602	32.1	09-101186	37	41	21	1	100
106	10.A.051	14.15	10-105049	19	45	34	2	100
107	10.A.051	32.25	10-105078	26	49	23	2	100
108	10.A.055	30.15	10-105237	28	48	22	2	100
109	10.A.054	40.25	10-105376	23	50	24	3	100
110	10.A.054	30	10-105428	21	49	27	3	100
111	10.A.052	63.55	10-105514	20	50	27	3	100
112	10.A.052	19.25	10-105529	36	45	17	2	100
113	10.A.052	6.5	10-105537	36	43	19	2	100
129	10.A.058	36.55	10-105732	70	22	8	0.4	100
130	10.A.058	44.05	10-105733	63	22	14	1	100
131	10.A.058	56.85	10-105771	66	32	1	1	100

Clay minerals are: smectite (sm); illite (Il); Kaolonite (Ko), Chlorite (Ch).

Figure 4.4d shows the relative distribution of smectite, kaolinite/chlorite and illite in the 97 samples from five Palaeogene clay formations. Generally, this diagram shows that the variation in clay mineralogy within each Palaeogene clay type is rather significant. Both the Holmehus and Ølst Clays are very rich in smectite, poor in kaolinite/chlorite and they plot totally outside the area in the diagram where Røsnæs Clay plots. The Lillebælt Clay is relatively poor in illite and also plots outside the Røsnæs Clay area. The Æbelø Clay is very poor in kaolinite/chlorite and relatively rich in illite and plots partly in the same area as the Ølst and Holmehus Clays.

XRD remains the most powerful and widely used method for the identification, characterization and semi-quantification of mineralogical composition of sediments. XRD quantitative evaluation is challenging, and Brindley (1961) presents a detailed discussion of this problem. Generally, XRD analysis provides semi-quantitative results of absolute mineral contents (± 10%), but provide good repeatability and relative mineral concentrations as long as results from similar methods are considered. The clay contents (wt %) of the bulk samples number 1 and 2 were also obtained by sedimentation method and compared with the clay content as obtained by XRD, the results are consistent. This indicates that the present results of semi-quantified mineralogy by XRD method are quite satisfactory. The XRD data presented in this study are useful for general characterization of the Palaeogene clay, but should not be viewed as precise quantitative data.

4.5.2. BET surface area

The results of the measured BET surface area of the 116 sediment samples are listed in Table 4.1. The Palaeogene clays show quite similar surface area above 60 $m^2 g^{-1}$ in average, whereas the surface areas of the Quaternary sediments range from 6 to 12 $m^2 g^{-1}$. A plot of smectite content versus surface area (for 116 samples of the Quaternary and Palaeogene clays) shows that the surface area may be controlled by the smectite content (Figure 4.4c). The Quaternary deposits include postglacial deposits (peat and gyttja) and lateglacial marine deposits (sand, silt and clay); in addition to the glacial deposits (upper and lower clay tills as well as melt-water sand and silt deposits).

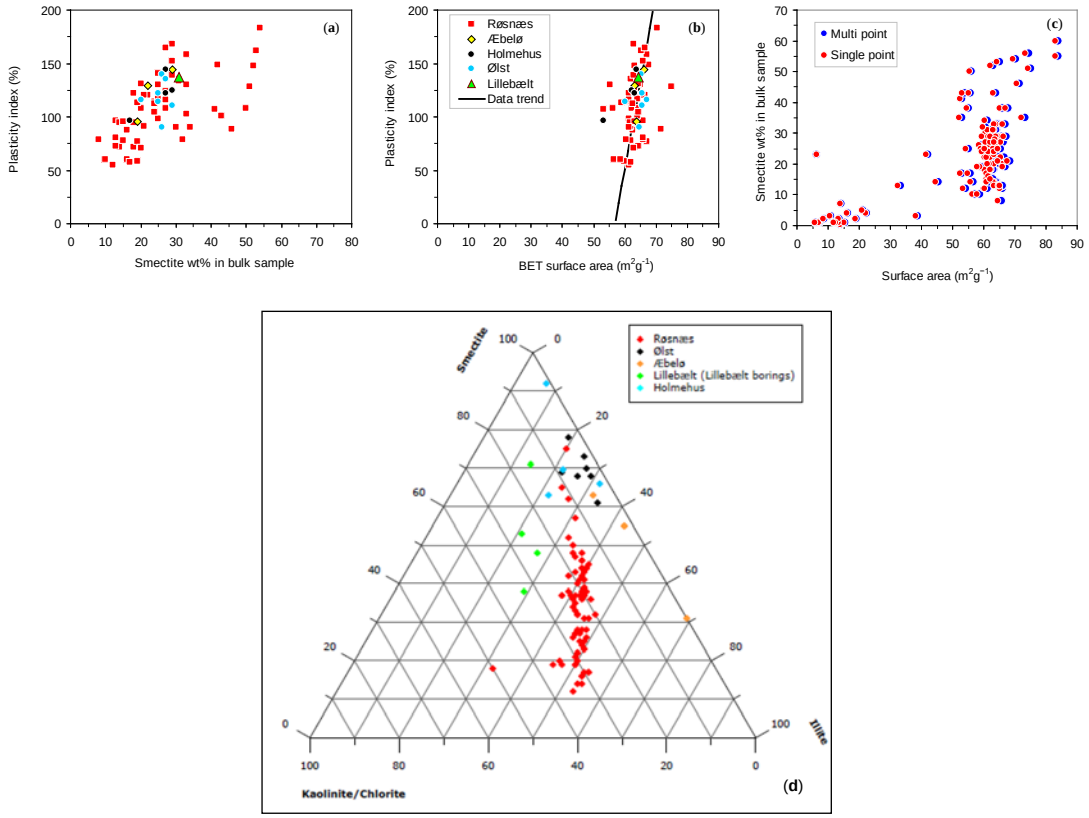

Figure 4.4: *Plasticity index plotted versus: smectite content in the bulk Palaeogene clay samples plotted; and (**b**) BET surface area. Plot (**c**) shows the smectite content for both the Quaternary and Palaeogene clay units plotted against BET surface area. Plot (**d**) is obtained from the Rambøll/Arup (2011). It shows the relative distribution of clay minerals of 97 Palaeogene clays samples from five formations.*

4.5.3. Geotechnical classification properties

Some results from geotechnical classification tests done on Palaeogene clay were collected from Jessen et al. (2011) and tabulated in Table 4.3. The data include initial water content (w_i), wet bulk density (ρ_b), specific gravity of solids (d_s), liquid limit (w_L), plastic limit (w_P), plasticity index (I_P), consistency index (I_C), and calcium carbonate content (CC) which is the ratio between the weight of calcium carbonate and the total weight of the grains. The water content is slightly above the plastic limit.

The present classification data, obtained in core plugs cut in the vertical, horizontal and tangential orientations for each of the ten Palaeogene clay samples, include initial and final water content; porosity, void ratio, bulk and dry densities are presented in Figure 4.5a–e. The bulk density (ρ_b) of water saturated samples should be higher than that of dry samples (Figure 4.5f) because the density of water is higher than of air.

The studied Palaeogene clay samples are not fully saturated (Table 4.3). This is due to lost of some water content during the sample preparation, handling of the core plugs, weighing and putting the sample into the triaxial Hoek cell for consolidation test. It is assumed here that the compressibility of the individual grains is negligible compared to the bulk compressibility of the studied Palaeogene clay, so that the pore volume changes can be considered equal to the bulk volume changes of the tested Palaeogene clay. According to Terzaghi (1923), consolidation involves decrease in water content of a saturated soil without replacement of water by air. During the present consolidation drained test, the volume of Palaeogene clay is reduced only when the porosity is reduced by expelling the pore-water from the pores. This can happen over a period of time during mechanical loading process, resulting in settlement which is an important concept in geotechnical engineering in the design of certain structural foundations. For example, the construction of high-rise structures over highly compressible underlying layers poses a considerable design constraint.

Table 4.3: *Results of smectite (sm %) and illite (il %) content from XRD analysis, BET measurements and geotechnical classification data of the 10 Palaeogene clay samples included in this study.*

Boring	Core	Sample	Sample	Geologi-			Geotechnical classification parameters													XRD	
number	number	number	depth	cal unit	σ'_{vo}	σ'_{pc}	w_i	S_w	ρ_b	ρ_g	d_s	ϕ_i	w_L	w_P	I_P	I_C	CC	Clay	BET	sm	il
			mbsf		kPa	kPa	%	%	g cm^{-3}	g cm^{-3}	g cm^{-3}	%	%	%	%		%	%	m^{2}g^{-1}	%	%
09.A.013	09-100196	1	94	Æbelø	1125		37	90	1.75	2.64		56						72	61	22	48
09.A.013	09-100310	2	94.55	Æbelø	1125		37	90	1.74	2.66		54						70	66	38	29
09.A.002	09-101463	8	85.05	Røsnæs	765		32	91	1.84	2.71		49					2.4	70	61	12	37
09.A.602	09-101191	15	20.13	Røsnæs	185	460	35	99	1.91	2.74	2.81	44	119	28	90.5	1.26	1.6	80	62	30	27
09.A.010	09-101082	29	49.35	Røsnæs	415		37	97	1.88	2.72	2.79	52	110	33	77.5	0.95	3.6	75	62	15	34
09.A.010	09-101096	31	31.25	Ølst	260		48	98	1.78	2.73	2.73	55	172	44	128	0.97	2.6	64	75	51	20
09.A.001	09-101232	37	45.1	Røsnæs	360	3300	35	98	1.91	2.72	2.79	49	173	29	144	0.96	3.0	78	64	23	28
10.A.803	10-105031	89	12.5	Lillebælt	214		45	98	1.74	2.71		57						73	65	28	21
10.A.057	10-106007	93	58.8	Ølst	575		45	98	1.65	2.69	2.85	62	136	49	86.6	1.05	4.7	42	84	60	14
10.A.802	10-108030	95	2.4	Lillebælt	40		47	95	1.71	2.63		55						26	45	14	5

σ'_{vo} is *in-situ* vertical effective stress, σ'_{PC} is pre-consolidation stress.The initial water content (w_i), wet bulk density (ρ_b), grain density (ρ_g), specific gravity of solids (d_s), initial porosity (ϕ_i), liquid limit (w_L), plastic limit (w_P), plasticity index (I_P), consistency index (I_C), and calcium carbonate ($CaCO_3$) content (CC), clay content (Clay) in bulk sample. BET is the surface area of bulk clay measured by nitrogen adsorption (BET method). The bulk sample refers to the total mass of the sample.

The Palaeogene clay from the Ølst Formation is very rich in smectite (samples no. 31 and 93). It shows higher moisture content, lower bulk density and higher porosity as well as higher consistency index (I_C) than the other four Palaeogene clay formations.

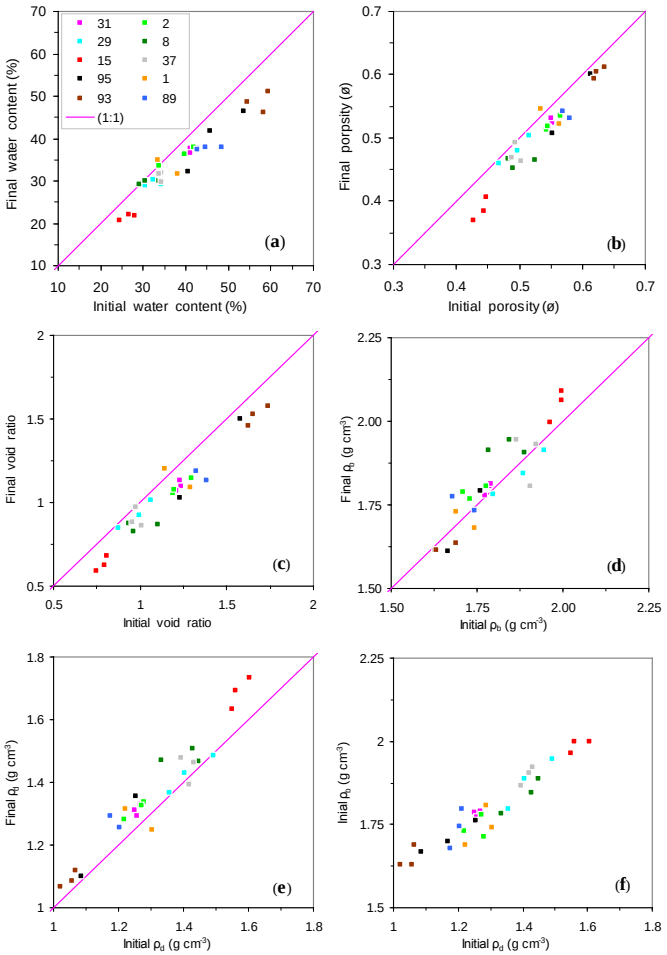

Figure 4.5: *Results from classification tests on Palaeogene clay. Cross plots of final versus initial results of (**a**) water content, (**b**) total porosity obtained from void ratio, (**c**) void ratio, (**d**) bulk density and (**e**) dry density. Plot (**f**) is for initial bulk density versus initial dry density. Each sample is represented by three data points that are measured in the vertical, horizontal and tangential (45^o) orientations (directions) with respect to the depositional bedding.*

4.5.4. Mechanical loading: stress-strain relationship

In dealing with the rock mechanical response of a porous medium, it is the effective stress on the material that is important, not the applied external stress. So stress-strain relationships are actually effective stress-strain relationships. The mechanical loading results of the naturally water-saturated Palaeogene clays, subjected to a maximum of 3 MPa uniaxial stress, are displayed in Figure 4.6. This figure illustrates the drained behaviour of the studied Palaeogene clay. Most of the samples show elastic stress–strain behaviour with the highest deformation of the sample 29. The samples 29, 95 and 8 are highly deformed relative to the other 7 samples. This may be due to their low smectite content which allows water to squeeze out faster than from those with high smectite content. The results of the uniaxial confined compressional test on the ten tested clay samples show similarities in the elastic deformation pattern and

properties. Generally, the studied Palaeogene clays are deformed less and retained high porosity, and lower bulk density than it would be expected along the whole stress path from 0.2 to 3.0 MPa (Figure 4.5). This means the pore-water expels slowly due to the low permeability. This agrees reasonably well with the compaction behaviour of the smectite-rich clays of Mondol et al. (2008). As the Palaeogene clay drains, the continuous porosity change is quantified by Eq. 4.8 and plotted in Figure (4.7) with uniaxial strain, Biot's coefficient (β), Poisson's ration and electrical resistivity.

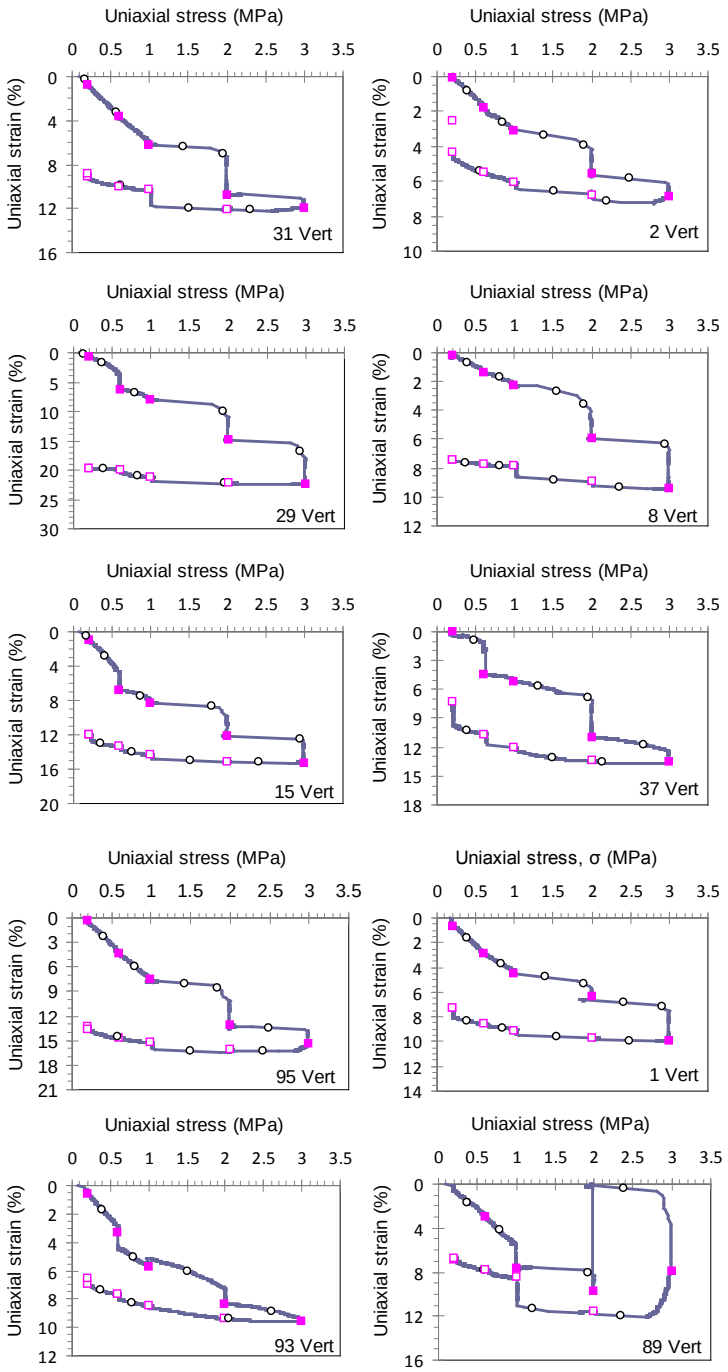

Figure 4.6: *Stress-strain curves produced during uniaxial confined compressional test (compaction or consolidation drained test) on ten vertical (axial) core plug samples under drained condition. The sample number is indicated in the bottom right hand corner of each plot panel. Triaxial Hoek cell restricts the radial deformation and axial strain gives the volume change due to applied stress. Open circles indicate*

the mid point of the part of the curve used for obtaining the drained modulus for that specific stress range. The closed and open rectangles indicate stress levels at which the elastic wave velocities were measured during the loading and unloading phases, respectively. Uniaxial strain (from uniaxial confined compressional test) means no lateral strain is allowed.

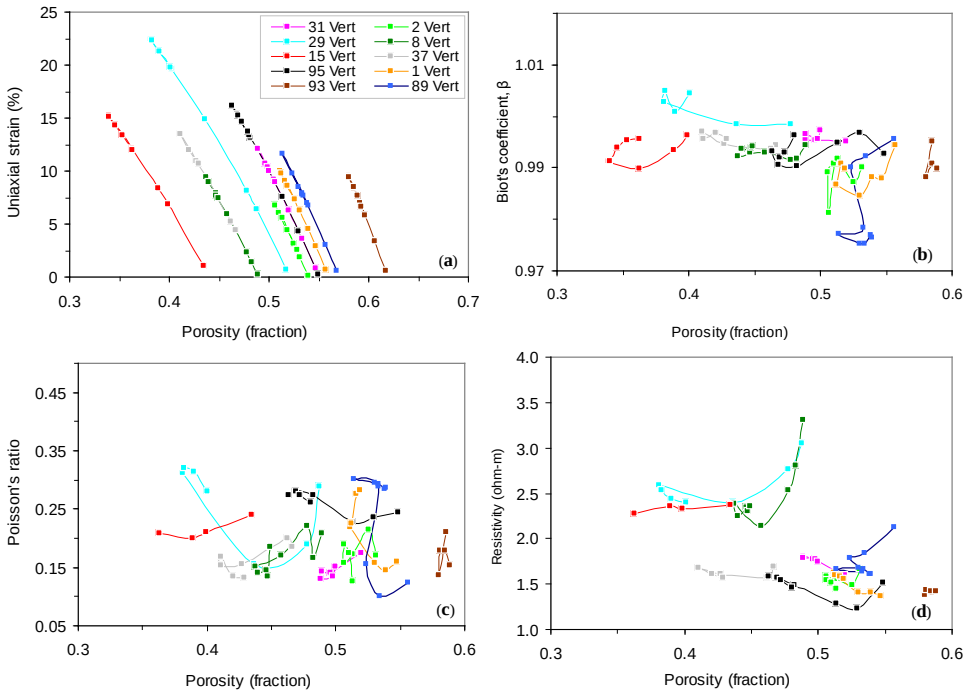

Figure 4.7: *Relationships between fluid-filled porosity changes (calculated from the uniaxial strain achieved during uniaxial confined compressional test) and the: (**a**) uniaxial strain which increases with the decrease of initial porosity; (**b**) Biot's coefficient for elastic deformation; (**c**) Poisson's ratio calculated from sonic velocity measured under uniaxial confined compressional stress; and (**d**) electrical resistivity measured during loading and unloading phases.*

4.5.5. Velocity and electrical resistivity

It was a challenge to determine the exact zero-crossing arrival times for the S-wave of the Palaeogene clays, especially at low stresses (0.2–1.5 MPa). This is in part due to the interface of the P-wave with the S-wave that makes noise in signal interpretation (Hornby 1998). A second factor is likely to be the presence of anisotropy, which is not accommodated in this study. Thus, the P-wave velocity should be faster in the saturated sample whereas the S-wave velocity should be similar for the dry and saturated samples. This is in accordance with Gassmann (1951) who assumes similar shear moduli for a rock under the dry and saturated conditions. Permeability of Palaeogene clay is very low. Consequently, for velocity measurements under drained condition, a very long drainage time is needed for the pore pressure to equalize throughout the sample after a change in axial stress or confining stress (Hornby 1998).

The P-wave and S-wave velocities were measured in three different orientations for each of the ten Palaeogene clay samples. However, only the velocities measured in the vertical direction are used here. Figure 4.8 shows P-wave velocity (on loading and unloading) plotted versus: (a) S-wave velocity, (b) uniaxial stress, (c) total porosity

and (d) bulk density. The P-wave velocity is shown to be sensitive to clay mineralogy and to axial stress. Plots of the P-wave acoustic impedance are shown in Figure 4.9.

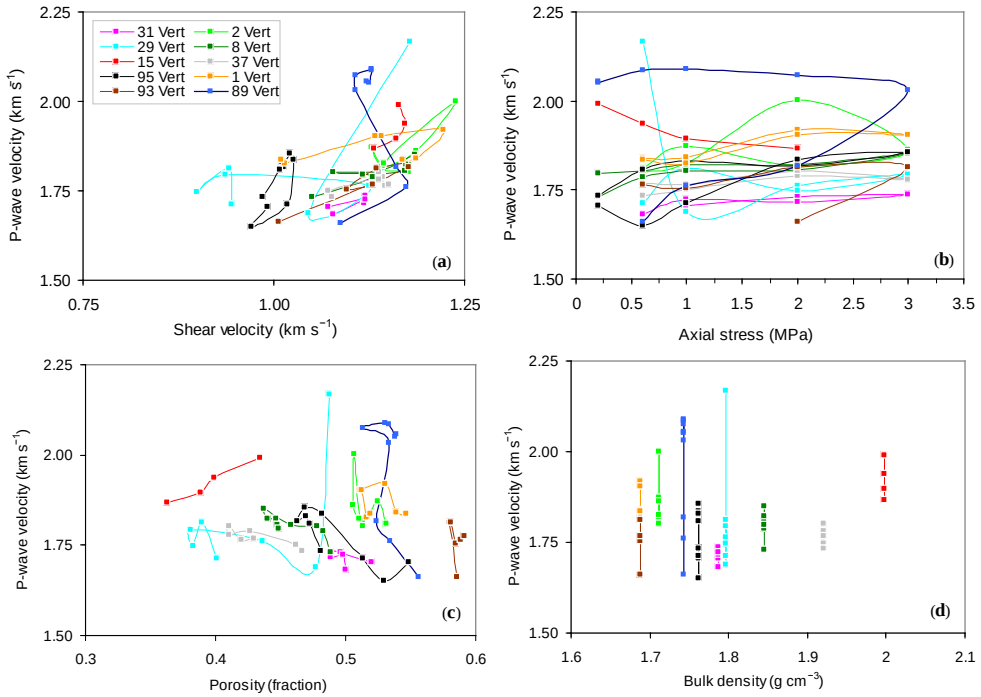

Figure 4.8: *P-wave velocity on loading and unloading plotted versus: (**a**) S-wave velocity, (**b**) uniaxial stress, (**c**) porosity and (**d**) bulk density.*

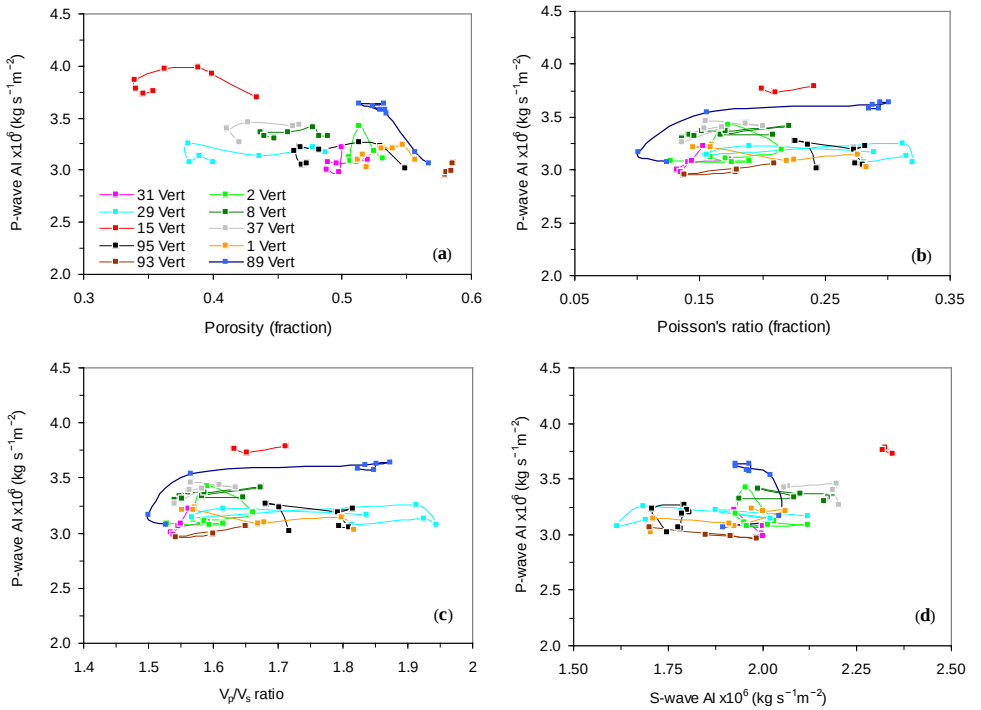

Figure 4.9: *P-wave acoustic impedance versus: (**a**) porosity change calculated from the strain achieved in the mechanical loading; (**b**) Poisson's ratio calculated from sonic velocity measured under uniaxial confined compression; (**c**) Vp/Vs ratio; and (**d**) S-wave acoustic impedance. The data are for both loading and unloading phases.*

The Poisson's ratio calculated by using Eq. 4.15 ranges from 0.2 to 0.3; and it seems to be sensitive to variations in smectite content. Samples poor in smectite content (e.g. sample 95) have relatively high Poisson's ratio. The Poisson's ratio is plotted versus total porosity and P-wave acoustic impedance in Figures 4.7c and 4.9b, respectively. The relationships between the axial stress and both electrical resistivity and porosity change are established for each sample (Figure 4.10). It is clear that the porosity decreases as a function of axial stress (Figure 4.10b) which is consistent with theory.

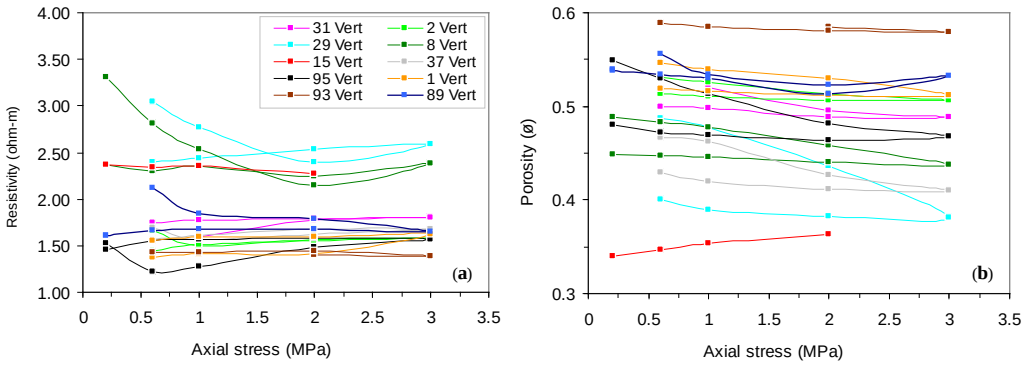

Figure 4.10: *Electrical resistivity obtained during loading and unloading plotted versus uniaxial stress (**a**). Porosity change obtained by Eq. 4.8 for the ten Palaeogene clay samples plotted versus uniaxial stress (**b**).*

4.5.6. Elastic moduli of Palaeogene clay

The obtained elastic moduli are plotted versus uniaxial confined stress as displayed in Figure 4.11. It shows plots of the static drained modulus (M_{drain}) as obtained from mechanical loading (black rectangular); the dynamic undrained (saturated) uniaxial compressional modulus (M_{sat}) as calculated from Vp and ρ_b (green triangular); and the dry compressional modulus (M_{dry}) as estimated using Gassmann (1951) (red circles). An estimate for the mineral modulus (M_{grain}) was found within the range of 120–140 GPa based on the correlation of Chen and Evans (2006). The present results show that the M_{sat} is significantly higher than the M_{drain}. This is because the M_{sat} is estimated based on pure elasticity, whereas the M_{drain} estimation accounts for both elastic and plastic deformation, leading to higher strain and so lower modulus. The M_{drain} is low because it is a measurement of the solid frame (structure) as the water is squeezed out the pores and the porosity is reduced. The M_{sat} is high because it is a measurement of the saturated modulus of the entire sediment (i.e. the combined modulus for both solid phase and water). Both the M_{sat} and the M_{drain} increase with increasing stress probably due to the removal of bedding and fracture effects resulting in enhancement of grains contact. This may possibly be interpreted as the confining stress increases the grain contact and makes the sample stiffer. The increase in compressional modulus (i.e. stiffness) means a decrease in compressibility. The confined measurements simulate *in-situ* conditions more realistic since the radial extension is negligible relatively to *in-situ* axial deformation. There is no large difference between the M_{drain} and M_{dry}. However, the M_{dry} is higher than the M_{drain}. The reason for this difference is probably that M_{drain} accounts for additional plastic deformation.

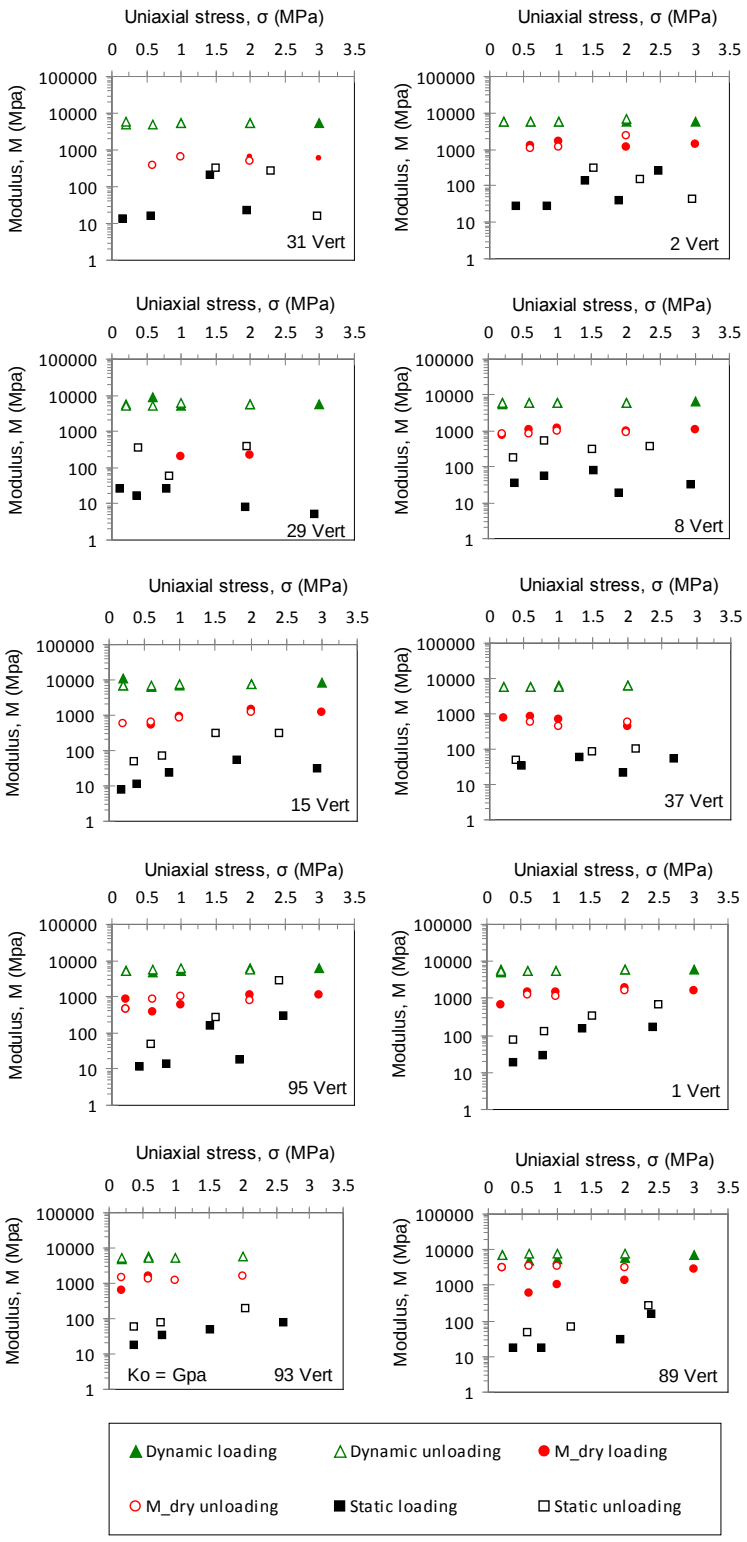

Figure 4.11: *Saturated compressional (P-wave) modulus (green), drained modulus (black), and dry modulus (red) for both loading (closed data points) and unloading (open data points) presented in logarithmic scale and plotted versus uniaxial confined stress for ten vertical core plugs. Sample number is indicated in the bottom right hand corner of each plot. Dry modulus (red) is approximated by using Gassmann's (1951) equation on velocity data of saturated samples. Experimental stage is indicated in Figure 4.6. Typical experiments consist of loading from 0.2 to 3 MPa and unloading from 3 to 0.2 MPa.*

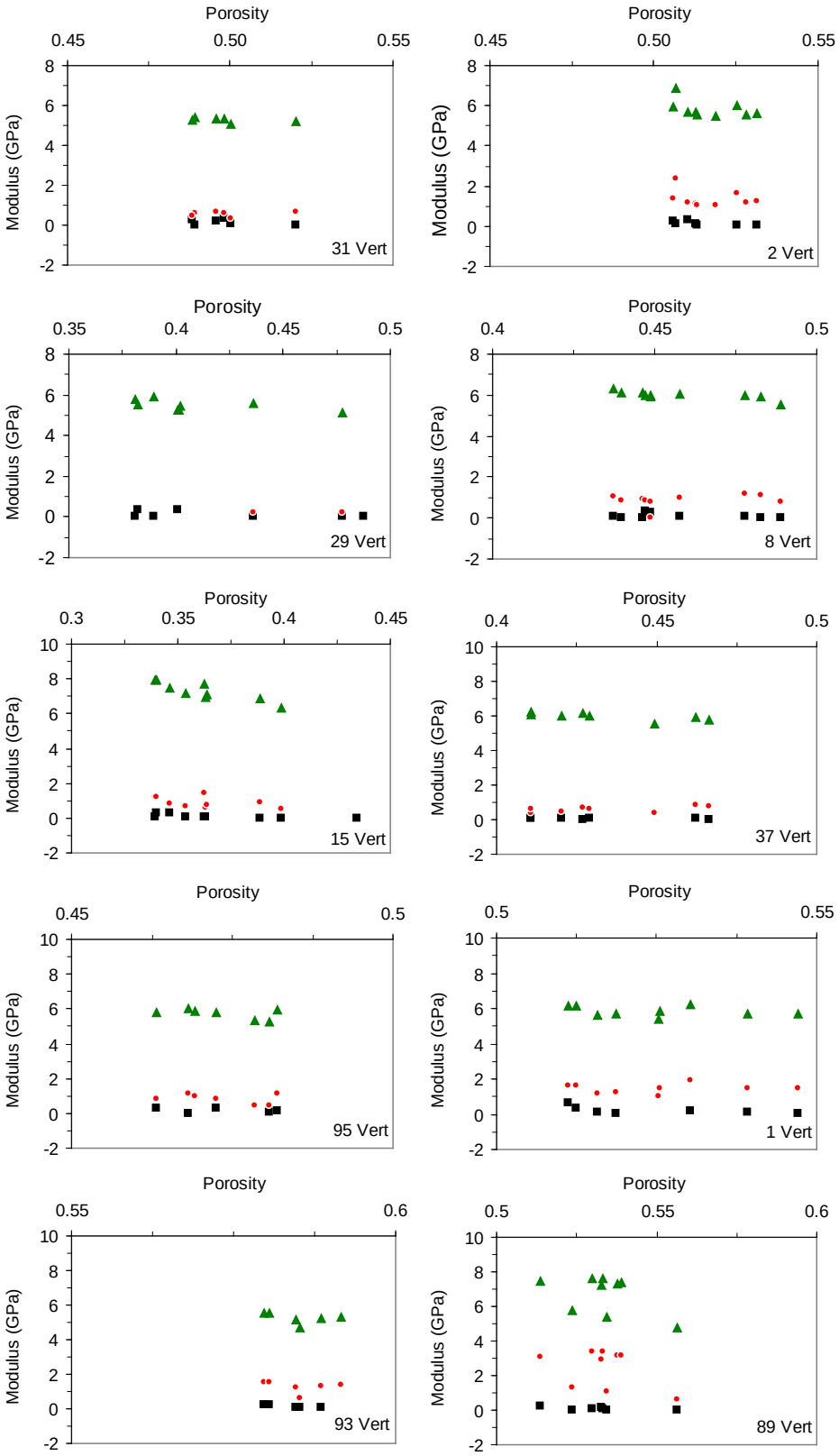

Figure 4.12: *Saturated compressional modulus (green triangular), drained modulus (black rectangular), and dry modulus (red circle) for both loading and unloading stress paths plotted versus porosity. Sample number is indicated in the bottom right hand corner of each plot. The dry and drained moduli are very small, but they are not zero as they may be seemed from the plots (see Figure 4.11).*

4.5.7. Biot's coefficient for elastic deformation

Biot's coefficient (β) is an indicator for sediment stiffness which is a property of sediment structure (i.e. frame). In this study, β is estimated from the dry modulus (M_{dry}) and the mineral modulus (M_{grain}) using Eq. 4.19. The resulting β is plotted versus porosity in Figure 4.7b and in Figure 4.13. In all cases, β value was found to be lower than but close to one (β value ranges from about 0.97 to about 1.00) which is low enough to describe the deformation of the studied Palaeogene clay as predominantly elastic. β apparently decreases with stress (Figure 4.13b) probably as a result of the plastic component in the mechanical deformation.

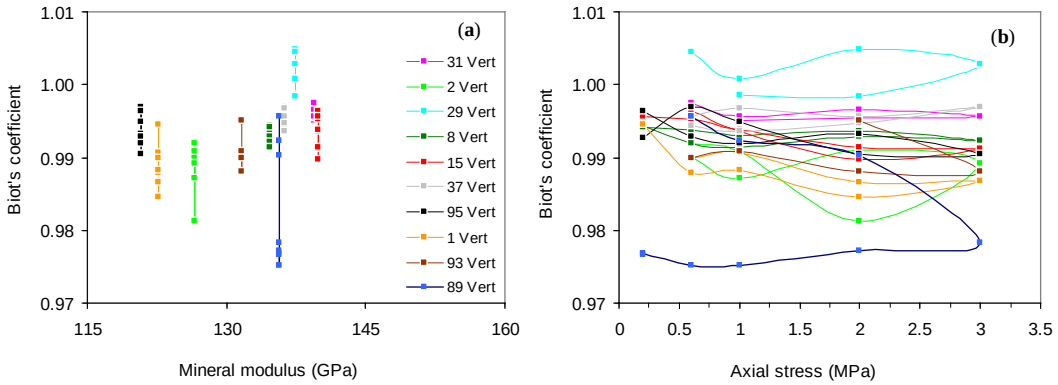

Figure 4.13: *Biot's coefficient calculated for the mechanical loading and unloading on the ten Palaeogene clay samples plotted versus mineral modulus and axial stress.*

5. Conclusions and future perspective

The changes of porosity and compressional wave velocity with burial depth were related to both vertical effective stress and TTI of chalk. Using Terzaghi's concept to calculate vertical effective stress on cemented chalk can lead to errors in the estimation of the actual effective stress which in return may cause severe engineering consequences. Therefore, the use of Biot's effective stress is recommended for more reliable porosity prediction.

Based on the present results, an equation that could be used to estimate Biot's vertical effective stress (from P-wave velocity data) which could be used to predict porosity is proposed. The predictive equation for porosity reduction with increasing burial stress is relevant for basin analysis and hydrocarbon exploration in deep-sea chalk to predict porosity if the vertical effective stress on the chalk is known.

The present porosity–effective stress trends did not exactly follow the porosity trends for the Pacific Ontong Java Plateau chalk. Atlantic Eocene chalk porosity data showed a broader porosity trend in the mechanical compaction interval, and the onset of limestone formation at a shallower burial depth than the porosity data of the Ontong Java Plateau chalk show. Porosity variations within the same effective stress may be due to variations in chalk texture.

Mechanical compaction is the principal cause of porosity reduction (at shallow depths) in the studied Eocene chalk, at least down to about 5 MPa Terzaghi's effective

stress corresponding to a porosity of about 35%. Within the compaction interval, deeply buried Eocene chalk is characterized by a slower, more linear compaction rate than the shallowly buried Eocene chalk. The present porosity data do not show or at least it is difficult to define a clear pore-stiffening contact cementation trend as in the Pacific Ontong Java Plateau chalk.

It is important to use the correct value of Biot's coefficient, β, when estimating the vertical effective stress because even for very small deviation in β value from 1, a significant effective stress can be obtained, especially in deep-sea sediments where water depth is high. For safety reasons, it is very important to be observed especially when drilling in the offshore. This may not be a big problem when drilling onshore.

The studied siliceous ooze contains significant amount of shale and it has shown to be a challenge to characterize accurately petrophysically. It is characterised by very high porosity, relatively high sonic travel time and exceptionally low bulk density, and low natural GR log response than shale. The true density porosity was calculated by taking the number of electrons per unit volume into account. The neutron porosity was corrected for hydrogen index contribution of the solid phase. The resulting corrected porosity data are consistent. Although the petrophysical interpretation presented here should be regarded as indicative rather than definitive, the application of the proposed approach is capable to give reasonable grain density log and consistent true porosity values and thus it is useful for the petrophysical community. However, it could be improved by more sophisticated modelling or by acquiring new data such as nuclear magnetic resonance to know the nature of the water in the siliceous ooze or may be by dehydration studies to indicate which proportion of the total water is chemically bonded. The studied siliceous ooze intervals apparently do not contain hydrocarbons.

Amorphous silica, such as opal-A, is quite difficult to detect by XRD analysis techniques. In this situation, the petrophysicist must be informed about it since this amorphous silica is light and hydrated. Failure to take it into account may induce an error in porosity calculation which may result in a large overestimation of water saturation of a hydrocarbon reservoir. In contrast, false detection of amorphous silica could be misleading. The AVO analysis revealed that at the angle of incidence greater than 15^{o}, oil saturated sandstone layer could be distinguished from water bearing siliceous ooze interval. The obtained β value ranges from about 0.90 to about 0.97. This indicates that the studied siliceous ooze is relatively stiff even though the porosity (ϕ) is high, which ranges from about 47–53%. It is obvious that taking β into account when calculating effective stress is crucial to obtain more realistic effective stress value. Assuming β as equal to one may underestimate the real effective stress which may cause bad consequences as reservoir rock may suffer compaction or elastic deformation as a result of changing in stress state while drilling operations or during hydrocarbons production.

Elastic deformation properties of naturally water saturated Palaeogene clays were determined by using elastic wave velocity measured during triaxial testing under drained conditions. The studied Palaeogene clay is rich in smectite and the smectite content controls the physical properties of the studied clay. When the uniaxial mineral modulus is predicted from grain density, then the drained purely elastic modulus (M_{dry}) can be predicted by Gassmann substitution. It is higher than but close to the geotechnically obtained drained uniaxial compressional modulus (M_{drain}). The

obtained results can aid in the estimation of geotechnical drained elastic modulus from bulk density and elastic wave velocity. Our results may have implications in engineering practice, including structural design and slope stability analysis. The obtained results indicate that the solid frame of the studied Palaeogene clay behaves elastically.

Three recommendations for future work are listed below that concern additional data collection. These recommendations emerge from the conclusions discussed above.
1. The scanning electron microscope (SEM) of Palaeogene clay is required to see the texture of the studied smectite rich clays.
2. The horizontal and vertical elastic wave velocity and other geotechnical data to study an isotropy of the Palaeogene clay.
3. Permeability and cabilary entry pressure measuremnts for both siliceous ooze and Palaeogene clay.

6. Paper abstracts

6.1. Abstract from manuscript I

The study aimed to relate changes in porosity and sonic velocity data, measured on water-saturated Eocene chalks from 36 Ocean Drilling Program drill sites in the Atlantic Ocean, to vertical effective stress and thermal maturity. Only chalk of Eocene age was considered here to avoid possible influence of geological age on compaction trends of chalk. For each depth, vertical effective stresses as defined by Terzaghi and by Biot were calculated. Bottom-hole temperature data were used to calculate the time–temperature index of thermal maturity (TTI) as defined by Lopatin. Porosity and compressional wave velocity data were correlated to effective stresses and to TTI.

The Eocene chalk porosity data showed a broader porosity trend in the mechanical compaction zone, and the onset of the formation of limestone at a shallower burial depth than the porosity data of the Ontong Java Plateau chalk show. The Eocene chalk porosity data do not show or at least it is difficult to define a clear pore-stiffening contact cementation trend as the Ontong Java Plateau chalk. Mechanical compaction is the principal cause of porosity reduction (at shallow depths) in the studied Eocene chalk, at least down to about 5 MPa Terzaghi's effective stress corresponding to a porosity of about 35%. This indicates that mechanical compaction is the principal agent of porosity reduction. Conversely, at deeper levels, porosity reduction is accompanied by a large increase in sonic velocity indicating pore-filling cementation. These deep changes are correlated with TTI. This indicates pore-filling cementation via an activation energy mechanism. We proposed an equation for porosity reduction with burial stress. This equation is relevant for basin analysis and hydrocarbon exploration to predict porosity if sonic velocity data for subsurface chalk is available.

6.2. Abstract from manuscript II

Pelagic siliceous ooze sediments occur above the hydrocarbon reservoir of the Ormen Lange gas field in Møre Basin, Norwegian Sea. A possible hydrocarbon prospect of siliceous ooze was proposed, but siliceous ooze is significantly different in texture

from most commonly known reservoir rocks. Logging and core analysis data were integrated to characterize and evaluate these sediments. True density porosity was obtained by taking the number of electrons per unit volume of bulk siliceous ooze into account and it was calibrated to the overburden-corrected core porosity. Grain density log was calculated from gamma ray log and empirical grain density data calibrated with X-ray diffraction analysis data. The grain density log was used with the calculated true porosity log and the brine density of 1.025 g/cm^3 to convert the bulk density log from conventional limestone and water scaling of electron density to opal and brine scaling of electron density.

The neutron porosity log was corrected for the hydrogen index contribution of solid phase. The corrected neutron porosity is lower than the conventional neutron porosity by about 3 to 4 porosity units. The true density porosity and the corrected neutron porosity are similar. This indicates that our interpretation is consistent, such that it can be applied elsewhere. The studied sediments apparently do not contain hydrocarbons.

The relatively low Biot's coefficient, of about 0. 94 on average, indicates that the siliceous ooze is relatively stiff. Amplitude versus offset analysis indicated that an oil saturated sandstone layer can be distinguished from water saturated siliceous ooze.

6.3. Abstract from manuscript III

This paper presents results of a comprehensive characterization study of Palaeogene clay collected from the Fehmarn Belt area. Ten naturally saturated Palaeogene clay samples were examined and analysed in terms of their physical, mineralogical and geotechnical properties. The deformation properties and elastic wave velocity were measured simultaneously from uniaxial confined compression stress testing using a triaxial Hoek cell, under drained conditions at laboratory temperature (22 ^{o}C).

We mainly focused here on the elastic properties of these clays. Elastic wave velocity is controlled by the elasticity and the density of a material. We used geotechnical and elastic wave velocity data to model the elasticity and then to relate it to mineralogy and surface area. The studied Palaeogene clay is rich in smectite content which controls the physical properties of the studied clay, so that plasticity index correlates with the specific surface as measured with nitrogen adsorption. The obtained results describe the deformation behaviour of the solid frame of the studied Palaeogene clay as predominantly elastic. Our results can aid in the estimation of drained elastic parameters from bulk density and velocity of elastic waves and thus may have implications in engineering practice.

7. References

Akai K. 1960. Die Strukturellen Eigenschaften von Schluff, *Mitteilunggen Heft* **22**, Die Technische Hochschule, Aachen.

Alam M.M. 2011. Rock physical aspects of CO_2 injection in chalk. Ph.D. thesis, Department of Environmental Engineering, Technical University of Denmark (DTU), Denmark.

Alam M.M., Borre M.K., Fabricius I.L. and Hedegaard K. et al. 2010. Biot's coefficient as an indicator of strength and porosity reduction: Calcareous sediments from Kerguelen Plateau, *Journal of Petroleum Science and Engineering*, **70**, 282–297.

Alam M.M., Fabricius I.L. and Christensen H.F. 2012. Static and dynamic effective stress coefficient of chalk, *Geophysics*, **77**, 1–11.

Anselmetti F.S. and Eberli G.P. 1993. Controls on sonic velocity in carbonates. *Pure and Applied Geophysics*, **141**, 287–323.

Awadalkarim A. and Fabricius I.L. 2009. Estimating effective stress in North Sea ooze. The sound of geology workshop. Bergen, Norway, May 6th–8th, 2009, University of Bergen.

Awadalkarim A. and Fabricius I.L. 2012. The influence of Biot's coefficient on the estimation of vertical effective stress on deep sea sediments. 74th EAGE meeting, Copenhagen, Denmark, Expanded Abstracts, P187.

Bailey S.W., Berman R.G., Bryndzia L.T. and Burt D.M. et al. 1988. Hydrous Phyllosilicates (exclusive of mica). Reviews in Mineralogy, volume **19**. Mineralogical Society of America, Washington, D.C., USA. ISSN 0275-0279, ISBN 0-939950-23-5. 725 p.

Bassinot F.C., Marsters J.C., Mayer L.A. and Wilkens R.H. 1993. Variations of porosity in calcareous sediments from the Ontong Java Plateau. In: Berger, W.H., Kroenke, L.W., Mayer, L.A. et al. (Ed.), Proc. ODP, Sci. Results, 130. College Station, TX (Ocean Drilling Program), 653–661.

Becker D.E., Crooks J.H.A., Been K. and Jefferies M.G. 1987. Work as a criterion for determining in-situ and yield stresses in clay, *Canadian Geotechnical Journal*, **24**, p. 549.

Bilodeau B.J. 1995. Determining water saturation in diatomite using wireline logs, Lost Hills Field, California. In SPE Western Regional Meeting, 369–382.

Biot M.A. and Willis D.G. 1957. The elastic coefficients of the theory of consolidation. *Journal of Applied Mechanics*, **24**, 594–601.

Biot M.A.1941. General theory of three-dimensional consolidation. *Journal of Applied Physics*, **12**, 155–164.

Bjørslev O. 2010. Personal communication with Ole Bjørslev at Aarhus University.

Blum P., Xu J. and Donthireddy S. 1996. Geotechnical properties of Pleistocene sediments from the New Jersey upper continental slope. In: Mountain, G.S., Miller K.G., Blum P., Poag C.W. and Twichell D.C. (Eds.), 1996. Proc. ODP, Sci. Results, 150. College Station, TX (Ocean Drilling Program), 377–384.

Borre M.K. and Fabricius I.L. 1998. Chemical and mechanical processes during burial diagenesis of chalk: an interpretation based on specific surface data of deep-sea sediments. *Sedimentology*, **45**, 755–769.

Brasher J.E., Vagle K.R. 1996. Influence of lithofacies and diagenesis on Norwegian North Sea chalk reservoirs. *American Association of Petroleum Geologists Bulletin*, **80**, 746–769.

Brindley G.W. 1961. Quantitative analysis of clay mixtures. In: Brown G, editor. The X-ray identification and crystal structures of clay minerals. London: *Mineralogical Society*. 489–516.

Brown G. 1961. The X-ray identification crystal structures of clay minerals. Crystal structures of clay minerals. *The Mineralogical Society*, London, 544p.

Brunauer S, Emmett P.H. and Teller E. 1938. Adsorption of gases in multimolecular layers. *Journal of American Chemistry Society*, **60** (2), 309–319.

Bryant W.R., Rack F.R. 1990. Consolidation characteristics of Weddell Sea sediments: results: results of ODP Leg 113. In: Barker P.R, Kennett J.P. et al. 1990. Proc. ODP, Sci. Results, 113: College Station, TX (Ocean Drilling Program), 211–223.

Casagrande A. 1936. The determination of the pre-consolidation load and its practical significance, Proceedings of the First International Conference on Soil Mechanics and Foundation Engineering, **3**, Discussion D-34, p. 60.

Chen B. and Evans J.R.G. 2006. Elastic moduli of clay platelets. *Scripta Materialia*, **54**, 1581–1585.

Ciesielski P.F. and Kristoffersen Y. et al. 1991. *Proc. ODP, Sci. Results*, **114**: College Station, TX (Ocean Drilling Program).

Clayton C.R.I. 2011. Stiffness at small strain: research and practice. *Geotechnique*, **61**, No. 1, 5-37 [**doi:** 10.1680/geot.2011.61.1.5]

Day R. and Jones B. 2008. Variation in water content in opal-A and opal-CT from geyser discharge aprons. *Journal of Sedimentary Research*, **78**, 301–315.

Delaney M.L. 1991. Inorganic geochemistry summary. *Proc. ODP Init. Repts*., **130**, 549–551. College Station.

Fabricius I.L. 2000. Interpretation of burial history and rebound from loading experiments and the occurrence of microstylolites in the mixed sediments of the Caribbean Sites 999 and 1001: Proc. ODP, Sci. Results, **165**, 177–190.

Fabricius I.L. 2003. How burial diagenesis of chalk sediments controls sonic velocity and porosity. *American Association of Petroleum Geologists Bulletin*, **87**, 1755–1778.

Fabricius I.L. and Borre M.K., 2007. Stylolites, porosity, depositional texture, and silicates in chalk facies sediments, Ontong Java Plateau – Gorm and Tyra fields, North Sea. *Sedimentology*, **54**, 183–205.

Fabricius I.L., Gommesen L., Krogsbøll A. and Olsen D. 2008. Chalk porosity and sonic velocity versus burial depth: influence of fluid pressure, hydrocarbons, and mineralogy. *American Association of Petroleum Geologists Bulletin*, **92**, 201–223.

Femern A/S. Geo Information System. www.https://geoarchive.fehmarnlink.com.

Fjær E., Holt R.M., Horsrud P., Raaen A.M. and Risnes R. 1992. Petroleum related rock mechanics. Amsterdam, Elsevier, Development in Petroleum Science, **33**. 338.

Gassmann F. 1951. Uber die elastizitat poroser medien. *Veirteljahrsschrift der Naturforschenden Gesellschaft in Zurich*, **96**, 1–23.

Geonics Ltd. 1980. Technical Note 5, Electrical Conductivity of Soils and Rocks, technical references (see the references page in this link).

Giles M.R., Indrelid S.L. and James D.M.D. 1998. Compaction – the great unknown in basin modelling. Geological Society, London, *Special Publications*, **141**.1: 15–43.

Glover P. 2012. Petrophysics MSc Course Notes, page 150–171. http://www2.ggl.ulaval.ca/personnel/paglover/CD%20Contents/GGL-66565%20Petrophysics%20English/Chapter%2015.PDF. Accessed date: December 03rd, 2012.

Graetsch H. and Ibel K. 1997. Small angle neutron scattering by opals. *Physics and Chemistry of Minerals*, **24**, 102–108.

Grange L. 1937. The geology of the Rotorua–Taupo subdivision, Rotorua and Kaimanawa Divisions. *New* Zealand Department of Scientific and Industrial Research, *Bulletin* **37**, 86–105.

Grützner J. and Mienert J. 1999. Physical property changes as a monitor of pelagic carbonate diagenesis: an empirically derived diagenetic model for Atlantic Ocean basins. *American Association of Petroleum Geologists Bulletin*, **83**, 1485–1501.

Hamilton E.L. 1974. Prediction of deep-sea sediment properties: state of the art. In: Inderbitzen, A.L. (ed.) Deep-Sea Sediments, Physical and Mechanical Properties. New York, Plenum Press, 1–43.

Hamilton E.L. 1976. Variations of density and porosity with depth in deep-sea sediments. Journal of Sedimentary Petrology, **46**, 280–300.

Hamilton E.L. 1980. Geoaeoustic Modeling of the Sea-floor, *Journal of Acoustical Society of America*, **68**, 1313–1340.

Hearst J.R., Nelson P.H. and Paillett F.L 2000. Well Logging for Physical Properties. A Handbook for Geophysics, Geologists, and Engineers. John Wiley & Sons, Ltd., 2nd ed. p483. ISBN 0-471-96305-4.

Heilmann-Clausen C., Nielsen O.B. and Gersner F. 1985. Lithostratigraphy and depositional environments in the Upper Palaeocene and Eocene of Denmark. *Bulletin of the Geological Society of Denmark*, **33**, 287–323.

Herdianita N.R., Browne P.R.L., Rodgers K.A. and Campbell K.A. 2000. Mineralogical and textural changes accompanying ageing in silica sinter. *Mineralium Deposita*, **35**, 48–62.

Hornby, B.E. 1998. Experimental laboratory determination of the dynamic elastic properties of wet, drained shales. *Journal of the geophysical research*, **103**, 29945–29964.

Janbu N. 1969. The resistance concept applied to deformation of soils. Proceedings of the 7th International Conference on Soil Mechanics and Foundation Engineering, Mexico City, **1**, p. 191.

Janus Web Database (http://iodp.tamu.edu/janusweb/links/links_all.shtml). Accessed date: November 6th, 2008.

Japsen P. 1993. Influence of lithology and Neogene Uplift on seismic velocities in Denmark: Implications for depth conversion of maps. *American Association of Petroleum Geologists Bulletin*, **77**, 194–211.

JCPDS-ICDD: JCPDS – International Center for Diffraction Data. PDF-2 Data Base, Version 2.13 (in a CD). Copyright 1987-1993. Swarthmore, PA 19081 – USA.

Jessen S.B., Hansen P.B., Hesthaven M. and Christensen H.G. 2011. Fehmarn Belt Fixed Link, Advanced Laboratory Testing, Clays of Palaeogene origin, Geotechnical Data Report prepared by GEO, 31/03/2011.

Jones M.E., Bedford J. and Clayton C.J. 1984. On natural deformation mechanisms in the chalk. *Journal of the Geological Society*, London, **141**, 675–683.

Jones L.D. and Terrington R. 2011. Modelling Volume Change Potential in the London Clay. *Quarterly Journal of Engineering Geology and Hydrogeology*. **44**, 109–122.

Kaarsberg E.A. 1958. Introductory studies of natural and artificial argillaceous aggregates by sound-propagation and X-ray diffraction methods. *Journal of Geology*, **67**, 447–472.

Kastner M. 1981. Authigenic silicates in deep-sea sediments: formation and diagenesis. In: Emiliani, C. (ed.): The oceanic lithosphere, Sea **7**, 915–980. John Wiley and Sons, New York.

Kastner M., Keene J.B. and Gieskes J.M. 1977. Diagenesis of siliceous oozes–I. Chemical controls on the rate of opal-A to opal-CT transformation–an experimental study. *Geochimica et Cosmochimica Acta* **41.8**: 1041–1059.

Keller M.A. and Isaacs C.M. 1985. An evaluation of temperature scales for silica diagenesis in diatomaceous sequences including a new approach based on the Miocene Monterey Formation, California. *Geo-Marine Letters* **5**, 31–35.

Krogsbøll A., Hededal O. and Foged N. 2012. Deformation properties of highly plastic fissured Palaeogene clay–Lack of stress memory? *DGF-Bulletin* **27**, 133–140.

Larsen G., Frederiksen J., Villumsen A. and Freddericia J. et al. 1995. A guide to engineering geological soil description. *DGF Bulletin***, 1**, Revision 1, Danish Geotechnical Society, 130p.

Lind I.L. 1993. Loading experiments on carbonate ooze and chalk from Leg 130, Ontong Java Plateau. In: Berger, W. H., Kroenke, L. W., and Mayer, L. A. (eds.): Proc.ODP, Sci. Results, **130**, 673–686.

Maliva R.G. and Dickson J.A.D. 1992. Microfacies and diagenetic controls of porosity in Cretaceous/Tertiary chalks, Eldfisk field, Norwegian North Sea. *American Association of Petroleum Geologists Bulletin*, **76**, 1825–1838.

Mallon A.J., Swarbrick R.E. 2002. A compaction trend for non-reservoir North Sea Chalk. Marine and Petroleum Geology, **19**, 527–539.

Matter A., Douglas R.G. and Perch –Nielsen K. 1975. Fossil preservation, geochemistry and diagenesis of pelagic carbonates from Shatsky Rise, northwest Pacific. In: Larson R.L. et al.(eds*)*, Initial Reports of Deep-Sea Drilling Project: Washington, D.C., U.S., Government Printing Office, **32**, 891–922.

Mavko G., Mukerji T. and Dvorkin J. 1998. The Rock Physics Handbook. The Press Syndicate of the University of Cambridge. Cambridge, UK., 329 p.

Mazzullo S.J., Meyer A. and Kidd R. 1988. New sediment classification scheme for the Ocean Drilling Program. In: Mazzullo S.J., Graham A.G. (eds), Handbook for Shipboard Sedimentologists: Texas A&M University, Ocean Drilling Program, Technical Note, **8,** 45–67.

Mody F.K. and Hale A.H. 1993. Borehole-stability model to couple the mechanics and chemistry of drilling-fluids/shale interactions. *Journal of Petroleum Technology*, **45**, 1093–1101.

Mondol N.H., Bjørlykke K. and Jahren J. 2008. Experimental compaction of clays: relationship between permeability and petrophysical properties in mudstones. *Petroleum Geoscience*, **14**, 319–337.

Montaron B. 2009. Connectivity theory–A new approach to modelling non-Archie rocks. *Petrophysics*, **50**(2), 102–115.

Moore D.M. and Reynolds R.C. 1997. X-ray diffraction and the identification and analysis of clay minerals, 2nd ed. xviii + 378 pp. Oxford, New York: Oxford University Press. ISBN 0 19 508713 5.

Moum J. 1965. Falling drop used for grain size analysis of fine grained materials. *Sedimentology*, **5**(4), 343–347. Also published in: Norwegian Geotechnical Institute. Publication, **70**, 1966

Mountain G.S., Miller K.G., Blum P. et al. 1994. Proceedings of the Ocean Drilling Program. Initial Reports, 150: College Station, TX (Ocean Drilling Program).

Moyle P.R. and Dolley T. P. 2003. With or Without Salt–a Comparison of Marine and Continental-Lacustrine Diatomite Deposits. Chapter D of Contributions to Industrial-Minerals Research. Bulletin 2209–D. U.S. Geological Survey. This publication is available only online at: http://pubs.usgs.gov/bul/b2209-d/.

Nicholson K. and Parker R. 1990. Geothermal sinter chemistry: towards a diagnostic signature and a sinter geothermometer: 12th New Zealand Geothermal Workshop, Proceedings, 92–102.

NPD, Norwegian Petroleum Directorate http://www.npd-no. Accede on 15 May 2012.

Nur A. and Byerlee J.D. 1971. An exact effective stress law for elastic deformation of rocks with fluids. *Journal of Geophysical Research*, **76**, 6414–6419.

O'Regan M. and Moran K. 2007. Compressibility, permeability, and stress history of sediments from Demerara Rise. In: Mosher, D.C., Erbacher J., Malone M.J. (Eds.), Proc. ODP, Sci. Results, 207: College Station, TX (Ocean Drilling Program), 1–35.

Øxnevad I.E. I. and Meshri I.D. 1997. Porosity evolution in chalks: crestal Valhall and flank areas. 59th EAGE, Conference Technical Exhibition, extended abstracts book, 552.

Palacky G.J. 1988. Resistivity characteristics of geologic targets. *Electromagnetic Methods in Applied Geophysics* **1**, 53–129.

Passy Q.R., Creaney S., Kullil J.B., Moretti F.J. and Sttoud J.D. 1990. A practical model for organic richness from porosity and resistivity logs, *American Association of Petroleum Geologists Bulletin*, **74**, 1777–1794.

Pedersen G.K. and Surlyk F. 1983. The Fur Formation, a late Paleocene ash-bearing diatomite from northern Denmark. *Bulletin of the Geological Society of Denmark*, **32**, 43–65.

Pedersen G.K., Pedersen S.A.S. and Steffensen J. *et al.* 2004. Clay content of a clayey diatomite, the Early Eocene Fur Formation, Denmark. *Bulletin of the Geological Society of Denmark*, **51**, 159–177.

Pettijohn F.J. 1975. Sedimentary Rocks. Third Edition. Harper and Row, Publishers, New York, USA, 628 p.

Poppe L.J., Paskevich V.F., Hathaway J.C. and Blackwood D.S. 2001. A Laboratory Manual for X-Ray Powder Diffraction. U.S. Geological Survey Open-File Report 01041. http://pubs.usgs.gov/of/2001/of01-041/htmldocs/methods/squant.htm?

Rambøll/Arup 2010a. Ground Investigation Report. GDR 01.0-001. June 2010.

Rambøll/Arup 2010b. Ground water conditions. GDR 01.5-001. November 2010.

Rambøll/Arup 2011. Summary of geological conditions. GDR 01.3-002. April 2011

Robertson A.H.F., Emeis K.C., Richter C. and Camerlenghi A. (Eds.) 1998. Proc. ODP, Sci. Results, **160**: College Station, TX (Ocean Drilling Program).

Schlanger S.O. and Douglas R.G. 1974. The pelagic ooze-chalk-limestone transition and its implications for marine stratigraphy. In: Hsu K.J., Jenkyns H.C. (eds), Pelagic Sediments: On Land and Under the Sea. Special Publication of the International Association of Sedimentologists Special Publications, **1**, 117–148.

Schlumberger 1989. Log Interpretation Principle/Applications, Schlumberger Education Services, Houston, Texas, USA.

Schlumberger 1994. Log Interpretation Charts, Schlumberger Wireline and Testing, Houston, Texas, USA.

Schmoker J.W. 1984. Empirical relation between carbonate porosity and thermal maturity: An approach to regional porosity prediction: *American Association of Petroleum Geologists Bulletin*, **68**, 1697–1703.

Scholle P.A. 1977. Chalk diagenesis and its relation to petroleum exploration: oil from chalks, a modern miracle? *American Association of Petroleum Geologists Bulletin*, **61**, 982–1009.

Schwartz D.E. 1988. Characterizing the Lithology, Petrophysical Properties, and Depositional Setting of the Belridge Diatomite, South Belridge Field, Kern County, California in Studies of the Geology of the San Joaquin Basin, S.A.

Graham, and Olson, H.C., Editors., The Pacific Section, Society of Economic Paleontologists and Mineralogists, Los Angeles, 281–301.

Segnit E.R., Stevens T.J and Jones J.B. 1965. The role of water in opal. *Journal of geological society of Australia (J.geol.Soc.Aust.)*, **12**(2). 221–226.

Serra O. 1984. *Fundamentals of well log interpretation. 1. The acquisition of logging data*. Elsevier Science Publishers B.V. p. 423. ISBN 0444421327.

Sheldon E. 2010. Fehmarn Belt Fixed Link Pre-Quaternary Biostratigraphy, GEUS Report. 15/12/2010.

Sigurdsson H., Leckie R.M. and Acton G.D. et al. 1997. Proceedings of Ocean Drilling Program. Initial Reports, **165**: College Station, TX (Ocean Drilling Program).

Stosur J.J. and David A. 1976. Petrophysical Evaluation of the Diatomite Formation of the Lost Hills Field, California. *Journal of Petroleum Technology*, **28**, 1138–1144.

Terzaghi K.V. 1923. Die Beziehungen zwischen Elastizitat und Innendruck. Mathematisch-Naturwissenschaftliche Klasse Abteilung 2A, **132**, 105–124.

Terzaghi K.V, Peck R.B. and Mesri G. 1996. Soil mechanics in engineering practice. 3rd ed. John Wiley & Sons, New York.

Tib D. and Donaldson E.C. 2004. Theory and practice of measuring reservoir rock and fluid transport properties. Second edition. Gulf professional publishing in imperial of Elsevier. 200 Wheeler Road, Burlington, MA01803, US.

Waples D.W. 1980. Time and temperature in petroleum formation: application of Lopatin's method to petroleum exploration: *American Association of Petroleum Geologists Bulletin*, **64**, 916–926.

Wetzel A. 1989. Influence of heat flow on ooze/chalk cementation: quantification from consolidation parameters in DSDP Sites 504 and 505 sediments. Journal of Sedimentary Petrology, **59**, 539–547.

Williams L.A. and Crerar D.A. 1985. Silica diagenesis, II. General mechanisms. Journal of Sedimentary Petrology, **55**, 312–321.

Part II: Appended papers

I

Paper I

Porosity and sonic velocity depth trends of Eocene chalk in Atlantic Ocean: influence of effective stress and temperature

Ahmed Awadalkarim and Ida Lykke Fabricius

Revised version submitted to Journal of Petroleum Science and Engineering

Porosity and sonic velocity depth trends of Eocene chalk in Atlantic Ocean: influence of effective stress and temperature

Ahmed Awadalkarim[*1] and Ida L. Fabricius[1]

[1]Centre for Energy Resources Engineering, Department of Civil Engineering, Technical University of Denmark, Brovej, Building 118, 2800 Kgs. Lyngby, Denmark

*Corresponding author (e-mail: ahma@byg.dtu.dk)

Abstract

We aimed to relate changes in porosity and sonic velocity data, measured on water-saturated Eocene chalks from 36 Ocean Drilling Program drill sites in the Atlantic Ocean, to vertical effective stress and thermal maturity. We considered only chalk of Eocene age to avoid possible influence of geological age on chalk compaction trends. For each depth, vertical effective stresses as defined by Terzaghi and by Biot were calculated. We used bottom-hole temperature data to calculate the time–temperature index of thermal maturity (TTI) as defined by Lopatin. Porosity and compressional wave velocity data were correlated to vertical effective stresses and to TTI.

Our porosity data showed a broader porosity trend in the mechanical compaction zone, and the onset of the formation of limestone at a shallower burial depth than the porosity data of the Ontong Java Plateau chalk show. Our porosity data do not show or at least it is difficult to define a clear pore-stiffening contact cementation trend as the Ontong Java Plateau chalk. Mechanical compaction is the principal cause of porosity reduction (at shallow depths) in the studied Eocene chalk, at least down to about 5 MPa Terzaghi's effective stress corresponding to a porosity of about 35%. This indicates that mechanical compaction is the principal agent of porosity reduction. Conversely, at deeper levels, porosity reduction is accompanied by a large increase in sonic velocity indicating pore-filling cementation. These deep changes are correlated with TTI. This indicates pore-filling cementation via an activation energy mechanism. We proposed a predictive equation for porosity reduction with burial stress. This equation is relevant for basin analysis and hydrocarbon exploration to predict porosity if sonic velocity data for subsurface chalk is available.

Keywords: Porosity, velocity, thermal maturity, compaction, effective stress, chalk, ODP

1. Introduction

It is known that both the *in-situ* stresses and thermal maturity acting on subsurface sediments increase with increasing burial depth (Fabricius et al., 2008; Wetzel, 1989). This causes changes in physical and mechanical properties of sediments. Consequently, as burial depth increases, a link between vertical effective stress and physical properties such as porosity and sonic velocity of chalk could be established. Additionally, an indirect temperature control on cementation in deep-sea chalk is advocated (Fabricius et al., 2008), and thus it may be possible to establish a relationship between thermal maturity and porosity of deep-sea chalk. In this paper,

we firstly aimed to compare the deep-sea Eocene chalk porosity data from the Atlantic Ocean with those of Fabricius et al. (2008) from the Pacific Ocean. We then focused on establishing porosity and compressional wave (P-wave) velocity depth trends for the Atlantic Ocean Eocene chalks, which we then related to vertical effective stress and thermal maturity (Fabricius et al., 2008). The relationship of P-wave velocity to vertical effective stress, taking into account the influence of cementation (Biot, 1941), can be used to estimate Biot's effective stress if seismic velocity data is available. The predicted Biot's effective stress could then be used to find the corresponding porosity for any given depth. Hence, a meaningful prediction of porosity of inaccessible subsurface layers of chalk could be made if the vertical effective stress and thermal maturity of chalk is known. This study is relevant for basin analysis modelling and hydrocarbon exploration in chalk sediments especially in deepwater basins where drilling is expensive.

Porosity reduction as a result of pore-filling calcite cementation may also be linked to the thermal maturity of the chalk, possibly as a result of increasing burial. Although vitrinite reflection (VR) data is a well accepted method (e.g. using the kinetics Burnham and Sweeney 1989) to directly determine the thermal maturity of sediments, vitrinite are generally not prevalent in chalks. In this study, we therefore expressed the thermal maturity of the studied Eocene chalk by the TTI as defined by Lopatin (Waples, 1980) and assume that heating is solely caused by burial as there is no reported evidence of non-burial related thermal processes such as hot fluid flows or proximal igneous activity to the studied sites. TTI describes the cumulative effect of the time a sedimentary rock experiences in each 10^{o}C temperature interval during burial (Waples, 1980).

Here, we used porosity and P-wave velocity data measured on water-saturated Eocene chalk from the Atlantic Ocean to address depth trends for porosity and P-wave velocity. To establish depth trends, the porosity and P-wave velocity data were correlated with the vertical effective stresses as defined by Terzaghi (1923) and by Biot (1941). The same data were also correlated with the time–temperature index of thermal maturity (TTI) as defined by Lopatin (Waples, 1980). Finally, the present results were compared with the results obtained by Grützner and Mienert (1999) on the Atlantic sediments, by Mallon and Swarbrick (2002) on non-reservoir North Sea Chalk, and by Fabricius et al. (2008) on deep-sea chalk from the Ontong Java Plateau of the western Pacific Ocean.

Grützner and Mienert (1999), Mallon and Swarbrick (2002), and Fabricius et al. (2008) included data of pelagic carbonate sediments from different geological ages in their studies. However, we focused only on Eocene chalk to avoid possible influence of chalk age (i.e. fossil assemblage) in diagenesis of chalk. Therefore, we restricted our dataset to chalk samples of the same age that represent only an Eocene time interval. In this way, also time since the deposition of the studied Eocene chalk is nearly constant, and thus the Eocene chalks primarily differ with respect to stress, pressure, temperature, and texture.

2. The litholoy of the Atlantic Eocene carbonates

During the Eocene, pelagic carbonate oozes were deposited in the Atlantic basins. As a result of diagenesis, pelagic carbonate oozes (unconsolidated) transformed to chalk (consolidated) or even further to limestone (indurated). Here, we used the term chalk

to refer to all three types of calcareous pelagic sediments: unconsolidated, consolidated, and indurated. The studied Eocene chalk is not purely calcitic as indicated by the variations in carbonate content (Table 2). The presence of fine clay content may reduce the calcite-to-calcite grain contacts and occupy some of the pore space in the chalk and thus reduce porosity. This may also make the frame of the chalk sediment weaker (i.e. more compressible), which in turn becomes more susceptible to mechanical deformation (Fabricius, 2000). Clay can also form locations for initiation of pressure dissolution. Apart from burial diagenesis, there must also be some impact of mineralogy and texture on the physical properties of chalk.

Porosity of newly deposited carbonate ooze sediments near the seafloor is very high, but it decreases with increasing burial depth, whereas sonic velocity and bulk density increases (e.g. Hamilton, 1980; Japsen, 1993). Porosity reduction with increasing burial depth is due to mechanisms such as mechanical compaction and thermo-chemical cementation of sediments (Giles et al., 1998). The porosity reduction with burial depth has been described by several authors not least because of the implications of this in hydrocarbon exploration (e.g. Hamilton et al., 1976; Scholle, 1977; Wetzel, 1989; Borre and Fabricius, 1998; Grützner and Mienert, 1999; Mallon and Swarbrick, 2002; Fabricius et al., 2008; Alam et al., 2010).

3. Previous related studies

Hamilton (1974) and several later authors have addressed mechanical compaction of carbonate ooze sediments. Mechanical compaction begins immediately after deposition of the calcareous ooze. It reduces porosity primarily through a more efficient packing of particles, but fossils and grain sizes of other particles may remain constant (e.g. Lind, 1993; Grützner and Mienert, 1999). This depends on chalk depositional texture, however, textural information of the studied chalk are not available, thus we assumed the same texture as in those deep-sea chalks studied by Lind (1993).

The geological age of the sediments in Grützner and Mienert (1999) study was not taken into account, and also the physical effect of “depth below seafloor” was not addressed. Similarly, Mallon and Swarbrick (2002) described two linear trends for porosity loss with burial depth for non-reservoir chalk of the Central North Sea. But, depth is only an approximation for thermal maturity and vertical effective stress (σ') in uniaxial strain condition described by Biot’s effective stress (Biot, 1941). Static and dynamic β of chalk from the North Sea was studied by Alam et al. (2012). They found that static and dynamic β values are not significantly different and below one. In this study, the laboratory measured sonic velocity and bulk density data of the studied Eocene chalk were used to estimate dynamic β as by Alam et al. (2012).

Fabricius et al. (2008) defined mechanical compaction, pore-stiffening contact cementation and pore-filling cementation as three different diagenetic processes in chalk. The sources of the calcite cement can be calcite dissolved at stylolite surfaces or from outside the system (Delaney, 1991). However, in the deep-sea chalk, we do not expect cement from external sources to be involved in the cementation process. Cement is internally derived by dissolution, of calcite particles, and re-precipitation of it on other particles within the system. Fabricius et al. (2008) defined mechanical compaction, pore-stiffening contact cementation and pore-filling cementation to occur in the ranges of 0–5, 5–7 and 7–10 MPa Terzaghi’s effective stress, respectively.

Pore-filling cementation apparently requires a threshold TTI possibly reflecting the transformation of opal-CT to quartz and a threshold stress for the onset of pressure dissolution (Fabricius et al., 2008). The onset of calcite cement precipitation is also governed by other factors such as temperature and the chemical composition of the pore-water (Øxnevad and Meshri, 1997). Stylolites could be a possible source for precipitation of calcite cement in the studied Eocene chalk. The study by Alam et al. (2010) on the deep-sea pelagic carbonates suggests that porosity reduction due to compaction and creep takes place via matrix porosity reduction, whereas the intra-particle porosity does not change much.

Fabricius (2000) studied burial history of pelagic clayey mixed carbonate sediments from the Caribbean Leg 165 Sites 999 and 1001 based on geotechnical data. O'Regan and Moran (2007) studied chalk and black shale sediments recovered during the ODP Leg 207 Sites 1257, 1258, 1259, and 1261. We included only the Eocene chalk sediments from these four ODP sites in our present study, whereas they included all chalk and black shale sediments from Neogene to Cretaceous in their study.

4. Material and methods

The methods of this study comprised two procedures. The first procedure was a detailed calculation of vertical effective stress as defined by Terzaghi (1923) and by Biot (1941) and the second procedure was the calculation of Lopatin's TTI (Waples, 1980).

The geological information and water depth data used in this paper were obtained from the proceedings of the Ocean Drilling Program (ODP) initial reports of the Atlantic Ocean sites (Fig. 1; Table 1). Shipboard physical properties data were obtained from the Janus Web Database at this link:
(http://iodp.tamu.edu/janusweb/links/links_all.shtml).

Initially, more than 242 ODP drill sites across the Atlantic Ocean were screened for obtaining suitable Eocene chalk data for this study. Data from 36 ODP drill sites covering a wide geographical area and water depths were selected (to give a representative porosity–depth trend) and included in this paper (Fig. 1; Table 1).

Shipboard bulk density, grain density, and porosity were measured by gravimetric methods on discrete samples. Shipboard sonic velocity was measured on water-saturated split core sections or on cut samples with no confining pressure or pore-pressure involvement. Shipboard P-wave velocity measurements were made in the horizontal and vertical directions with respect to the core axis and at ambient temperature and pressure after thermal equilibration. Detailed descriptions of the methods and measurement procedures for these physical properties can be found in the explanatory notes chapters of any of the ODP initial reports of the 36 ODP drill sites included here (e.g. Robertson et al., 1998; Ciesielski et al., 1991). The P-wave velocity data measured in the vertical direction of the cores (i.e. along core axis and perpendicular to the bedding plane) were used in this paper. The ODP reported carbonate data included weight percentages of inorganic carbon, organic carbon, total carbon, calcium carbonate, nitrogen, and sulfur. Although other carbonates may be present, all acid-soluble carbon is calculated as calcium carbonate. Here, the ODP reported weight percentages of the calcium carbonate content (Table 2) was used as an indicator of the purity of the investigated Eocene chalk.

The available stratigraphical information from the 36 ODP drill sites was used to estimate the ages of pelagic and hemi-pelagic sediments from Eocene to Holocene/Pleistocene. However, due to the lack of bottom-hole temperature data for 12 of the 36 ODP drill sites, the bottom-hole temperature and the age–depth information from only 24 ODP drill sites were used here to calculate Lopatin's TTI values (Table 4).

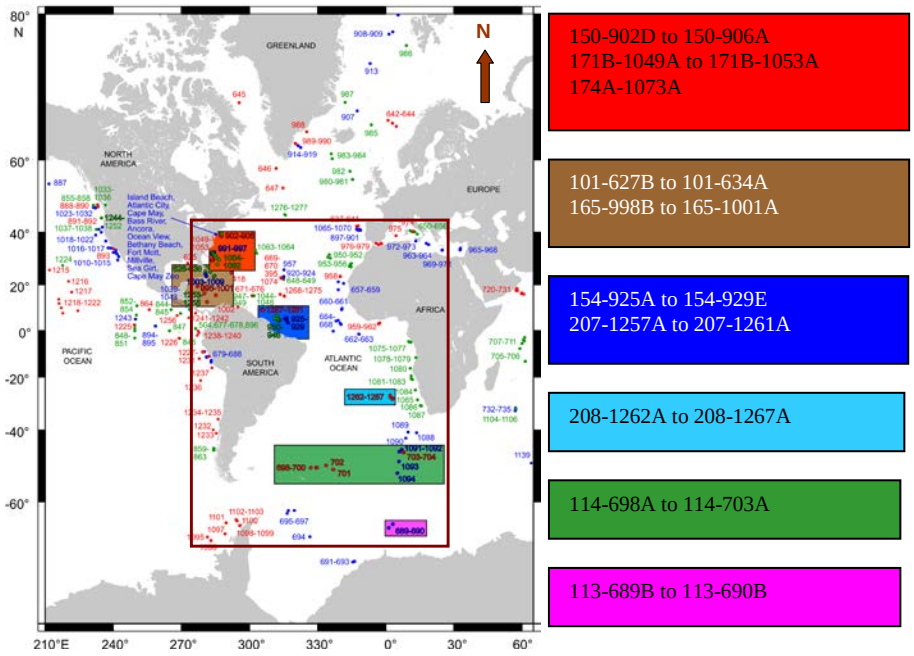

Fig. 1. Map showing the locations of Ocean Drilling Program (ODP) sites (modified after http://iodp.tamu.edu/scienceops/maps/odpmap.pdf). The studied sites are enclosed by a rectangle and highlighted by colouring. They comprise all sites with information on porosity for Eocene chalk. The purpose of highlighting studied sites, by the coloured rectangles, is to help the reader to get an idea about the geographical distributions of the studied ODP site. The red, brown, dark blue, light blue, dark green and magenta colours used here have nothing to do with the colours used for sample legends in the other figures in this paper. Each ODP site in this map comprises only 3-4 digits as a site name which may have 2 to 5 drilled boreholes with the names A, B, C, D and E. The following example explains how the name for each site (in this study) is structured; e.g. 154-929E means ODP Leg 154, Site 929, Hole E. The ODP sites included within each coloured rectangle in the map are shown in the legend to right of the map.

4.1. Calculation of overburden stress, pore-pressure and effective stress

As our current study is on deep-sea chalk (i.e. in the marine environment), the toat overburden stress, σ, (i.e. *in-situ* total vertical stress caused by the load of sediments and water) was calculated, to a fair approximation, as follows:

$$\sigma = g\left(h_w\rho_w + \sum_{i=1}^{i=n}\left(\rho_i h_i\right)\right) \qquad (1)$$

Table 1
A list of the 36 ODP sites, included in this study, with their geographical coordinates and the Eocene chalks depth intervals. The geographical coordinates are found at following website: http://iodp.tamu.edu/janusweb/coring_summaries/sitedetails.cgi

ODP Site	Geographical coordinates		Water	Depth
	Latitude	Longitude	depth (m)	interval (mbsf)
101-627B*	27°38.1000' N	78°17.6520' W	1036	181-220
101-628A*	27°31.8480' N	78°18.9480' W	976	260-289
101-634A*	25°23.0220' N	77°18.8820' W	2835	144-163
113-689B*	64°31.0200' S	3°5.9940' E	2080	130-204
113-690B*	65° 9.6288' S	1°12.2958' E	2914	97-133?
114-698A	51°27.5400' S	33°5.9580' W	2138	0-61
114-699A*	51°32.5200' S	30°40.6200' W	3706	316-497
114-700B*	51°31.9800' S	30°16.6860' W	3601	26-229
114-701C*	51°59.1000' S	23°12.7020' W	4637	424-471.8
114-702B*	50°56.7600' S	26°22.1160' W	3084	40-247
114-703A*	47°03.0600' S	07°53.6820' E	1796	120-364
150-902D	38°56.0790' N	72°46.3752' W	808	680-740
150-903C*	72°46.3752' W	72°49.0236' W	446	1070-1150
150-904A*	38°51.8058' N	72°46.0842' W	1123	341-577
150-906A*	38°57.8958' N	72°45.9972' W	913	555-602
154-925A*	4°12.2490' N	43°29.3340' W	3042	773-930
154-929E*	5°58.5678' N	43°44.4000' W	4356	491-770
160-967E	34°4.1060' N	32°43.5250' E	2553	130-167
165-998B	19°29.3870' N	82°56.1600' W	3180	590-905
165-999B*	12°44.5970' N	78°44.4180' W	2828	727-960
165-1001A*	15°45.4270' N	74°54.6270' W	3260	165-232
171B-1049A*	30°08.5436' N	76°06.7312' W	2656	19-93
171B-1050A*	30°05.9977' N	76°14.1011' W	2300	0 - 224
171B-1051A*	30°03.1740' N	76°21.4580' W	1983	3-508
171B-1052E*	29°57.0906' N	76°37.5966' W	1345	0-165
171B-1053A*	29°59.5385' N	76°31.4135' W	1630	11-183
174A-1073A*	39°13.5214' N	72°16.5461' W	639	654-663
207-1257A	9°27.2302' N	54°20.5184' W	2951	42-150
207-1258A*	9°26.0003' N	54°43.9994' W	3192	8-253
207-1259A	9°17.9989' N	54°11.9984' W	2354	125-445
207-1260A	9°15.9485' N	54°32.6327' W	2549	35-335
207-1261A	9° 2.9168' N	54°19.0384' W	1900	367-391
208-1262A	27°11.1601' S	1°34.6200' E	4759	80-182
208-1263A	28°31.9702' S	2°46.7690' E	*2717*	92-335
208-1265A	28°50.1010' S	2°38.3602' E	3060	192-318
208-1267A	28°5.8805' S	1°42.6586' E	4355	145-232

***** These are the 24 ODP sites with bottom-hole temperature data used in the TTI calculations, see Table 4.

where g is the acceleration due to gravity (9.81 m/s^2), h_w is water depth (m) measured from sea level, ρ_w is ocean water density (assumed to be 1.1 g cm^{-3} throughout), ρ_i is the water-saturated bulk density of sediment at each data point and h_i is depth interval (m) between measured data points. Here, we used the shipboard water-saturated bulk density data measured on discrete chalk samples.

The pore-fluid pressure, P_p, was calculated under the assumption of a hydrostatic fluid pressure of a column of pore-water extending to the surface, as follows:

$$P_P = gh\rho_w \qquad (2)$$

where h is the measured depth below sea level ($h = h_w + \sum h_i$), and pore-water density is assumed equal to ocean water density, ρ_w.

Table 2
Non-carbonate minerals (clay and non-clay minerals), and carbonate content expressed as $CaCO_3$ of the selected depth intervals for the studied Eocene chalk samples. Data are from the 36 ODP sites shown in Figure 1

ODP Site	Depth interval (mbsf)	Non-Carbonates (wt %)	Calcium carbonate, $CaCO_3$ (wt %)		
			Average	Standard deviation	Number of data points
101-627B	181-220	14	86	6	4
101-628A	260-289	12	88	1	2
101-634A	144-163	12	88	7	3
113-689B	130-204	10	90	6	25
113-690B	97-133?	22	78	4	13
114-698A	0-61	7	93	3	10
114-699A	316-497	37	63	15	50
114-700B	26-229	21	79	10	49
114-701C	424-471.8	20	80	8	5
114-702B	40-247	9	91	4	32
114-703A	120-364	9	91	4	14
150-902D	680-740	49	51	8	4
150-903C	1070-1150	50	50	9	4
150-904A	341-577	50	50	5	17
150-906A	555-602	57	43	5	3
154-925A	773-930	37	63	10	44
154-929E	491-770	50	50	16	83
160-967E	130-167	17	83	9	3
165-998B	590-905	13	87	2	11
165-999B	727-960	36	64	14	119
165-1001A	165-232	34	66	18	12
171B-1049A	19-93	29	71	8	19
171B-1050A	0 - 224	35	65	10	52
171B-1051A	3-508	31	69	21	162
171B-1052E	0-165	18	82	3	4
171B-1053A	11-183	25	75	4	27
174A-1073A	654-663	Na	na	na	na
207-1257A	42-150	34	66	13	13
207-1258A	8-253	47	53	13	49
207-1259A	125-445	33	67	15	72
207-1260A	35-335	32	68	9	61
207-1261A	367-391	26	74	12	8
208-1262A	80-182	25	75	31	75
208-1263A	92-335	7	93	4	85
208-1265A	192-318	15	85	15	100
208-1267A	145-232	36	64	30	64

Note: na = not analyzed.

Because of the high water depth in the Atlantic Ocean which reaches about 4356 m at Site 154-929E, pore-fluid pressure is high and thus a relatively large influence of Biot's coefficient, β, on the estimation of vertical effective stress is expected.

The vertical effective stress, σ', was first calculated as defined by Terzaghi (1923) as:

$$\sigma' = \sigma - P_P \qquad (3)$$

When the sediment stiffens due to cementation, β becomes less than one and the effect of pore-fluid pressure on resisting overburden stress may be reduced (Biot and Willis, 1957). This is because the sediment frame (skeleton) links the particles in the vertical direction; and the pore-fluid pressure becomes less than 100% effective in counteracting the effect of increased overburden loading (stress). Thus, for cemented sediments the *in-situ* vertical effective stress, σ', may be calculated according to Biot (1941) as follows:

$$\sigma' = \sigma - \beta P_P \qquad (4)$$

Terzaghi's effective stress concept as defined by Eq. (3) is appropriate for uncemented sediments (i.e. sediments with open framework of particles) such as ooze or loose sand, where β value is one. But, most chalks are cemented to some extent and therefore have more stable grain-to-grain contacts and lower compressibility. Consequently, cemented chalk must have higher dry bulk modulus. Thus, the ratio of the higher dry bulk modulus to the calcite mineral modulus must be higher than that of the uncemented chalk which is highly compressible. Thus, β should be less than one in cemented chalk (Nur and Byerlee, 1971; Alam et al., 2012). Accordingly, β is expressed as follows:

$$\beta = \left(1 - \frac{K_{dry}}{K_o}\right) \tag{5}$$

where K_{dry} and K_o are bulk modulus of dry porous rock (modulus of the mineral frame) and bulk modulus of the solid material (mineral grains) that makes up the rock, respectively (Biot and Willis, 1957). According to Fjær et al. (1992), values of β lie in the range of porosity (ϕ) and one, (i.e. β cannot be smaller than porosity, $\phi \le \beta \le 1$)

To use Eq. (4), the value of β must be determined. In a linear-elastic isotropic sediment, β may be calculated from sonic velocity and density data (e.g. Mavko et al., 1998). In this study, due to the lack of shear velocity data, β was calculated (Fig. 2) by using iso-frame modelling (Fabricius et al., 2008). The bulk modulus of dry rock (K_{dry}) was calculated from iso-frame values and porosity data. We assumed a critical porosity of 100% and calcite mineralogy for this modelling, hence considered a bulk modulus for pure calcite, K_o, equal to 71 GPa (citation in Mavko et al., 1998). See Eq. (5) above.

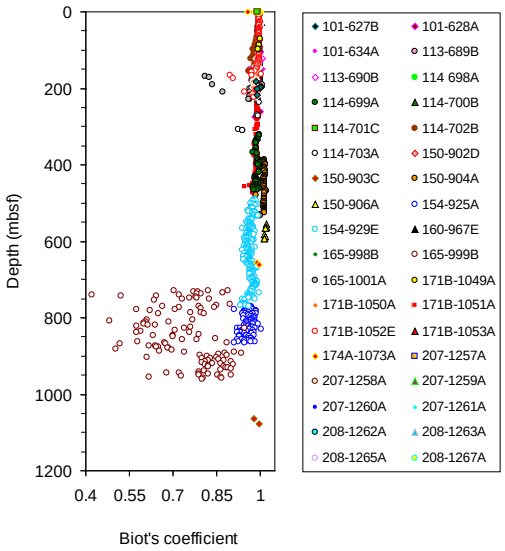

Fig. 2. Plot showing the variation in the calculated Biot's coefficient with depth.

4.2. Calculation of Lopatin's TTI

Lopatin's method was applied by using the bottom-hole temperature data and the stratigraphical information given in the proceedings of the ODP and IODP initial reports. The bottom-hole temperature data used in this study were as reported by the

ODP. First, the burial histories for 24 ODP drill sites were reconstructed. This was accomplished according to Waples (1980) by plotting depth of burial versus geological age. Examples of 8 burial history reconstructions are shown in Figure 3. The ages of sediments that were included in the reconstruction of the burial histories range from Eocene (37–58 Ma) to Holocene/Pleistocene (0–2 Ma), and thus, represent a broad time interval. However, the TTI was calculated only for the sediments of Eocene age. Possible faulting was disregarded in the reconstruction of the burial histories mentioned above. An assumption that burial-controlled porosity change may be disregarded was also made. Please note that this assumption is valid only for the purpose of reconstruction of the burial histories. The impact of this assumption in the calculation of TTI values is investigated as follows: A decompaction (i.e. backward) approach was used to reconstruct the burial histories of the 8 ODP sites (i.e. 150-903C, 150-904A, 150-906A, 154-925A, 154-929E, 165-999B, 171B-1051A and 174A-1073A) with the deepest burial (i.e. 500 mbsf) of the Eocene interval. For each of the eight ODP sites stated here, a corresponding 'normal' chalk porosity-depth trend of that site was used when decompacting the present-day (preserved) thicknesses of the deeper intervals to estimate the past thickness (at deposition). The decompaction was done by using the past thicknesses of the sediments when they were deposited assuming that the amount of solid grain thickness (m) is constant since its deposition. This method was first done by plotting the amount of solid grain thickness (m) versus depth below sea floor (mbsf) from which the past thicknesses of the sediments were obtained. The obtained past thicknesses are larger than the present thicknesses because the latter is compacted. The past thicknesses were then plotted against the geological ages according to Lopatin's method as introduced by Waples (1980). The results obtained by both approaches were compared.

Second, the geothermal gradient at each of the 24 ODP drill sites was assumed to be constant since the Eocene so that the subsurface temperature was specified for every depth. Thus, the temperature grid is defined as a series of equally spaced lines of constant depth. Accordingly, 10 ^{o}C spacing was used to draw the temperature grid (Fig. 3). The regional geothermal gradient in the studied area ranges from 17.1 to 50 ^{o}C km^{-1}. For Sites 165-999B and 165-1001A, no geothermal data are available; therefore, the minimum (17.1 ^{o}C km^{-1}) and the maximum (50 ^{o}C km^{-1}) geothermal gradients were applied and the results were compared.

The following equation was used to calculate Lopatin's TTI (Waples, 1980):

$$\mathrm{TTI} = \sum(\Delta T_n)(r^n) \qquad (6)$$

where n is the appropriate index value for each 10 ^{o}C temperature interval (n = -1 represents 90–100 ^{o}C, n = 0 represents 100–110 ^{o}C and n = 1 represents 110–120 ^{o}C, etc.), ΔT_n is the time in million years (Ma) the sediments reside in a given temperature interval, and r is a factor which reflects the exponential dependence of maturity on temperature. A constant value of 2 was assumed for r (Waples, 1980).

Our TTI results showed that the decompaction method yields higher TTI values than the compaction method for sediments deeper than 663 mbsf. It gives an average difference in the TTI values of about 6% at the top of Eocene, and around 10% at the base of Eocene. However, the TTI values obtained by both approaches are consistent for the sediments that are at the depth of about 663 mbsf or shallower. The TTI data

obtained from the decompaction approach are deemed more accurate than those obtained from the former compaction method; therefore, they are used in this paper.

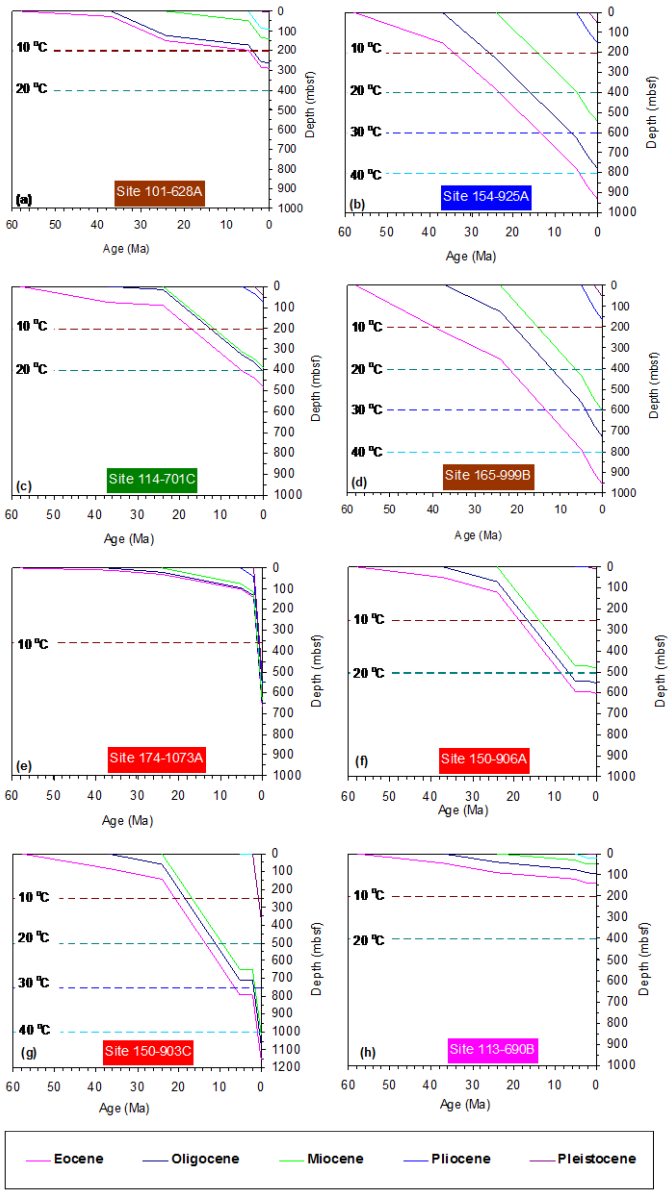

Fig. 3. Examples of the reconstructed depositional history for five sedimentary horizons (from Eocene to Pleistocene) for six ODP sites. Isotherms (dashed horizontal lines) were derived from geothermal gradients that represent the present bottom-hole and seafloor temperatures. The ODP sites highlighted here by coloured rectangles are according to the geographical colour codes given in Fig. 1.

5. Results

5.1. Changes of physical properties with stress

Fig. 4 shows the bulk density, P-wave velocity, and porosity plotted versus depth in meters below seafloor (mbsf). The porosity–depth trend (Fig. 4 c) appears to fit Mallon and Swarbrick's (2002) shallow normal compaction trend fairly well down to around 700 mbsf, and no signs of overpressure development were noticed in the Eocene chalk (except that indicated by the data of ODP site 150-903C) included here.

In this study, the stress–porosity and stress–sonic velocity relationships were also used to explore how the vertical effective stress obtained by two different concepts influence the depth trends for porosity and P-wave velocity. When the porosity and P-wave velocity data were plotted versus total overburden stress, σ, trends are less easy to define (Fig. 5). However, when the same data were plotted as a function of Terzaghi's effective stress, it is possible to define more than one trend for porosity decline, and for P-wave velocity increase (Fig. 6a, d). This implies that porosity reduction trends due to Terzaghi's effective stress may provide information on different mechanisms for porosity reduction with burial depth.

In contrast, when the same porosity and P-wave velocity data were plotted versus Biot's effective stress, they showed a better correlation (Fig. 6c, f). Moreover, the plots showed a smooth, single stress trend regardless of lithology. The results in Fig. 6c, indicate that the scatter of the data in Fig. 6a is improved when applying Biot's effective stress. This may be because high porosity chalk (e.g. uncemented chalk) tends to have a high β, and hence, a relatively low effective stress, whereas low porosity chalk (e.g. cemented chalk) tends to have a low β, and thus, a relatively high effective stress (Fabricius et al., 2008).

The black curves in Fig. 6c represent the lower inferred (poorly sorted sediments) and upper inferred (well sorted sediments) porosity trend limits for our porosity data. The blue curve in Fig. 6a represents the normal mechanical compaction trend for Fabricius et al. (2008) porosity data from the Ontong Java Plateau chalk in the Pacific Ocean. It could be assumed to represent the mid point between the lower and the upper inferred

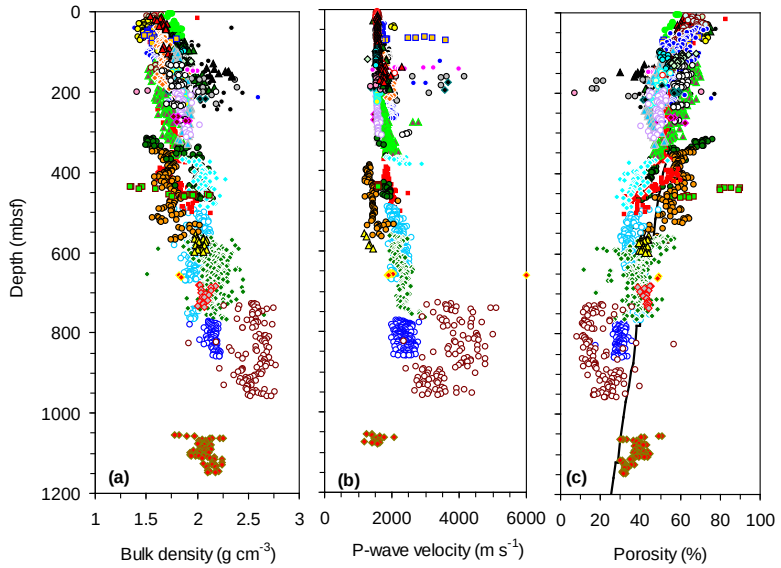

Fig. 4. Physical properties for water-saturated Eocene chalk versus depth below seafloor (mbsf) with the points colour-coded according to Figure 2. (**a**) Bulk density, (**b**) compressional wave (P-wave) velocity, and (**c**) porosity. Data are from the 36 ODP sites shown in Fig. 1. The black solid curve in Figure 4c represents the shallow porosity depth trend for Mallon and Swarbrick (2002) porosity data (as shown in their Figure 10) from the North Sea chalk.

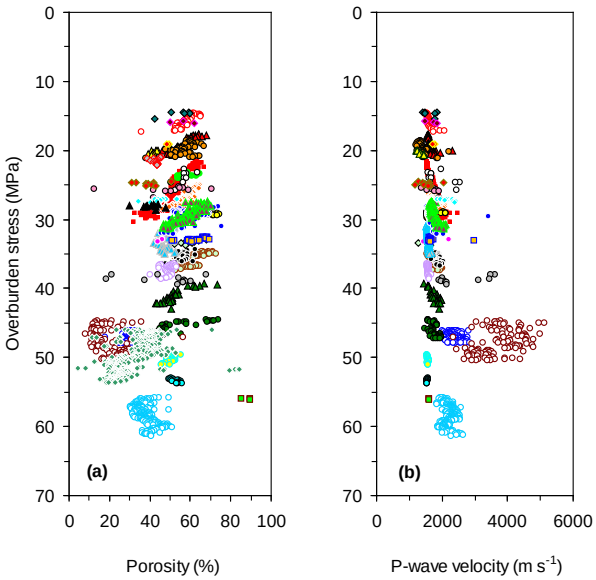

Fig. 5. (**a**) Porosity and (**b**) P-wave velocity data for the studied Eocene chalk plotted as a function of total overburden stress. P-wave velocity data are only available for 34 ODP sites. For sample legend, refer to Fig. 2.

extreme compaction trends for our present porosity data. The green curve in Fig. 6a, b represents porosity trend due to pore-filling calcite cementation for the Ontong Java Platea chalk porosity (Fabricius et al., 2008). This curve is referred to here as a cementation front that represents the burial depth interval at which the pore-filling calcite cementation has formed within the Ontong Java Platea chalk. It is the effective stress interval at which limestone has started to form. It is clear that the cementation front of Fabricius et al. (2008) does not fit our current porosity data. Some of our data points are off the trends; these data points may represent clay mixed chalk sediments that are not yet cemented. The variation in chalk texture causes some scattering. However, possible reasons for this apparent anomaly will be addressed in detail in the discussion section. Most of our data follow the same smooth porosity trend when they were plotted in Fig. 6c. This smooth porosity trend is the most suitable one for deriving a predictive equation for porosity. Especially, an estimation of vertical effective stress is easy to obtain even if drilling information is not available. Biot's effective stress could be fairly estimated from the relationship with P-wave velocity as shown in Fig. 6f, which shows a good correlation (R^2 = 0.93). Porosity prediction equations for the studied Eocene chalk were derived based on the porosity and P-wave velocity trends in Fig. 6c, f. The derived equations are presented in Table 3.

5.2. Changes of physical properties with Lopatin's TTI

Table 4 summarizes the results for calculated TTIs. Plots of P-wave velocity and porosity data as a function of log TTI are shown in Fig. 7. They show non-linear correlations (Fig. 7a, b). Both P-wave velocity and porosity show poor correlations at the higher values of TTI (i.e. at high temperature). However, we observed a threshold TTI of about 0.07 for onset of pore-filling cementation corresponding to about 50% porosity (Fig. 7b) which might correspond to about 5–6 MPa Terzaghi's effective stress (Fig. 6a).

When we assumed the maximum regional geothermal gradient of 50 ^{o}C km^{-1} at the ODP Sites 165-999B and 165-1001A, the obtained results for P-wave velocity and

porosity trends at the two sites follow the same trends as the results of P-wave velocity and porosity data from other sites do (Fig. 6a, b). However, when the minimum geothermal gradient of 17.1 ^{o}C km^{-1} was used at the same two sites, the resulting trends do not follow the same trends as the data from other sites do (Fig. 6c, d). Hence, we assumed that the geothermal gradient at the two sites could be close to the upper extreme of 50 ^{o}C km^{-1}.

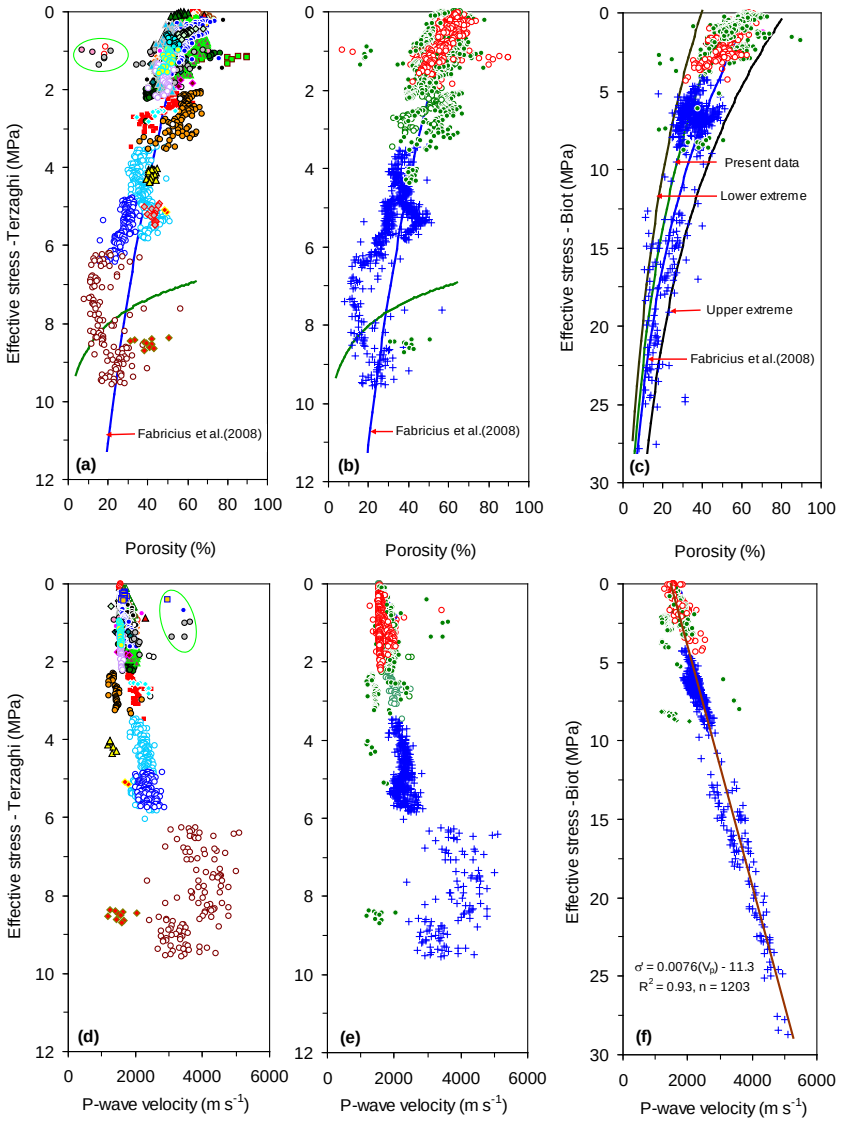

Fig. 6. Eocene chalk porosity data versus (**a**, **b**) Terzaghi's effective stress and (**c**) Biot's effective stress of our data compared with a porosity prediction relations reported by Fabricius et al., (2008). Eocene chalk P-wave velocity data versus (**d, e**) Terzaghi's effective stress and (**f**) Biot's effective stress. In plots 6a and 6d all data points are annotated according to ODP drill sites. For sample legend, refer to Fig. 2. In plots 6 b, c, e and f, all data points are annotated with respect to lithology (i.e. ooze (red open circle), chalk (green closed circle) and limestone (blue cross)). Our porosity data are compared with the porosity trend obtained in the Pacific Ontong Java Plateau by Fabricius et al. (2008). The blue and green curves in (***C***) represent the porosity trends for Fabricius et al. (2008) data and the average/best-fit trend of our present work porosity data. Some data points are off the trends, they are enclosed by a green oval shape on Fig. 6a, d.

Table 3
Predictive equations for porosity reduction as a function of vertical effective stress

Process	Equation*	
Porosity–Biot's effective stress (Fig. 5c)		
1. Fabricius et al. (2008)	$\phi\,(\%) = e^{\left(\frac{65.2-\sigma'}{15.4}\right)MPa}$	(7)
2. Present data	$\phi\,(\%) = e^{\left(\frac{65.2-\sigma'}{16.17}\right)MPa}$	(8)
3. Lower extreme	$\phi\,(\%) = e^{\left(\frac{65.2-\sigma'}{18.6}\right)MPa}$	(9)
4. Upper extreme	$\phi\,(\%) = e^{\left(\frac{65.2-\sigma'}{14.7}\right)MPa}$	(10)
Sonic velocity–Biot's effective stress (Fig. 5f)		
1. Biot's effective stress	$\sigma'(MPa) = -(11.3 - 0.0076V_p)$	(11)

***** The ϕ symbol is porosity, σ' is vertical effective stress (MPa) and V_p is P-wave velocity (ms^{-1}).

6. Discussion

We assumed that the changes in porosity and P-wave velocity with increasing burial depth are linked to vertical effective stress and it may also be linked, to some extent, to thermal maturity of Eocene chalk in the Atlantic. Whereas, mechanical compaction and chemical dissolution of calcite grains at stylolites are controlled by vertical effective stress (Fabricius et al., 2008), pore-filling calcite cementation may be related to thermal maturity of chalk. Therefore, in this context, we base our discussion on the correlations of our porosity and P-wave velocity data with the calculated vertical effective stresses and TTI data. We used the trends in Fig. 6c, f to derive equations that could be used to predict porosity reduction with burial stress. These equations could be relevant for basin analysis and hydrocarbon exploration in chalk. Thus, our discussion is divided into two parts; the first part focuses on the influence of burial stress on physical properties of chalk; and the second part considers the influence of TTI on porosity and P-wave velocity of chalk.

6.1. The influence of burial stresses on physical properties

Porosity reduction with increasing vertical effective stress according to Eqs. (3) and (4) is compared in Fig. 6. When our porosity and P-wave velocity data were correlated with Terzaghi's effective stress, the data cover a wide range for a given effective stress (Fig. 6a, d). This could be related to the textural variation in chalk. Also, it may be referred to impurity of chalk (i.e. mixed sediments). Porosity data, especially from the Sites 165-999B, 165-1001A, 150-903C, 171B-1052E, and 113-689B are clearly showing the influence of variations in chalk texture. The chalk sediments from these sites are mixed with clay (Table 2). Porosity reduction according to Biot's effective stress (Fig. 6c) does not show similar pattern as that

when β is excluded (Fig. 6a). This implies that porosity and P-wave velocity change as relatively simple functions of Biot's effective stress. This probably suggests that chalk is in elastic equilibrium (Fabricius et al., 2008). The relationships in Fig. 6c, f are good enough to be used to derive predictive equations that could be used to predict porosity loss with burial stress.

Table 4
Calculated Lopatin's time–temperature index of thermal maturity (TTI) for the Eocene sediments from burial curves of the 24 ODP sites as described in the text. Each reported geothermal gradient is for that entire ODP site and not the temperature gradient within the Eocene chalk interval. We used it to estimate the temperature of the chalk interval

ODP Site	Depth	Thickness	Temperature gradient	Lopatin's TTI	
	(mbsf)	(m)	^{o}C km^{-1}	Base of Eocene	Top of Eocene
101-627B	181-220	39	50	0.059	0.036
101-628A	260-289	29	50	0.062	0.040
101-634A	130-163	33	50	0.057	0.036
113-689B	180-210	30	50	0.060	0.036
113-690B	94-140	46	50	0.057	0.036
114-699A	310-488	178	50	0.138	0.061
114-700B	25-230	205	50	0.093	0.005
114-701C	405-480	75	50	0.082	0.048
114-702B	40-240	200	50	0.093	0.036
114-703A	115-364	249	50	0.097	0.036
150-903C	1070-1150	80	40	0.135	0.086
150-904A	348-577	229	40	0.089	0.038
150-906A	551-602	51	40	0.092	0.065
154-925A	777-930	153	50	0.221	0.116
154-929E	491-770	280	50	0.182	0.063
165-999B	730-960	230	*17.1**	0.070	0.041
165-999B	730-960	230	*50**	0.229	0.096
165-1001A	165-232	67	*17.1**	0.057	0.023
165-1001A	165-232	67	*50**	0.059	0.023
171B-1049A	18.6-93	74	17.1	0.057	0.036
171B-1050A	0.3-224	224	17.1	0.057	0.002
171B-1051A	3-508	505	17.1	0.057	0.002
171B-1052E	4-165	161	17.1	0.057	0.002
171B-1053A	0.4-183	183	17.1	0.057	0.002
174A-1073A	654-663	9	28	0.058	0.038
207-1258A	9-173	164	50	0.057	0.036

* These values are not true data. First, the geothermal gradients at the Sites 165-999B and 165-1001A were assumed to be equal to the maximum geothermal gradient of 50 ^{o}C km^{-1}. Second, the geothermal gradients at the same two sites were assumed to be equal to the lower extreme geothermal gradient of 17.1 ^{o}C km^{-1}.

The trends of the current porosity data were compared with those of Fabricius et al. (2008) in Fig. 6a, c. If we assume that the average of the lower and upper limit trends in Fig. 6c represents the general trend for the present porosity data; it seems to be relatively in agreement with that of Fabricius et al. (2008). Our porosity data show a broader trend than Fabricius et al. (2008) porosity data. Generally, we conclude that overall agreement is good between the present data and those of Fabricius et al. (2008) especially at deep burial depths. Thus, the Eq. (8) in Table 3 could be used to predict a reasonable estimate of porosity if the Biot's vertical effective stress is known (e.g. obtained from Eq. (11)).

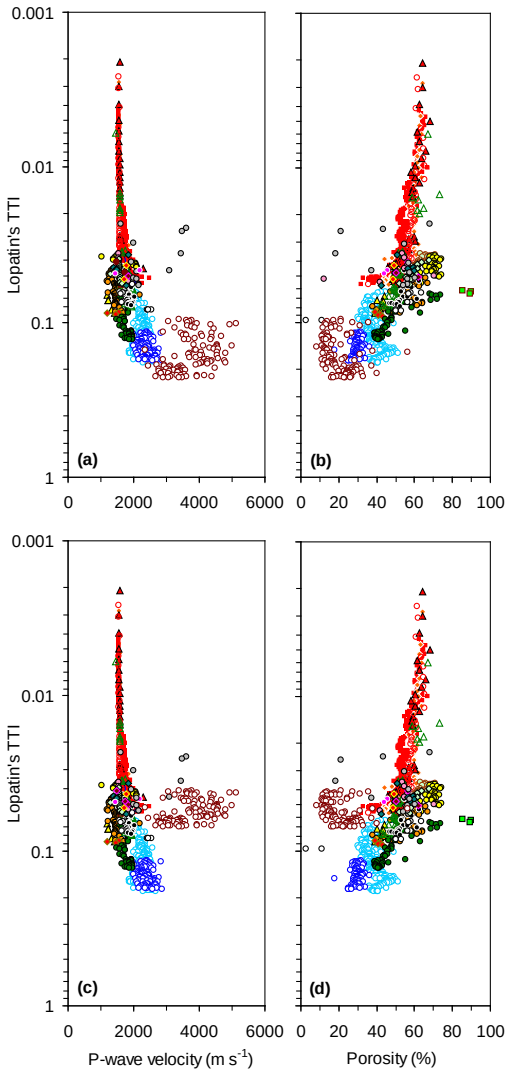

Fig. 7. Relationships between Lopatin's time–temperature index of thermal maturity (TTI) and P-wave velocity and porosity. In this figure, we look at log TTI as it increases with P-wave velocity ((**a**) and (**c**)) and porosity ((**b**) and (**d**)). In Fig. 7a, b the geothermal gradients at the Sites 165-999B and 165-1001A were assumed to be equal to 50 ^{o}C km^{-1} which is the upper extreme geothermal gradient at the study area. In Fig. 7c, d the geothermal gradients at the same two sites were assumed to be equal to 17.1 ^{o}C km^{-1} which is the lower extreme geothermal gradient. Data from 24 ODP sites were used to produce these figures. For sample legend, refer to Fig. 2.

Porosity reduction according to Terzaghi's effective stress concept may give information on different porosity reduction mechanisms such as mechanical compaction and pore-filling cementation (Fig. 6a). Some authors (e.g. Jones et al., 1984; Lind, 1993; Fabricius, 2003) have documented that mechanical compaction on chalk is the major porosity reduction agent down to porosities of 50% and in some cases even to 40% or lower. This is in agreement with the present porosity results that show porosity change due to mechanical compaction from ~70% to ~35% at about 5 MPa Terzaghi's effective stress. The low porosity may be because the studied Eocene chalks contain clay and silt size materials (Table 2) that may enhance mechanical compaction process. But, if the mechanical compaction trend is extended through the pore-filling cementation interval (i.e. through the limestone lithology (Fig. 6b) at

greater than 5 MPa Terzaghi's effective stress), it follows the trend of speculative compaction of calcite crystals as in the diagenetic stage five of Grützner and Mienert (1999), or as it is normally termed as due to creep of the chalk (Alam et al., 2010). The mechanical compaction as defined by Grützner and Mienert (1999) in their diagenetic stage one is only for pelagic carbonate sediments of about 4 Ma old (i.e. Pliocene age), whereas the present data show mechanical compaction trend for chalk as old as 37–58 Ma (i.e. Eocene age).

Rapid porosity reduction occurs in the upper layers of chalk sediments, in the ooze interval, (Fig. 6a, b). The reason for the high porosity (~70%) shown in the ooze zone could be due to a high content of hollow nano- and micro fossils. Some data points from the Sites 113-689B, 171B-1052E, and 165-1001A are off the trend; these data points are enclosed by green oval shapes in Fig. 6a, d. They showed very low porosity values (range from 5–15%) and high P-wave velocity of ~ 3500 m s^{-1}. These data may represent sedimentary hard grounds formed by seafloor diagenesis.

Contact cement causes pore-structure stiffening (Biot and Willis, 1957). Our porosity data did not show or at least it is difficult for us to define a pore-stiffening contact cementation trend as clear as the Ontong Java Plateau chalk (Fabricius et al., 2008).

Pore-filling calcite cementation is reflected by increasing TTI values and a gradual decline in porosity as shown by Fig. 7b. It causes porosity reduction with nearly constant Terzaghi's effective stress (Fig. 6a, b). It may be equivalent to the diagenetic stage three of Grützner and Mienert (1999). It may also occur as a result of calcite pressure dissolution at stylolites (Fabricius et al., 2008) when vertical effective stress is greater than 5 MPa (Fig. 6a, b, d, e). In the Terzaghi's effective stress interval 5–10 MPa (Fig. 6a, d) porosity declines and P-wave velocity rapidly increases due to pore-filling calcite cementation which mainly stiffens the whole rock and significantly reduces the porosity.

Our porosity data showed a different cementation front (Fig. 6b) from that shown by Fabricius et al. (2008) from the Ontong Java Plateau chalk (i.e. green curve in Fig. 6a, b). We would suggest explaining this difference as that pore-filling calcite cementation in the studied Eocene chalk probably started earlier (i.e. at shallower depths) than that in the Ontong Java Plateau chalk. The reason why the pore-filling calcite cementation front of Fabricius et al. (2008) data does not fit our data could be due to the different temperature-gradients in the deep-sea sediments of western Pacific in comparison to the Atlantic Ocean. This interpretation is supported by the evidence obtained via Lopatin's TTI results (Table 4) that showed the temperature gradient of some of the investigated ODP sites is about 50 ^{o}C km^{-1}. However, none of the studied Eocene chalk reached the isotherm 50 ^{o}C, the maximum is about 47 ^{o}C at the ODP site 154-925A, and may be at the ODP site 165-999B as well (Fig. 3). Moreover, the evidence reported by Moutain et al. (1994) shows that calcite cement is dominant in the Eocene chalk section from 1105 mbsf at Site 150-903C. This also supports the above explanation because our data from ODP Sites 150-903C and 165-999B fall within our pore-filling calcite cementation zone.

In conclusion of this part, the porosity and P-wave velocity trends in Fig. 6c, f are adequate to assume that effective stress is most likely the main factor controlling porosity reduction at least at the compaction zone. Hence, we used the trends in Fig.

6c, f to derive predictive equations for porosity loss with burial depth (Table 3). If P-wave velocity data are available (e.g. from seismic data), the Eq. (11) in Table 3 could be applied to estimate Biot's effective stress which could be used in Eq. (8) (Table 3) to predict a reasonable approximation of porosity value. Eq. (11) is derived from the best possible fit of our P-wave velocity data through what we assumed to be compacted (shallower buried chalk) and pore-filling calcite cementation (deeper buried chalk) intervals. These equations could be relevant for basin analysis and hydrocarbon exploration in chalk, especially in deepwater basins where drilling is expensive. However, a question may arise, to which extend these equations are reliable. No further study is done to test their reliability, but it is remarkable that the porosity and sonic velocity data of the Atlantic chalk fall close to the effective stress trend defined in the Pacific Ontong Java Plateau chalk.

6.2. The influence of Lopatin's TTI on physical properties

The correlations of our P-wave velocity and porosity data with burial depth as represented by Lopatin's TTI of thermal maturity are illustrated by Fig. 7. The data showed a slow decrease in porosity from around 70% (near the seafloor, log TTI of about 0.002) to about 50% (at burial depth corresponding to log TTI of about 0.07). In the same interval, the P-wave velocity slowly increases from around 1500 to 2000 m s^{-1} (Fig. 7a). The porosity–log TTI relationship from this study does not agree with the porosity results of the study conducted by Schmoker (1984) on a range of carbonate sediments where he obtained a log-linear relationship between TTI and porosity. This may be because Schmoker (1984) used mixed data from carbonate sediments of different geological ages. However, we could define compaction and probably pore-filling calcite cementation trends from Fig. 7 in the same way as we did in the previous section as shown in Fig. 6a.

Due to the influence of pore-filling calcite cementation, we observed a gradual increase in P-wave velocity (from around 2000–4250 m s^{-1}) and a decrease in porosity (from 50–10%) at the depth interval corresponding to log TTI of about 0.07 and higher (Fig. 7a, b). A study of mineralogical composition of chalk done by X-ray diffraction (XRD) analysis on chalk samples from the Sites 165-999B, 165-1001A, 150-904A, and 150-603C shows a change in chalk mineralogy as opal-CT converted into quartz at a depth corresponding to log TTI of about 0.07 (see Mountain et al. 1994; Sigurdsson et al. 1997). The data from these four sites fall within what we interpreted as a pore-filling calcite cementation trend (between about 5–10 MPa Terzaghi's effective stress, Fig. 6a, b). The conversion of opal-CT to quartz is in accordance with the observation shown by Figure 12d of Fabricius et al. (2008) at the Ontong Java Plateau chalk in the Pacific. This agreement is supporting the hypothesis of Fabricius and Borre (2007) which proposed that the activation energy for pore-filling calcite cementation is associated with the transformation of opal-CT to quartz. In this process, calcium (Ca) is released from Ca–silica complexes in pore-water. The conversion of opal-CT to quartz is controlled by temperature, time, and properties of host sediment such as pore-water chemistry (e.g. Kastner, 1981; Williams and Crerar, 1985). Our conclusions are also in agreement with the results of Wetzel (1989) from DSDP Sites 504 and 505 that are located in the Pacific Ocean. He observed more calcite cement in chalk at Site 504 where the temperature is high and less cement in chalk at Site 505 where the temperature is low. Thus increasing temperature by progressive burial favours porosity occlusion by pore-filling calcite cementation mechanism.

Our study has several advantages over other studies in this area. First, we included data from many different locations that cover the entire study area which is larger than that in other similar studies. Second, we considered only the data that represent Eocene chalk to avoid any possible influence of sediment age on diagenesis of chalk that may be reflected on physical property depth trends. We correlated our data with two main physical property controlling factors such as effective stress and TTI rather than depth. The physical property depth trends for both controlling factors are supporting and confirming each other by telling the same story about the diagenesis of the studied Eocene chalk. The porosity–TTI relationships from this study were not used to derive predictive equations for porosity lost with burial depth, because this link is still controversial.

7. Conclusions

We related the changes of porosity and P-wave velocity with burial depth to both vertical effective stress and TTI of chalk. Terzaghi's effective stress underestimates the actual effective stress of cemented chalk, and this may cause severe engineering consequences. Therefore, it is more appropriate to use the Biot's concept to obtain more realistic vertical effective stress. Thus, we recommend using Biot's effective stress to predict porosity.

We proposed an equation that could be used to estimate Biot's vertical effective stress (from P-wave velocity data) which could be used to predict porosity (Table 3). To obtain Biot's vertical effective stress, the predictive Eq. (11) should be applied. The obtained effective stress could then be used in Eq. (8) to predict porosity. The proposed equation is relevant for basin analysis and hydrocarbon exploration in deep-sea chalk to predict porosity if the vertical effective stress on the chalk is known.

The porosity–effective stress trends from this study did not exactly follow the porosity trends for the Pacific Ontong Java Plateau chalk which spans a time interval from the Cretaceous to present. Our porosity data showed a broader porosity trend in the mechanical compaction zone, and the onset of the formation of limestone at a shallower burial depth than the porosity data of the Ontong Java Plateau chalk show. Porosity variations within the same effective stress may be due to variations in chalk texture.

Mechanical compaction is the principal cause of porosity reduction (at shallow depths) in the studied Eocene chalk, at least down to about 5 MPa Terzaghi's effective stress related to a porosity of about 35%. Within the compaction interval, deeply buried Eocene chalk is characterized by a slower, more linear rate of compaction than the shallowly buried Eocene chalk. Our porosity data do not show or at least it is difficult to define a clear pore-stiffening contact cementation trend as in the Ontong Java Plateau chalk.

We have also shown clear relationships between the Lopatin's TTI and the porosity as well as the P-wave velocity. This implies that increasing sediment temperature controls chalk diagenesis by activating energy for the pore-filling calcite cementation process which probably also requires pressure dissolution of calcite at stylolites.

6. Acknowledgements

Data used to produce this paper were collected by the Shipboard Scientific Parties during the ODP Legs 101, 113, 114, 150, 154, 160, 165, 171, 174, 207, and 208. We thank the ODP Shipboard Scientific Parties for making their data and information available for public use and hence for the production of this paper. We thank the anonymous reviewers for their constructive criticisms and valuable comments which improved our paper.

7. References

Alam, M.M., Borre, M.K., Fabricius, I.L. and Hedegaard, K. et al., 2010. Biot's coefficient as an indicator of strength and porosity reduction: Calcareous sediments from Kerguelen Plateau, Journal of Petroleum Science and Engineering, 70, 282-297.

Alam, M.M., Fabricius, I.L., Christensen, H. F., 2012. Static and dynamic effective stress coefficient of chalk, Geophysics. 77, 1-11.

Anselmetti, F.S., Eberli, G.P., 1993. Controls on sonic velocity in carbonates. *P*ure and Applied Geophysics, 141, 287-323.

Bassinot, F.C., Marsters, J.C., Mayer, L.A. and Wilkens, R.H., 1993. Variations of porosity in calcareous sediments from the Ontong Java Plateau. In: Berger, W.H., Kroenke, L.W., Mayer, L.A. et al. (Ed.), Proc. ODP, Sci. Results, 130. College Station, TX (Ocean Drilling Program), 653-661.

Biot, M.A.,1941. General theory of three-dimensional consolidation. J. Appl. Phys. 12, 155-164.

Biot, M.A., & Willis, D.G., 1957. The elastic coefficients of the theory of consolidation. J. Appl. Phys. Mechanics, 24, 594-601.

Blum, P., Xu, J., Donthireddy, S., 1996. Geotechnical properties of Pleistocene sediments from the New Jersey upper continental slope. In: Mountain, G.S., Miller, K.G., Blum, P., Poag, C.W. and Twichell, D.C. (Eds.), 1996. Proc. ODP, Sci. Results, 150. College Station, TX (Ocean Drilling Program), 377-384.

Borre, M.K., Fabricius, I.L., 1998. Chemical and mechanical processes during burial diagenesis of chalk: an interpretation based on specific surface data of deep-sea sediments. Sedimentology, 45, 755-769.

Brasher, J.E., Vagle, K.R., 1996. Influence of lithofacies and diagenesis on Norwegian North Sea chalk reservoirs. AAPG Bulletin, 80, 746-769.

Bryant, W.R., Rack, F.R., 1990. Consolidation characteristics of Weddell Sea sediments: results: results of ODP Leg 113. In: Barker, P.R, Kennett, J.P., et al., 1990. Proc. ODP, Sci. Results, 113: College Station, TX (Ocean Drilling Program), 211-223.

Burnham, A.K. and Sweeney, J. J., 1989. A chemical kinetic of vitrinite maturation and reflectance. Geochimica et Cosmochimica Acta, 53.10, 2649-2657.

Ciesielski, P.F., Kristoffersen, Y. et al., 1991. Proc. ODP, Sci. Results, 114: College Station, TX (Ocean Drilling Program).

Fabricius, I.L., 2000. Interpretation of burial history and rebound from loading experiments and the occurrence of microstylolites in the mixed sediments of the Caribbean Sites 999 and 1001: Proc. ODP, Sci. Results, 165, 177-190.

Fabricius, I.L. 2003. How burial diagenesis of chalk sediments controls sonic velocity and porosity. AAPG Bulletin, 87, 1755-1778.

Fabricius, I.L., Borre, M.K., 2007. Stylolites, porosity, depositional texture, and silicates in chalk facies sediments, Ontong Java Plateau – Gorm and Tyra fields, North Sea. Sedimentology, 54, 183-205.

Fabricius, I.L., Gommesen, L., Krogsbøll, A. and Olsen, D. 2008. Chalk porosity and sonic velocity versus burial depth: influence of fluid pressure, hydrocarbons, and mineralogy. AAPG Bulletin, 92, 201-223.

Fjær, E., Holt, R.M., Horsrud, P., Raaen, A.M. and Risnes, R., 1992. Petroleum related rock mechanics. Amsterdam, Elsevier, Development in Petroleum Science, 33. 338.

Giles, M.R., Indrelid, S.L. and James, D.M.D., 1998. Compaction – the great unknown in basin modelling. Geological Society, London, Special Publications 141.1: 15-43.

Grützner, J., Mienert, J., 1999. Physical property changes as a monitor of pelagic carbonate diagenesis: an empirically derived diagenetic model for Atlantic Ocean basins. AAPG Bulletin, 83, 1485-1501.

Hamilton, E.L., 1974. Prediction of deep-sea sediment properties: state of the art. In: Inderbitzen, A.L. (ed.) Deep-Sea Sediments, Physical and Mechanical Properties. New York, Plenum Press, 1-43.

Hamilton, E.L., 1976. Variations of density and porosity with depth in deep-sea sediments. J. Sediment. Petrol. 46, 280-300.

Hamilton, E.L., 1980. Geoaeoustic Modeling of the Sea-floor, Journal of Acoustical Society of America, 68, 1313-1340.

Janus Web Database (http://iodp.tamu.edu/janusweb/links/links_all.shtml). Accessed date: November 6th, 2008.

Japsen, P., 1993. Influence of lithology and Neogene Uplift on seismic velocities in Denmark: Implications for depth conversion of maps.AAPG Bull, **77**, 194-211.

Jones, M.E., Bedford, J., Clayton, C.J., 1984. On natural deformation mechanisms in the chalk. Journal of the Geological Society, London, 141, 675-683.

Kastner, M., 1981. Authigenic silicates in deep-sea sediments: formation and diagenesis. In: Emiliani, C. (ed.): The oceanic lithosphere, Sea **7**, 915-980. John Wiley and Sons, New York.

Lind, I.L., 1993. Loading experiments on carbonate ooze and chalk from Leg 130, Ontong Java Plateau. In: Berger, W. H., Kroenke, L. W., Mayer, L. A. (eds.): Proc.ODP, Sci. Results, 130, 673-686.

Maliva, R.G., Dickson, J.A.D., 1992. Microfacies and diagenetic controls of porosity in Cretaceous/Tertiary chalks, Eldfisk field, Norwegian North Sea. AAPG Bulletin, 76, 1825-1838.

Mallon, A.J., Swarbrick, R.E., 2002. A compaction trend for non-reservoir North Sea Chalk. Marine and Petroleum Geology, 19, 527-539.

Matter, A., Douglas, R.G., Perch –Nielsen, K., 1975. Fossil preservation, geochemistry and diagenesis of pelagic carbonates from Shatsky Rise, northwest Pacific. In: Larson , R.L. et al.(eds*)*, Initial Reports of Deep-Sea Drilling Project: Washington, D.C., U.S., Government Printing Office, 32, 891-922.

Mavko, G., Mukerji, T., Dvorkin, J., 1998. The Rock Physics Handbook. The Press Syndicate of the University of Cambridge. Cambridge, UK., 329 p.

Mazzullo, S.J., Meyer, A., Kidd, R., 1988. New sediment classification scheme for the Ocean Drilling Program. In: Mazzullo, S.J., Graham, A.G. (eds), Handbook for Shipboard Sedimentologists: Texas A&M University, Ocean Drilling Program, Technical Note, 8**,** 45-67.

Mountain, G.S., Miller, K.G., Blum, P. et al., 1994. Proceedings of the Ocean Drilling Program. Initial Reports, 150: College Station, TX (Ocean Drilling Program).

Nur, A., Byerlee, J.D., 1971. An exact effective stress law for elastic deformation of rocks with fluids. Journal of Geophysical Research, 76, 6414-6419.

O'Regan, M., Moran, K., 2007. Compressibility, permeability, and stress history of sediments from Demerara Rise. In: Mosher, D.C., Erbacher, J., Malone, M.J. (Eds.), Proc. ODP, Sci. Results, 207: College Station, TX (Ocean Drilling Program), 1-35.

Øxnevad, I.E. I., Meshri, I.D., 1997. Porosity evolution in chalks: crestal Valhall and flank areas. 59th EAGE, Conference Technical Exhibition, extended abstracts book, 552.

Pettijohn, F.J., 1975. Sedimentary Rocks. Third Edition. Harper and Row, Publishers, New York, USA., 628 p.

Robertson, A.H.F., Emeis, K.C., Richter, C., Camerlenghi, A. (Eds.), 1998. Proc. ODP, Sci. Results, 160: College Station, TX (Ocean Drilling Program).

Schlanger, S.O., Douglas, R.G., 1974. The pelagic ooze-chalk-limestone transition and its implications for marine stratigraphy. In: Hsu, K.J., Jenkyns, H.C. (eds), Pelagic Sediments: On Land and Under the Sea. Special Publication of the International Association of Sedimentologists Special Publications, 1, 117-148.

Schmoker, J.W., 1984. Empirical relation between carbonate porosity and thermal maturity: An approach to regional porosity prediction: AAPG Bulletin, 68, 1697-1703.

Scholle, P.A., 1977. Chalk diagenesis and its relation to petroleum exploration: oil from chalks, a modern miracle? AAPG Bulletin, 61, 982-1009.

Sigurdsson, H., Leckie, R.M., Acton, G.D. et al., 1997. Proceedings of Ocean Drilling Program. Initial Reports, 165: College Station, TX (Ocean Drilling Program).

Terzaghi, K.V. 1923. Die Beziehungen zwischen Elastiztat und Innendruck. Mathematisch-Naturwissenschaftliche Klasse Abteilung 2A, 132, 105-124.

Waples, D.W., 1980. Time and temperature in petroleum formation: application of Lopatin's method to petroleum exploration: American Association of Petroleum Geologists Bulletin, 64, 916-926.

Wetzel, A. 1989. Influence of heat flow on ooze/chalk cementation: quantification from consolidation parameters in DSDP Sites 504 and 505 sediments. J. Sediment. Petrol. 59, 539-547.

Williams, L.A., Crerar, D.A., 1985. Silica diagenesis, II. General mechanisms. J. Sediment. Petrol. 55, 312–321.

II

Paper II

Petrophysical analysis of siliceous ooze sediments, Møre Basin, Norwegian Sea

Ahmed Awadalkarim, Morten K. Sørensen and Ida L. Fabricius

Manuscript submitted to Petrophysics

Petrophysical analysis of siliceous ooze sediments, Møre Basin, Norwegian Sea

Ahmed Awadalkarim[*1], Morten Kanne Sørensen[1] and Ida Lykke Fabricius[1]

[1]Center for Energy Resources Engineering, Department of Civil Engineering
Technical University of Denmark, Brovej, Building 118, 2800 Kgs. Lyngby, Denmark

[*]Corresponding author (email: asmama67@yahoo.com; ilfa@byg.dtu.dk)

Abstract

Pelagic siliceous ooze sediments occur above the hydrocarbon reservoir of the Ormen Lange gas field in Møre Basin, Norwegian Sea. A possible hydrocarbon prospect of siliceous ooze was proposed, but siliceous ooze is significantly different in texture from most commonly known reservoir rocks. Logging and core analysis data were integrated to characterize and evaluate these sediments. True density porosity was obtained by taking the number of electrons per unit volume of bulk siliceous ooze into account and it was calibrated to the overburden-corrected core porosity. Grain density log was calculated from gamma ray log and empirical grain density data calibrated with X-ray diffraction analysis data. The grain density log was used with the calculated true porosity log and the brine density of 1.025 g/cm^3 to convert the bulk density log from conventional limestone and water scaling of electron density to opal and brine scaling of electron density.

The neutron porosity log was corrected for the hydrogen index contribution of solid phase. The corrected neutron porosity is lower than the conventional neutron porosity by about 3 to 4 porosity units. The true density porosity and the corrected neutron porosity are similar. This indicates that our interpretation is consistent, such that it can be applied elsewhere. The studied sediments apparently do not contain hydrocarbons.

The relatively low Biot's coefficient, of about 0. 94 on average, indicates that the siliceous ooze is relatively stiff. Amplitude versus offset analysis indicated that an oil saturated sandstone layer can be distinguished from water saturated siliceous ooze.

Keywords:
Logging, Petrophysics, Opal, Siliceous ooze, Diatomite, Biot's coefficient, AVO.

1. Introduction

Diatoms and radiolarians are planktonic microscopic algae with siliceous skeletons. Through compaction and lithification, skeletal remains of siliceous algae and sponge spicules form biogenic-rich fine-grained highly porous pelagic siliceous ooze deposits, which comprise amorphous hydrous opaline silica. Diatomite, which is formed mainly from diatom remnants, is a well known example of siliceous ooze that can be distinguished from chalk by a lack of effervescence when tested with dilute hydrochloric acid. Burial diagenesis of siliceous ooze involves textural and mineralogical changes. Major controls of burial diagenesis are temperature and time (Kastner 1979).

Zones of clean pelagic siliceous ooze sediments are reported by the Deep Sea Drilling Program (Leg 38) and by the Ocean Drilling Program (Leg 104) in the outer Vøring Plateau (Talwani *et al.* 1976; Eldholm *et al.* 1987). Siliceous ooze is also assumed to occur along the Norwegian west coast (Dalland *et al.* 1988). Pelagic siliceous ooze intervals of Eocene to Mid Miocene occur above the reservoir of the Ormen Lange gas field which is located in the Møre Basin deep-water area (the water depth varies from about 800 m to about 1100 m) in the southern part of the Norwegian Sea (Fig. 1). It is the second largest gas field in Norway. The main gas reservoir is the Palaeocene "Egga" sandstone of the Våle Formation (NPD). The siliceous ooze intervals have been interpreted in drilling reports as siltstones and mudstones based on the descriptions of drilling cuttings and core material, measurement while drilling (MWD) logs and drilling parameters. But the very high porosity and extremely low bulk density of these intervals with respect to the burial depth and the departure from the normal compaction trend of shale suggest that they are siliceous ooze sediments (Awadalkarim and Fabricius 2009, 2012). Our interpretation was supported by petrographical and mineralogical analyses of the siliceous ooze core material which has qualitatively proved the presence of diatomaceous facies. The occurrence of diatomaceous Mid Miocene siliceous ooze is common worldwide and no special conditions unique to the Ormen Lange area are needed to explain this occurrence.

The siliceous ooze sediments (intervals) of the Ormen Lange area are known in Norway as Brygge Formation (NPD) which was the target for this study. We informally divided it here into two units: 1) an upper opal-A dominated siliceous ooze interval which is characterized as having exceptionally high porosity (but very low permeability), extremely low bulk density, low natural gamma ray (GR) log and very high sonic interval travel time (Δt); 2) a lower opal-CT dominated interval which is typified by a relative increase in bulk density and a decrease in Δt (i.e. high velocity) as shown by the sonic log. Other logs (gamma ray, resistivity and neutron) do not show characteristic changes. The contact between the two units forms a regional seismic reflector with medium amplitude and high continuity, which is believed to represent a diagenetic event of opal-A transformation, at shallow burial depth, into to opal-CT below a critical depth (Keller and Isaacs 1985). At the contact, opal-A undergoes a phase transition into opal-CT, where the formation temperature is expected to reach about 43^{o} C (110^{o} F) (Bilodeau 1995; Keller and Isaacs 1985). In this paper, we focus on the opal-A siliceous ooze interval where core material was extracted and the relevant core data are available to calibrate our results.

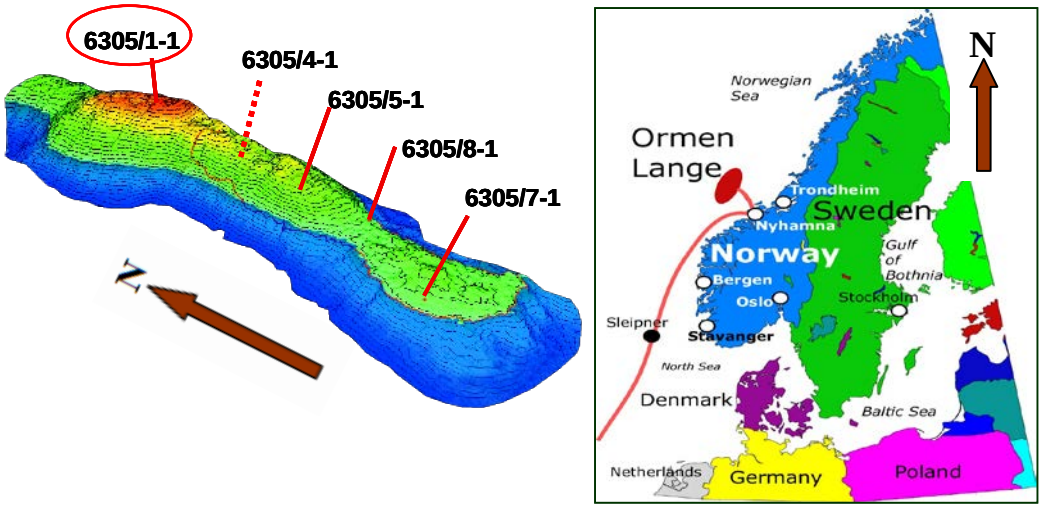

Figure 1 Location map of the Ormen Lange Field (right), not to the scale, (The source is: http://www.rigzone.com/news/image_detail.asp?img_id=317). The four wells included in this study are shown to the left figure on the North-South trending doubly plunging anticline with two structural highs (The source is Norwegian Petroleum Directorate (NPD): http://www.npd.no). The well 6305/1-1 was excluded from this study because it was included in another study by Awadalkarim and Fabricius (2009).

A possible hydrocarbon prospect of siliceous ooze sediments has been proposed (NPD), but these sediments are significantly different in texture from most commonly known hydrocarbon reservoir rocks. For instance, the pore structure is complex and the solids are mechanically fragile and hydrous. Therefore, we need electron microscopy to inspect pore structure. Due to the unique nature of siliceous ooze, interpretation of petrophysical logs obtained through siliceous ooze-rich intervals is not straight forward. The problem is that the biogenic silica starts as low-density amorphous opal-A ($SiO_2.nH_2O$) which is relatively rich in the water of hydration, structural water, (nH_2O with n about 0.121) that represents one of the most fundamental attributes of opal-A. During burial diagenesis, opal-A transforms into denser crystalline opal-CT ($SiO_2.nH_2O$, with reduced n) which still contains some water of hydration before further dehydration transforms it into microcrystalline quartz (SiO_2), (Kastner 1979). A further complication is that the opal is often mixed with clay (Pedersen *et al.* 2004) and possibly organic matter. Most published studies on petrophysical analysis of siliceous sediments (e.g. diatomite) are focussed, for instance, on the Miocene Monterey diatomite Formation and on the diatomite of the Lost Hills field in California (Stosur and David 1976; Zalan *et al.* 1998), but siliceous ooze is also found in the Cenozoic sequence in the North Sea Basin in the Norwegian (NPD) and Danish sectors (Thomsen and Danielsen 1995).

Normal petrophysical methods used in formation evaluation might not be suitable for interpreting siliceous ooze. For example, the density and neutron logging tools are calibrated in freshwater saturated pure limestone to give correct porosity readings in a limestone formation, but apparent porosity indications in any other lithology, such as siliceous ooze, should be corrected (Glover 2012). The apparent bulk density and the neutron porosity logging tools are influenced by the hydrogen in opal structure because they are sensitive to the amount of hydrogen in a formation and less to other elements. Grain density is a main challenge when deriving porosity from a bulk

density log acquired through siliceous ooze intervals, because the grain density is very low and variable, depending on the amounts of opal content and the structural water in opal, which has an impact on density porosity calculation. For example, the grain density of the Lost Hills diatomite in California ranges from 1.73–2.30 g/cm^3 (Stosur and David 1976). If a constant grain density is used to calculate density porosity of siliceous ooze, the obtained porosity is inaccurate. Neutron logging tools measure the hydrogen index (HI) of a formation which is primarily related to fluids in the porosity. It is normally assumed that the contribution to the neutron porosity measurement comes entirely from the hydrogen in fluids fully occupying the pore space, but, elements other than hydrogen that constitute the rock matrix do contribute to the signal. Some minerals of siliceous ooze, such as opal, have hydrogen in their structures which has a high influence in the measured HI. The neutron tool obtains the combined signal of the HI of the solid phase and of the water that occupies the true porosity. The HI is equal to true porosity for completely freshwater saturated limestone. In this study, we considered all the possible contributions to the neutron porosity measurement. Therefore, we took into account the moderating power (the slowing down power) of all minerals that were identified by the X-ray diffraction (XRD) analysis of siliceous ooze core material.

In this study, we aimed to develop and use a new procedure to analyse and interpret logging data acquired through siliceous ooze intervals. Our main objectives were to characterize and evaluate the petrophysics of siliceous ooze sediments and to find the correct grain density and true porosity of siliceous ooze sediments. From geophysical (seismic) data, water bearing siliceous ooze can be mistaken for highly porous oil bearing sandstone. This may mislead explorationists to locate and drill an exploration well in water bearing siliceous ooze interval as they may think that it is an oil bearing sandstone reservoir. Therefore, our secondary objective was to find and observe the amplitude versus offset (AVO) signature of water saturated siliceous ooze to establish if it is distinguishable from oil bearing sandstone. This may enable explorationists to avoid locating a dry exploration well in a water saturated siliceous ooze interval. All these objectives have similar priorities and to achieve them we used and integrated high quality conventional core analysis data of opal-A siliceous ooze core material with logging data from four Ormen Lange wells (Table 1 and Fig. 1), and included XRD data. Additionally, available information and data such as total organic content (TOC), carbonate content (CC), backscatter electron micrographs (BSEM), together with the geological description of the drilling cuttings, drilling records and parameters, and other published data were used here to help interpreting lithology and the unusual physical properties of the studied siliceous ooze intervals. The integration of all these data has enabled a consistent interpretation to be made and revealed that the investigated siliceous ooze sediment is a mixture of opal and non-opal (shale) at variable ratios. It consists mainly of extremely fine-grained diatomaceous ooze with well-preserved opal-A frustules. Our new approach allowed determination of volume fractions of opal and non-opal components which were used with the empirical grain densities for opal and non-opal to calculate the grain density logs through the studied intervals. Consequently, the apparent density porosity was obtained based on the calculated grain density log and the wireline apparent bulk density data, whereas the true porosity was calculated by taking the number of electrons per unit volume into account. We also corrected the neutron porosity log for the hydrogen index contribution from the solid phase. Our results proved to be reasonably consistent. The studied intervals apparently do not contain hydrocarbons.

Table 1 Summary of general well data. The wells used in this study are all close to vertical, and where not otherwise stated, depths are given in meters with reference to Rotary Kelly Bushing (m RKB). Depths to the tops of the different formations are based on the logging data and on the information provided by the Norwegian Petroleum Directorate (2012) fact pages (www.npd-no). MSL is mean sea level

		6305/1-1	6305/4-1	6305/5-1	6305/7-1	6305/8-1
	Well type	**Exploration**	**Appraisal**	**Exploration**	**Appraisal**	**Appraisal**
	Well content	Dry well	Gas	Gas	Gas	Oil and gas
	Kelly Bushing elevation above MSL (m)	24	25	26	26	25
	Water depth (m MSL)	840	1002	889	857	837
	Total depth logger (m RKB)	4560	2975	3053	3377	3175
	Total depth driller (TD), (m RKB)	4546	2974	3053	3377	3175
	Free water level (m MSL)	-	2786	2789	2913	2899
	Maximum inclination (°)	-	5.75	13	1.6	1.7
	Formation temperature at TD (°C)	-	96.1	81	90	90
	Assumed seafloor temperature (°C)		-1.8	-2	-2	-1.8
	Temperature gradient (°C/100 mTVD)	4.6	4.84		4.33	4.6
	Borehole diameter in ooze interval (inches)	12.25	12.25	12.25	12.25	12.25
	Drilling mud type (water based mud, WBM)	WBM	WBM [1)]	WBM [1)]	WBM [2)]	WBM
	Drilling mud weight (g/cm^3)	1.36	1.30	1.30	1.30	1.30
	Available drilling cuttings intervals at NPD (m)	1620 - 4555	1780 - 2961	1550 - 3055	1710 - 3377	1560 - 3175
	Siliceous ooze core interval (m) for this study	-	1761 - 1779	-	-	-
Top Norland Gp.[4)]	Top Naust Formation (m)	863	1027	914	883	862
	Top Kai Formation (m)	1703	1662	1642	1503	1591
Top Hordaland Gp.[4)]	Top Brygge (siliceous ooze) Formation (m)[3)]	**1740**	**1701**	**1664**	**1529**	**1745**
	Top Opal-CT (m RKB)	**1895**	**1988**	**1933**	**1922**	**1993**
Top Rogaland Gp.[4)]	Top Tare (Balder) Formation (m)	2172	2394	2327	2562	2508
	Top Tang (Sele) Formation (m)	2355	2529	2446	2657	2596
	Top Egga (Vâle) Formation (Reservoir) (m)	2558	2769	2551	2911	2898
Top Shetland Gp.[4)]	Top Jorsalfare (Spring) Formation (m)	2606	2829	2780	2992	2976
	Top Nise (Kyrre) Formation (m)	2827	2880	2841	3377	3132
	Top Kvitnos Formation (m)	3048		3053		
	Opal-CT seismic interval velocity (m/s)	1842	2000		2030	2000
	Opal-CT VSP/seismic TWT[5)] (ms)	2258 (± 15)	2316 (± 3)	2221 (± 7)	2214 (± 5)	2298 (± 6)

[1)] Water based KCl polymer mud.
[2)] Water based NaCl/KCl polymer mud.
[3)] Opal-A dominated siliceous ooze.
[4)] Gp. is group.
[5)] TWT is two way time.

2. Material, data and methods

This study was based on data from conventional core analysis, mineralogical and petrographical analyses, and petrophysical well logs. The well data are in the public domain at www.npd.no. The results we have obtained include opal and non-opal volume fraction logs, grain density log, the amount of water of hydration in opal structure log, true density porosity and true neutron porosity logs, Biot's coefficient for elastic deformation (β) and AVO analysis. All the four wells we used in this study are close to vertical. All references to depth here (in text, tables and figures) are driller's measured depth along wellbore in metres referring to Rotary Kelly Bushing elevation (m RKB).

2.1. Petrophysical borehole logs

The 12¼ inch (12.25") borehole sections in the four wells included in this study were drilled using 1.30 g/cm^3 water-based drilling mud (WBM) system (Table 1). The suite of the wireline logs run in the 12.25" borehole sections were performed by Schlumberger using 'modern technology logging tools' such as Platform Express (PEX) tool string. The well logs used here include calliper, GR, bulk density, sonic (compressional and shear wave velocities), neutron porosity (thermal neutron is excluded), and resistivity logs. The quality of the logging data we used here was good, with the exception of the neutron log in the well 6305/7-1 where extremely high siliceous ooze porosity and borehole rugosity caused some spikes in the data. Corrections were applied to enable the data to be presented as neutron porosity. The resistivity logs were environmentally and mud-filtrate invasion corrected in real time.

The density log was corrected for bit size; the neutron log was corrected for borehole size, borehole and formation salinities, mud weight, mud cake, temperature and pressure. The sonic log quality was good and no correction has been applied. These data corrections were applied during data acquisition. No additional correction was made by us. Mud logs were also used here to help interpreting lithology and to see if any gas show was detected during drillings. For more information about the logging data we have included here, please refer to the NPD fact pages at www.npd.no. For more information about any of the above mentioned logs or logging tools please refer to the website of Schlumberger at: http://www.slb.com.

2.2. Calculated and modelled data

The studied siliceous ooze is a mixture of opal and non-opal (shale). It is modelled here as a mixture of water, opal and non-opal minerals as identified by XRD. We assumed that both opal and water are non-radioactive and give no GR response. We also ignored mud filtrate (KCl mud) effect as it is a minor one. Thus, the GR log response of the studied siliceous ooze is due to the contributions from the non-opal minerals (shale) only.

2.2.1. Calculation of opal volume fraction and grain density logs

The average (arithmetic mean) core grain density of ten core plugs from about 10 m core material of opal-A dominated siliceous ooze was obtained and denoted as ($\rho_{g\text{-}core}$) g/cm^3. From the XRD analysis information, we calculated the average grain density of non-opal minerals (shale content) and denoted as (ρ_{g_rest}) g/cm^3. Before obtaining the ρ_{g_rest}, the grain density (ρ_g) of each individual non-opal mineral was obtained from the literatures and normalized to its weight percentage in the bulk siliceous ooze as obtained by XRD analysis. The content of pyrite is variable and since its grain density is high (~4.99 g/cm^3), this may produce a potential error in the estimated average grain density of non-opal component. An average grain density of 2.78 g/cm^3 for non-opal (shale) was obtained from ten data points. We used the grain density of 2.16 g/cm^3 for opal-A ($\rho_{g\_opal\ A}$), according to Serra (1984). Opal-A grain density ranging from 1.5 to 2.3 g/cm^3 is reported in literature (e.g. Herdianita *et al.* 2000).

The volume fractions of opal and non-opal in the analysed siliceous ooze core material were not obtained form XRD analysis. Since the average core grain density is known, the relative volume fractions of opal and non-opal in the bulk siliceous ooze were calculated as following (by assuming opal volume fraction is *x*, and non-opal is 1-*x*.):

$$\rho_{g\_core} = \left(\rho_{g\_opal\,A}\right)\cdot x + \left(\rho_{g\_rest}\right)\cdot\left(1-x\right) \qquad (1)$$

By substituting the values of $\rho_{g\text{-}core}$, $\rho_{g\_opal\ A}$, and ρ_{g_rest} g/cm^3 and solving for *x*, we found that $x = 0.57$ (i.e. volume fraction of opal is 57% and of non-opal is 43%).

Based on this fixed data point for calibration, we calculated the volume fraction logs of non-opal and opal through the entire opal-A dominated siliceous ooze intervals from the GR log as follows:

$$Volume\ of\ non{-}opal\ component = \frac{GR_{\log} - GR_{\min}}{GR_{\max} - GR_{\min}} \qquad (2)$$

where GR_{log}, GR_{min} and GR_{max} are wireline, minimum and maximum GR log responses, respectively.

The opal volume fraction, only in opal-A dominated siliceous ooze interval, was obtained by subtracting the above calculated non-opal volume fraction from one. Then the grain density log was calculated as following:

$$\rho_{g\_calcu} = \left(\rho_{g\_opal\ A}\right) \cdot x + \left(\rho_{g\_rest}\right) \cdot (1 - x) \qquad (3)$$

where x and (1-x) are volume fraction logs of opal and non-opal, respectively (as calculated by equation (2).

The calculated grain density log was correlated with the core grain density. Based on the calculated grain density log and the measured bulk density log data, the apparent density porosity can be obtained. The true density porosity was calculated by taking into account the number of electrons per unit volume (electron density) of the bulk siliceous ooze. We calibrated it to the overburden corrected core porosity (total porosity), and then it was compared with the apparent density porosity. The overburden stress correction was done by applying a relationship between porosity and uniaxial compressibility that was obtained from the wireline compressional wave velocity and the bulk density logging data. The overburden correction was done to overcome the amount of elastic rebound (i.e. increase in volume) that has occurred after the removal of the core material from overburden stress in the borehole. To obtain the log of the number of electrons per unit volume (electron density) of the bulk siliceous ooze, we calculated the number of electrons in both fluid that occupies porosity and solid (opal-A and non-opal components) phases. Before calculating the number of electrons in opal-A, we searched the literature to see if we could establish a reliable relationship between the grain density and amount of hydrated water in opal structure. This relationship may be helpful in selecting and defining the correct amount of structural water in opal-A, and the corresponding grain density of opal-A.

2.2.2. The relationship between opal structural water content and grain density

Structural (bound) water content is the mass of water in a sample expressed as a percentage of mass of solids. Authors have used several different methods to determine water content. For instance, Graetsch and Ibel (1997) used coulometric Karl Fischer titration and near infrared absorption spectroscopy using plane polished plates (cf. Langer and Flörke 1974). They found that diatomite contains 1–10 wt. % water. Herdianita *et al.* (2000) obtained water content of opal by oven drying at <110^{o} C (i.e. standard Courville-Penfield-determined water) and by the thermogravimetric analysis (TG), whereas other authors (e.g. Day and Jones 2008) used electron microprobe (EMP) and micro-Fourier transform infrared (FTIR) analyses of opal. Jones and Renaut 2004 (and references herein) estimated the amount of water in precious and natural opal to be in the range of 1.5–15.3 wt. %. Day and Jones 2008 reported that opal-A contains 2.1–12.1 (average 7.3) wt. % total water whereas opal-CT contains 1.0–8.9 (average 5.5) wt. % total water. Herdianita *et al.* 2000 found opal-A grain density of 1.5–2.1 g/cm^3, and total water of 4–10 wt. %. They also found that when opal-A transforms into opal-CT, the total water content drops to <7 wt. % and grain density increases to ~ 2.3 g/cm^3. It is important to note that the ranges for the total water content of opal-A and opal-CT overlap with each other (Jones and

Renaut 2004). Based on the available data, we did not obtain a significant correlation that could be used in the present study (Fig. 2).

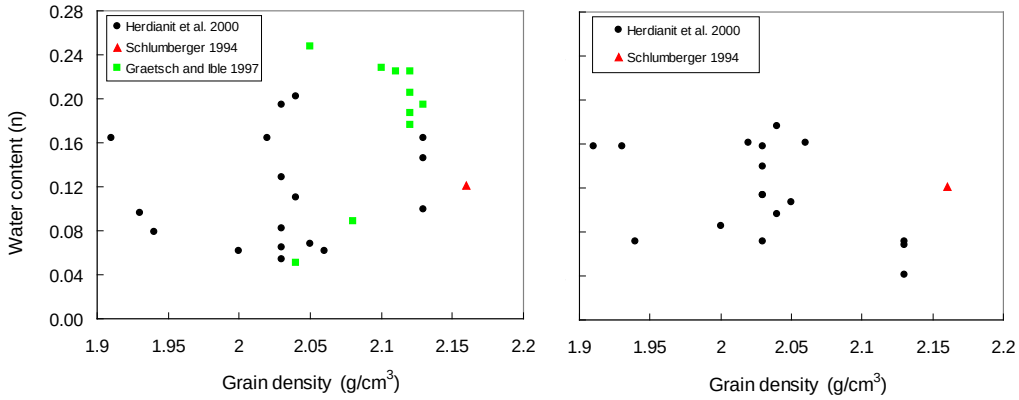

Figure 2 Water content versus grain density of opal-A. Opal water content is expressed as a number of water molecules (*n*) in opal structure ($SiO_2.nH_2O$). (**a**) the water content obtained at temperature less than100^o C; and (**b**) the water content obtained at temperature greater than 100^o C.

2.2.3. Calculation of structural water electron density and true porosity of opal-A
To calculate the number of electrons per unit volume (electron density) of opal-A, we used a true grain density and opal structural water content of 2.16 g/cm^3 and 3.5 wt. %, respectively (Schlumberger 1994, Serra 1984). This value of water content is within the range of 1.2–5.8 wt. % values that Grange (1937); and Nicholson and Parker (1990) obtained for opal. This is also in agreement with the range of total water content in opal-A as reported by Day and Jones (2008). The number of moles of water, *n*, in opal structure ($SiO_2.nH_2O$) was calculated as follows:

$$n = \frac{60.09\, f}{18.02(1-f)} \tag{4}$$

where *n* is the moles of water (H_2O) in the opal structure, *f* is the opal structural water content, in fraction (i.e. *f* = 0. 035), the 60.09 and 18.02 are the molar mass of silica (SiO_2) and water (H_2O) in g/mol, respectively, (Table 2). In the present case of *f* = 0.035, we obtained *n* = 0.121.

The number of electrons per cubic centimetre (cm^3) of opal-A was calculated as follows:

$$\text{The number of electrons per cm}^3 = \frac{\left(\rho_{g\_opal\ A}\right)}{\left(60.09+18.02n\right)} \times \left(30+10n\right) \times N_A \tag{5}$$

where $\rho_{g\_opal\ A}$ = 2.16 g/cm^3; *n* = 0.121; 30 and 10 are number of electrons per formula unit of silica (SiO_2) and water (H_2O), respectively. N_A is Avogadro's number = 6.02214x10^{23} mol^{-1}.

By using the same concept, we have calculated the number of electrons per cubic centimetre (electron density) of each component (mineral) listed in Table 2. To calculate the number of electrons per cubic centimetre of non-opal component, the calculated number of electrons per cubic centimetre of each non-opal mineral was

multiplied by its volume fraction in the non-opal component and summed up together. Now the sum of the number of electrons per cubic centimetre of opal and non-opal components is known, and it represents the electrons density in the solid phase, *c*, that we used in equation (6), where the true density porosity was obtained as follows:

$$\phi_{true} = \frac{a - c}{b - c} \tag{6}$$

where *a* is the bulk electron density log when the density logging tool is calibrated to calcite matrix; *b* is the electrons density log of water occupies the true porosity, and *c* is the electrons density log of the solid phase.

The calculated true density porosity log was correlated with the overburden corrected core porosity (to test its reliability), and then used with the calculated grain density log and the estimated nominal pore-fluid (brine) density (ρ_f = 1.025 g/cm^3) to calculate the true bulk density (ρ_{b_corct}) log as follows:

$$\rho_{b\_corct} = \left((1 - \phi_{true}) * \rho_{g\_calcu}\right) + \left(\rho_f * \phi_{true}\right) \tag{7}$$

We also used a simpler approach where the apparent density porosity log ($\phi_{\_Density}$) was obtained by equation (8) assuming that our lithology is sandstone. This is done based on quartz grain density and the apparent bulk density log as measured by the density tool.

$$\phi_{\_Density} = \frac{\rho_g - \rho_b}{\rho_g - \rho_{fl}} \tag{8}$$

where $\phi_{\_Density}$ is the apparent density porosity; ρ_g is quartz grain density (= 2.65 g/cm^3); ρ_b is the apparent bulk density; and ρ_{fl} is the pore-fluid (brine) density (= 1.025 g/cm^3).

2.2.4. Hydrogen index and correction of wireline neutron log response

A neutron porosity log is equivalent to a HI log as function of depth. Certain minerals, such as opal and clay, contain hydrogen in their crystal lattice. Although this hydrogen is not associated with porosity, it is nevertheless counted by the neutron tool. Neutron tools respond to all the hydrogen in a formation, even if some of this hydrogen is not associated with porosity, such as bound water associated with shale and opal. It is not only hydrogen that affects the passage of neutrons in a formation. Other elements have an effect on slowing down of neutrons in a formation, but their effect is small compared with that of hydrogen (Glover 2012). It is obvious that siliceous ooze has an influence on the measurement of HI. Thus, the simplistic HI concept no longer describes the situation here adequately. In this study, we estimated the true neutron porosity of siliceous ooze that has hydrogen in the structures of some of its minerals such as opal and clays. The slowing down power (which is equivalent to HI) of each mineral in the bulk siliceous ooze was also taken into account.

The neutron tool reads the combined signal of the HI of the solid phase and of the water (H_2O) that occupies the true porosity. For fully freshwater-saturated pure limestone (100% calcite), the HI is equal to the neutron porosity as measured by the

logging tool (Serra 1984). Here, since our neutron tool is calibrated into freshwater-saturated pure limestone, we calculated the HI log as function of depth (by including the calculated equivalent HI of calcite equal to 0.113 as reported in Table 3) as following:

$$HI_{Log} = (\phi_n) \times (HI_{water}) + (1 - \phi_n) \times (HI_{calcite}) \quad = \quad (\phi_n \times 1) + (1 - \phi_n) \times 0.113 \qquad (9)$$

where ϕ_n is the neutron porosity of a formation as measured by the neutron logging tool when calibrated with calcite matrix; 1 and 0.113 are the HI for water, HI_{water}, (H_2O) and calcite ($CaCO_3$), respectively.

Table 2 Parameters used for calculation of the number of electrons per unit volume of the bulk siliceous ooze sediment. All these components, except calcite, constitute the bulk siliceous ooze

Components	Formula	Density (g/cm^3)	Molar mass (g/mol)	Moles/cm^3	Electrons/ formula unit	Electrons per cm^3 of mineral
Water	H_2O	1.00	18.02	0.05551	10	3.34281×10^{23}
Calcite	$CaCO_3$	2.71	100.0	0.02710	50	8.15981×10^{23}
Opal-A	$SiO_2.nH_2O$	2.16	62.30	0.034688	31.21	6.51928×10^{23}
Quartz	SiO_2	2.65	60.09	0.04410	30	7.94904×10^{23}
Kaolinite[1)]		2.52	516.70	0.00488	260	7.67203×10^{23}
Illite[2)]		2.79	787.90	0.00354	399	8.40972×10^{23}
Smectite[3)]		2.79	746.90	0.00374	552	12.29933×10^{23}
K-feldspar	$KAlSi_3O_8$	2.52	278.40	0.00905	139	7.57538×10^{23}
Plagioclase	$NaAlSi_3O_8$	2.59	262.20	0.00988	131	7.79415×10^{23}
Pyrite	FeS_2	4.99	120.00	0.04158	60	15.02369×10^{23}

Kaolinite[1)]: $(Al_{3.64},Fe_{0.07})(Si_{4.05},Ti_{0.1})O_{10}(OH)_8$
Illite[2)] 1: $(Ca_{0.02},Na_{0.04},K_{0.86})(Al_{2.75},Fe_{1.18},Mg_{0.08})(Si_{6.98},Ti_{0.13},Al_{0.89})O_{20}(OH)_4(H_2O)_{1,60}$
Illite[2)] 2: $(Ca_{0.1},Na_{0.18},K_{0.92})(Al_{2.94},Fe_{0.64},Mg_{0.38})(Si_{7.00},Ti_{0.08},Al_{0.92})O_{20}(OH)_4(H_2O)_{0.20}$
Smectite[3)]: $Ca_{0.05},Na_{0.23},K_{0.13})(Al_{3.36},Fe_{0.68},Mg_{0.86})(Si_{7.83},Ti_{0.04},Al_{0.13})O_{20}(OH)_4(H_2O)_{16.622}$
Note: the grain densities and chemical structures of kaolonite, illite and smectite used here are based on Table 6.2 of Kurniawan (2005), (after Brindley, 1951). The 2.79 g/cm^3 for illite is the average of the grain densities of illite structure 1 and illite structure 2. The grain density of K-feldspar (orthoclase), plagioclase (albite) and pyrite were obtained from Serra (1984). These grain densities are a bit lower than those reported on Table 6.1 of Hearst et al. (2000). We assume n = 0.121 in opal-A (Schlumberger 1994 and Serra 1984).

We obtained the neutron slowing down powers (i.e. HI values) of H, C, O, Si, Cl and Ca elements from Fig. 8-2 of Serra (1984). For the rest of the elements in Table 3, we used the equation 6.75 of Hearst *et al*. (2000) to calculate the average logarithmic energy decrement or what is called by Serra (1984) as energy lost per collision, ξ. When we compared the calculated ξ of each element with its relative neutron slowing down power as reported by Serra (1984), we found that they are equivalent, (please compare the HI and ξ of the 6 elements mentioned above and reported in the last two right-hand columns of Table 3).

Here, the above calculated HI log (Equation (9)) is related to the true neutron porosity of siliceous ooze as shown below:

$$HI_{Log} = \left(\phi_{n\_true}\right) \times \left(HI_{water}\right) + \left(1 - \phi_{n\_true}\right) \times \left(HI_{Solid}\right) \quad (10)$$

Table 3 Neutron content and the slowing down power of the principal elements, and the related energy lost per collision (ξ) used in the calculation of the hydrogen index (HI) of the compounds in Table 4 (Serra 1984)

Element	Atomic Number (Z)	Atomic mass (A) (g/mol)	Number of neutrons	Energy[1)] (MeV)	Energy lost[2)] (%)	Slowing down power[3)] (MeV)	HI[4)]	ξ
H	1	1.008	0.008	2.23	50	18	1	1
C	6	12.000	6.000	4.95	14	114	0.158	0.158
O	8	16.000	8.000		11	150	0.120	0.120
Si	14	28.090	14.090	6.40	6	257	0.070	0.070
Cl	17	35.000	18.000	7.77	5	329	0.055	0.055
Ca	20	40.070	20.070	6.42	4	368	0.049	0.049
Al	13	26.980	13.980	0.23		290	0.062	0.072
Ti	22	47.870	25.870					0.041
Fe	26	55.850	29.850			539	0.033	0.035
K	19	39.098	20.098					0.050
Mg	12	24.310	12.310	8.16	14	235	0.077	0.081
Na	11	22.990	11.990			190	0.095	0.085
S	16	32.070	16.070	5.43				0.060

[1)] Energy of emitted gamma rays

[2)] Mean loss of energy by collision

[3)] Neutron slowing down power of an element is the number of collisions needed to reduce the energy of a neutron from 2 million electron volts (MeV) to thermal energy of 0.025 electron volts (eV) at 25°C in a medium consisting only of this element, (Serra 1984).

[4)] HI here refers to the ratio of slowing down power of hydrogen (H) to that of concerned element (Serra1984). Note that H is about more than six times as effective at slowing down neutrons as carbon (C) and even more than other available elements.

We used the HI of the elements in Table 3 to calculate the HI of the components in Table 4. The HI of each mineral is normalized to its wt % (based on XRD analysis) to find its HI contribution in bulk siliceous ooze. For instance, to obtain the HI of calcite ($CaCO_3$), the atomic fraction of *Ca*, *C* and *O* elements in calcite are 0.2, 0.2 and 0.6, respectively. Their corresponding HI or ξ are 0.049, 0.158 and 0.120, respectively, (Table 3). Thus the HI of calcite was calculated as following: (0.2x0.049) + (0.2x0.158) + (0.6x0.120) = 0.113. The same concept was applied to calculate the HI of each compound listed in the first row of Table 4. The calculated HI (or ξ) results of each compound are presented in the second row from the bottom of Table 4. To obtain the total HI contribution of all non-opal minerals, their calculated HI were weighted by their respective concentrations as reported in the bottom row of Table 4. The products were added together. The sum of the HI of all non-opal minerals is about 0.203 which was multiplied by the non-opal volume fraction log as obtained in section 2.2.1. The same concept was applied for opal, and the calculated HI is about 0.168, which was multiplied by the opal volume fraction log as obtained in section 2.2.1. The above HI contributions from non-opal and opal were combined together and used equation (10) as the HI of solid phase (HI_{solid}).

Table 4 The calculated stopping power, ξ, for water, calcite, opal and non-opal components and the parameters used in the calculation of ξ

				Non-opal minerals of the bulk siliceous ooze						
Compound	**Water**	**Calcite**	**Opal-A**	**Quartz**	**K-feldspar**	**Plagioclase**	**Pyrite**	**Kaolinite**	**Illie**	**Smectite**
Formula	H_2O	$CaCO_3$	$SiO_2.nH_2O$*	SiO_2	$KAlSi_3O_8$	$NaAlSi_3O_8$	FeS_2	**	**	**
A_H	1		1							
A_i	16	40; 12; 16	28; 16	28; 16	39; 27; 28; 16	23; 27; 28; 16	56; 32			
n_i	1	1; 1; 3	1; 2.121	1; 2	1; 1; 3; 8	1; 1; 3; 8	1; 2			
$\Sigma n_i A_i$	16	100	62	60	278	262	120	509	1204	1037
nH	2	0	0.242	0	0	0	0	8	12	37
Density (g/cm^3)	1	2.71	2.16	2.65	2.62	2.59	4.99	2.52	2.79	2.79
Ca (fraction)		0.200								
S (fraction)							0.667			
O (fraction)	0.333	0.600	0.631	0.667	0.615	0.615				
H (fraction)	0.667		0.072							
C (fraction)		0.200								
Si (fraction)			0.297	0.333	0.231	0.231				
K (fraction)					0.0769					
Al (fraction)					0.077	0.077				
Na (fraction)						0.0769				
Fe (fraction)							0.333			
Calculated ξ	**0.707**	**0.113**	**0.168**	**0.103**	**0.099**	**0.101**	**0.052**	**0.359**	**0.240**	**0.870**
Fractions of non-opal minerals as reported in Table 2				0.362	0.045	0.090	0.073	0.177	0.215	0.038

***** $n = 0.121$

****** For the formulas of kaolinite, illite and smectite, refer to footnotes of Table 2

A_H = the atomic mass of hydrogen atoms in the material

A_i = the atomic mass of non-hydrogen element *i*

n_i = the number of non-hydrogen atoms of element *i* in a formula unit of the material

nH = the number of hydrogen atoms in a formula unit of the materia

Solving equation (10) for true neutron porosity (ϕ_{n_true}) as follows:

$$\phi_{n\_true} = \frac{d-g}{e-g} \tag{11}$$

where *d* is the calculated *HI log* that neutron tool reads if it is calibrated for limestone; *e* is the *HI* of water occupies the true porosity, and *g* the *HI* of solid phase.

2.2.5. Biot's coefficient for elastic deformation

At the first glance, one could refer the high porosity of the siliceous ooze to overpressure, or to unusual siliceous ooze stiffness that resists compaction and therefore high porosity is maintained at higher effective stress. Biot's coefficient, β, which is an indicator of how well grains in a rock are cemented (β is indicator for sediment stiffness), is used here to help us interpret siliceous ooze stiffness. The value of β depends on the degree of contact cementation between particles. It is obtained here as follows (Biot and Willis 1957):

$$\beta = \left(1 - \frac{K_{dry}}{K_o}\right) \tag{12}$$

where K_{dry} is the bulk modulus log of a dry rock (i.e. rock frame) and it was found here by Gassmann substitution (Gassmann 1951) of the wireline logging data under assumption of 100% water saturation. K_o is the mineral bulk modulus log of the grains that form the rock, and it was obtained here (K_o = 5 GPa) based on the results of Awadalkarim and Fabricius (2009).

If β equals to 1, the rock follows the normal compaction trend according to Terzaghi (1923). If β is less than 1, this indicates that the particles are cemented and hence they compact at lower rate than the normal compaction rate of the rock because more overburden stress is supported by the rock frame and therefore, the compaction is less. Thus, high porosity is maintained because of contact cementation between the grains and not because of the overpressure as there is no evidence or clue for overpressure in the studied siliceous ooze intervals (Awadalkrim and Fabricius 2009). Awadalkarim and Fabricius (2012) addressed the influence of using correct value of β when estimating vertical effective stress on deep-sea sediments. They noticed that even for small deviation in β value from 1, a significantly higher vertical effective stress can be obtained. Because the calculated β is less than 1, and the water depth in the Ormen Lange area is very high, thus, β has a relatively large influence on the estimation of vertical effective stress (Awadalkarim and Fabricius 2009).

2.2.6. AVO analysis

Seismic waves are reflected with different amplitudes depending on the angle of incidence relative to an interface. The relation between reflected amplitude and angle of incidence is dependent on the acoustic impedance (AI) contrast and shear impedance (SI) contrast of the interface. At the surface, the change in amplitude versus angle of incidence (AVA) is registered as a change in amplitude versus offset (AVO). By tracing the path of the seismic wave, the AVA may be related to the measured AVO response. AVO based on acoustic velocity and bulk density logging data is more reliable than that from seismic data, as in the first the lithology is already known from logs, but in the case of seismic data, the litholgy is unknown and it is inferred based on guess.

Siliceous ooze is characterized by high porosity, very low bulk density and low sonic velocity, and consequently a low AI, which is a product of formation bulk density and sonic velocity. Thus, siliceous ooze may be mistaken for a highly porous, poorly consolidated oil bearing sandstone interval and thus constitute a disappointing target for explorationists. Knowing the AVO signature of siliceous ooze may help to distinguish it from sandstone and hence tackling the above problem. In this study, we used the acoustic velocity and bulk density logging data to determine the change in amplitude versus angle of incidence (AVA) response of the siliceous ooze by using Zoeppritz equations cast in the formulation of Aki and Richards (1980). We compared the AVA of siliceous ooze with that of a modeled hydrocarbon bearing sandstone interval with similar reflection strength at normal incidence. By comparing these we address whether AVO may help to distinguish water saturated siliceous ooze interval from an oil bearing sandstone interval.

3. Results

3.1. Conventional core analysis data

The conventional core analysis results of the studied opal-A siliceous ooze core material indicated very little variation in porosity and permeability between the analysed ten core plug samples. The grain density is low and variable, depending on the amount of opal and non-opal contents. This is in agreement with the results of Stosur and David (1976). One important aspect of low and variable grain density is its effect on the calculation of density porosity. The core helium porosity (total porosity)

is high and it varies from 50–56% (standard deviations of 0.02). This is in agreement with the data reported by Schwart (1988) for the Belridge diatomite. As core helium porosity decreases to about 50%, the grain density increases from about 2.38 g/cm^3 to around 2.47 g/cm^3.Core material samples rich in opal-A (dried at 60^o C) have the lowest grain densities of about 2.38 g/cm^3, the highest porosities of about 56% and the lowest permeability of about 0.210 millidarcies (mD). The core permeability ranges from 0.210–0.412 mD (standard deviations of 0.06). The arithmetic, geometric and harmonic averages of the core permeability values are very close (0.304, 0.300 and 0.295 mD, respectively) implying that the analyzed core material is homogeneous (Tib and Donaldson 2004). The permeability among the studied siliceous ooze intervals, as expected, is very low if no open fractures are present. It is even lower than the permeability of the Lost Hills field diatomite that ranges from 1–10 mD (Stosur and David 1976). Nevertheless, the porosity and permeability here are higher than most of the Monterey diatomaceous ooze of the Buena Vista Hills field that shows an average permeability of about 0.112 mD.

3.2. Mineralogical and petrographical analyses

The non-opal fraction of siliceous ooze has variable mineral composition of different grain densities. Cross plots assisted in finding that illite is a dominating mineral of non-opal fraction (Awadalkarim and Fabricious 2009). This is confirmed by XRD analysis.

The results of the grain size distribution analysis of four siliceous ooze samples showed similar grain size distribution, and they mainly consist of silt with fine sand (<0.125 mm) in the larger fraction. The grain density for the four analysed specimens ranges from 2.42 to 2.46 g/cm^3 which is in agreement with the core grain density.

The results from the carbonate content (CC) and TOC analyses of the opal-A siliceous ooze core material are low, in the range of 0.15–0.36% and 1.8–2.3%, respectively; with an error of ± 10%. High TOC in a formation means more porosity of that formation, because TOC can cause anomalously high porosity value from standard logging tools (Passy *et al.* 1990).

The XRD results referred to here, only give the relative contents of the minerals which are possible to quantify from the peaks detected above the background interference, and thus excludes opal-A. The results of the bulk sample analyses indicated a high percentage of clay minerals (including mica and glauconite) relative to the total content of minerals. The four opal-A siliceous ooze samples analysed by the XRD appeared quite similar.

Textural and morphological observations of the studied siliceous ooze were undertaken with backscatter analysis which showed abundant diatoms (Fig. 3).

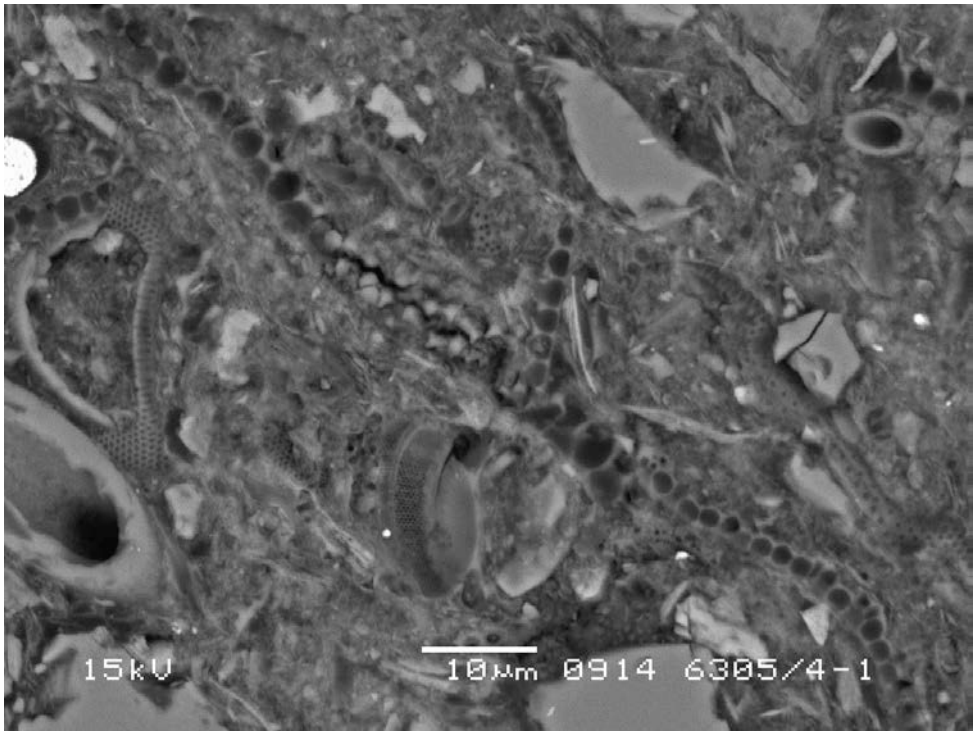

Figure 3 Backscattered electron (BSE) image of the siliceous ooze from well 6305/4-1 shows absence of lamination. The diatomaceous ooze contains clay, pyrite and silt. There is a framework of whole diatoms besides fragments and fine diatom dust. The sample has bimodal grain population and very high porosity. There are thus three kinds of porosity: large-scale intragranular (within uncompacted whole diatoms), small-scale intragranular (within individual bits of diatom fragments), and intergranular.

3.3. Standard petrophysical logs

The petrophysical logs of selected siliceous ooze intervals are shown in Figures 4–7. The depth to the top of the siliceous ooze and its thickness vary from one well to another (Table 1). The gaps in some logs especially in the Figures 4 and 7 are due to the lack of logging data in those intervals. Some tightly cemented sandstone stringers or calcareous nodules are seen as peaks (spikes) on sonic velocity, bulk density and resistivity logs throughout the siliceous ooze sections, especially at about 1685 m and 1792 m intervals in the well 6305/5-1 (Fig. 5c, d and h). A sharp increase in GR log and a decrease in both bulk density and resistivity values at about 1664 m marks the top of the siliceous ooze interval in the well 6305/5-1 (Fig. 5). The Opal-CT contact occurs at about 1988 m, 1933 m, 1922 m and 1993 m in the Figures 4, 5, 6 and 7, respectively. Low density and high porosity are characteristics of siliceous ooze dominated by opal-A, whereas relatively high density and low porosity are typical for siliceous ooze dominated by opal-CT and quartz. No significant change in neutron porosity log is observed.

The logging responses throughout the studied intervals show very low bulk density and GR; as well as high total neutron porosity and very low sonic velocity with respect to the same logging responses of the adjacent shale and/or other intervals. In the four wells, within the siliceous ooze intervals, the neutron porosity is quite similar and it is also close to neutron porosity recorded in the shale interval above the siliceous ooze in the well 6305/5-1 which is the only well where logging data of the

lithology above the siliceous ooze are available. The density porosity is lower when corrected for low grain density. Likewise, the neutron porosity is lower when corrected for the HI contribution of the solid phase.

The calliper log showed evident borehole caving at about 1762–1803 m and 1711–1720 m intervals in the Figures 4 and 6, respectively. However, the boreholes at the lower part of the opal-A dominated siliceous ooze intervals in the two figures are generally in gauge, over sections of interest, indicating excellent holes. Apart from that, the borehole conditions over the sections of interest were generally good resulting in good logging quality. The GR log response in the siliceous ooze intervals is lower than its readings in the overlying and underlying shale intervals. The opal-CT dominated siliceous ooze intervals are relatively clean compared to the opal-A dominated siliceous ooze intervals.

In the well 6305/7-1, the density and sonic velocity logs showed a marked increase at around 1922 m (Figs. 6c and 6d). This may reflect the change in character of opal-A content of the siliceous ooze, and it was interpreted as opal-CT reflector. The resistivity logs showed little character with the deep and medium resistivity curves overlay each other at around 0.8–1.1 ohm-m, especially in the lower part of siliceous ooze intervals, but they separate in the upper part, especially in the Figures 6 and 7.

The true density porosity (ϕ_{true}) as calculated by equation (6) is lower than the total apparent density porosity as derived by equation (8). The former corresponds well with the overburden corrected core porosity ($\phi_{\_Core}$), (Fig. 5e). The average ϕ_{true} is about one porosity unit lower than the average $\phi_{\_Core}$, within the same 10 m depth interval where the core porosity data were measured. The ϕ_{true} represents the total in-situ porosity as should be obtained from bulk density log.

Pyrite over 6% invalidates resistivity measurements due to the conductivity of pyrite (Palacky 1988; Geonics Ltd. 1980). The average pyrite content as estimated by the XRD analysis of the siliceous ooze material is very close to this number. This may be one of the reasons that why the studied siliceous ooze has very low resistivity log response. Despite the high porosity of the studied intervals, the small or the lack of separation between the deep and medium resistivity curves indicates that the permeability is very low (Figs. 6h and 7h). This suggests that either there is only very shallow mud filtrate invasion or there is very deep mud filtrate invasion so that both resistivity curves read the disturbed zone. We are aware that if the resistivities of mud filtrate and formation water are the same (depending on the salinity), this may hide the separation even if it is present. Since no drilling mud losses were observed when drilling these intervals, it is reasonable to assume that no or very shallow mud filtrate invasion has occurred, and hence the deep and medium resistivity curves may not be affected by mud filtrate invasion. Less invasion correction is needed since water based drilling mud was used, if we accepted that clues of shallow mud filtrate invasion are seen at the upper part of siliceous ooze intervals where the shallow resistivity curve reads lower than the deep and medium resistivity curves.

3.4. Siliceous ooze stiffness

The calculated Biot's coefficient, β, of about 0.90 –0.97 is less than 1 indicates that the investigated siliceous ooze is relatively stiff (i.e. cemented). Thus, the high porosity of the siliceous ooze can not simply be due to loosely consolidated siliceous

ooze. Analogues of unconsolidated sands from Tobermory (well: W05214/4-01) and Peon (well: Møre 35/2-1) do not show as high porosity response as the current siliceous ooze did. The high porosity is probably related to the diatomitic intra-fossil porosity of siliceous ooze.

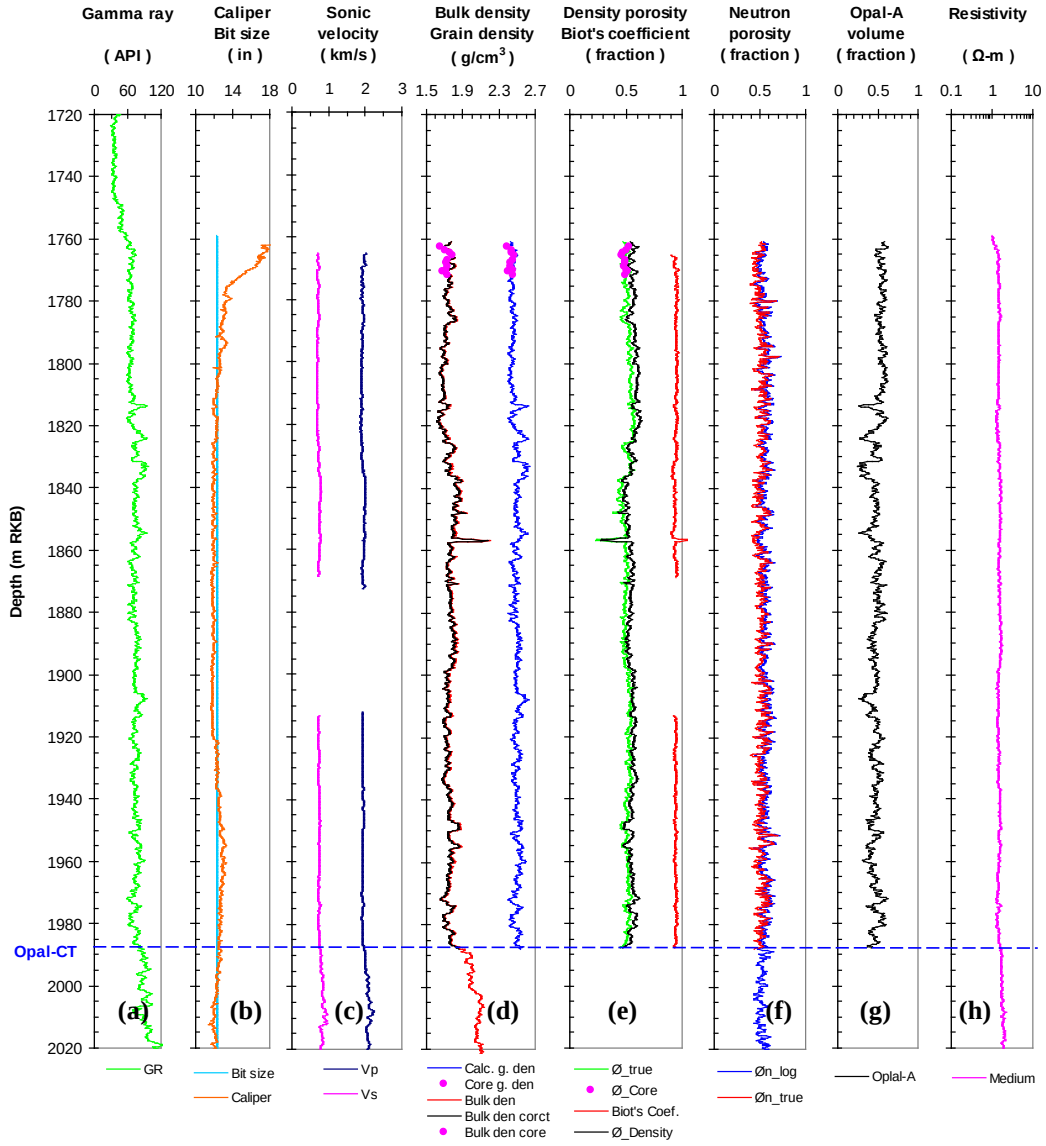

Figure 4 Petrophysics logs of a selected siliceous ooze interval in the wellbore 6305/4-1. Comparison of the wireline bulk density (Bulk den), core bulk density (Bulk den core) and wireline corrected bulk density (Bulk den corct), as well as the comparison of the calculated (Cal. G. den) and core grain (Core g. den) densities are shown in (d). The true density porosity (Ø_true), core porosity (Ø_core) and the apparent density porosity when quartz lithology is assumed (Ø_Density) are compared in (e). The true neutron porosity (Øn_true) and wireline neutron porosity (Øn_log) are compared in (f). The top of the opal-A dominated siliceous ooze is at about 1701 m, but no logging data are available for upper part of this interval, except gamma ray log. The opal-CT contact is at around 1988 m (Table 1). A very evident spike at about 1857 m is shown on GR, density, resistivity and permeability logs.

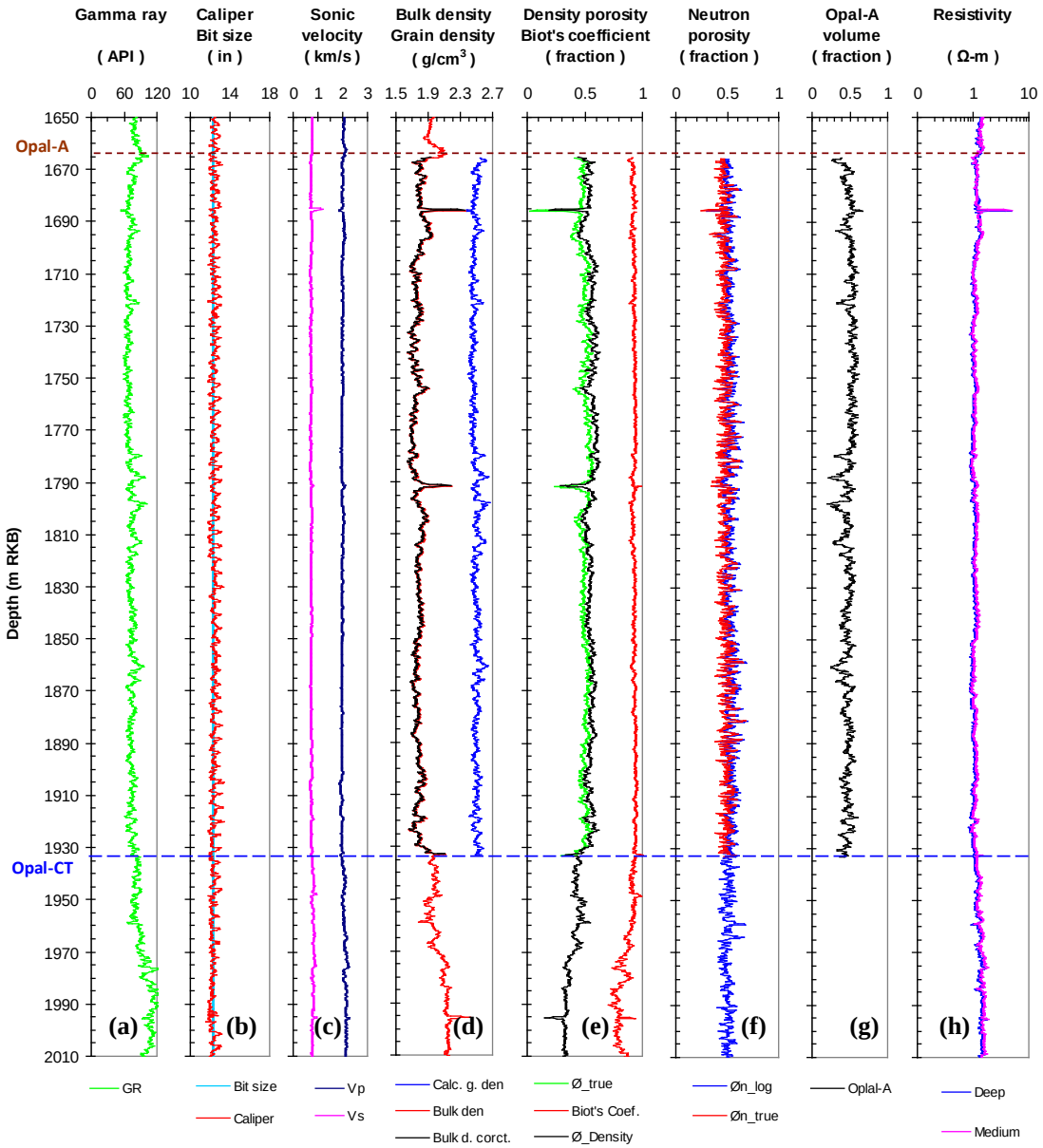

Figure 5 Petrophysics logs of a selected siliceous ooze interval in the wellbore 6305/5-1. Comparison of the wireline bulk density (Bulk den) and wireline corrected bulk density (Bulk d. corct.) is shown in (d). The true density (Ø_true) porosity and the apparent density when quartz lithology is assumed (Ø_Density) are compared in (e). The true neutron porosity (Øn_true) and wireline neutron porosity (Øn_log) are compared in (f). The top of the opal-A dominated siliceous ooze is at about 1664 m. The opal-CT contact is at around 1933 m (Table 1). Some spikes (anhydrite streaks) at depth intervals of about 1685 m and 1793 are very evident on GR, sonic velocity, density, resistivity and permeability logs.

3.5. AVO analysis

Figure 8 is a plot of the AI (from P-wave velocity and bulk density) of the different formations encountered in the four wells included here. The opal-A dominated siliceous ooze showed the same AI value of about 3.5×10^{-6} Pa.s/min, in all the four wells, whereas the opal-CT siliceous ooze showed a range of AI values from 4 to 4.5×10^{-6} Pa.s/min.

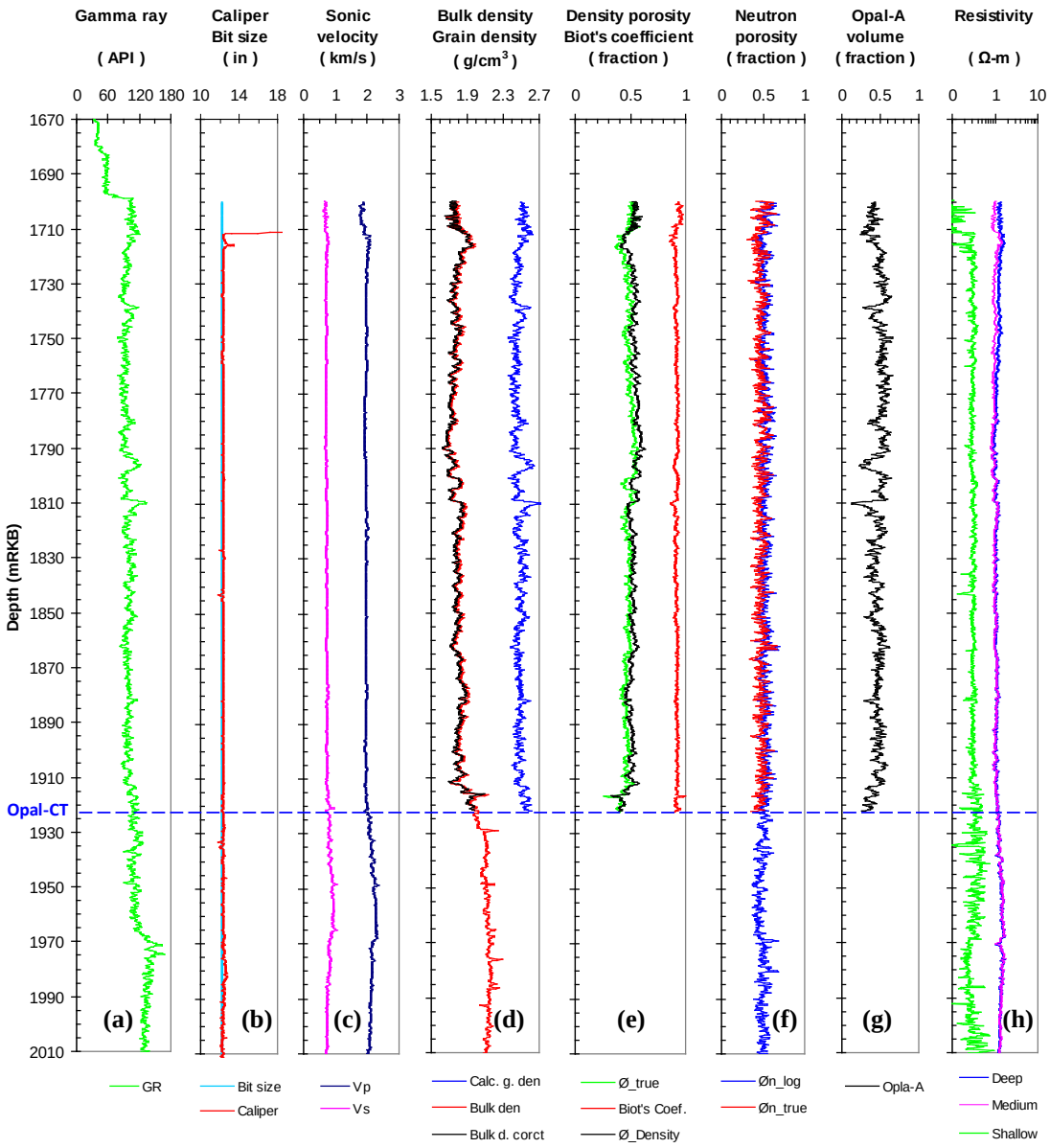

Figure 6 Petrophysics logs of a selected siliceous ooze interval in the wellbore 6305/7-1. Comparison of the wireline bulk density (Bulk den) and wireline corrected bulk density (Bulk den corct) is shown in (d). The true density porosity (Ø_true) and the apparent density when quartz lithology is assumed (Ø_Density) are compared in (e). The true neutron porosity (Øn_true) and wireline neutron porosity (Øn_log) are compared in (f). The top of the siliceous ooze dominated by opal-A is at about 1529 m, but no logging data for the upper part of this interval, except gamma ray log. The opal-CT contact is at around 1922 m (Table 1). An evident spike at about 1810 m is shown on GR, density, resistivity and permeability logs.

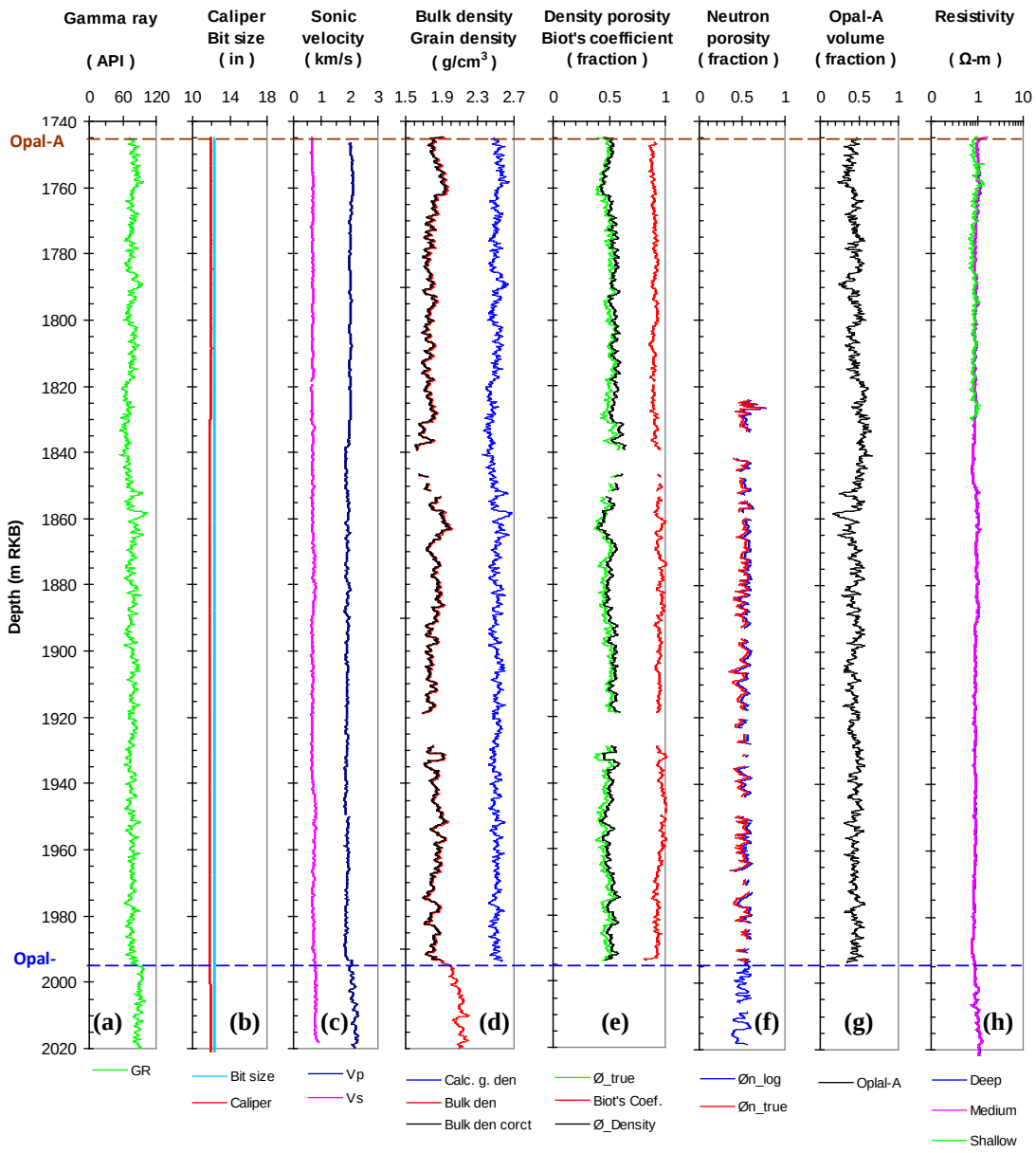

Figure 7 Petrophysics logs of a selected siliceous ooze interval in the wellbore 6305/8-1. Comparison of the wireline bulk density (Bulk den) and wireline corrected bulk density (Bulk den corct) is shown in (d). The true density porosity (Ø_true) and the apparent density porosity when quartz lithology is assumed (Ø_Density) are compared in (e). The true neutron porosity (Øn_true) and wireline neutron porosity (Øn_log) are compared in (f). The top of the opal-A dominated siliceous ooze is at about 1745 m. The opal-CT contact is at around 1993 m (Table 1). The gabs in some logs are due to the lack of the logging data at these depth intervals.

The P-wave reflection coefficient (R_{pp}) for the interface between the shale (Kai Formation) and the top of the opal-A siliceous ooze is illustrated in Figure 9. The opal-CT reflector is shown by Figure 10 whereas the interface between the base of the opal-CT dominated siliceous ooze and the shale below (Tare Formation) is shown by Figure 11. The AVO response of water saturated opal-A dominated siliceous ooze is compared with that of a modelled clean oil-saturated sandstone (Fig. 12). The AI of the sandstone is tuned to assure equal reflection strength at normal incidence. The reflection coefficient for the water saturated opal-A dominated siliceous is constant at

zero angle of incidence up to around 10^o and then slightly increases with increasing the angle of incidence. When the porosity of the hydrocarbon saturated sandstone is very high, it is difficult to distinguish it from siliceous ooze especially at the low angle of incidence (Fig. 12). However, at the angle of incidence greater than 15^o, it would possibly be distinguished from the siliceous ooze even though the effect is not great.

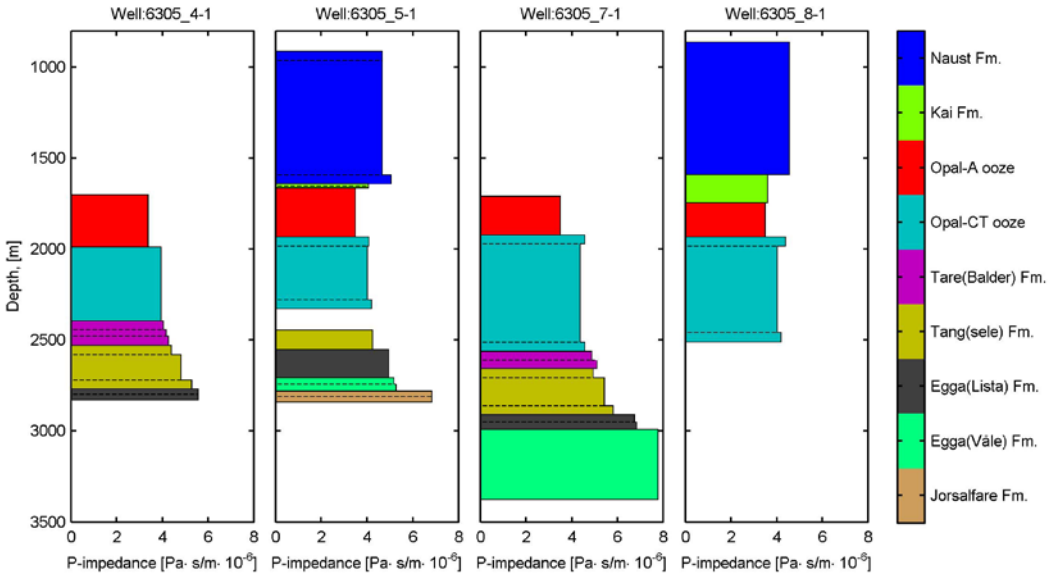

Figure 8 Acoustic impedance (AI), from P-wave velocity and bulk density, of the different formations encountered in the four wells. No sonic velocity data are available for the Tare Formation in the well 6305/5-1.

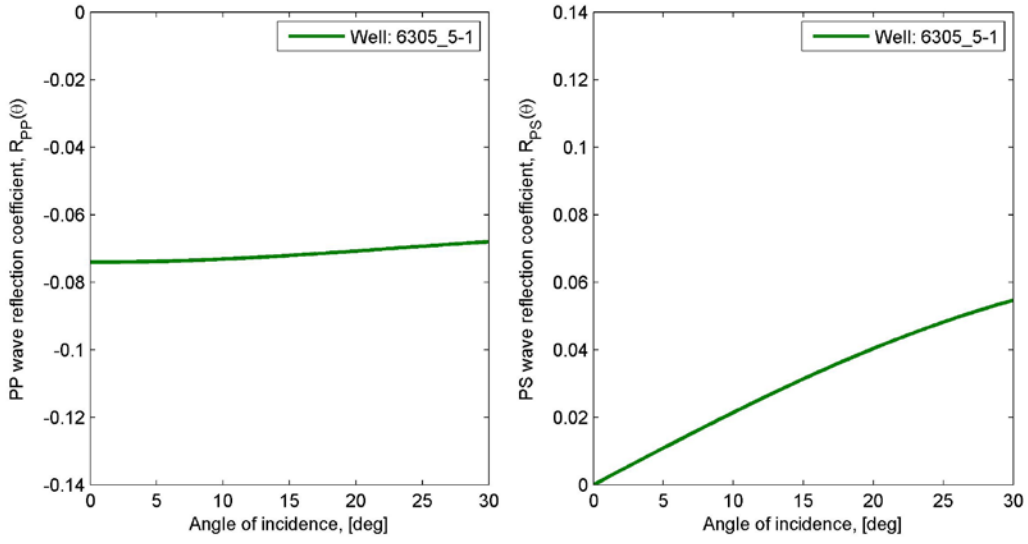

Figure 9 P-wave reflection coefficient, R_{PP} (θ), (left) and S-wave reflection coefficient, R_{PS} (θ), (right) for the interface between the top shale (Kai Formation) and the top of the opal-A siliceous ooze (i.e. shale/top siliceous ooze interface). We have the sonic velocity data for the top shale (Kai Formation) for the well 6305/5-1 only. There is only P-wave velocity (no shear velocity) data for the Kai Formation in the well 6305/8-1.

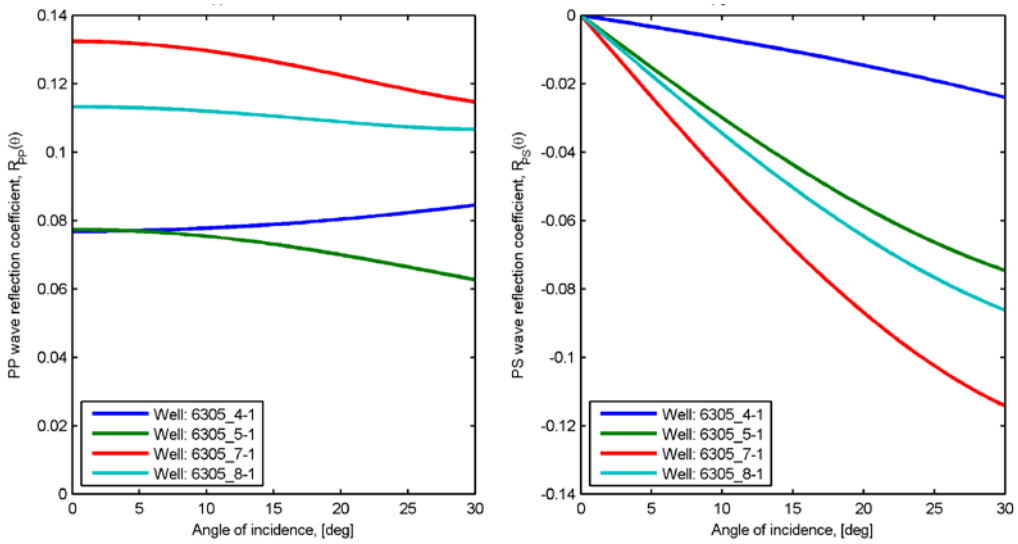

Figure 10 P-wave reflection coefficient, R_{pp} (θ), (left) and S-wave reflection coefficient, R_{ps} (θ), (right) of the opal-CT reflector (i.e. opal-A/opal-CT interface). We found different values of the reflection coefficients in the four wells. This may be because the opal-CT contact represents a diagenetic event through different lithologies.

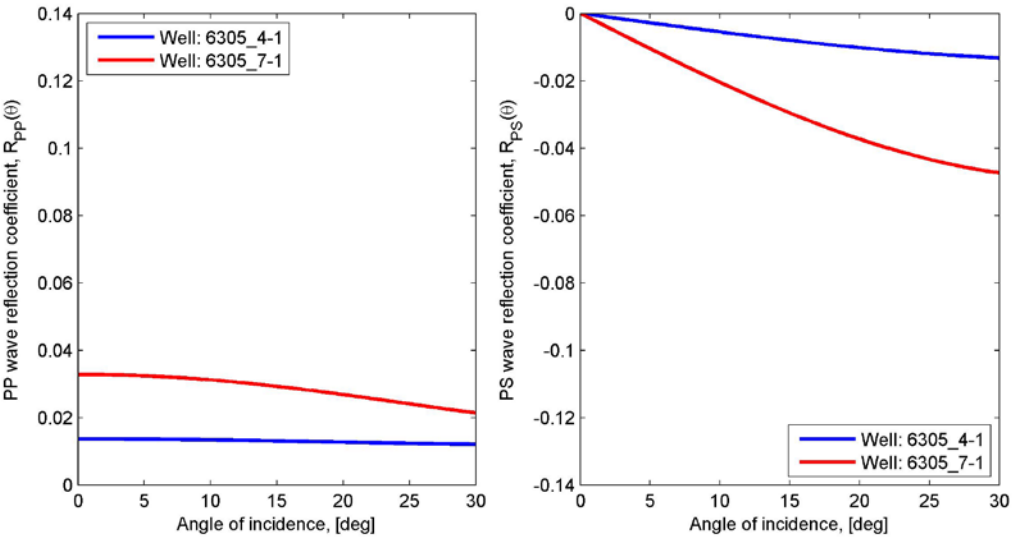

Figure 11 P-wave reflection coefficient, R_{pp} (θ), (left) and S-wave reflection coefficient, R_{PS} (θ), (right) for the bottom of the opal-CT ooze (i.e. opal-CT/shale interface). Sonic velocity data for the Tare (Balder) Formation are available for the wells 6305/4-1 and 6305/7-1 only. No Sonic velocity data are available for the wells 6305/5-1 and 6305/8-1.

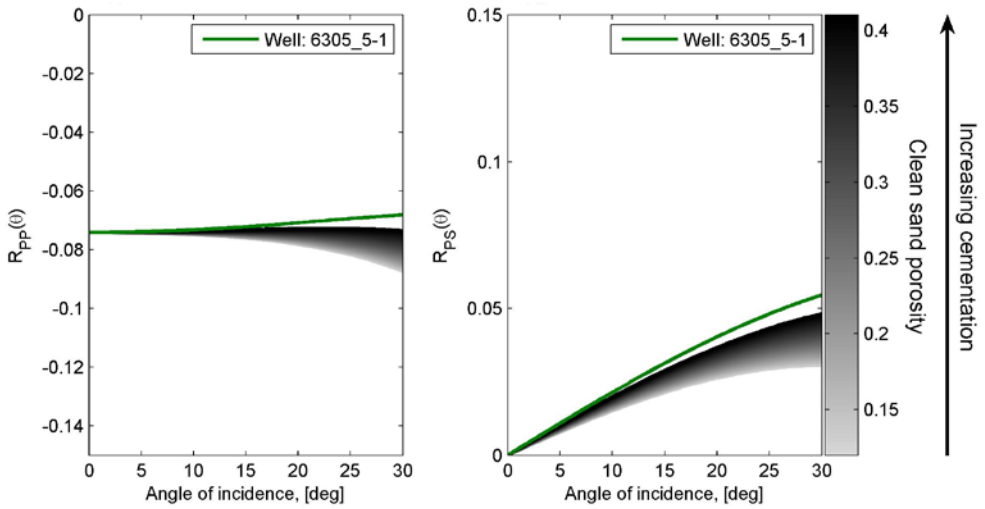

Figure 12 AVO response of water saturated opal-A dominated siliceous ooze and hydrocarbon bearing sandstone. P-wave reflection coefficient, R_{pp} (θ), (left) and S-wave reflection coefficient, R_{ps} (θ), (right) of the top of the water saturated opal-A siliceous ooze compared with the modelled clean oil saturated sandstone with irreducible water saturation of 0.1.

4. Discussion

The integration of the available data such as well logs, core analysis, grain size distribution measurements, petrographical analysis and XRD results revealed that the studied siliceous ooze is a mixture of opal and non-opal (shale) at variable ratios. The non-opal fraction has variable mineral composition of predominantly different grain densities. Cross plots assisted in finding that illite is a dominating mineral of non-opal fraction (Awadalkarim and Fabricious 2009). This is confirmed by the results of the XRD analysis of the clay-size fraction which revealed that illite constitutes about 50% of the total clay minerals in the bulk siliceous ooze material.

The density log appears to be the most useful tool for porosity determination of siliceous ooze if the correct grain density is used. The neutron log is more effective at low porosity ranges (Stosur and David 1976). This is because its depth of investigation decreases at higher porosity and increase somewhat at lower porosity, whereas the reverse is true for density tool. Since the amount of structurally bound water is considered here, the applied HI correction to the neutron porosity log is accurate.

When we used the quartz grain density (2.65 g/cm^3) to calculate the apparent density porosity, the result is about 5 to 10 porosity units higher than the true density porosity as calculated by taking mineralogy into account (Equation (6)). The true neutron porosity obtained by equation (11) is lower (by about 3 to 4 porosity unit) than the wireline neutron porosity log. This is because the former is corrected for the HI contribution from the solid phase. Thus it should give low and consistent neutron porosity throughout the studied intervals. We found that the calculated true density porosity and the corrected neutron porosity are very similar which indicates that our interpretation is consistent.

5. Conclusions

The studied siliceous ooze contains significant amount of shale and it is characterized as having very high porosity, extremely low bulk density, low natural gamma ray log readings, and relatively high sonic interval travel time. The true porosity was calculated based on fundamental relationships. Although the petrophysical interpretation presented here should be regarded as indicative rather than definitive, the application of the proposed approach is capable to give reasonable grain density log and consistent porosity values and thus it should be useful for the petrophysical community.

Amorphous silica, such as opal-A, is quite difficult to quantify by XRD analysis techniques. In this case, the petrophysicist must be informed about it since this amorphous silica is light and hydrated. Failure to take this into account may induce an error in porosity calculation which may result in a large overestimation of water saturation of a reservoir. The AVO analysis revealed that at the angle of incidence greater than 15^{o}, oil saturated sandstone reservoir could be distinguished from water bearing siliceous ooze interval. The obtained Biot's coefficient (0.90 to 0.97) indicates that the studied siliceous ooze is relatively stiff even if the porosity (ϕ) is high (the ϕ ranges from about 47–53%). The studied siliceous ooze intervals apparently do not contain hydrocarbons.

6. Acknowledgements

The work was undertaken in collaboration with DONG Energy of Denmark. We are grateful to DONG Energy for funding this research project and providing raw logging data. We thank all DONG petrophysicists, especially Tomas Hansen and Mevan K. Ranasinghe, for helpful discussions. We are grateful to Jørgen E. Knudsen and Robert O. Jorro, the former DONG Petrophysicists, for proof-reading the manuscript and for their constructive comments. We also thank Aymen Abouardini for allowing us to use a BSEM image from his M.Sc. thesis at Denmark Technical University.

7. References

Aki K. and Richards P.G.1980. *Quantitative Seismology: Theory and Methods.* W.H. Freeman and Company, San Francisco, California. ISBN 0-935702-96-2. 932pp.

Awadalkarim A. and Fabricius I.L. 2009. Estimating effective stress in North Sea ooze. The sound of geology workshop. Bergen, Norway, May 6^{th} -8^{th}, 2009, University of Bergen.

Awadalkarim A. and Fabricius I.L. 2012. The influence of Biot's coefficient on the estimation of vertical effective stress on deep sea sediments. 74^{th} EAGE meeting, Copenhagen, Denmark, Expanded Abstracts, P187.

Bilodeau, B.J. 1995. Determining water saturation in diatomite using wireline logs, Lost Hills Field, California. In *SPE Western Regional Meeting*, 369–382.

Biot M.A. and Willis D.G. 1957. The elastic coefficients of the theory of consolidation. *Journal of Applied Mechanics*, **24**, 594–601.

Brindley, G.W. 1951. The Kaolin Minerals: X-Ray Identification and Structure of the Clay Minerals. *Mineralogy Society of Great Britain Monograph*, 32–75.

Dalland A., Worsley D. and Ofstad K. (eds) 1988. A lithostratigraphic shceme for the Mesozoic and Cenozoic succession offshore mid-and northern Norway. *NPD-Bulletin No. **4***, 65 pp.

Day R. and Jones B. 2008. Variation in water content in opal-A and opal-CT from geyser discharge aprons. *Journal of Sedimentary Research* **78**, 301–315.

Eldholm O., Thiede J., Taylor E. *et al.* 1987. *Proc, Init. Repts. (Pt. A), ODP,* **104**.

Gassmann F. 1951. Uber die elastizitat poroser medien. *Veirteljahrsschrift der Naturforschenden Gesellschaft in Zurich*, **96**, 1–23.

Geonics Ltd. 1980. Technical Note 5, Electrical Conductivity of Soils and Rocks, technical references (see the references page in this link).

Glover P. 2012, Petrophysics MSc Course Notes, page 150–171. http://www2.ggl.ulaval.ca/personnel/paglover/CD%20Contents/GGL-66565%20Petrophysics%20English/Chapter%2015.PDF. Accessed date: 03 December 2012.

Graetsch H. and Ibel K. 1997. Small angle neutron scattering by opals. *Physics and Chemistry of Minerals* **24**, 102–108.

Grange L. 1937. The geology of the Rotorua–Taupo subdivision, Rotorua and Kaimanawa Divisions. *New Zealand Department of Scientific and Industrial Research, Bulletin* **37**, 86–105.

Hearst J.R., Nelson P.H. and Paillett F.L 2000. Well Logging for Physical Properties. A Handbook for Geophysics, Geologists, and Engineers. John Wiley & Sons, Ltd., 2nd ed. p483. ISBN 0-471-96305-4.

Herdianita N.R., Browne P.R.L., Rodgers K.A. and Campbell K.A. 2000. Mineralogical and textural changes accompanying ageing in silica sinter. *Mineralium Deposita* **35**, 48–62.

Jones B. and Renaut R.W. 2004. Water content of opal-A: implications for the origin of laminae in geyserite and sinter. *Journal of Sedimentary Research* **74**, 117–128.

Kastner M. 1979. Authigenic silicates in deep sea sediments: formation and diagenesis. 915–980 in Emiliani, C. ed., *The Sea* **7**, New York, John Wiley & Sons.

Keller M.A. and Isaacs C.M. 1985. An evaluation of temperature scales for silica diagenesis in diatomaceous sequences including a new approach based on the Miocene Monterey Formation, California. *Geo-Marine Letters* **5**, 31–35.

Kurniawan B. 2005. Shaly Sand Interpretation Using CEC-Dependent Petrophysical parameters. Adissertation submitted to the graduate faculty of the Louisiana State University and Agricultural and Mechanical College.

Langer K. and Flörke O.W. 1974. Near infrared absorption spectra (4000–9000 cm^{-1}) of opals and the role of "water" in these $SiO_2.nH_2O$ minerals. *Fortschr Mineral* **52**, 17–51.

Nicholson K. and Parker R. 1990. Geothermal sinter chemistry: towards a diagnostic signature and a sinter geothermometer: 12th New Zealand Geothermal Workshop, Proceedings, 92–102.

NPD, Norwegian Petroleum Directorate http://www.npd-no. Accede on 15 May 2012.

Palacky G.J. 1988. Resistivity characteristics of geologic targets. *Electromagnetic Methods in Applied Geophysics* **1**, 53–129.

Passy Q.R., Creaney S., Kullil, J.B., Moretti, F.J. and Sttoud, J.D. 1990. A practical model for organic richness from porosity and resistivity logs, *AAPG Bulletin*, **74**, 1777–1794.

Pedersen G.K., Pedersen S.A.S., Steffensen J. *et al.* 2004. Clay content of a clayey diatomite, the Early Eocene Fur Formation, Denmark. *Bulletin of the Geological Society of Denmark* **51**, 159–177.

Schlumberger 1994. *Log Interpretation Charts*, Schlumberger Wireline and Testing, Houston, Texas, USA.

Schwartz D.E. 1988. Characterizing the Lithology, Petrophysical Properties, and Depositional Setting of the Belridge Diatomite, South Belridge Field, Kern County, California in Studies of the Geology of the San Joaquin Basin, S.A. Graham, and Olson, H.C., Editors., *The Pacific Section, Society of Economic Paleontologists and Mineralogists*, Los Angeles, 281–301.

Serra O. 1984. *Fundamentals of well log interpretation. 1. The acquisition of logging data*. Elsevier Science Publishers B.V. 423p. ISBN 0444421327.

Stosur J.J. and David A. 1976. Petrophysical Evaluation of the Diatomite Formation of the Lost Hills Field, California. *Journal of Petroleum Technology*, **28**, 1138–1144.

Talwani M., Udintsev G. *et al.* 1976. Initial Reports of the Deep Sea Drilling Project, Volume **38**, Washington (U.S. Government Printing Office), 1256 p.

Terzaghi K.V. 1923. Die Beziehungen zwischen Elastiztat und Innendruck. Mathematisch-Naturwissenschaftliche Klasse Abteilung 2A, 132, 105-124.

Thomsen E. and Danielsen M. 1995. Transitional Paleocene-Eocene ash-bearing diatomite in the Eastern North Sea. *Tertiary Research* **15**, 111–120.

Tib D. and Donaldson E.C. 2004. Theory and practice of measuring reservoir rock and fluid transport properties. Second edition. Gulf professional publishing in imperial of Elsevier. 200 Wheeler Road, Burlington, MA01803, US.

Xu, L., Schultz, W., and Huiszoon, C., 2010, A Comprehensive Investigation of Source Effects on Neutron Porosity Response for Logging-While-Drilling Measurements, *Petrophysics*, **51**(3), 185–198.

Zalan T.A., Morea M.F., Julander D.R. and Denoo S.A. 1998. Applying integrated formation evaluation to advanced reservoir characterization in California's Monterey Formation siliceous shales. SPWLA Symposium Transaction, Paper: BB.

III

Paper III

Elastic properties of Palaeogene clay from Fehmarn Belt area

Ahmed Awadalkarim, Niles Nielsen Foged and Ida Lykke Fabricius

Article submitted to Quarterly Journal of Engineering Geology and Hydrogeology.

Elastic properties of Palaeogene clay from Fehmarn Belt area

A. Awadalkarim[*1], N. N. Foged[1] and I. L. Fabricius[1]

[1]Centre for Energy Resources Engineering
Department of Civil Engineering
Technical University of Denmark
Brovej, Building 118, 2800 Kgs., Lyngby, Denmark

*Corresponding authors (e-mail: asmama67@yahoo.com; ilfa@byg.dtu.dk)

Abstract

This paper presents results of a comprehensive characterization study of Palaeogene clay collected from the Fehmarn Belt area. Ten naturally saturated Palaeogene clay samples were examined and analysed in terms of their physical, mineralogical and geotechnical properties. The deformation properties and elastic wave velocity were measured simultaneously from uniaxial confined compression stress testing using a triaxial Hoek cell, under drained conditions at laboratory temperature (22 ^{o}C).

We mainly focused here on the elastic properties of these clays. Elastic wave velocity is controlled by the elasticity and the density of a material. We used geotechnical and elastic wave velocity data to model the elasticity and then to relate it to mineralogy and surface area. The studied Palaeogene clay is rich in smectite which controls the physical properties of the studied clay, so that plasticity index correlates with the specific surface as measured with nitrogen adsorption. The obtained results describe the deformation behaviour of the frame of the studied Palaeogene clay as predominantly elastic. Our results can aid in the estimation of drained elastic parameters from bulk density and velocity of elastic waves and thus may have applications in engineering practice.

Introduction

The Fehmarn Belt is located between Denmark and Germany. The study area is about 19 km long, and it links Rødbyhavn in Lolland, Denmark, and Puttgarden in Fehmarn, Germany (Fig. 1). Palaeogene clay samples were obtained with a Geobore S-system during the extensive site investigations that have been carried out to help the design and construction of a tunnel. Comprehensive laboratory tests were done by Fugro-McClelland (in Netherlands) and by Danish Geotechnical Institute, GEO (in Denmark) on Palaeogene clays. Some of their data are included in this study. Ten Palaeogene clay samples were selected and used here to study the elastic properties of the Palaeogene clay.

In general, elastic properties of shale (clay) are known to be anisotropic (e.g. Hornby 1998). Kaarsberg (1958) made an in depth study of ultrasonic elastic anisotropy of saturated shale samples coupled with mineralogical compositions by X-Ray diffraction (XRD) analysis. However, his measurements were not made under stress. To address anisotropic elastic properties of shale, Hornby (1998) used elastic wave velocities of fluid saturated shale samples under drained conditions as a function of

confining stress. Based on detailed statistical and spatial analyses of data across the London Clay outcrop, Jones & Terrington (2011) studied the shrink–swell behaviour of the London Clay. Based on back-analysis of construction in London, in the UK, Clayton (2011) showed that field stiffnesses are much greater than those obtained from routine laboratory tests. The results of swelling and traditional oedometer tests done by Jessen *et al.* (2011) show that when Palaeogene clay is mounted in an oedometer cell without access to water and loaded to its *in-situ* vertical effective stress and then saturated with its native salt pore water, the clay absorbs water and swells. This behaviour indicates that the Palaeogene clay in nature should expand at its mean effective *in-situ* stress. A study by Krogsbøll *et al.* (2012) on Palaeogene clay from Fehmarn Belt provides clues about the deformation behaviour during unloading and swelling states. In this study, we focus on the elastic properties of the naturally water saturated Palaeogene clay. Elastic wave velocities are controlled by the elastic stiffness and the density of a material. We used geotechnical and elastic wave velocity data to model the elasticity and then to relate it to mineralogy and BET surface area. We measured the mineralogy, BET surface area, bulk density, porosity, water content and saturation, elastic wave velocity and strain (deformation) caused by mechanical loading. They were used together to interpret the geotechnical data. We aimed to see which physical property is a main controlling factor for the elasticity of the Palaeogene clay and whether we can explain the deformation behaviour from elasticity alone.

The obtained results can aid in the estimation of drained elastic parameters from bulk density and elastic wave velocity and may have applications in engineering practice, including structural design and slope stability analysis.

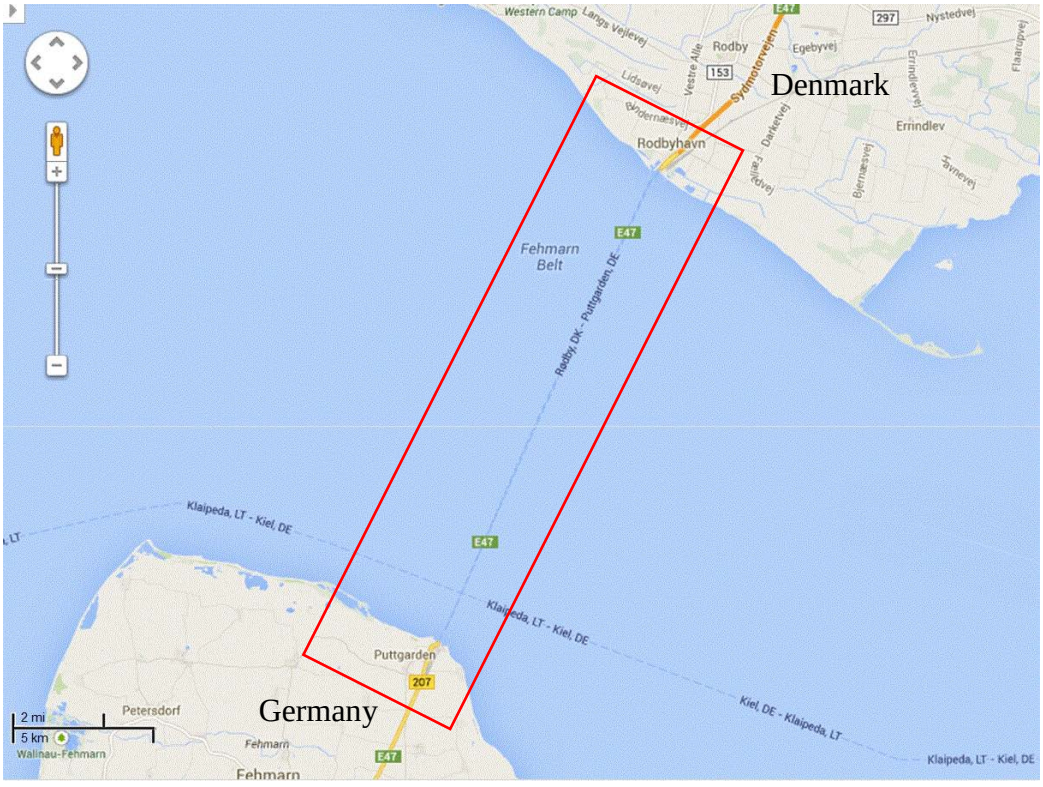

Fig. 1: Location map of the study area. Modified from: Map data © 2013 GeoBasis-DE/BKG © 2009-Google, at https://maps.google.com/.

Geological setting

The mapped geological units of the study area are listed here from the youngest first as following: 1) Quaternary deposits; 2) Palaeogene clay and 3) Cretaceous chalk (Fig. 2). The water depth at the central part of the study area is up to 29 m. The Palaeogene clay unit consists of five geological formations (Sheldon 2010). Below is a very brief geological description of the mapped geological units. More geological information about each geological unit can be found in Rambøll/Arup (2011).

The Quaternary deposits include postglacial and late glacial marine deposits (peat, gyttja, sand, silt and clay deposits), in addition to the glacial deposits (upper and lower clay tills as well as associated sand and silt deposits). The Quaternary deposits overlay clay of Palaeogene age, described as having high to very high plasticity, which itself overlies the Cretaceous chalk. The Palaeogene clay consists of five formations which are listed below from the oldest listed first to the youngest (the one at the top) listed last, with ranges of their estimated thickness given in the brackets: Æbelø (15–60m), Holmehus (3–40m), Ølst (10–15m), Røsnæs (15-28m) and Lillebælt (40–100m) clays. The microfossil analyses of a significant number of Palaeogene clay samples have shown that all the five formations and maybe the younger Søvind marl as well, are present in the borings at the study area (Sheldon 2010; Rambøll/Arup 2011). The Æbelø, Holmehus and Ølst formations are of Palaeocene age whereas the Røsnæs, Lillebælt and the Søvind marl formations are of Eocene age.

The Palaeogene clay has been subdivided into upper folded (disturbed) clay and lower intact (undisturbed) clay. The interface between them is identified as a significant, sudden increase with depth of the net cone resistance (Rambøll/Arup 2011). In Fig. 2, the interface is indicated by a dotted line on the parts of the geological profile where it has been mapped with insufficient certainty. The folded Palaeogene clay is weakened compared to the intact clay. In this study, the folded and the intact clays are considered as one unit even though they possibly have different geotechnical properties. Further detailed information about the areal distribution, post depositional deformations and observations on strength of the Palaeogene clay have been given by Jessen et al. (2011) and Rambøll/Arup (2011) which can be found at the Fehmern A/S Geo Information System at www.fehmarnlink.com.

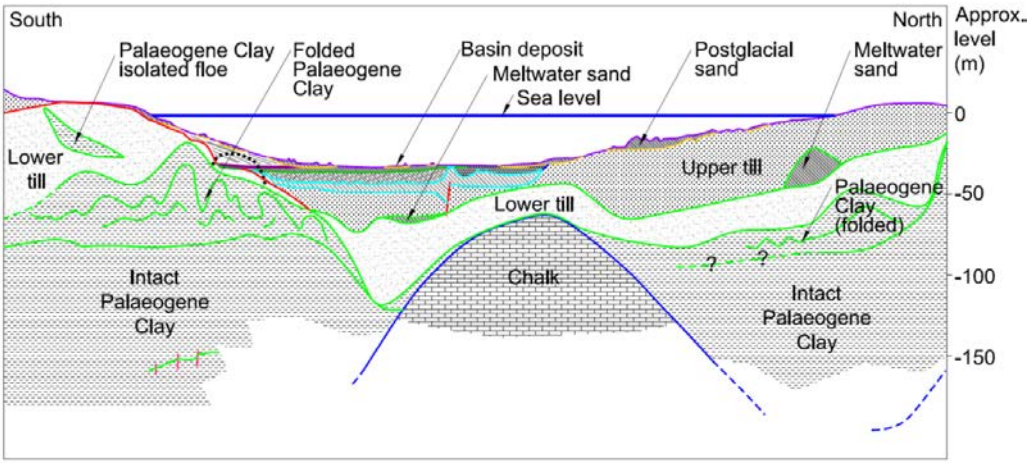

Fig. 2. Simplified geological profile across Fehmarn Belt showing the studied Palaeogene clays. The folds shown in the folded Palaeogene Clay should only be understood as a signature. The real pattern is supposed to be much more intense and complicated. The cross-section is taken from Rambøll/Arup (2011).

Theory and methods

Classification parameters and other geotechnical data

The classification parameters including the initial and final bulk and dry densities, water content and void ratio were collected from the same 30 core plug samples. The classification parameters are obtained based on the measured sample dimensions, volume and weight before and after each test and once again after sample drying at 60 ^{o}C for two days in the oven. We used 60 ^{o}C to avoid change in smectite mineral water. The grain density (ρ_g) in Table 1 is calculated from porosity and dry density (ρ_d). The void ratio is obtained here form dry density (ρ_d) and grain density (ρ_g). Porosity (ϕ), in fraction, is calculated from void ratio (e). $\phi = e\ (1- e)$. The continuous changes in porosity (ϕ) with stress is calculated using the initial porosity (ϕ_i) and the uniaxial strain (ε_A) as resulted from sample being deformed and measured by Linear Voltage Deformation Transducers (LVDTs), as follows:

$$\phi = \frac{\phi_i - \varepsilon_A}{1 - \varepsilon_A} \qquad (1)$$

The saturated water content (w_{sat} %) was calculated from the void ratio and grain density. The water saturation (S_w %) was calculated from the initial water content (w_i) and w_{sat}.

Table 1. *Results of smectite (sm %) and illite (il %) content from XRD analysis of bulk sample, BET measurements and some other geotechnical classification data of 10 Palaeogene included in this study*

Boring	Core	Sample	Sample	Geologi-			Geotechnical classification parameters													XRD	
number	number	number	depth	cal unit	σ'_{vo}	σ'_{pc}	w_i	S_w	ρ_b	ρ_g	d_s	ϕ_i	w_L	w_P	I_P	I_C	CC	Clay	BET	sm	il
			mbsf		kPa	kPa	%	%	g cm^{-3}	g cm^{-3}	g cm^{-3}	%	%	%	%		%	%	m^{2}g^{-1}	%	%
09.A.013	09-100196	1	94	Æbelø	1125		37	90	1.75	2.64		56						72	61	22	48
09.A.013	09-100310	2	94.55	Æbelø	1125		37	90	1.74	2.66		54						70	66	38	29
09.A.002	09-101463	8	85.05	Røsnæs	765		32	91	1.84	2.71		49					2.4	70	61	12	37
09.A.602	09-101191	15	20.13	Røsnæs	185	460	35	99	1.91	2.74	2.81	44	119	28	90.5	1.26	1.6	80	62	30	27
09.A.010	09-101082	29	49.35	Røsnæs	415		37	97	1.88	2.72	2.79	52	110	33	77.5	0.95	3.6	75	62	15	34
09.A.010	09-101096	31	31.25	Ølst	260		48	98	1.78	2.73	2.73	55	172	44	128	0.97	2.6	64	75	51	20
09.A.001	09-101232	37	45.1	Røsnæs	360	3300	35	98	1.91	2.72	2.79	49	173	29	144	0.96	3.0	78	64	23	28
10.A.803	10-105031	89	12.5	Lillebælt	214		45	98	1.74	2.71		57						73	65	28	21
10.A.057	10-106007	93	58.8	Ølst	575		45	98	1.65	2.69	2.85	62	136	49	86.6	1.05	4.7	42	84	60	14
10.A.802	10-108030	95	2.4	Lillebælt	40		47	95	1.71	2.63		55						26	45	14	5

σ'_{vo} is *in-situ* vertical effective stress, σ'_{PC} is pre-consolidation stress.The initial water content (w_i), wet bulk density (ρ_b), grain density (ρ_g), specific gravity of solids (d_s), initial porosity (ϕ_i), liquid limit (w_L), plastic limit (w_P), plasticity index (I_P), consistency index (I_C), and calcium carbonate ($CaCO_3$) content (CC), clay conetent (Clay) in bulk sample. BET is the surface area of bulk clay measured by nitrogen adsorption (BET method). The bulk sample refers to the total mass of the sample.

XRD analysis

X-Ray diffraction (XRD) analyses have been done using a Philips 1830 X-ray diffractometer equipped with Ni-filtered Cu K-α radiation (wavelength of 1.54051 Å) and an automatic divergent slit. The mineralogical composition has been determined for the bulk sample (on randomly oriented powder of a sample) as well as for the clay size fraction, separately. XRD analyses were done on the orientated samples of the <2

µm fraction with multiple treatments in the following sequences: untreated air-dried, ethylene glycol-solvated at 60 ^{o}C for 2 days, subsequently oven-heated to 350 ^{o}C for 2 hours and further heated to 550 ^{o}C for 2 hours.

Identification of the bulk and clay minerals was made by comparing the resulting XRD diffraction peaks of each sample to the standard JCPDS-ICDD diffraction patterns from PDF-2, Sets 1–43 database (Brown 1961). ICDD is the International Centre for Diffraction Data and PDF-2 is the Powder Diffraction File-2. Semi-quantification of the mineral contents is based on calculation of the integrated peak height and peak area measurements on a selected diffraction peak of a respective mineral phase, multiplied by in-house calibrated correction factors developed by Ole Bjørslev (2010) at University of Aarhus. On a bulk sample net peak height (*h*) was measured on the following peaks and multiplied by a correction factor: quartz 0.25*h* (4.25 Å); K-feldspar 0.10*h* (3.25 Å); plagioclase: 0.10*h* (3.18 Å); calcite: 0.076*h* (3.03 Å); dolomite: 0.076*h* (2.88 Å); siderite: 2.79h (2.79 Å); and total clay minerals 1.0*h* (4.46 Å). Then the bulk minerals were semi-quantified from the corrected peak heights. Clay minerals were semi-quantified, from the ethylene glycol oriented samples, as main groups: smectite, illite, kaolinite, and chlorite. To estimate the relative contents of smectite, illite, and combined chlorite/kaolinte, the integrated peak areas at the 17 Å, 10 Å, and 7 Å peaks were measured and multiplied by the correction factors 1, 3 and 1.15, respectively. Chlorite and kaolinite were then semi-quantified from the ratio of the height of the 14 Å peak after heating to 550 ^{o}C to the height of the 7 Å peak (after ethylene glycol treatment) corrected by a factor 1.5.

Generally, XRD analysis provides semi-quantitative results of absolute mineral contents (± 10%), but provide good repeatability and relative mineral concentrations as long as results from similar methods are considered. The XRD data presented in this study are useful for general characterization of the Palaeogene clay, but should not be viewed as precise quantitative data.

BET surface area

The internal surface area of the grains per unit weight (m^2/g) of the ten Palaeogene clay bulk samples were measured by nitrogen adsorption technique developed by Brunauer *et al.* (1938) and known as BET method. A Gemini III 2375 surface area analyzer apparatus (Micrometrics Instruments Corporation) was used to measure surface area which was done after degassing each sample for 4 hours at 70 ^{o}C on a FlowPrep060 degasser using nitrogen as a carrier gas. Here, we refer to the obtained surface areas as BET.

Uniaxial strain experiments

Ten preserved whole-core samples (in their natural moisture conditions) of Palaeogene clay were selected and used for laboratory experiments. An overview of the ten samples is given in Table 1. From these cores thirty naturally water saturated core plugs of 37.5 mm (1.5 inches) in diameter and nominally 25 mm (1.0 inch) long were prepared and used for measuring elastic wave velocity, deformation properties, and classification parameters. The 30 core plugs comprise sets of three core plugs cut in the vertical, horizontal and 45^{o} orientations from each of the ten whole-core samples. The laboratory measurements of uniaxial strain and elastic wave velocity were done under drained conditions as a function of uniaxial compressional stress with axial (principal) stress levels increasing from 0.2 to 3 MPa and subsequently

unloaded to 0.2 MPa using a triaxial Hoek cell. The ratio of the confining stress (radial stress) to the axial stress is determined based on the values of the coefficient of earth pressure at rest (K_0) reported by Jessen et al. (2011) and by Krogsbøl et al. (2012). The uniaxial stress and the uniaxial strain (uniaxial deformation) were measured simultaneously during the elastic wave velocity measurements, so the static drained modulus of uniaxial strain (M_{drain}) can be determined from the mechanical loading compaction curve.

Elastic wave velocity

During geotechnical testing elastic wave velocity (i.e. ultrasonic velocity with a frequency of 200 kHz) was measured for the compressional wave (P-wave, Vp) and shear wave (S-wave, Vs). The determination of the arrival time for P-wave is taken as the first break arrival of the waveform which is relatively easy to pick. Knowing the arrival times of transmitted ultrasonic pulses, the system delay times, and the actual sample length corrected for deformation, the elastic wave velocity was computed. In this study, only the elastic wave velocities measured in the vertical direction (on the 10 vertical core plugs) are used in the further discussion.

Elastic modulus of Palaeogene clay

The P-wave modulus (M) and the S-wave modulus (G) describe the propagation of acoustic elastic waves. In this study, the P-wave velocity (Vp) and the bulk density (ρ_b) of the naturally water saturated Palaeogene clay samples were measured. Thus, the elastic undrained uniaxial P-wave modulus was calculated as follows:

$$M_{sat} = \rho_b V_p^2 \qquad (2)$$

The static drained modulus (M_{drain}) is an elastic property describing the stress increment ($\Delta\sigma$) relative to the strain increment ($\Delta\varepsilon$) under linear elastic uniaxial confined condition:

$$M_{drain} = \frac{\Delta\sigma}{\Delta\varepsilon} \qquad (3)$$

The static uniaxial compressional drained modulus (M_{drain}) of each sample is determined on a series of selected slopes on the compaction curve. The M_{drain} was compared with both the undrained, uniaxial compressional modulus (M_{sat}) and the dry uniaxial compressional modulus (M_{dry}). The M_{sat} was estimated by using equation (2). The M_{dry} was estimated from M_{sat}, porosity (ϕ) and uniaxial mineral modulus (M_{grain}) according to approximated Gassmann's equation (Gassmann 1951, Mavko et al. 1998):

$$M_{dry} = \frac{M_{sat}\left(\phi M_{grain}/M_{fl} + 1 - \phi\right) - M_{grain}}{\phi M_{grain}/M_{fl} + M_{sat}/M_{grain} - 1 - \phi} \qquad (4)$$

where M_{fl} is the P-wave modulus for the pore water which is assumed here as 2.4 GPa.

In order to do this, we must establish uniaxial mineral modulus (M_{grain}): we assumed that Young's modulus of grains to represent a lower bound for M_{grain}. Young's

modulus of grains (E), in GPa, can be estimated from grain density (ρ_g), in kg/m^3, according to the correlation of Chen & Evans (2006):

$$E = -377 + 0.189\rho_g \quad (5)$$

Biot's coefficient for elastic deformation (β) can thus be calculated according to Alam et al. (2012):

$$\beta = \left(1 - \frac{M_{dry}}{M_{grain}}\right) \quad (6)$$

Results

Geotechnical classification data

Results from geotechnical classification tests done on Palaeogene clay were collected from Jessen *et al.* (2011) and tabulated in Table 1. These data include initial water content (w_i), wet bulk density (ρ_b), specific gravity of solids (d_s), liquid limit (w_L), plastic limit (w_P), plasticity index (I_P), consistency index (I_C), and calcium carbonate ($CaCO_3$) content (CC) which is the ratio between weight of calcium carbonate and total weight of grains. The Palaeogene clay from the Ølst Formation is very rich in smectite content (samples no. 31 and 93). It shows higher moisture content, lower bulk density and higher porosity as well as higher consistency index (I_C) than the other four Palaeogene clay formations.

XRD and BET surface area

The XRD analysis reveals the presence of smectite, illite, kaolinite and chlorite minerals. Smectite and Illite occur in all samples and form a major part of the clay mineral assemblage (Table 1). In most samples, the smectite content exceeds that of illite. Smectite is the most important constituent of the clay fraction, where it often forms more than 50% of the solid of some Palaeogene clay samples. Kaolinite and chlorite form a minor part of the clay mineral fraction of most of the analysed Palaeogene clay samples. However, the amount of chlorite is lesser than that of kaolinite.

The XRD results show a rather significant variation in smectite content within the five Palaeogene clay formations. Generally, the variation in clay mineralogy within each Palaeogene clay type is rather significant. The Røsnæs Clay is rich in smectite, illite and relatively poor in Kaolinite and chlorite. The Holmehus and Ølst Clays are very rich in smectite, poor in kaolinite and chlorite. The Lillebælt Clay is relatively poor in illite. The Æbelø Clay is very poor in kaolinite and chlorite, but relatively rich in illite.

The results of the measured BET surface area of the 10 Palaeogene clay samples are reported in Table 1. The Palaeogene clays show quite similar surface area above 60 $m^2\ g^{-1}$ in average. Plots of the plasticity index and of the Biot's coefficient versus smectite content and BET surface area are shown in Fig. 3a-b and in Fig. 3c-d, respectively. Fig. 3a shows two trends for Røsnæs clay and one trend for the rest of the other Palaeogene clays. The plot of plasticity index versus BET surface area shows relatively clear trend which indicates that plasticity index may be linked with

BET surface area (Fig. 3b). There is no correlation between the Biot's coefficient and smectite content or BET surface area (Figs. 3c, d).

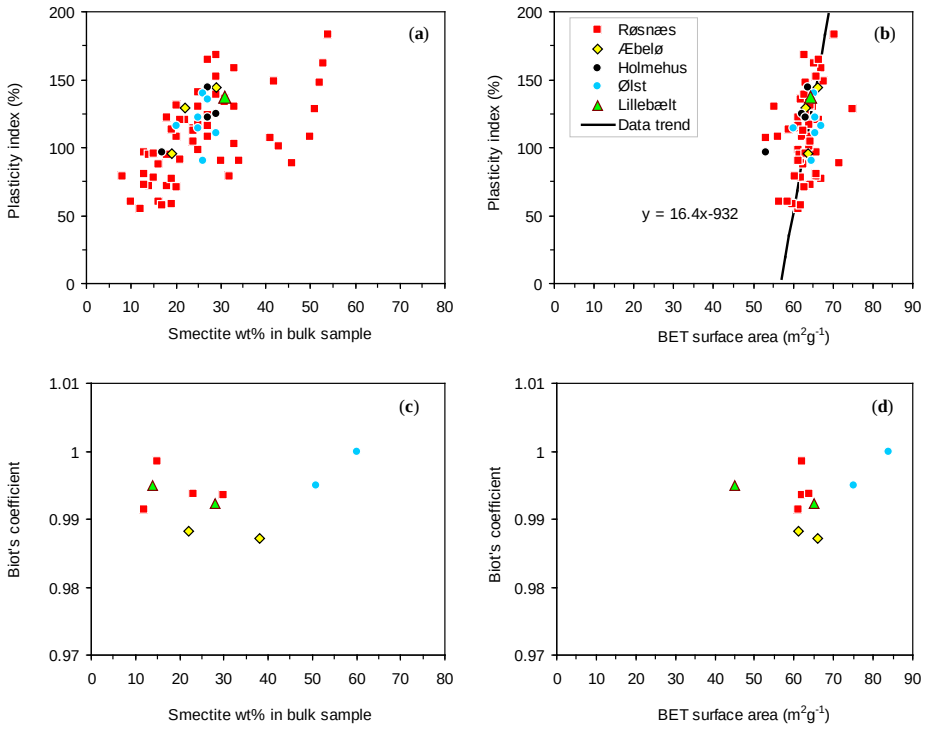

Fig. 3. Plots of plasticity index (%) versus: (**a**) smectite content, and (**b**) BET surface area. Biot's coefficient versus: (**c**) smectite content, and (**d**) BET surface area.

Stress–strain relationship

Results of the mechanical loading of the naturally water-saturated Palaeogene clays, subjected to a maximum of 3 MPa uniaxial stress, are displayed in Fig. 4. This figure illustrates the drained behaviour of the studied Palaeogene clays. Most of the samples show elastic stress–strain behaviour with the highest deformation of sample 29. The samples 29, 95 and 8 are highly compacted relative to the other 7 samples. This may be due to their low smectite content which allows water to squeeze out faster than from those with high smectite content. The results show similarity in elastic deformation pattern. Generally, the studied Palaeogene clays are deformed less and retained high porosity along the whole stress path from 0.2 to 3.0 MPa (Figs. 4 &5). This means the pore-water expels slowly due to the low permeability. Generally, this agrees with the compaction behaviour of smectite-rich clays of Mondol *et al.* (2008).

Elastic wave velocity

The P-wave velocity is sensitive to both clay mineralogy (Fig. 6a) and to the axial stress (Fig. 6c).

Elastic moduli of Palaeogene clay

Fig. 7 shows plots of the static drained uniaxial compressional modulus (M_{drain}) as obtained from mechanical loading (black rectangular); the dynamic undrained uniaxial compressional modulus (M_{sat}) as calculated from Vp and ρ_b (green triangular); and the dry uniaxial compressional modulus (M_{dry}) as estimated according to Gassmann (1951) (red circles). An estimate for the mineral modulus (M_{grain}) was

found within the range of 120–140 GPa based on Chen & Evans (2006). The present results show that the M_{sat} is significantly higher than the M_{drain}. Both of them increase with stress. There is no large difference between the M_{drain} and M_{dry}. However the M_{dry} is higher than the M_{drain}. The reason for this difference is probably that M_{drain} accounts for additional plastic deformation.

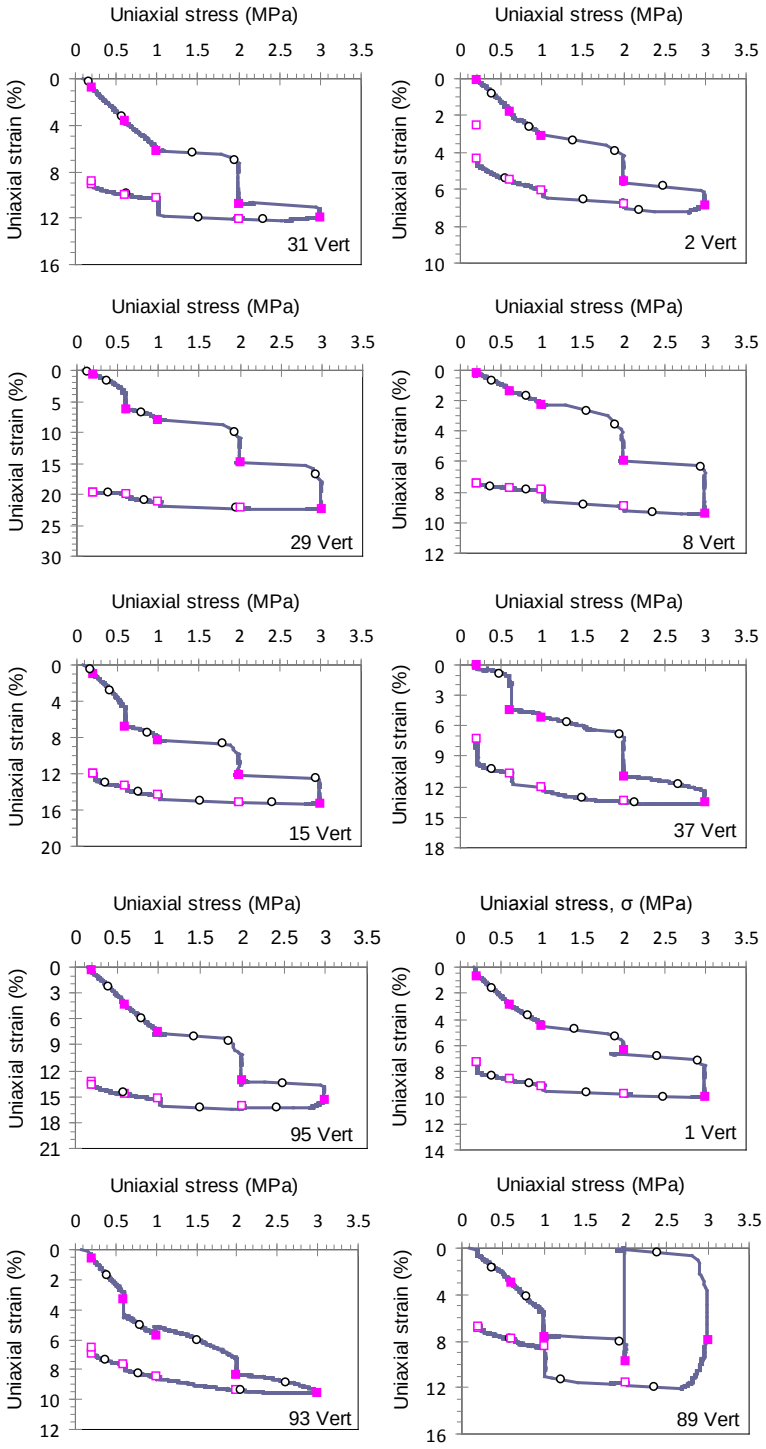

Fig. 4. Stress–strain curves produced during uniaxial confined compressional test of ten vertical core plugs under drained conditions. Open circles on the loading curves indicate the mid point of the part of the curve used for obtaining the M_{drain}. The closed and open rectangles indicate stress levels at which the elastic wave velocities were measured during loading and unloading, respectively.

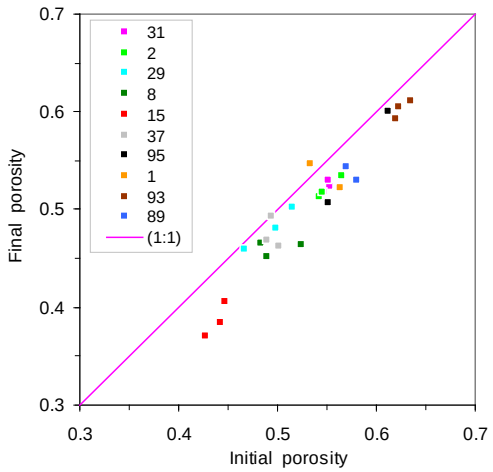

Fig. 5. Cross plot of final versus initial results of total porosity. Each sample is represented by three data points measured in vertical, horizontal and 45^{o} orientations (directions) with respect to the depositional bedding. The 1:1 line is shown for reference.

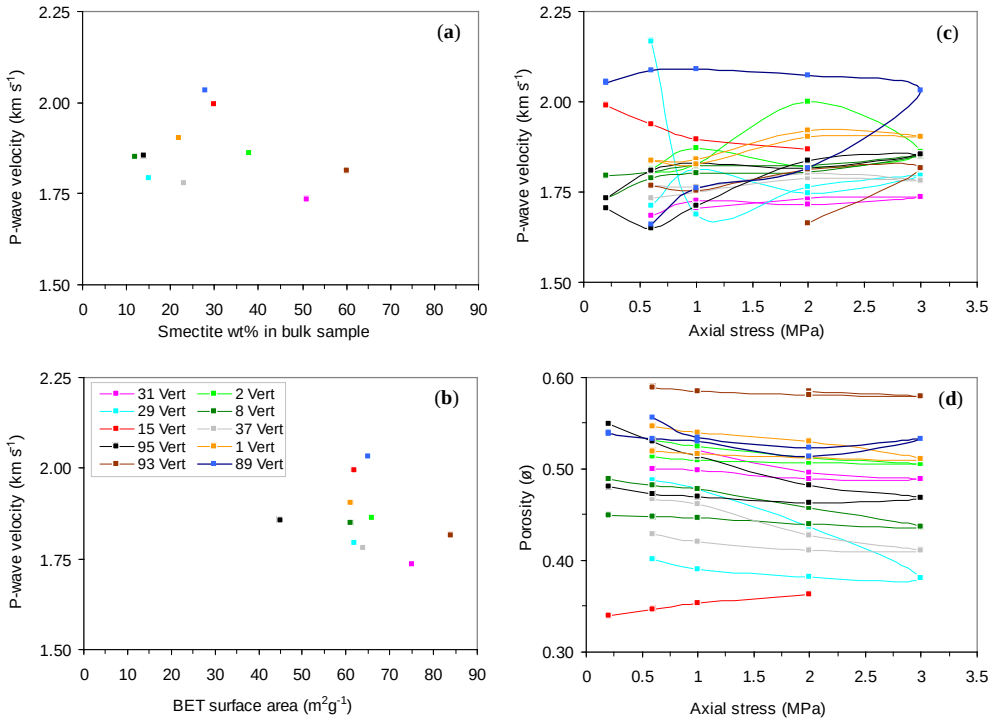

Fig. 6. P-wave velocity measured during loading and unloading plotted versus: (**a**) smectite content; (**b**) BET surface area; (**c**) axial stress; and (**d**) porosity change calculated using equation (1) plotted versus axial stress. The P-wave velocity data plotted in (**a**) and (**b**) are those measured at the 3 MPa axial stress.

Biot's coefficient for elastic deformation

Biot's coefficient (β) in all cases was found to be lower than but close to one. It apparently decreases with stress (Fig. 8) as a result of the plastic component in the mechanical deformation.

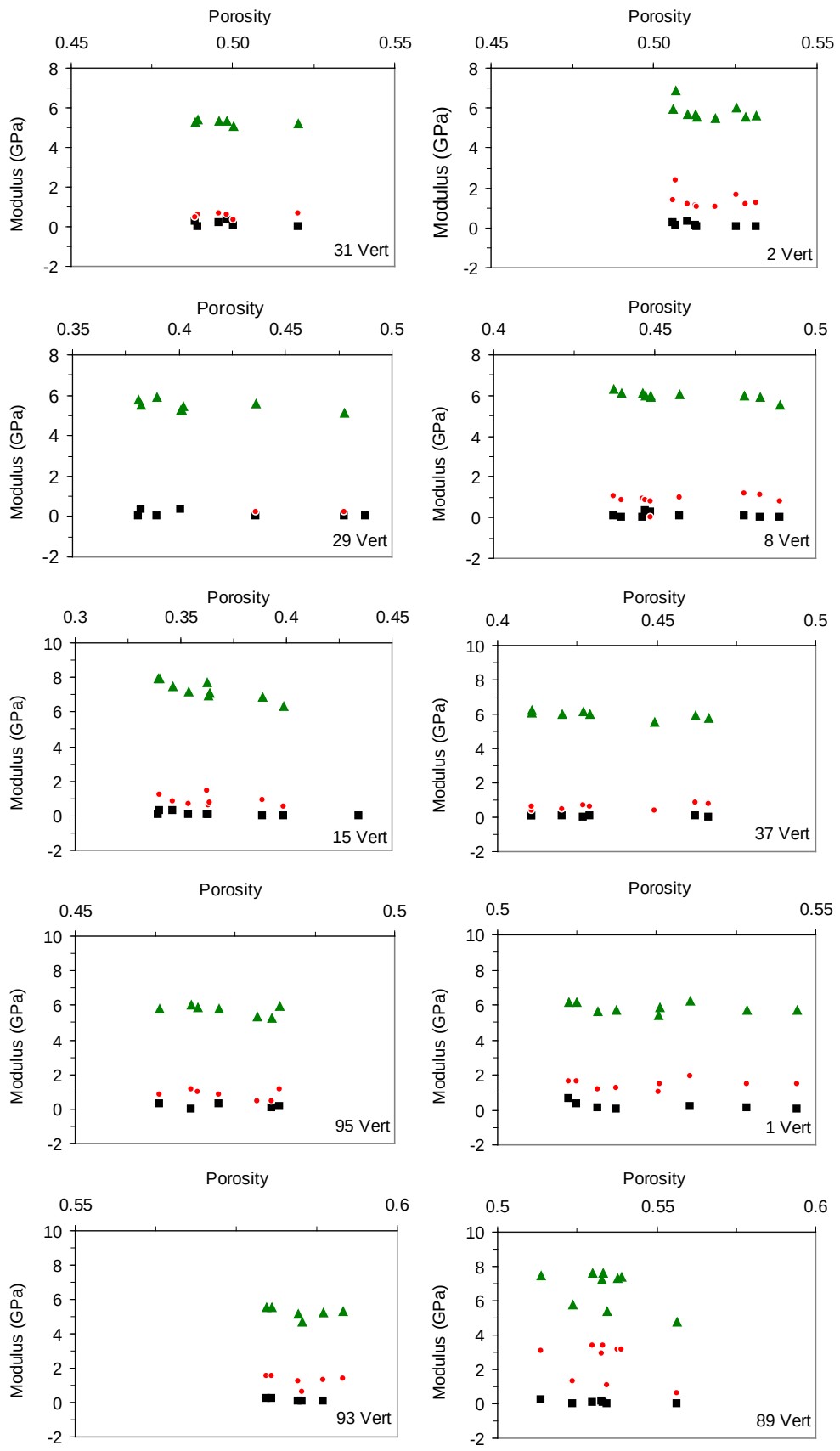

Fig. 7. Plots of M_{sat} (green triangular), M_{drain} (black rectangular), and M_{dry} (red circles) for both loading and unloading stress paths plotted versus porosity. The sample number is indicated in the bottom right-hand corner of each plot.

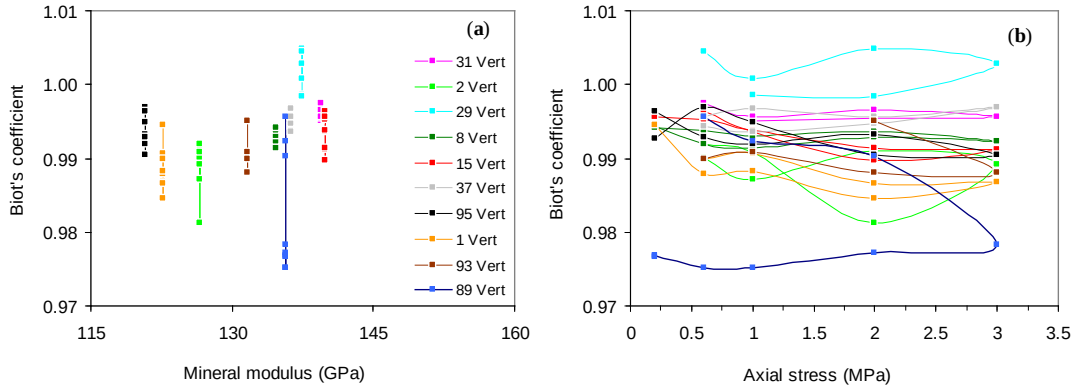

Fig. 8. Biot's coefficient calculated for the mechanical loading and unloading on the ten Palaeogene clay samples plotted versus mineral modulus and axial stress.

Discussion

Discussion of Geotechnical data

The studied Palaeogene clay samples are not fully saturated (Table 1). This may be due to some water lost during the preparation and handling of the core plugs resulting in sample trimming, weighing and sample mounting into the triaxial Hoek cell for consolidation testing. According to Terzaghi (1923), consolidation involves decrease in water content of a saturated soil without replacement of water by air. During the present drained tests, the volume of the studied Palaeogene clay reduced only when the porosity is reduced by squeezing the pore-water out of the pores. This can happen over a period of time during mechanical loading process, resulting in settlement which is an important concept in geotechnical engineering in the design of certain structural foundations. For example, the construction of high-rise structures over highly compressible sediments poses a considerable design constraint.

We aimed here to see which physical property is a main controlling factor for the elasticity of the studied Palaeogene clay and whether we can explain the deformation behaviour from elasticity alone. When $\beta = 1$ which is the highest value it can be, the sediment follows the normal compaction trend according to Terzaghi (1923) who assumes drained condition but in this situation, there is no elastic deformation at all, everything here is plastic deformation. We already stated that the pore space and structure of the studied Palaeogene clay are dominated by smectite which has closed pore system (i.e. very poor pore connectivity) and thus behaves as sponge. Consequently, β should be less than 1.

The obtained mineral modulus based on the correlation of Chen and Evan (2006) results in β of 0.97 to 1.00 which is low enough to describe the deformation of the studied Palaeogene clay as predominantly elastic.

Conclusions

Elastic deformation properties of naturally water saturated Palaeogene clays were determined by using elastic wave velocity measured during triaxial testing under drained conditions. The studied Palaeogene clay is rich in smectite and the smectite content controls the physical properties of the studied clay. When the uniaxial mineral

modulus is predicted from grain density, then the drained purely elastic modulus (M_{dry}) can be predicted by Gassmann substitution. It is higher than but close to the geotechnically obtained drained uniaxial compressional modulus (M_{drain}). The obtained results can aid in the estimation of geotechnical drained elastic modulus from bulk density and elastic wave velocity. Our results may have applications in engineering practice, including structural design and slope stability analysis. The obtained results indicate that the solid frame of the studied Palaeogene clay behaves elastically.

Acknowledgments

We thank Femern A/S for providing samples and for acceptance to publish the presented data. Sinh Nguyen and Vita Larsen are thanked for technical assistance in the laboratory.

References

Alam, M. M., Fabricius, I. L. & Christensen, H. F. 2012. Static and dynamic effective stress coefficient of chalk, *Geophysics*, **77**, 1–11.

Brindley, G. W. 1961. Quantitative analysis of clay mixtures. In: Brown G, editor. The X-ray identification and crystal structures of clay minerals. London: Mineralogical Society, 489–516.

Brown, G. 1961. The X-ray identification crystal structures of clay minerals. Crystal structures of clay minerals. The Mineralogical Society, London, 544p.

Brunauer, S., Emmett, P. H. & Teller, E. 1938. Adsorption of gases in multimolecular layers. *Journal of the American Chemical Society*, **60**(2), 309–319.

Chen, B. & Evans, J. R. G. 2006. Elastic moduli of clay platelets. *Scripta Materialia*, **54**, 1581–1585.

Clayton, C. R. I. 2011. Stiffness at small strain: research and practice. *Geotechnique*, **61**, No. 1, 5-37 [**doi:** 10.1680/geot.2011.61.1.5].

Femern A/S. Geo Information System. www.https://geoarchive.fehmarnlink.com.

Gassmann, F. 1951. Uber die elastizitat poroser medien. *Veirteljahrsschrift der Naturforschenden Gesellschaft in Zurich*, **96**, 1–23.

Hornby, B. E. 1998. Experimental laboratory determination of the dynamic elastic properties of wet, drained shales. *Journal of the geophysical research*, **103**, 29945–29964.

JCPDS-ICDD: JCPDS – International Center for Diffraction Data. PDF-2 Data Base, Version 2.13 (it is a CD). Copyright 1987-1993. Swarthmore, PA 19081 – USA.

Jessen, S. B., Hansen, P. B., Hesthaven, M. & Christensen H. F. 2011. Fehmarn Belt Fixed Link, Advanced Laboratory Testing, Clays of Palaeogene origin, Geotechnical Data Report prepared by GEO, 31/03/2011.

Jones, L. D. & Terrington, R. 2011. Modeling Volume Change Potential in the London Clay. *Quarterly Journal of Engineering Geology and Hydrogeology*. **44**, 109–122.

Kaarsberg, E. A. 1958. Introductory studies of natural and artificial argillaceous aggregates by sound-propagation and X-ray diffraction methods. *Journal of Geology*, **67**, 447–472.

Krogsbøll, A., Hededal, O. & Foged, N. 2012. Deformation properties of highly plastic fissured Palaeogene clay–Lack of stress memory? *DGF-Bulletin* **27**, 133–140.

Mavko, G., Mukerji, T. & Dvorkin, J. 1998. The Rock Physics Handbook. The Press Syndicate of the University of Cambridge. Cambridge, UK., 329 p.

Mondol, N. H., Bjørlykke, K. & Jahren, J. 2008. Experimental compaction of clays: relationship between permeability and petrophysical properties in mudstones. *Petroleum Geoscience*, **14**, 319–337.

Rambøll/Arup 2011. Geotechnical Data Report. Summary of geological conditions. GDR 01.3-002. April 2011.

Sheldon, E. 2010. Fehmarn Belt Fixed Link Pre-Quaternary Biostratigraphy, GEUS Report. 15/12/2010.

Terzaghi, K. V. 1923. Die Beziehungen zwischen Elastizitat und Innendruck. *Mathematisch-Naturwissenschaftliche Klasse Abteilung 2A*, **132**, 105–124.

IV

Paper IV

Burial diagenesis of Eocene chalk

Ahmed Awadalkarim and Ida L. Fabricius

Presented at the 72nd European Association of Geoscientists and Engineers (EAGE) Conference & Exhibition incorporating SPE EUROPEC 2010, held in Barcelona, Spain, 14–17 June 2010. Volume 4, pp.2724–2728

Introduction

During the Eocene, pelagic carbonate-rich sediments (ooze, chalk and limestone) were deposited in the Atlantic Ocean. Porosity of newly deposited ooze sediment is very high, but it reduces with burial. The Eocene chalk of the Atlantic Ocean is not pure calcite as reflected in its huge variations in physical properties. Texture could also play an important role in determining physical properties. However, chalk porosity is a main determining factor for other properties. Porosity reduction mechanisms in pelagic carbonate-rich sediments of different ages are already addressed by several authors (Fabricius et al., 2008).

Mechanical compaction, pore stiffening and pore-filling cementation are defined by e.g. Fabricius et al. (2008) as three different diagenetic processes. Mechanical compaction reduces porosity by shifting particles relative to each other. Pore-stiffening cementation fuses grains without porosity reduction, whereas pore-filling cementation is accompanied by porosity reduction.

In this paper we address burial diagenesis of Eocene chalk as reflected on porosity. Our main objective here is to study the influence of chalk burial depth (i.e. overburden stress and fluid pressure) on the physical properties of Eocene chalk from Atlantic Ocean. Previous authors (Grützner and Mienert, 1999; Fabricius et al., 2008) included chalk data from different geological ages in their studies, however, in this paper only Eocene chalk is considered to limit the effect of time in diagenesis. The geological information and water depths data used in this paper are obtained from the proceedings of the Ocean Drilling Program (ODP) and Integrated Ocean Drilling Program (IODP) initial reports of the Atlantic Ocean sites (Figure 1). Shipboard physical properties data, such as water-saturated bulk density, P-wave velocity and porosity were obtained from the Janus Web Database.

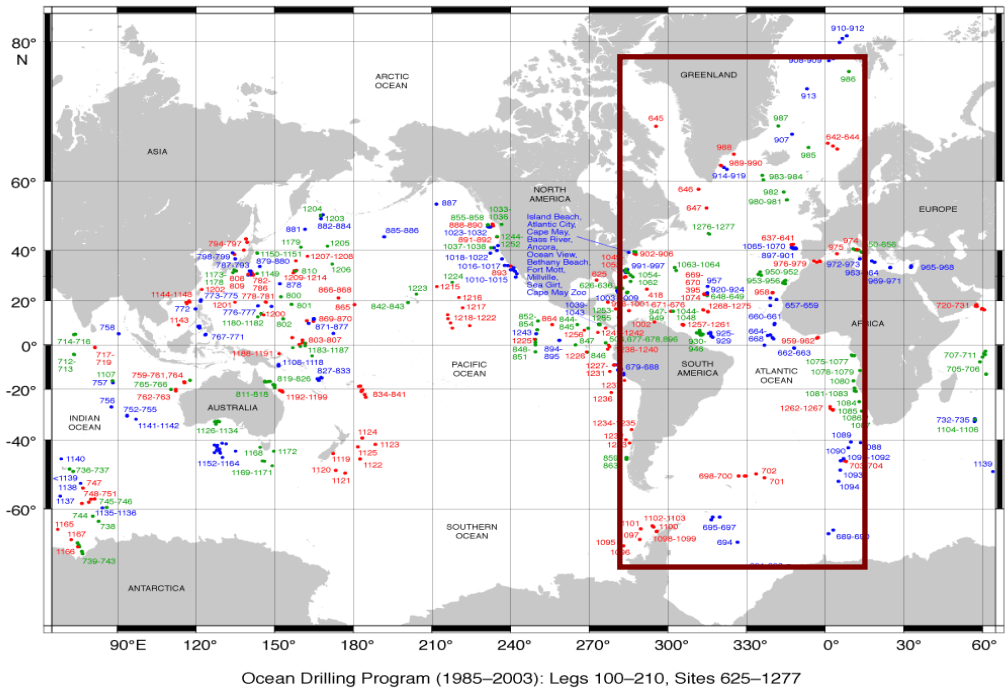

Figure 1 *Map showing the locations of the ODP sites included in this paper. The studied area is marked with a rectangle (http://www.iodp.org/).*

Theory and methods

Shipboard bulk density, grain density and porosity were measured by gravimetric methods on discrete samples. Shipboard sonic velocity was measured on split core sections or on cut samples. We used the compressional wave velocity (Vp) data measured in the vertical direction of the cores.

In the present study, we calculated the total vertical stress, σ, by adding the weight of the water to the weight of the column of sediments:

$$\sigma = g\,(h_w * \rho_w + \Sigma(\rho_b * h_{di})\,), \qquad (1)$$

Where g is acceleration of gravity assumed to be 9.82 m/s^2; h_w is water depth (m) measured from sea level, ρ_w is water density (1.1 g/cm^3) ρ_b is the wet bulk density from shipboard and h_{di} is depth interval (m) between measured data points.

Fluid pressure, P_f, was calculated under assumption of a hydrostatic pressure gradient:

$$P_f = g * h*\rho_w \qquad (2)$$

Where h is the measured depth below sea level.

The effective stress, σ´ is first calculated for uncemented rocks as defined by Terzaghi (1923).

$$\sigma' = \sigma - P_f \qquad (3)$$

For cemented rocks the effective stress, σ' may be calculated according to Biot, 1941.

$$\sigma' = \sigma - \beta P_f \qquad (4)$$

Because of the high water depth in the ocean (which reach about 4356 m at site 154-929E) β has a relatively large influence on the estimation of effective stress as defined by equation 4.

Equation 4 describes how as cementation increases, the pore pressure will be less effective in counteracting the overburden stress. β is a measure of sediment stiffness. The σ´ may be used to discuss the effect of the burial diagenesis (Fabricius et al., 2008).

To apply Equation 4 we need to obtain β. In a linear-elastic isotropic sediment, β may be calculated from elastic moduli, and if only one modulus is available (as the case in present study), by iso-frame modeling, IF (citation in Fabricius et al., 2008). β may be expressed as:

$$\beta = (1-K_{dry}/K_o) \qquad (5)$$

Where K_{dry} and K_o are bulk modulus of dry rock and bulk modulus of mineral material making up rock respectively (Biot and Willis, 1957).

Results and discussion

When total vertical stress, σ, is plotted versus porosity (Figure 2), the compaction trend is not easy to define. However, when Terzaghi's effective stress is plotted versus porosity (Figure 3a), mechanical compaction of the chalk is visible and it is possible to interpret porosity decline trends. The steep green curve on Figure 3a shows porosity reduction due to compaction from 70% to about 30%. The mechanical compaction is mainly governed by the effective stress (σ´) as defined by Terzaghi (1923) (Equation 3).

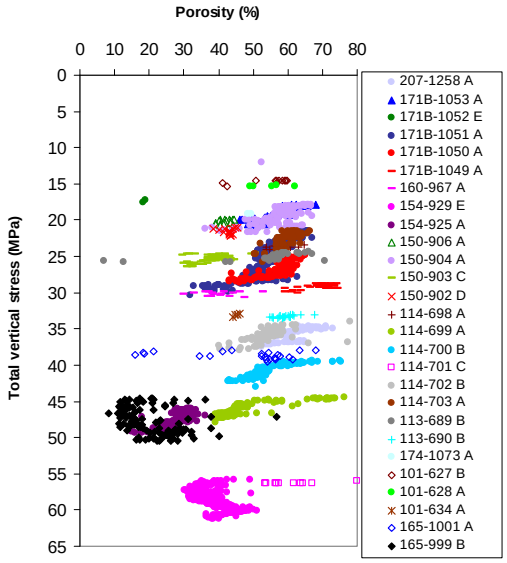

Figure 2 *Chalk porosity data versus total vertical stress.*

The steep blue curve in Figure 3a represents the mechanical compaction trend of Fabricius et al. (2008) from the Ontong Java Plateau in the Pacific. The present data shows a broader data trend than the Ontong Java Plateau data. The blue semi-horizontal curves represent pore-filling cementation trends for the Pacific chalk. The present data seems to show two cementation fronts one below and the other above the Ontong Java Plateau cementation front trend. The difference in front location could be due to different temperatures, but we have not made temperature model yet for the present data. The effect of texture may also play a role here. The process of pore-filing cementation will cause porosity to decrease with constant effective stress state. The present porosity data does not show a clear pore-stiffening trend as the Ontong Java Plateau chalk does.

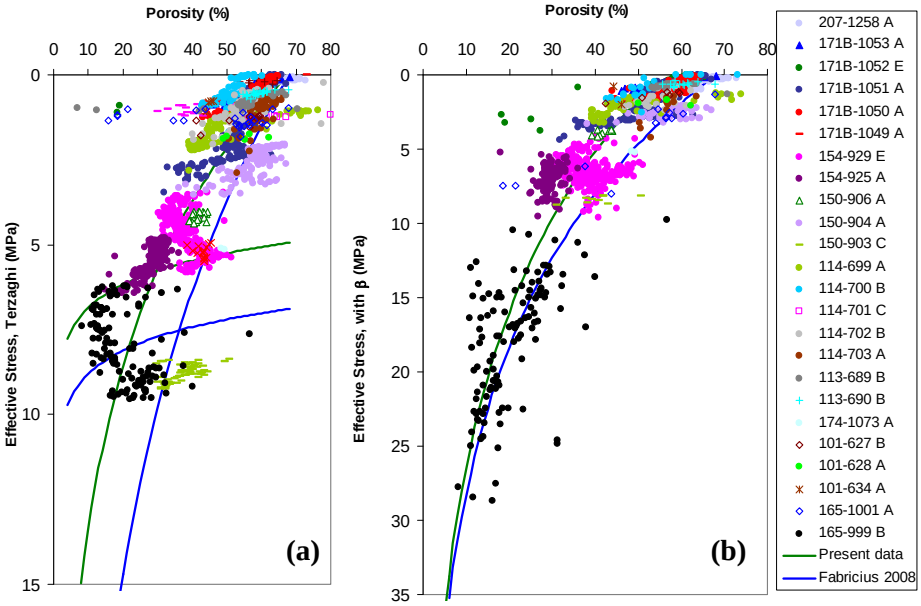

Figure 3 *Chalk porosity data versus Terzaghi's effective stress (a) and Biot's effective stress (b). The blue and green curves represent the mechanical compaction as well as pore-filling cementation trends for Fabricius et al. (2008) data and the present data respectively.*

When the effective stress calculated by taking β into account is plotted versus porosity, it shows that the porosity decreases with effective stress follows a smooth trend (Figure 3b). This is in agreement with data of Fabricius et al. (2008) for samples from water saturated chalk. When Equation 1 is used, the porosity covers a wide range for a given effective stress as a reflection of difference in texture.

Cement precipitation is a chemical process. The source of pore-filling cementation in the studied Eocene chalk is unknown, but it could be assumed as a result of pressure dissolution at the clay-calcite interface in a stylolite (Maliva and Dickson, 1992; Fabricius and Borre, 2007), rather than at calcite-calcite interface. Fabricius et al. (2008) suggests that the transition of opal-CT to quartz, rather than the precipitation of calcite, is more likely the controlling chemical process for cement precipitation. Because the opal-CT transformation depends on temperature and time and it will change the concentration of Si in the pore water. The pore-filling cementation of this Eocene chalk may be in agreement with this conclusion.

Figure 3 shows that faster porosity reduction occurs in the shallower ooze zone. Porosity reduces at a slower rate in the deeper chalk. The reason for the high porosity shown in the ooze zone may be due to high content hollow micro fossils. Below in the deeper chalk zone, the rate of porosity reduction is slightly lower than in shallower ooze zone. The low porosity (ranges between 5-15%) of some samples from sites 113-689B, 171B-1052E and 165-1001A, is probably due to the poor sorting of particles as a results of high content of fine grained non-carbonate fraction.

Conclusions

The porosity decreases by increasing burial depth either via mechanical compaction or pore filling cementation. Our porosity-effective stress trends on Eocene chalk do not follow the trends for the Ontong Java Plateau which spans a time interval from the Cretaceous to present. Mechanical compaction of Eocene chalk is a result of increasing effective stress. Pore filling cementation may be caused indirectly via pressure dissolution at stylolites. Deep burial depth characterizes by a slower, more linear rate of compaction. Our data indicates that mechanical compaction is the principal agent of porosity reduction in the chalk, at least down to about 5 MPa effective stress corresponding to a porosity of about 35%.

References

Biot, M.A., and Willis, D.G., 1957. The elastic coefficients of the theory of consolidation. Journal of Applied Maechnics, December. 594-601.

Fabricius, I.L. and Borre M.K. 2007. Stylolites, porosity, depositional texture, and silicates in chalk facies sediments. Ontong Java Plateau – Gorm and Tyra fields, North Sea. Sedimentology 54, 183-205.

Fabricius, I.L., Gommesen, L., Krogsbøll, A., Olsen, D., 2008. Chalk porosity and sonic velocity versus burial depth: influence of fluid pressure, hydrocarbons, and mineralogy. AAPG Bull 92 (2), 201–223.

Grützner, J., Mienert, J., 1999. Physical property changes as a monitor of pelagic carbonate diagenesis: an empirically derived diagenetic model for the Atlantic Ocean basins. AAPG Bull 83 (9), 1485–1501.

Maliva, R.G. and Dickson, J.A.D, 1992. Microfacies and diagenetic controls of porosity in Creataceous/Tertiary chalks, Eldfisk field, Norwegian North Sea. American Association of Petroleum Geologists Bulletin 76, 1825-1838.

Terzaghi, K., 1923. Erdbaumechanik auf bodenphysikalischer Grundlage. Franz Deuticke, Leipzig, Germany. 399 pp.

V

Paper V

The influence of Biot's coefficient on the estimation of vertical effective stress on deep-sea sediments

Ahmed Awadalkarim and Ida Lykke Fabricius

Presented at the 74th EAGE Conference & Exhibition incorporating SPE EUROPE 2012, held in Copenhagen, Denmark, 4–7 June 2012

Introduction

Shale is the most common sedimentary rock worldwide. Shale contains substantial quantities of clay minerals and quartz, in addition to variable amount of organic content. Those rich in organic content could be a source rock for hydrocarbons. In many oil fields, shale forms the geologic seal that prevents hydrocarbons to escape from the reservoir. In some basins as in the United States (e.g. the Barnett Shale in the Fort Worth basin of North Central Texas), shale also form reservoir for natural gas (Joseph, 2005). Burial diagenesis of shale has received great attention from both industrial and academic researchers. Shale diagenesis at different basins with different burial depths, and geological ages have been addressed by several authors (e.g. Jeans 1986; Bjørlykke 1999, Moore 2000 and references therein). Physical properties of shale vary due to initial mineralogical and burial diagenesis.

In sedimentary basins, porosity decreases whereas bulk density and sonic velocity increase with depth due to the combined effects of compaction and cementation. The rate of burial and the geothermal gradient of the basin control sediment compaction (Potter et al. 2005). The compaction effects on porosity and on sonic velocity of shale have been studied by several authors. Compaction of sediments is a function of its mineralogical composition, effective stress, and the time-temperature history (Japsen, 2007). Physical properties of shale are controlled by mineralogical composition and burial depth. Texture, grain size and fabric could also play an important role in shale compaction. The smectite content is important for the compaction behavior of shale because of its small grain size, low permeability, and very high surface area.

In this paper we address the changes in physical properties of the Eocene and Paleocene shale from the Atlantic Basin, as a function of burial diagenesis. We also show the influence of using correct Biot's coefficient (β) on the estimation of vertical effective stress. We do this by correlating porosity and P-wave velocity data with the calculated effective stresses to show how different vertical effective stress influences shale compaction trends. This may provide a basis to understand how physical properties vary with effective stress and shale mineralogy. Our results may be relevant for drilling, basin analysis modeling, seismic interpretation and hydrocarbon exploration.

Theory and methods

The geological information and the data used here were obtained from the proceedings of the Ocean Drilling Program (ODP) initial reports of the Atlantic Ocean sites (Figure 1a).

The Eocene and Paleocene shale data from 24 ODP drill sites were included in this paper. Shipboard bulk density, grain density, and porosity were measured by gravimetric methods on discrete samples. Shipboard sonic velocity was measured on water-saturated shale samples with no confining pressure or pore-pressure involvement. Shipboard P-wave velocity measurements were made in the horizontal and vertical directions with respect to the core axis. The P-wave velocity data measured in the vertical direction of the cores were used here. The velocity data were not corrected to the in-situ stresses.

The total overburden stress, σ, was calculated, to a fair approximation, as following:

$$\sigma = g\left(h_w \rho_w + \sum_{i=1}^{i=n} (\rho_i h_i) \right) \qquad (1)$$

where g is gravitational acceleration (9.81 m/s^2), h_w is water depth (m) measured from sea level, ρ_w is ocean water density (assumed as 1.1 g cm^{-3}), ρ_i is the water-saturated bulk density of sediments at each data point and h_i is depth interval (m) between measured data points.

The pore pressure, P_p, was calculated under the assumption of a hydrostatic pore pressure as:

$$P_P = gh\rho_w \qquad (2)$$

where h is the measured depth below sea level ($h = h_w + \sum h_i$).

The vertical effective stress was estimated as defined by Terzaghi (1923) and by Biot (1941). Terzaghi's effective stress is appropriate for uncemented sediments where β is unity. It was calculated by subtracting the pore pressure (P_p) from the total overburden stress (σ) as:

$$\sigma' = \sigma - P_P \qquad (3)$$

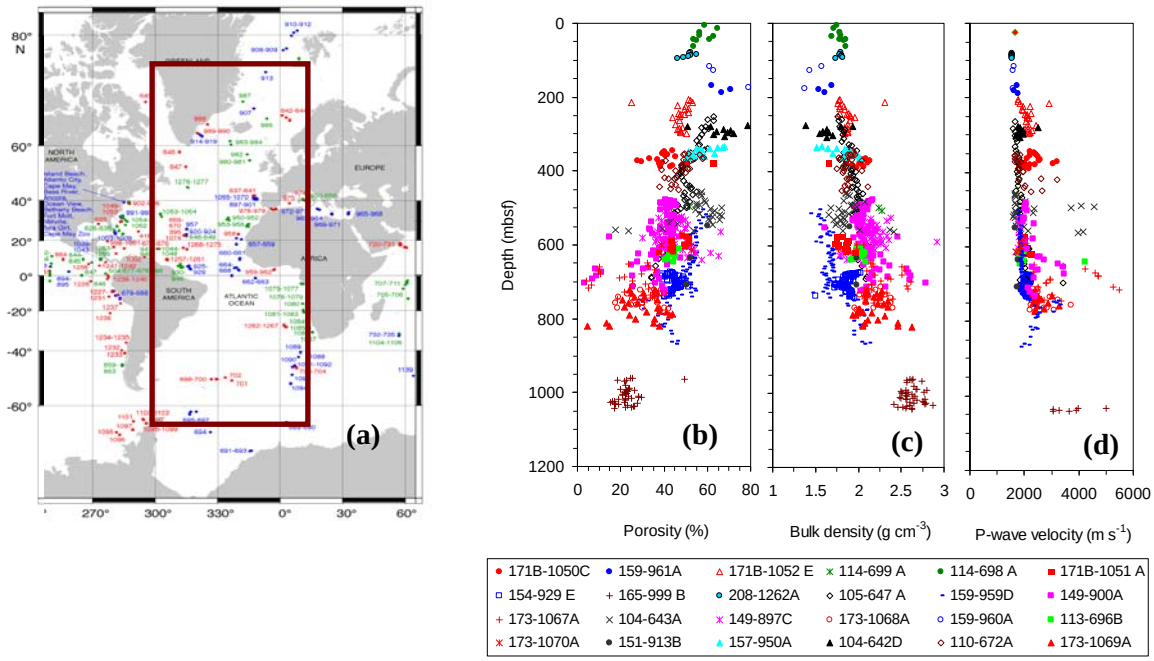

Figure 1: *(**a**) Map showing the locations of the ODP sites. The studied sites are enclosed by a rectangle (modified after http://iodp.tamu.edu/scienceops/maps/odpmap.pdf). Physical properties for the studied shale versus depth below seafloor (mbsf) are shown by (**b**) porosity, (**c**) Bulk density, (**d**) P-wave velocity. Data are from the 24 ODP sites shown in Figure 1**a**. The following example explains how we structure the name for each site; e.g. 154-929E means ODP Leg 154, Site 929, Hole E.*

In cemented rocks, β becomes less than unity and the effect of pore pressure on resisting overburden stress may be reduced (Biot & Willis 1957). For any cemented sedimentary rocks the in-situ vertical effective stress, σ', may be calculated according to Biot (1941) as follows:

$$\sigma' = \sigma - \beta P_P \qquad (4)$$

where β is Biot's coefficient, that is less than unity. It depends on degree of contact cementation.

Because of the high water depth in the Atlantic Ocean, β has a relatively large influence on the estimation of vertical effective stress. In a linear-elastic isotropic sediment, β may be calculated from sonic velocity and density data (e.g. Biot and Willis 1957). In this study, due to the lack of shear-wave velocity data, β was calculated by using iso-frame modelling. The bulk modulus of dry rock (K_{dry}) was calculated from iso-frame values and porosity data. We assumed a critical porosity of 100% and assumed a bulk modulus for shale, K_o, equal to 20.24 GPa (Awadalkarim and Fabricius 2009). Thus, β is expressed as follows:

$$\beta = \left(1 - \frac{K_{dry}}{K_o}\right) \qquad (5)$$

Results and discussion

Figure 1 shows the physical properties data plotted versus depth in meters below seafloor (mbsf). They all show general depth trends. Some data points are off the trend; they may represent a mixture of shale and other lithologies.

Figure 1b shows broader variations in porosity values and in rate of porosity reduction. This variation depends on the shale mineralogical composition and burial depth. The porosity–depth trend shows rapid porosity reduction rate in the shallowly buried shale, and slower porosity reduction rate in the relatively deeply buried shale. The reason for the high porosity (>40%) shown by some shale samples in the depth interval 400–800 mbsf is unknown. However, it may be due to high smectite content. A similar variability in P-wave velocity and density is also noticed at this depth interval (Figure 1c, d). The very low porosity (<20%) shown by some shale samples from 550–700 mbsf is probably due to mixed lithology. During early burial of muddy materials, the porosity–depth trend is mostly affected by packing and ductile grain deformation. Although cementation may occur during shallow burial, it is more common at higher burial depths. The shale diagenesis is mainly controlled by mechanical compaction during shallow burial. In the deeper intervals below 800 mbsf, the rate of porosity reduction is slightly lower than that in the shallower intervals. In this interval, burial stress collapses more and more grains and the individual platelets become more parallel. As a result of this, shale becomes denser and thus P-wave velocity increases. Chemical processes in shale begin at an intermediate diagenetic level (80–140^{o} C), including transformation of smectite to illite and liberation of organic acids from organic matter. Since the maximum reported temperature data for Eocene and Palaeocene shale is not exceeding 80^{o} C. Our deeply buried shale interval may be dominated by both mechanical and chemical compactions. Thus semectite may be transformed into illite as evidenced by higher bulk densities and very low porosity.

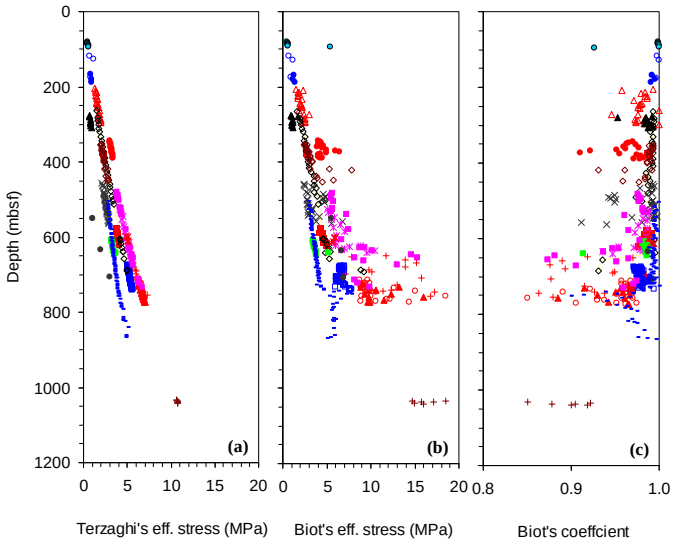

Figure 2: *Depth plots for the calculated vertical effective stresses (**a**) Terzaghi's effective stress, (**b**) Biot's effective stress and (**c**) Biot's coefficient (β). The β is an indicator of sediment stiffness.*

An obvious velocity trend is observed in the shallowly buried shale at the depth from 0–400 mbsf (Figures 1 d), below this depth the velocity data are scattered. Below 800 mbsf burial depth, the velocity increases significantly compared to shallower intervals. At burial depths shallower than 400 mbsf, low velocities and densities of shale may be related to high smectite contents. The variation in P-wave velocity at the same depth is most likely caused by varying mineralogical composition.

The changes in porosity and P-wave velocity are also correlated with the effective stresses (Figure 3). When these data were plotted versus total overburden stress, σ, rather than depth below seafloor, trends are not shown. When the same data are plotted versus Terzaghi's and Biot's effective stress; obvious trends are observed (Figure 3). This implies that porosity reduction is a function of effective stress. The physical properties depth trend could be improved if Biot's effective stress is used instead of Terzaghi's effective stress (Figures 3b, d).

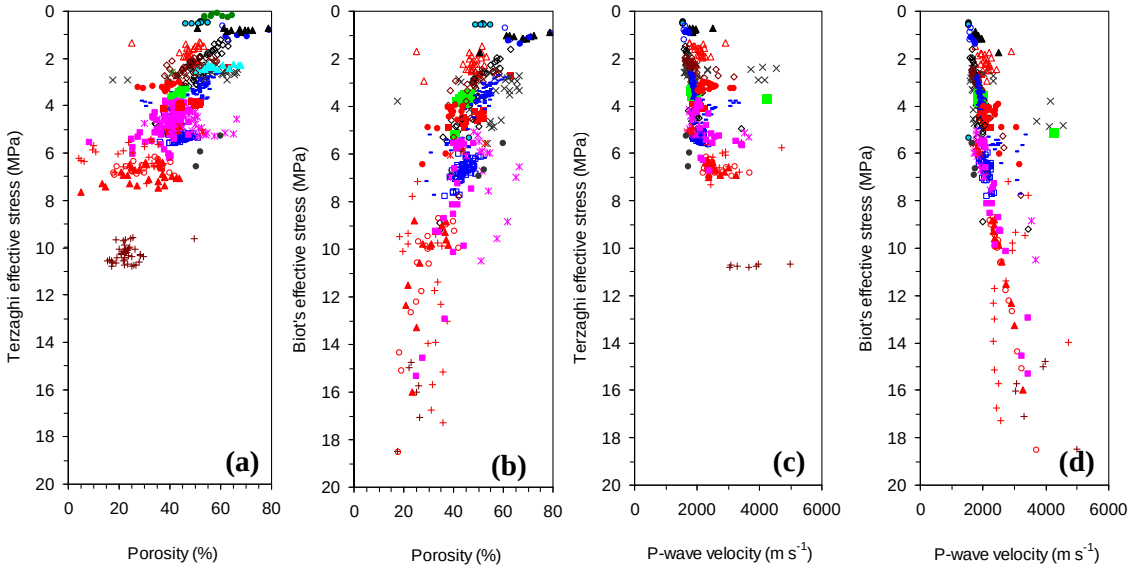

Figure 3: *Porosity data versus (**a**) Terzaghi's, and (**b**) Biot's effective stress .P-wave velocity data versus (**c**) Terzaghi's, and (**d**) Biot's effective stress, for the studied shale.*

Conclusions

The physical properties of shale vary due to the initial mineralogical composition and burial diagenesis. We related the changes in the physical properties to the vertical effective stress due to burial depth. Physical property variations within the same effective stress may be due to variations in shale mineralogical composition. Even for small deviation in β value from 1, a significant effective stress can be obtained. For safety reasons, this is very important to be observed especially when drilling in the deep-water. This is not problem when drilling onshore. Using the Terzaghi's concept to calculate vertical effective stress on cemented sediments leads to underestimation of the actual effective stress and this may cause severe engineering consequences. Therefore, it is more appropriate to use the Biot's effective stress concept to obtain more realistic vertical effective stress.

References

Awadalkarim, A., Fabricius, I.L., 2009. Estimating effective stress in North Sea ooze. An extended abstract, Sound of Geology Workshop. Bergen, Norway.

Bjørlykke, K., 1999. Clastic diagenesis and porosity prediction in sedimentary basins. Am. Assoc. Pet. Geol. Bull. 83, 1877.

Biot, M.A., 1941. General theory of three-dimensional consolidation. Journal of Applied Physics, 12(2), 155-164.

Biot, M.A. and Willis, D.G., 1957. The elastic coefficients of the theory of consolidation. Journal of Applied Maechnics, 24, 594-601.

Japsen, P., Mukerji, T, and Mavko, G., 2007. Constraints on velocity-depth trends from rock physics models. Geophysical Prospecting, 55, 135–154.

Jeans, C. V., 1986. Features of mineral diagenesis in hydrocarbon reservoirs: an introduction. Clay Miner. 21, 429–441.

Joseph, H., Frantz, Jr. and Jochen, V., 2005. Schlumberger. Shale gas.

Moore, D.M., 2000. Diagenesis of Purington shale in Illinois basin and implications for the diagenetic state of sedimentary rocks of shallow Paleozoic basins. The Journal of Geology, 108, 553–567.

Potter, P.E., Maynard, J.B., Depet.ris, P.J., (2005). Mud and Mudstone: introduction and overview. Springer- Verlag Berlin Heidelberg, Germany.

Terzaghi, K.V., 1923. Die Beziehungen zwischen Elastiztat und Innendruck. Mathematisch-Naturwissenschaftliche Klasse Abteilung 2A, 132, 105-124.

VI

Paper VI

Estimating the effective stress in North Sea ooze

Ahmed Awadalkarim, Maria Altaie, Andreas Lyonga, Niels Trads and Ida Fabricius

Presented at the Sound of Geology Workshop held in Bergen, Norway, 6–8 May 2009

Estimating Effective Stress in North Sea Ooze

Ahmed Awedalkarim; Maria Altaie, Andreas Lyonga Keke, Niels Trads, and Ida Lykke Fabricius.

Technical University of Denmark,
Department of Environmental Engineering

The Ormen Lange field is located in the Møre Basin in the southern part of Norwegian North Sea. It contains natural gas in the Egga sand of the Paleocene Tang Formation (Norwegian Petroleum Directorate, NPD). Following the work of Thomsen and Danielsen (1995) on diatomaceous sediments in the Eastern North Sea, we were on the alert for possible diatomaceous sediments or their diagenetic equivalents in the North Sea and noticed reports on the Eocene/Miocene ooze above the reservoir of the Ormen Lange field. We chose to study well 6305/1-1 (where the Egga sand is very thin) and obtained data from NPD.

Diatomites of the exposed Danish Fur Formation (Pedersen and Surlyk, 1983) are highly porous, yet stiff, so we expected that the ooze, also when diagenetically transformed might have a relatively low effective stress coefficient, which would be relevant to find for the purpose of pore pressure prediction. We would then approximate the effective stress coefficient from Biot's coefficient, β:

$$\beta = 1 - K_{dry}/K_o \qquad \text{Equation 1}$$

Where K_{dry} and K_o are effective bulk modulus of dry rock and bulk modulus of mineral material making up rock respectively.
Because of the high water depth over the Ormen Lange field and the assumed hydrostatic pressure in sediments, Biot's coefficient has a relatively large influence on the estimation of effective stress, σ':

$$\sigma' = \sigma - \beta P_f \qquad \text{Equation 2}$$

Where σ is total vertical stress and P_f is pore fluid pressure. Because the Eocene ooze is so old (34-56 Ma) and found below a depth of ca. 1000m below the sea floor corresponding to more than 30°C, in sediments of that age, we expect any original opal-A would have transformed to opal-CT and probably further to quartz (Figure 1). However, for sediments of Miocene age (5 – 23 Ma) and shallower burial depth, opal-A may be preserved.

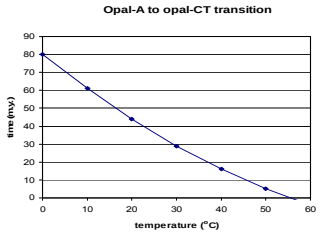

Figure 1. Transformation of opal-A to opal-CT in sediments with low carbonate content (Kastner 1977).

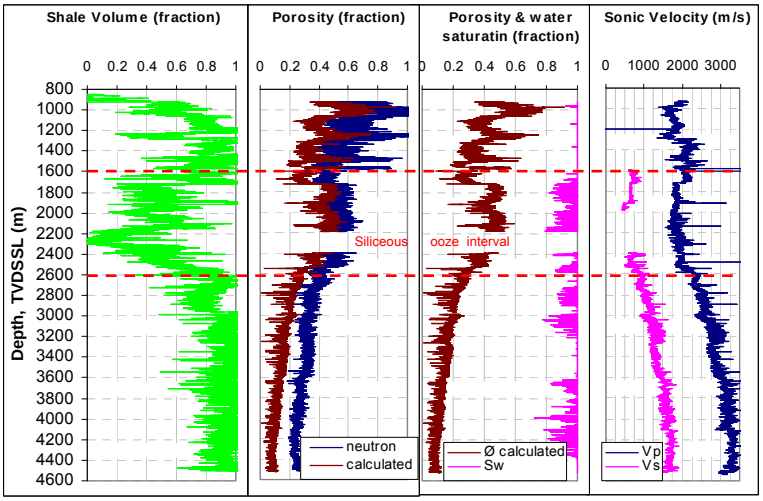

Figure 2. Interpreted logs from well 6305/1-1.

We interpreted the logs under assumption of a mixed diatomite-shale lithology, and found that ooze probably does not contain significant gas (Figure 2). To estimate Biot's coefficient from equation 1, we need information on mineral bulk modulus, K_o. For opal-A and opal-CT, we used values of K_o equal to 5 and 12 GPa respectively, as estimated by using the Hashin-Shtrikman bounds model (Hashin and Shtrikman, 1963) on laboratory measured data on dry samples (Figure 3). For shale, we used bulk shale density, ρ_{sh}, compressinal wave velocity, V_P and shear wave velocity, V_S, as measured in the assumed 100% shale at depth below 3000m (Figure 2), for calculating bulk modulus of shale, $K_{o,\,shale}$.

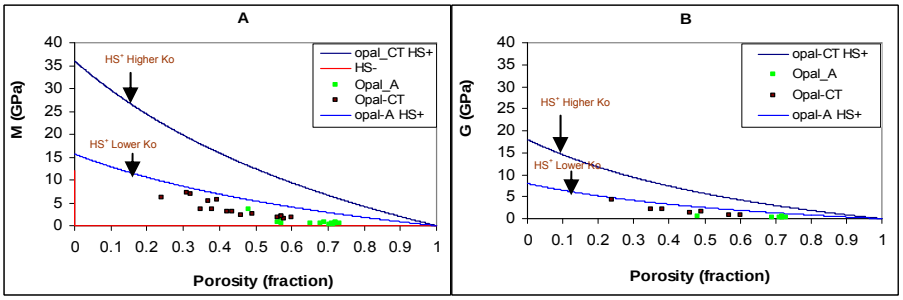

Figure 3. Estimation of mineral bulk modulus of opal-A (lower Ko) and opal-CT (higher Ko) by using Hashin-Shtrikman bounds model (Hashin and Shtrikman, 1963) on laboratory measured data of dry samples. (A) compressional modulus and (B) shear wave modulus.

At every depth point, the resulting K_o was estimated as the average of the Voigt (1910) and Reuss (1929) bounds for the mixing of shale and opal or of shale and quartz. For using equation 1, we also need bulk modulus of the dry rock, K_{dry}. This was found by Gassmann substitution (Gassmann 1951) of logging data under assumption of 100% water saturation. If a content of gas had been taken into account, the resulting K_{dry} would have been lower. The calculated β must thus be seen as an upper bound.

We calculated the total vertical stress, σ, by adding the weight of the water to the weight of the column of sediments:

$$\sigma = g (h_w * \rho_w + h_u * \rho_{av} + \Sigma (\rho_b * h_{log})) \quad \text{Equation 3}$$

Where g is acceleration of gravity, h_w is water depth, ρ_w is density of water assumed to be 1.1 g/cm^3, h_u is depth of the upper well interval with no density log, ρ_{av} is assumed average bulk density of 2 g/cm^3, ρ_b is bulk density from the density log and h_{log} is the depth interval between logging data points.

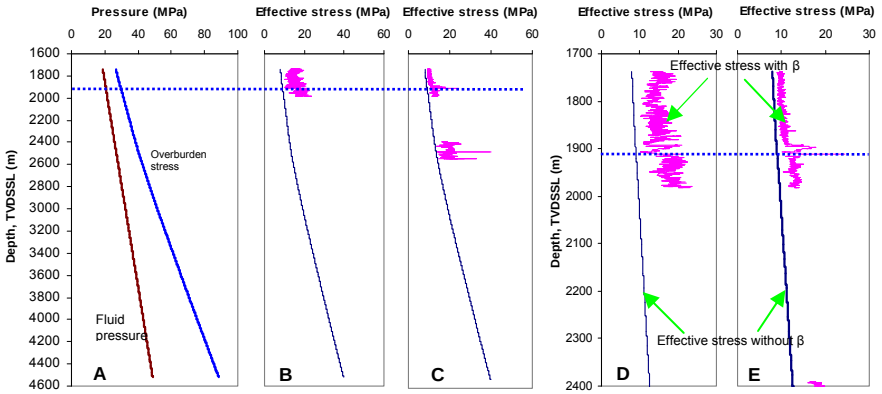

Figure 4. (A) Calculated pore fluid pressure and overburden stress. (B) Effective stress when lower Ko is used and (C) effective stress when higher Ko is used by including and disregarding the β. (D) Detail of (B) and (E) is detail of (C).

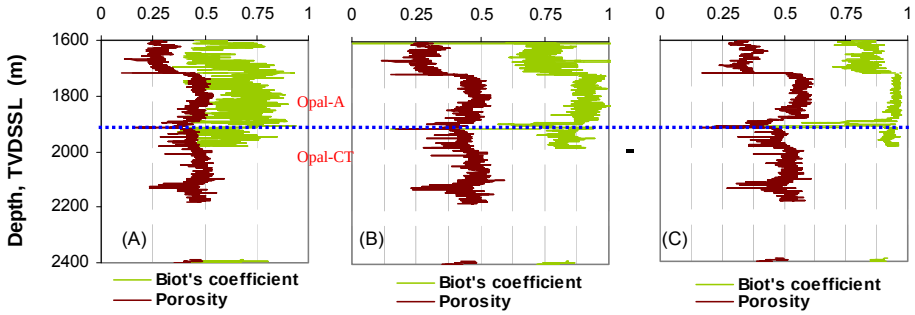

Figure 5. Comparison of the estimated Biot's coefficient, β; (A) when the ooze is assumed composed of opal-A, (B) when the ooze is assumed to be transformed to opal-CT, and (C) when further transformed to quartz. The horizontal doted line is assumed to be a transitional line between opal-A and opal-CT.

When the ooze is assumed to be transformed to quartz, the corresponding average estimated β is about 0.95 which is higher than if it is modeled as opal-CT where the β is about 0.85 or as opal-A where the β is about 0.75. The estimated effective stress in the cases of opal-A and opal-CT is about 26% and 12% higher, respectively, than if it is estimated under the assumption of quartz, but, the calculated porosity is higher than neutron porosity only in the quartz case.

Fluid pressure, P_f, was calculated under assumption of a hydrostatic pressure gradient:

$P_f = g * depth * \rho_w$ Equation 4

The resulting effective stress as calculated from equation 2, was compared to the result from using the more simple equation according to Terzaghi (1923) (Figure 4):

$\sigma' = \sigma - P_f$ Equation 5

It is obvious that taking Biot's coefficient into account when calculating effective stress is crucial to obtain more realistic effective stress value. Assuming Biot's coefficient as equal to one may lead to underestimation of the real effective stress. Underestimating effective stress may lead to bad consequences as reservoir rock may suffer compaction or elastic deformation as a result of changing in stress state during the production of hydrocarbons.

References

Gassmann, F. 1951. Uber die elastizitat poroser medien. Veirteljahrsschrift der Naturforschenden Gesellschaft in Zurich, **96**, 1–23.

Hashin , Z. and Shtrikman, S. 1963. A variational approach to the elastic behavior of multiphase materials. J. Mech. Phys. Solids, 11, 127-140.

Kastner, M. 1981. Authigenic silicates in deep-sea sediments: formation and diagenesis. In: Emiliani, C. (ed.): The Oceanic Lithosphere, Sea 7, 915-980. John Wiley & Sons, New York.

Mavko G., Mukerji, T. and Dvorkin, J. 1998. The Rock Physics Handbook: Cambridge University Press. Reprinted 1999. p 329.

NPD, Norwegian Petroleum Directorate http://www.npd-no

Pedersen, G.K. and Surlyk, F. 1983. The Fur Formation, a late Paleocene ash-bearing diatomite from northern Denmark. Bulletin of the Geological Society of Denmark 32, 43-65.

Reuss, A. 1929. Berechnung der fliessgrense von mischkristallen auf grund der plastizitatbedingung fur einkristalle. Zeitschriftfür Angewandte Mathematik aus Mechnik, v. 9, 49-58.

Terzaghi, K.1923. Die berecbnung der durchlassigkeitsziffer des tones aus dem verlauf der hydrodynamischen spannungserscheinungen. Akademie der Wissenschaften in Wien. Sitzungsberichte. Mathematisch-naturwissenschaftliche Klasse. Part 11 a, Vol. 132, No. 3/4, 125-138.

Tood, T. and Simmons, G. 1972. Effect of pore pressure on the velocity of compressional waves in low-porosity rocks. Journal of Geophysical Research v. 77, No. 20. July 10, 1972, 1731-1743.

Thomsen, E. and Danielsen, M. 1995. Transitional Paleocene-Eocene ash-bearing diatomite in the Eastern North Sea. Tertiary Research 15, 111-120.

Voigt, W. 1910. Lehrbuch der kristallphysik. Leipzig, B. G. Terebner, 964.

VII

Paper VII

Petrophysical analysis of siliceous ooze sediments, Møre Basin, Norwegian Sea

Ahmed Awadalkarim and Ida Lykke Fabricius

Presented at the 75th EAGE Conference & Exhibition incorporating SPE EUROPE 2013, held in London, UK, 10–13 June 2013

Introduction

Skeletal remains of siliceous algae form biogenic fine grained highly porous pelagic siliceous ooze sediments that were found above the reservoir of the Ormen Lange gas field which is located in the southern part of the Norwegian Sea (Figure 1a). The Palaeocene sandstone of the "Egga" Formation is the main gas reservoir (NDP). In this study, we are interested in the siliceous ooze intervals only.

A possible hydrocarbon prospect of siliceous ooze is proposed, but siliceous ooze is significantly different in structure from most commonly known hydrocarbon reservoir rocks. For instance, the pore structure is complex and the solids are mechanically fragile and hydrous. Normal petrophysical methods used in formation evaluation might not be suitable for interpreting siliceous ooze. For example, density and neutron logging tools are calibrated to give correct porosity readings in a limestone formation, but apparent porosity indications in any other lithology, such as siliceous ooze, are wrong and they should be corrected. The apparent bulk density log should be influenced by the hydrogen in opal as also the neutron porosity tools because they are sensitive to the amount of hydrogen in a formation and to a lesser extent upon other elements. It is normally assumed that the contribution to the neutron porosity measurement comes entirely from the hydrogen in fluids fully occupying the pore space. But, elements other than hydrogen that exist in the rock matrix do contribute to the signal; and hydrogen is also present in the solid. Some minerals of siliceous ooze, such as opal, have hydrogen in their structures which influences the measured hydrogen index (HI). The neutron tool obtains the combined signal of the HI of the solid phase and of the water that occupies the true porosity. The HI is equal to true porosity for completely freshwater saturated limestone. In this study, all the possible contributions to the neutron porosity measurement have been considered. Therefore, the slowing down power of all siliceous ooze minerals is taken into account.

In this study we aimed to develop and use a new procedure to analyse and interpret logging data acquired through siliceous ooze sediments. Our main objectives were to characterize and evaluate the petrophysics of siliceous ooze and to find the true porosity and water saturation to test its hydrocarbon reservoir potential. We used and integrated core analysis data with logging data from four Ormen Lange wells, and included X-ray diffraction analysis (XRD) data. Additionally, other available information such as petrographic thin-section analysis, core computed tomography scans (CT-scans), scanning electron microscope (SEM), and other published data were used here to interpret lithology and the unusual physical properties of the studied intervals. The integration of all these data revealed that the studied siliceous ooze is a mixture of opal and non-opal (shale). Our results proved to be reasonably consistent. The studied intervals apparently do not contain hydrocarbons.

Data and Methods

The data included here comprise conventional core analysis, mineralogical and petrographic analyses, and well logs. The authors' calculated data included opal and non-opal volume fraction logs, grain density log, the amount of water in opal structure and true porosity logs. Siliceous ooze core material of about 18 m (1761-1779 m RKB) from the Ormen Lange well 6305/4-1 was available. Conventional core analysis had been done on ten core plugs from this core material. This included grain density, helium porosity and gas permeability. The core porosity was corrected for overburden stress to estimate in-situ porosity. Klinkenberg-corrected gas permeability was obtained.

The standard well logs used here included caliper, gamma ray (GR), sonic, bulk density, neutron, and resistivity logs. The density, neutron and resistivity logs were environmentally corrected. The sonic log quality was good.

The average core grain density of the bulk siliceous ooze is 2.43 g/cm^3. From mineralogical analysis, the average grain density of non-opal minerals was calculated to be 2.79 g/cm^3. We used 2.13 g/cm^3 for opal-A (Schlumberger 1989). Opal was not included in the mineralogical analysis, so the relative volume fractions of opal and non-opal in the siliceous ooze must be calculated as following (by assuming opal volume fraction is x, and non-opal is 1-x.):

$$\rho_{g\_core} = \left(\rho_{g\_opal\ A}\right)\cdot x + \left(\rho_{g\_rest}\right)\cdot\left(1-x\right) \qquad (1)$$

By substituted $\rho_{g\text{-}core}$ = 2.43 g/cm^3; $\rho_{g\_opal\ A}$ = 2.13 g/cm^3; and ρ_{g_rest} = 2.79 g/cm^3; and solving for x, it was found that x = 0.55 (i.e. volume of opal is 55% and non-opal is 45%) in the bulk core samples.

We assumed that the GR log response is due to contributions from non-opal minerals only. The GR log was then used to estimate the volume fraction of opal and non-opal as function of depth, which were used with the empirical grain densities to calculate the grain density log of siliceous ooze, as following:

$$\rho_{g\_calculated} = \left(\rho_{g\_opal\ A}\right)\cdot x + \left(\rho_{g\_rest}\right)\cdot(1-x) \;=\; 2.13x + 2.79(1-x) \qquad (2)$$

where, x and (1-x) are volume fraction logs of opal and non-opal, respectively.

The calculated grain density log is calibrated to the core grain density. To calculate the number of electrons per unit volume of opal-A, the grain density of 2.13 g/cm^3 and molecular water content of 3.5 % were used here, respectively (Schlumberger 1989). The n in opal structure ($SiO_2.nH_2O$) is calculated as following:

$$n = \frac{60.09\,f}{18.02(1-f)} = 0.121 \qquad (3)$$

where, n is the number moles of water in opal structure, f is the opal molecular water content, in fraction (i.e. f = 0. 035), the 60.09 and 18.02 are the molar mass of silica (SiO_2) and water (H_2O) in g/mol, respectively.

The number of electrons per cubic centimetre (cm^3) of opal-A is calculated as:

$$\text{Number of electrons} = \frac{\left(\rho_{g\_opal\ A}\right)}{(60.09+18.02n)}\times(30+10n)\times N_A \qquad (4)$$

where, $\rho_{g\_opal\ A}$ = 2.13 g/cm^3; n = 0.121; 30 and 10 are number of electrons per molecule of silica and water, respectively. N_A is Avogadro's number = 6.022x10^{23}.

By using the same concept, we have obtained the log of the number of electrons per unit volume of bulk siliceous ooze as function of depth. The true density porosity is obtained as:

$$\phi_{true} = \frac{a-c}{b-c} \qquad (5)$$

where, ***a***, ***b***, and ***c***, are the number of electrons in 100% water saturated limestone of 1.70 g/cm^3 bulk density as used in calibration; in water that occupies true porosity, and in solid phase, respectively.

The calculated true density porosity log is calibrated to the overburden corrected core porosity, and it is used with the calculated grain density log and brine density (ρ_f) of 1.025 g/cm^3 to calculate the correct bulk density log which is compared with the measured bulk density log. We found that the difference is so small that it could be disregarded. The corrected bulk density log ($\rho_{b\_corrected}$) is calculated as following:

$$\rho_{b\_corrected} = \left((1-\phi_{true})*\rho_{g\_calculated}\right) + \left(\rho_f * \phi_{true}\right) \qquad (6)$$

Consequently, the apparent density porosity ($\phi_{\_Density}$) is obtained by Equation (7) based on the calculated grain density log by Equation (2) and the corrected wireline bulk density log data.

$$\phi_{\_Density} = \frac{\rho_{g\_calculated} - \rho_{b\_corrected}}{\rho_{g\_calculated} - \rho_{fl}} \quad (7)$$

where, $\rho_{g\_calculated}$ is the calculated grain density log; $\rho_{b\_corrected}$ is the corrected bulk density log; and ρ_{fl} is the fluid density (= 1.025 g/cm^3), according to the operator data on Ormen Lange field.

The HI log is related to the true neutron porosity as following:

$$HI_{Log} = (\phi_{n\_true}) \times (HI_{water}) + (1 - \phi_{n\_true}) \times (HI_{Solid}) \quad (8)$$

The HI for both solid (HI_{solid}) and water (HI_{water}) phases were calculated according to Serra (1984). Solving for true neutron porosity, ϕ_{n_true}, the following formula was reached:

$$\phi_{n\_true} = \frac{a - c}{b - c} \quad (9)$$

where, ***a*** is the calculated *HI log* that neutron tool should read if it was not calibrated for limestone; ***b*** is the *HI* of water occupies true porosity, and ***c*** the *HI* of solid phase.

Results and Discussion

The CT scans showed the presence of small-scale heterogeneity throughout the scanned core material. The SEM analysis results showed that diatoms are very abundant but of limited variety. The results of thin section analysis are in agreement with those of XRD. Figure 1 shows the petrophysical data plotted versus measured true vertical depth in meters referring to Kelly Bushing (m TVD RKB). The studied siliceous ooze intervals are characterized by very low GR and bulk density; high total neutron porosity and sonic interval transit time readings with respect to the same logging responses of the adjacent shale intervals (Awadalkarim & Fabricious 2009). The grain density of the studied siliceous ooze is very low and variable which has an effect on density porosity calculation. The density porosity is therefore lower when corrected for the lower grain density. An assumption of constant grain density is definitely the weakest if one aims to obtain reliable density porosity of siliceous ooze. If a constant grain density value is used, the calculated porosity is inaccurate. When too low grain density is used, the porosity is underestimated by the density log, and the opposite is true when higher grain density is used. The overburden corrected core porosity ranges from 50-56% (53% in average). The core permeability of the same samples ranges from 0.21-0.41 mD. These results agree reasonably well with those reported by Schwartz (1988) for diatomite.

The calculated apparent density porosity (Equation 7) is nevertheless similar to the calculated true density porosity (Equation 5), and fits well to the overburden corrected core porosity. This relative agreement in porosity suggests that perhaps both techniques are likely valid interpretations of siliceous ooze if the correct grain density is used. The true density porosity represents the total in-situ porosity, because of the evidence of some dead-end pores in samples as shown by petrographic analysis; the effective porosity actually may be even lower. The in-situ density porosity of siliceous ooze is much more reliable than the core helium porosity. As helium porosimetry measurements rely upon full penetration of helium molecules into all open pores in the network, honoring proper equilibration time during the measurement is paramount in these low-permeable sediments.

Neutron tools respond to all the water in a formation, even if some of this water is not associated with porosity, such as bound water associated with shale and opal. Since the HI contribution of clay bound water is considered, the HI correction to porosity can be applied accurately. Here, the neutron porosity is corrected for the hydrogen index contribution from the solid phase. The true neutron porosity (Equation 9) is a bit lower than the wireline neutron porosity, but the difference is not significant.
The true density porosity is lower than the corrected neutron porosity. The reason for this difference is unknown at present, but it could be due to the presence of bound water associated with clay and opal. The neutron porosity is lower when corrected for the bound water (high hydrogen index).

The resistivity log shows resistivity of less than 2 Ohm-m. Despite the high porosity of the siliceous ooze, but, the small or the lack of separation between the resistivity curves in other wells confirm that the permeability is very low. The studied siliceous ooze intervals apparently do not contain gas.

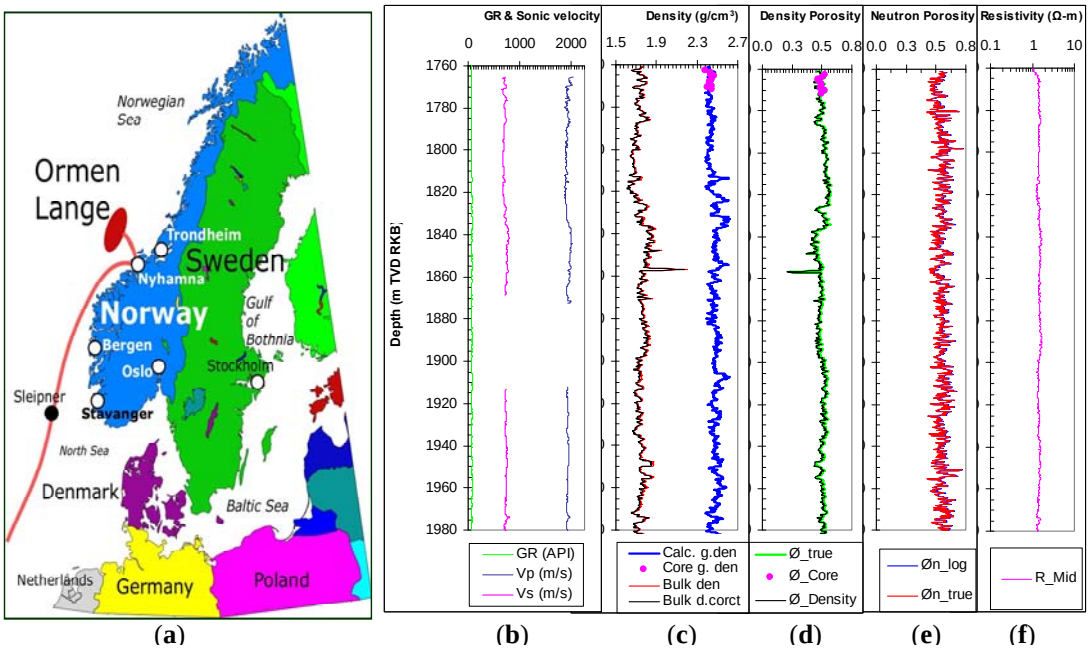

Figure 1: *(**a**) Location of the Ormen Lagne field (NDP). The petrohysical data for the studied siliceous ooze interval in well 6305/4-1 versus depth are shown by (**b**) GR & sonic velocity, (**c**) bulk & grain density, (**d**) density porosity, (**e**) neutron porosity, and (**f**) resistivity.*

Conclusions

The studied siliceous ooze has proven challenging to characterize accurately from petrophysics. The siliceous ooze show very high porosity and exceptionally low bulk density, and lower GR logs response than shale. In this study, the calculation of true porosity is based upon the fundamental relationships. This approach is capable to give reliable grain density and true porosity. The studied intervals apparently do not contain hydrocarbons. The application of this approach clearly has great potential in obtaining reliable porosity of siliceous ooze intervals elsewhere.

Acknowledgements

We thank DONG Energy, in Denmark, for funding this project and providing data for this study.

References

Awadalkarim, A. and Fabricius, I.L. [2009] Estimating effective stress in North Sea ooze. An extended abstract, Sound of Geology Workshop. Bergen, Norway.

NPD, Norwegian Petroleum Directorate http://www.npd-no.

Schlumberger, [1989] Log Interpretation Principle/Applications, Schlumberger Education Services, Houston, USA.

Serra, O. [1984] Fundamentals of well-log interpretation. 1. The acquisition of logging data. Elsevier Science Publishers. The Netherlands.

Schwartz, D.E. [1988] Characterizing the Lithology, Petrophysical Properties, and Depositional Setting of the Belridge Diatomite, South Belridge Field, Kern County, California in Studies of the Geology of the San Joaquin Basin, S.A. Graham, and Olson, H.C., Editors., The Pacific Section, Society of Economic Paleontologists and Mineralogists, Los Angeles, 281–301

VIII

Paper VIII

Elastic properties of Palaeogene clay from Fehmarn Belt area

Ahmed Awadalkarim, Niels Nielsen Foged and Ida Lykke Fabricius

Submitted to the 76th EAGE Conference & Exhibition 2014, Amsterdam RAI, the Netherlands, 16–9 June 2014

Introduction

Palaeogene clay samples were obtained by high quality boring and sampling techniques (Geobore S-system), during the extensive site investigations for building a bridge in the Fehmarn Belt area to link between Rødbyhavn in Denmark and Puttgarden in Germany. The Palaeogene clay is rich in smectite and of high to very high plasticity. Comprehensive and advanced laboratory tests were done by Fugro-McClelland (in Netherlands) and by Danish Geotechnical Institute (in Denmark) on Palaeogene clays. Some of their data are included in this study. Ten Palaeogene clay samples were selected and used in this study.

Results of odometer tests done by Jessen et al. (2011) show that when Palaeogene clay is mounted in an odometer cell without access to water and loaded to its *in-situ* vertical effective stress and then saturated with its native salt water, the clay absorbs water and swells. This behaviour indicates that the Palaeogene clay in nature should expand at its mean effective *in-situ* stress. A study by Krogsbøll et al. (2012) provides some important clues about the deformation behaviour during unloading and swelling of the Palaeogene clay. In this study, we mainly focused on the elastic properties of the Palaeogene clays. Elastic wave velocities are influenced by the elastic stiffness and the density of a material. We used geotechnical and elastic wave velocity data to model the elasticity and then to relate it to mineralogy and BET surface area. We measured the mineralogy, BET surface area, bulk density, porosity, water content and saturation, elastic wave velocities, electrical resistivity and strain caused by mechanical loading. They were used together to interpret the geotechnical data. We aimed to see which physical property is a main controlling factor for the elasticity of the studied Palaeogene clay and whether we can explain the deformation behaviour from elasticity alone.

Theory and methods

Ten wet Palaeogene clay samples were examined and analysed in terms of their mineral composition, BET surface area, elastic wave velocity and electrical resistivity, as well as classification parameters (bulk and dry densities, water content, void ratio, total porosity, water saturation) and elastic moduli.

The mineralogy was determined by XRD analyses using a Philips 1830 X-ray diffractometer. A Gemini III 2375 surface area analyzer apparatus was used to measure the surface area by BET method.

Elastic wave velocity (P-wave and S-wave velocities) and electrical resistivity were measured on 10 naturally saturated vertical core plugs of 37.5 mm in diameter and nominally 25 mm long. The measurements were done at laboratory temperature of about 22^{o} C and under drained conditions as a function of uniaxial confined compression stress with different axial stress levels (from 0.2 to 3.0 MPa and further unloaded to 0.2 MPa) using a triaxial Hoek cell. The uniaxial stress and strain were measured simultaneously during the velocity measurements, so the uniaxial compressional drained modulus (M_{drain}) can be determined.

Knowing the arrival times of transmitted ultrasonic pulses, sample length and system delay times, the elastic wave velocity was computed. The classification data are obtained based on the measured sample dimensions, volume and weight before and after each test and once again after sample drying at 60^{o} C in the oven. We have used 60^{o} C to avoid change in smectite mineral water.

The continuous changes in porosity (ϕ) with stress is calculated using the initial porosity (ϕ_i) and the uniaxial strain (ε_A) resulting from sample being deformed, and it is measured by LVDTs, as follows:

$$\phi = \frac{\phi_i - \varepsilon_A}{1 - \varepsilon_A} \qquad (1)$$

The P-wave modulus (M) and the S-wave modulus (G) describe the propagation of acoustic elastic waves. In this study, the P-wave velocity (Vp), the S-wave velocity (Vs) and the bulk density (ρ_b) of the water saturated Palaeogene clay samples were measured. Thus, the elastic moduli are calculated as follows:

$$M = \rho_b V_p^2 \quad (2)$$

$$G = \rho_b V_S^2 \quad (3)$$

The Poisson's ratio (ν) is estimated from the P- and S-wave velocities as follows:

$$\nu = \frac{V_P^2 - 2V_S^2}{2(V_P^2 - V_S^2)} \quad (4)$$

The drained modulus (M_{drain}) is an elastic property describing the stress increment ($\Delta\sigma$) relative to the strain increment ($\Delta\varepsilon$) under linear elastic uniaxial confined condition:

$$M_{drain} = \Delta\sigma/\Delta\varepsilon \quad (5)$$

The drained modulus (M_{drain}) of each sample is determined on a series of selected slopes on the compaction curve (see Figure 2a–d). The M_{drain} was compared with both the saturated, uniaxial compressional modulus, (M_{sat}) and the dry compressional modulus (M_{dry}). The M_{sat} was estimated (by using equation (2). The M_{dry} was estimated by modified Gassmann's equation (Gassmann 1951). In this study we assume that Young's modulus as predicted from grain density (Chen and Evans 2006) is a lower bound for uniaxial mineral modulus ($M_{mineral}$).

Results and discussion

The XRD analysis reveals the presence of smectite, illite, kaolinite and chlorite. Smectite and Illite occur in all samples and form a major part of the clay mineral assemblage (Table 1). In most samples, the smectite content exceeds that of illite. Smectite is the most important constituent of the clay fraction; it forms more than 50% of the solid of some Palaeogene clay samples. The XRD results show a rather significant variation in smectite content within the five Palaeogene clay units. High smectite content of a sample means high plasticity of that sample (i.e. high I_p). The results of the measured BET surface area are listed in Table 1. The Palaeogene clays show quite similar surface area above 60 $m^2 g^{-1}$ in average. The surface area is controlled by the smectite content.

Table 1: *Results of smectite (sm %) and illite (il %) content from XRD analysis, BET measurements and some other geotechnical classification data of 10 Palaeogene clay samples included in this study.*

Boring number	Core number	Sample number	Sample depth	Geological unit	σ'_{vo}	σ'_{pc}	Geotechnical classification parameters										XRD	
							w_i	S_w	ρ_b	d_s	w_L	w_P	I_P	I_C	CC	Clay	BET	sm	il
			mbsf		kPa	kPa	%	%	g cm^{-3}	g cm^{-3}	%	%	%		%	%	m^2g^{-1}	%	%
09.A.013	09-100196	1	94	Æbelø	1125		37	90	1.75							72	61	22	48
09.A.013	09-100310	2	94.55	Æbelø	1125		37	90	1.74							70	66	38	29
09.A.002	09-101463	8	85.05	Røsnæs	765		32	91	1.84						2.4	70	61	12	37
09.A.602	09-101191	15	20.13	Røsnæs	185	460	35	99	1.91	2.81	119	28	90.5	1.26	1.6	80	62	30	27
09.A.010	09-101082	29	49.35	Røsnæs	415		37	97	1.88	2.79	110	33	77.5	0.95	3.6	75	62	15	34
09.A.010	09-101096	31	31.25	Ølst	260		48	98	1.78	2.73	172	44	128	0.97	2.6	64	75	51	20
09.A.001	09-101232	37	45.1	Røsnæs	360	3300	35	98	1.91	2.79	173	29	144	0.96	3.0	78	64	23	28
10.A.803	10-105031	89	12.5	Lillebelt	214		45	98	1.74								65	28	21
10.A.057	10-106007	93	58.8	Ølst	575		45	98	1.65	2.85	136	49	86.6	1.05	4.7	42	84	60	14
10.A.802	10-108030	95	2.4	Lillebelt	40		47	95	1.71								45	14	5

σ'_{vo} is the *in-situ* vertical effective stress, σ'_{PC} is the pre-consolidation stress, S_W is water saturation.

Some results from geotechnical classification tests done on Palaeogene clay were collected from Jessen et al. (2011) and tabulated in Table 1. These data include initial water content (W_i), wet bulk density (ρ_b), specific gravity of solids (d_s), liquid limit (W_L), plastic limit (W_P), plasticity index (I_P), compressibility index (I_C), and calcium carbonate ($CaCO_3$) content (CC). The present classification data are presented in Figure 1a–c. The Palaeogene clay from the Ølst unit is very rich in smectite content (samples no. 31 and 93). It shows higher moisture content, lower bulk density and higher porosity. The studied Palaeogene clays are compacted less and retained higher porosity, and lower bulk density than it would be expected along the whole stress path from 0.2 to 3.0 MPa (Figure 1). This means the pore-water expels slowly due to the low permeability. This agrees reasonably well with the compaction behaviour of smectite-rich clays of Mondol et al. (2008).

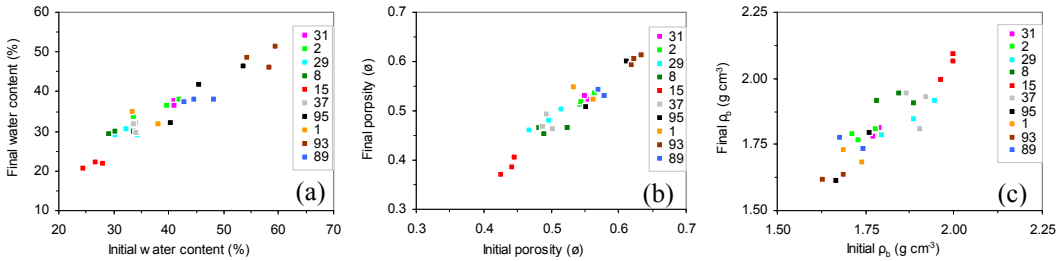

Figure 1: *Cross plots of initial versus final results of (**a**) water content, (**b**) porosity, (**c**) and bulk density. Each sample is represented by three data points measured in vertical, horizontal and tangential orientation.*

Results of the mechanical loading of pore-water-saturated Palaeogene clays, subjected to a maximum of 3 MPa uniaxial stress, are shown in Figure 2a-d. This figure illustrates the drained behaviour of the studied Palaeogene clay. Most of the samples show elastic stress–strain behaviour with the highest deformation of sample 29. The samples 29, 95 and 8 are highly compacted relative to the other 7 samples. This may be due to their low smectite content which allows water to squeeze out faster than from those with high smectite content. The results show similarity in elastic deformation pattern.

Plots of P-wave velocity (on loading and unloading) versus both S-wave velocity and uniaxial stress were also prepared. The P-wave velocity is shown to be sensitive to both clay mineralogy and to the effective stress. The relationships between the electrical resistivity and the axial stress; and between the porosity and axial stress were established for each sample. The Poisson's ratio calculated from equation (4) ranges 0.20 to 0.30. Poisson's ratio is shown to be sensitive to variations in smectite content. Samples poor in smectite content (e.g. sample 95) have relatively high Poisson's ratio.

Figure 2e-h shows plots of the static drained modulus (M_{drain}); the dynamic compressional modulus (M_{sat}); and the dry compressional modulus (M_{dry}). In the following discussion, the calculated M_{sat} is considered as an upper bound for dynamic compressional modulus of a saturated sample. The present results show that the M_{sat} is significantly higher than the M_{drain}. Both of them increase with increasing stress due to the removal of bedding and fracture effects resulting in enhancement of grain contact. There is no large difference between the M_{drain} and M_{dry}. However the M_{dry} is slightly higher than the M_{drain}. The reason for this difference is probably that M_{drain} accounts for some plastic deformation.

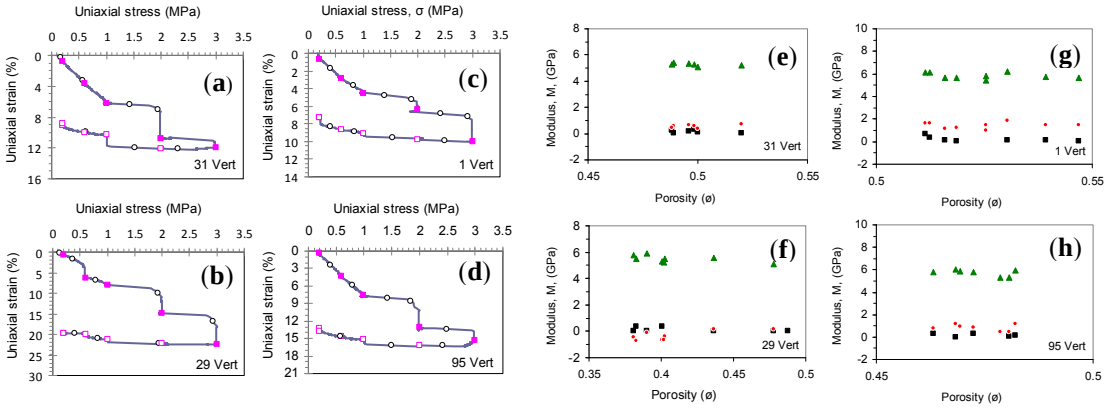

Figure 2: *(a)-(d) Stress–strain curves produced during uniaxial confined compressional test of four vertical core plugs under drained conditions. Open circles indicate the mid point of the part of the curve used for obtaining the M_{drain}. The closed and open rectangles indicate stress levels at which the velocities were measured during loading and unloading, respectively.* ***(e)-(h)*** *M_{sat} (green triangular), M_{drain} (black rectangular), and M_{dry} (red circle) for both loading and unloading stress paths plotted versus porosity. Sample number is indicated in the bottom right hand corner of each plot.*

Conclusions

Pore space and structure of the Palaeogene clays are dominated by smectite and thus they behave as sponge. The classification results generally indicate that the studied clays behave elastically. The obtained results can aid in the estimation of drained elastic parameters from bulk density and velocity of elastic waves and may have implications in engineering practice, including structural design and slope stability analysis.

Acknowledgements

We thank Femern A/S for providing samples and for acceptance to publish these data. Sinh Nguyen and Vita Larsen are thanked for assistance in laboratory work.

References

Biot, M.A. and Willis, D.G., 1957. The elastic coefficients of the theory of consolidation. Journal of Applied Maechnics, **24**, 594–601.

Chen B. and Evans J.R.G. 2006. Elastic moduli of clay platelets. Scripta Materialia, **54**, 1581–1585.

Gassmann F. 1951. Uber die elastizitat poroser medien. Veirteljahrsschrift der Naturforschenden Gesellschaft in Zurich, **96**, 1–23.

Jessen, S.B., Hansen, P.B., Hesthaven, M. and Christensen, H.G., 2011. Fehmarn Belt Fixed Link, Advanced Laboratory Testing, Clays of Palaeogene origin, Geotechnical Data Report.

Krogsbøll, A., Hededal, O. and Foged, N., 2012. Deformation properties of highly plastic fissured Palaeogene clay–Lack of stress memory? DGF-Bulletin **27**, 133–140.

Mavko, G., Mukerji, T. and Dvorkin, J., 1998. The Rock Physics Handbook. The Press Syndicate of the University of Cambridge. Cambridge, UK, 329 p.

Mondol, H., Bjørlykke, K. and Jahren, J. 2008. Experimental compaction of clays: relationship between permeability and petrophysical properties in mudstones. Petroleum Geoscience, **14**, 319–337.

Part III: Appendixes

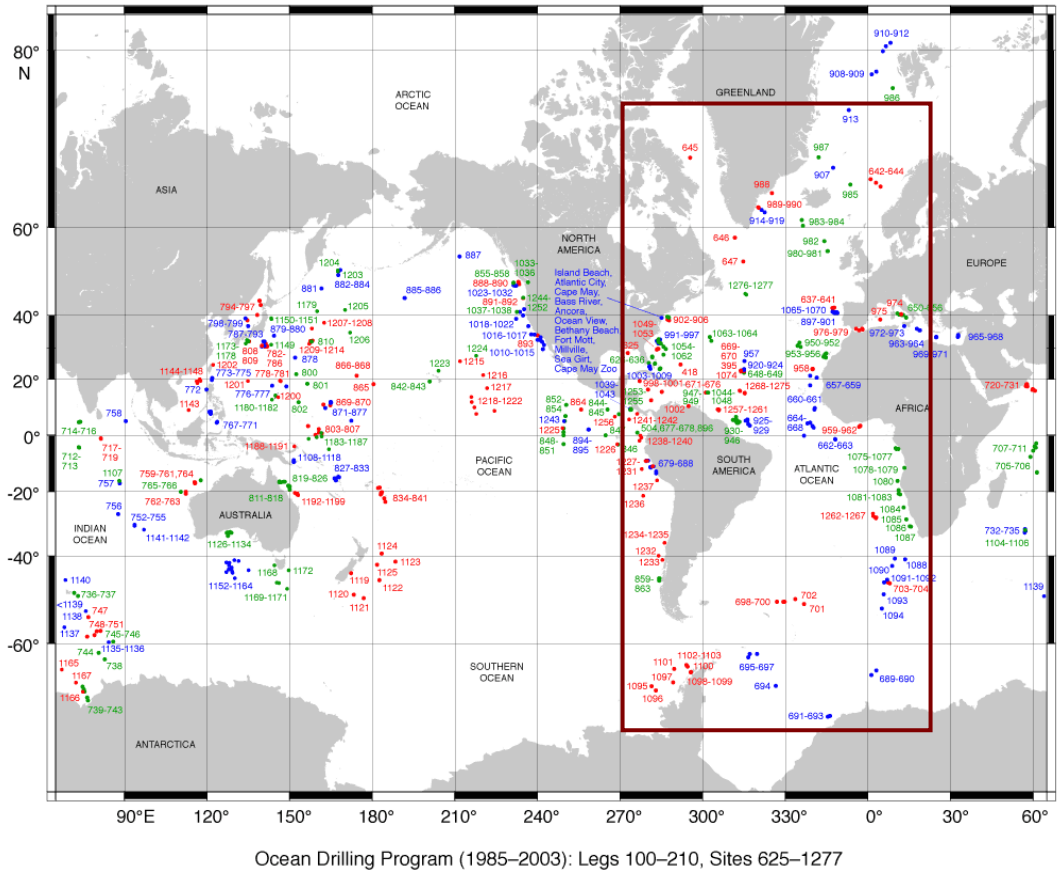

Figure A-I-1: *Palaeogene lithology map of Atlantic Ocean based on the geographical coordinates of the ODP sites. Map showing the locations of the ODP sites included in this research. The studied area is enclosed with a rectangle (http://www.iodp.org/).*

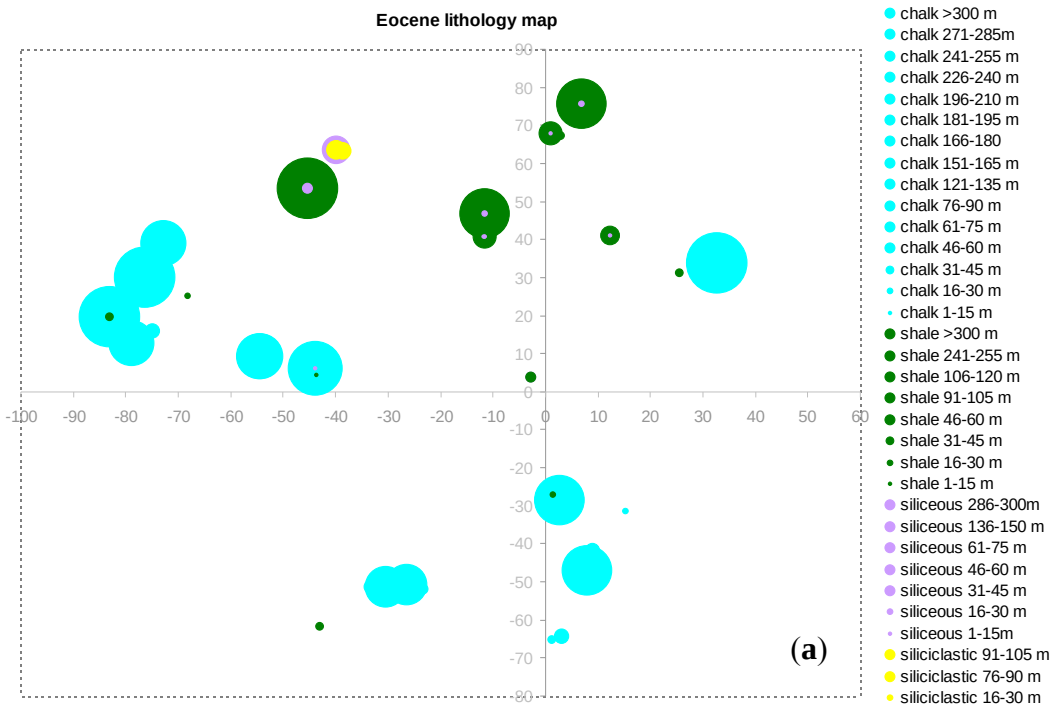

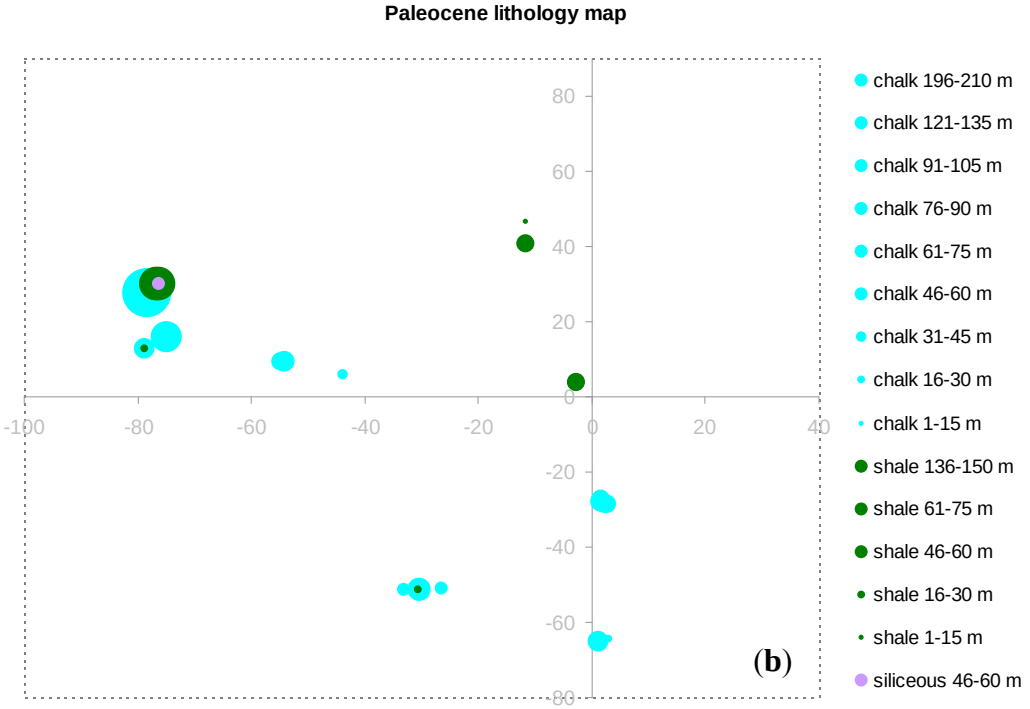

Figure A-I-2: *Eocene lithological map (**a**) and Palaeoecene lithological map (**b**) for chalk, shale, siliceous ooze and siliciclastic sediments.*

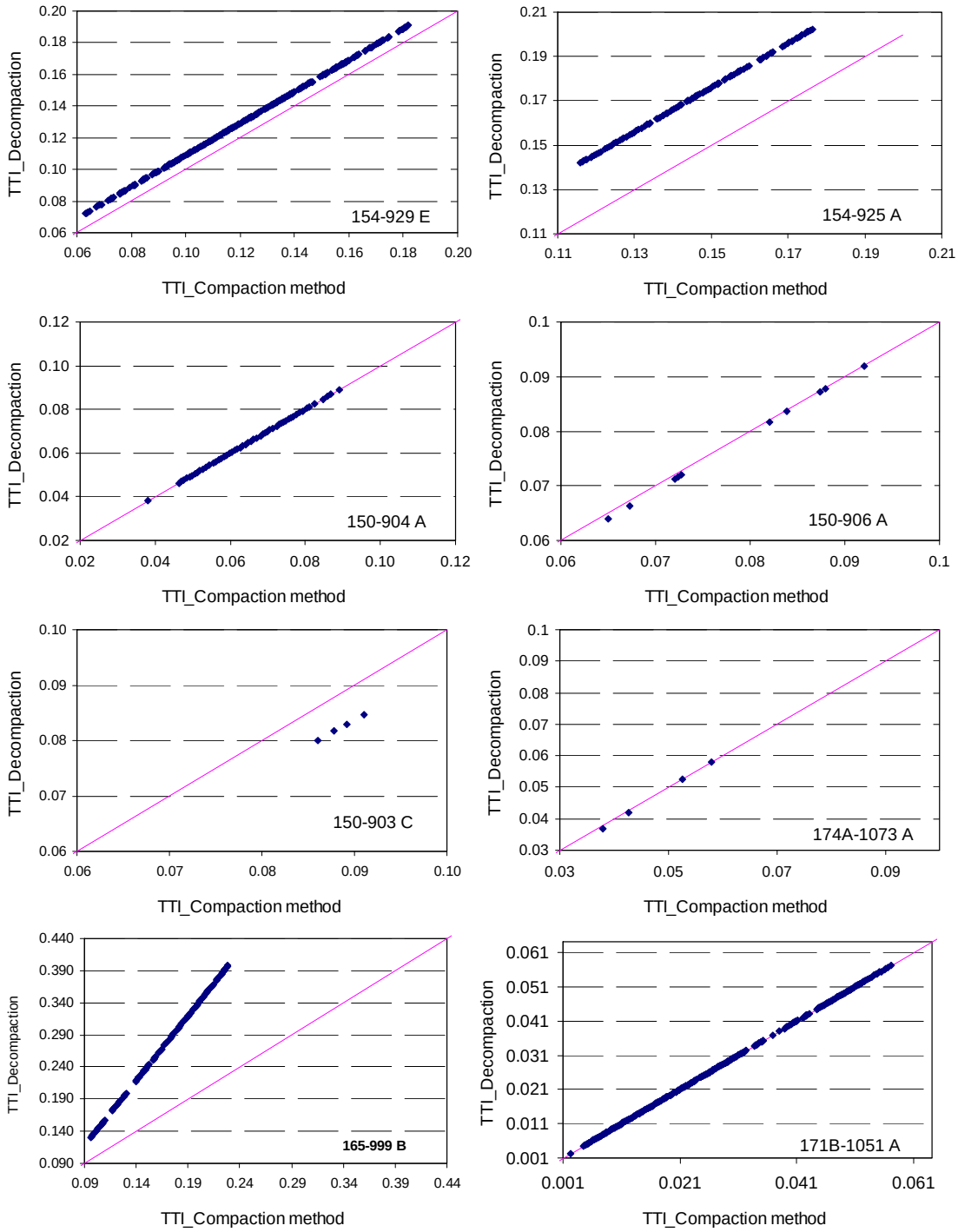

Figure A-I-3: *Comparing TTI results as obtained by compaction and decompaction methods.*

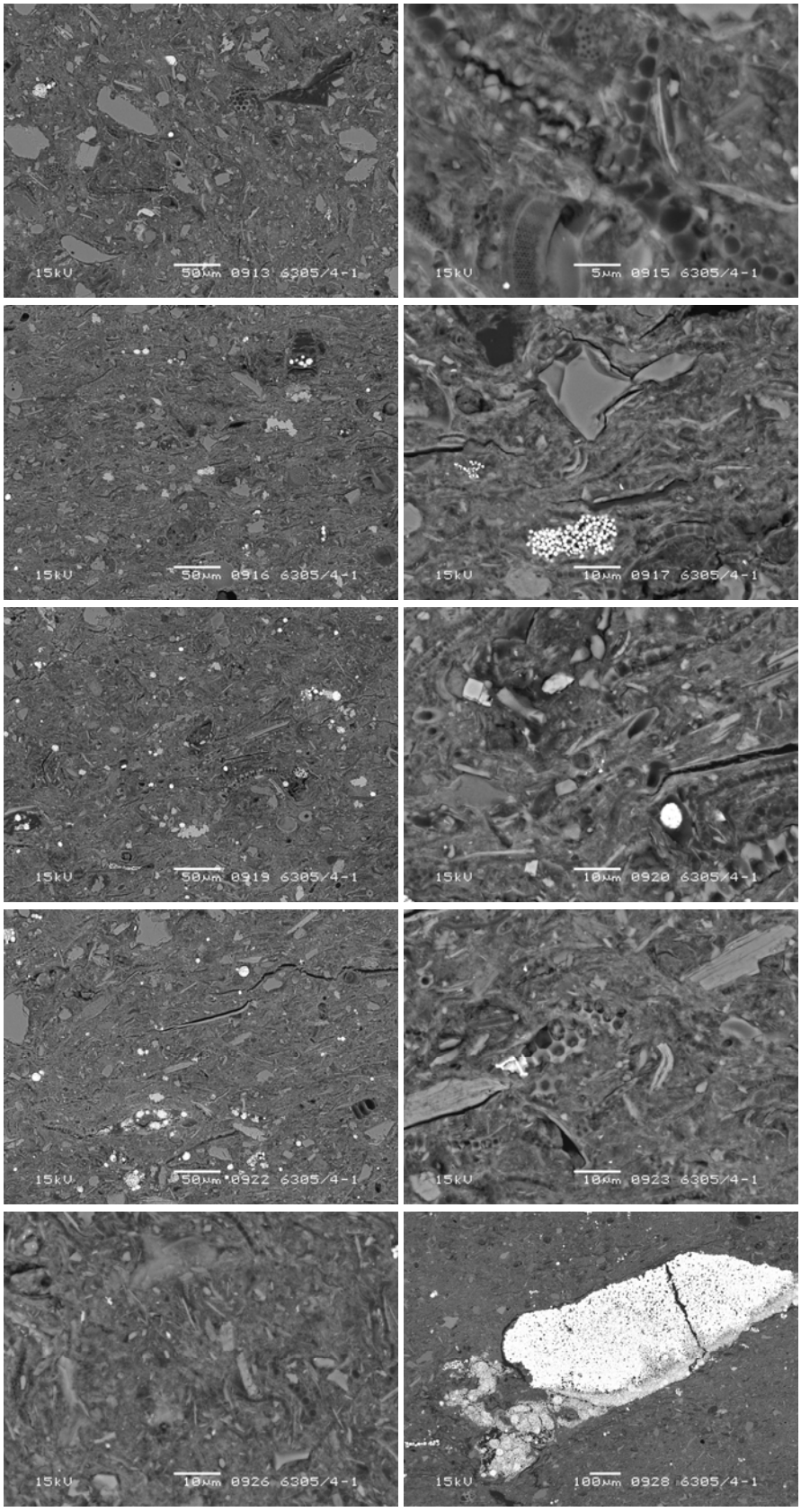

Figure A-II-4: *Backscatter electron micrographs (SEM) from siliceous ooze from well 6305-4-1.*

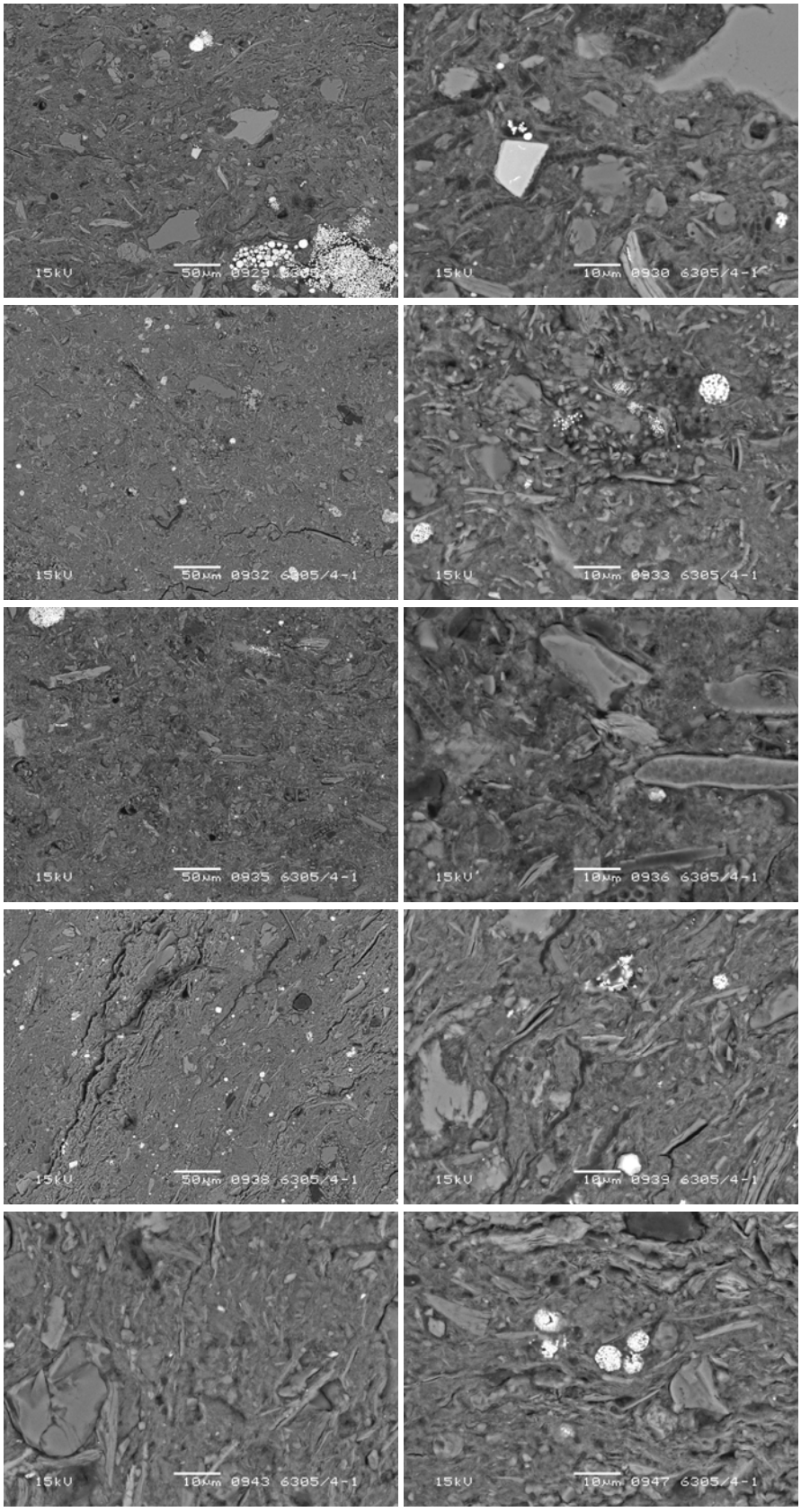

Figure A-II-4: *Continued*

Appendix A-III-1: Procedure of X-ray diffraction analysis: bulk and clay mineralogy

1. Introduction

A total of 116 brine-saturated sediment samples (in their natural moisture condition) from different geological formations/units from more than 30 boreholes in the Fehmarnbelt area were analysed for whole-sample (bulk) and clay-sized fraction (<2 μm) mineralogy by using XRD analysis method. The samples were prepared and analysed according to the Sediment Lab procedure at Technical University of Denmark (DTU). Preparation, analysis and interpretation procedures are modified from Moore and Reynolds (1997) and Hillier (2003). Semi-quantification is based on calculation of the integrated peak area and peak height measurements on selected diffraction peaks of respective mineral phases, multiplied by in-house calibrated weight factors (Pearson and Small, 1988; Ramm, 1991).

To determine the mineral compositions of each sample, XRD analyses were conducted on random and on orientated samples. XRD analyses of bulk sample mineralogy (normal and slow scan) and of clay-sized fraction mineralogy (untreated, slow scan, ethylene glycol and heat treated) were prepared, run, interpreted and evaluated by the authors. To identify and semi-quantify the mineral compositions of bulk samples, we analysed the powdered bulk sample from the interval 2°–60° 2θ (2-theta). For general identification and semi-quantification of clay minerals, the <2 μm clay-sized fraction, four XRD analyses were done from the interval 2°–35° 2θ with multiple treatments in the following sequences: air-dried, ethylene glycol-solvated, subsequently heated to 350^{o} C and further heated to 550^{o} C. The concentration of some of the important components was estimated from peak height measurements on selected diffraction peaks. The peak heights were then corrected with weighting factors and compared with those of pure individual minerals.

2. Equipment

The XRD analysis was performed in a Philips X-ray diffractometer model pw 1830 equipped with a Philips X-ray tube model pw 2273/20 (using Ni-filtered Cu K-α radiation which generates X-rays with a wavelength of 1.54051Å), and an automatic divergent slit system (monochrometer) Philips model pw 1050/25. The acquisition is based on Bragg's Law and controlled by a Philips diffractometer control unit model pw 1710. Instrument settings (operating conditions) were 40 kV tube potential, 25 mA tube current, goniometer scan ranges from 2°– 60° 2θ (2-theta) for bulk samples, step-size 0.1° 2θ, scan speed at 0.1° 2θ/2 seconds. The control unit was computed to measure peak areas and heights. Data were recorded at a scanning rate of 0.1^{o} 2θ per second. An interactive software package (Origin Version 3.78) was used on a computer to process the data and identify the main minerals. The XRD patterns were analyzed using Origin software and standard reference patterns. The XRD equipment measuring range is from 2° to 70° 2θ, with limit detection of 5% of the material in question, and its accuracy is ± 0.7% based on d-spacing (crystal spacing) of quartz.

3. Detailed analysis procedures

3.1. XRD analysis on bulk sample

The mineralogical composition of the 116 bulk samples was identified by powder XRD analysis of the whole sediment samples. For bulk samples standard and slow scan recordings were performed.

For bulk mineralogy analysis of the sediment samples, a representative sample of about one gram (1g) of untreated, whole-sediment sample was air-dried at room temperature (22^{o} C), crushed, and it was ground, to homogenize the material, in an agate mortar to produce powder fragments of about <50 μm in diameter. About 0.5 g of the finely produced powder was packed into a standard brass sample holder to form a pressed powder cavity mount with a random orientation. The random orientation ensures that the incident X-rays have an equal chance of diffracting off any given crystal lattice plane of the minerals in the sample. The surface of the powder is smoothed by a glass plate, and then standard XRD analysis was undertaken at step size 0.1^{o} 2θ per 2 seconds from the interval 2^{o}–60^{o} 2θ. An additional slow scan at step 0.01^{o} 2θ per 2 seconds was run from the interval 26^{o}–28^{o} 2θ for accurate feldspar determination. Slow scan resolves the K-feldspar, plagioclase and quartz peaks used for semi-quantification. All peaks were measured, and bulk minerals were determined.

3.2 XRD analysis on clay-sized (<2 μm) fraction

To obtain the clay-size fraction (particle-size <2 μm in diameter) from the studied Palaeogene clays, about 20–50 g of the bulk wet sediment sample was put in a plastic container, filled with distilled water and tightly closed. The plastic flask with the sample was mounted in a shaker and left shaking overnight for about 18 hours. Then the plastic container was put in ultrasonic bath for approximately 20 minutes treatment to disintegrate strongly aggregated particles. The resulting slurry was then sieved through a 0.063 mm (63-μm) sieve. The portion of the sample's slurry (suspension) that passed the 63-μm sieve was transferred into a glass cylinder container (Andreessen Pipette) for sedimentation. All the glass cylinder containers have the same length of 10 cm from the top, so they can give the same sedimentation time of about 7.36 hours. The clay fraction (<2 μm) was extracted from a suspension of the bulk sample by a method based on Stokes' law where the particles settling speed (velocity) follows Stokes' settling law:

$$V = \frac{2R^2.g\left(\rho_g - \rho_w\right)}{9\mu}, \qquad t = \frac{h}{v}$$

where, V is settling speed of the particles, R is average radius of the particles (cm), (all particles diameters are assumed the same and equal 2 μm), g is acceleration of gravity = 9.81 m/s^2, ρ_g and ρ_w are density of the particles (ρ_g = 2.65 g/cm^3) and the suspension fluid (ρ_w = 1 g/cm^3), respectively. μ is viscosity of suspension fluid = 0.95–1.0 poise (it depends on temperature that ranges between 20^{o} C–22^{o} C), h is the height of the suspension column in the pipette (10 cm), t is the time required for settlement before extracting the <2μm fraction below the ''0''mark on the Andreessen Pipette.

Since the settling speed and the 10 cm distance (height) that particles larger than 2 μm travel are known, so the required time that particles do need to settle below the 10 cm is calculated as about 442 min (7.36 hours). We assumed that the remaining suspended material in the top 10 cm of the glass cylinder represents the <2 μm particles of the sample because they settle slower than the coarser particles according to the Stokes' law. To concentrate the clay fraction (<2 μm), the resulting slurry in the top 10 cm was carefully decanted into a special centrifuge plastic flask and tightly

closed then centrifuged for 20 minutes at velocity of 5000 rpm. The excess water was removed and the remaining concentrated clay pasta was mixed well with a spatula and then extracted and smeared into cavity (60 μm deep) of a glass slide (27x45 mm) to make an oriented mount. The smeared slide was left for air-drying overnight/for 24 hours at the laboratory temperature of about 22°C. To identify the mineralogy of the clay-size fraction (<2 μm), XRD analysis was done, on each air-dried smear slide oriented sample, in the interval 2°–35° 2θ at step 0.1° 2θ per second. An additional slow scanning speed, at 0.01° 2θ per second, was also done for the interval 24°–26° 2θ. The slower scanning was done to accurately separate out 002 kaolinite reflections from 004 chlorite reflections. Each air-dried smeared slide was subsequently exposed to liquid ethylene glycol and heating treatments as explained below.

3.2.1 Glycolation with ethylene glycol

The air-dried smeared slide samples were placed in a desiccator and expose to a vapour supersaturated in ethylene glycol at 60° C for two days. Then, XRD analysis was run in the interval 2°–35° 2θ. The glycolated sample confirms the presence or the absence of expandable clays such as smectite.

3.2.2 Heat treatment

To confirm the presence or the absence of smectite, the glycolated sampes were heated to 350°C (for 2 hours) after which the XRD analysis was done in the interval 2°–35° 2θ. To distinguish chlorite reflections (004) from kaolinite reflections (002), each 350°C heated slide was further heated to 550° C (for 2 hours) and again the XRD analysis was done in the interval 2°–35° 2θ. At 350° C kaolinte & chlorite are interfere but by heating up to 550° C, kaolinite will disappear while chlorite will survive. Chlorite & illite are not affected by heating treatment up to 550° C or when the sample is glycolated.

3.3 Quantification

The clay minerals were identified as main groups: illite, smectite, kaolinite, and chlorite. Area and height of peaks (as a measure of peak intensity) of each mineral phase were determined by an automated procedure, and quantified according to Poppe et al. (2001). The bulk mineral composition is assessed semi-quantitatively.

4. Risk assessment

Extra care will be taken during sample preparation to prevent sample contamination or lost of any clay fraction during sample cleaning to remove salts from soil specimens. Due to sensitivity of some clay minerals, extra care was also taken during heat treatment of samples as well as during exposed to X-ray. After heating to 350° C and 550° C, samples were left to cool down to the room temperature before removed out of oven and putting into XRD machine.

5. Measuring range, limit of detection and accuracy

We have performed quality control checks frequently. Reference quartz from Roth/Bie and Berntsen, as well as the Stevens chalk (calcite), were included in quality control checks. If the results were outside the acceptable range (±0.7%) on d-spacing based on quartz, the position of the sample holder must be checked. Samples were prepared and kept at the laboratory temperature at about 22°C.

Physical properties of sediments are controlled by several factors such as mineralogical composition, texture, burial stress and sediment stiffness. The main objective here was to investigate, evaluate and characterize the influence of these factors on the properties of chalk, siliceous ooze and shale. If the factors governing physical properties are well defined and understood, this would benefit various areas in petroleum industry. We proposed a predictive equation for chalk porosity reduction with burial stress. The equation is relevant for hydrocarbon exploration. A new approach for obtaining reliable grain density and porosity of siliceous ooze is proposed and it is useful for the petrophysical community. The elastic moduli of shale are related to mineralogy and the deformation behaviour of the Palaeogene clay is explained as totally elastic.

DTU Civil Engineering
Department of Civil Engineering
Technical University of Denmark

Brovej, Building 118
2800 Kgs. Lyngby
Telephone 45 25 17 00

www.byg.dtu.dk

ISBN: 9788778773852
ISSN: 1601-2917